



HAL
open science

Study of the molecular mobility of biosourced polyesters with controlled chemical structures

Kylian Hallavant

► To cite this version:

Kylian Hallavant. Study of the molecular mobility of biosourced polyesters with controlled chemical structures. Material chemistry. Normandie Université, 2024. English. NNT : 2024NORMR041 . tel-04783629

HAL Id: tel-04783629

<https://theses.hal.science/tel-04783629v1>

Submitted on 14 Nov 2024

HAL is a multi-disciplinary open access archive for the deposit and dissemination of scientific research documents, whether they are published or not. The documents may come from teaching and research institutions in France or abroad, or from public or private research centers.

L'archive ouverte pluridisciplinaire **HAL**, est destinée au dépôt et à la diffusion de documents scientifiques de niveau recherche, publiés ou non, émanant des établissements d'enseignement et de recherche français ou étrangers, des laboratoires publics ou privés.



Normandie Université



THÈSE

Pour obtenir le diplôme de doctorat

Spécialité **PHYSIQUE**

Préparée au sein de l'**Université de Rouen Normandie**

Etude de la mobilité moléculaire de polyesters biosourcés à structures chimiques contrôlées

Présentée et soutenue par
KYLIAN HALLAVANT

Thèse soutenue le 03/10/2024
devant le jury composé de :

MME ALLISSON SAITER-FOURCIN	Professeur des Universités - Université de Rouen Normandie (URN)	Directeur de thèse
M. DENIS LOURDIN	Directeur de Recherche - Centre Régional de l'Inrae Angers-Nantes Pays de la Loire	Président du jury
MME ANTONELLA ESPOSITO	- Université de Rouen Normandie (URN)	Co-encadrant
M. FRANCK COLLAS	-	Membre du jury
M. ERIC LEROY	Directeur de Recherche - Nantes Université	Rapporteur du jury
MME ALICE MIJA	Professeur des Universités - UNIVERSITE NICE SOPHIA ANTIPOLIS	Rapporteur du jury

Thèse dirigée par **ALLISSON SAITER-FOURCIN** (GROUPE DE PHYSIQUE DES MATERIAUX)



General content

Introduction	11
Chapter I - State of the art.....	17
I. Crystallization kinetics	18
I.1 Three-phase model.....	18
I.2 Nucleation process	20
I.3 Hoffman-Lauritzen theory	23
I.4 Isothermal and non-isothermal crystallization	24
I.5 Crystalline polymorphism.....	26
I.6 Melting	27
II. The glassy state	28
II.1 Amorphization upon cooling	28
II.2 The glass transition.....	29
II.3 Physical aging	37
III. Polyesters: a class of polyvalent polymers.....	39
III.1 Development of bio-sourced and biodegradable polyesters.....	39
III.2 Diol length variation and odd-even effect.....	41
III.3 Fields of application.....	44
References	46
Chapter II - Materials and methods	57
I. Materials.....	58
I.1. Poly (lactic acid) (PLA)	58
I.2. Poly (alkylene <i>trans</i> -1,4-cyclohexanedicarboxylate)s	58
I.3. Co-polyesters of hydroxy-fatty acids.....	61
II. Experimental techniques	63
II.1. Structural characterization	63
II.2. Thermal analysis	67
References	80
Chapter III - Crystallization kinetics of co-polyesters obtained from tomato peel agro-wastes	83
I. Preliminary thermal analyses of the monomers and of the polyester networks	85
II. Cooling-rate dependence of the crystallization process	90
III. Isothermal crystallization kinetics of the polyester network.....	93

III.1 Thermal protocol.....	93
III.2 Estimation of the melting enthalpy Δh_m° of the polyester network	95
III.3 Application of the Avrami model for isothermal crystallization	97
IV. Effect of polymerization on the crystallization kinetics.....	99
IV.1 Thermal protocol.....	99
IV.2 FSC measurements.....	101
IV.3 Application of the Avrami model for isothermal crystallization	104
IV.4 Melting enthalpy Δh_m°	105
References	111
Chapter IV. Crystallization kinetics of a series of poly (alkylene <i>trans</i>-1,4-cyclohexanedicarboxylate).....	115
I. Preliminary analyses.....	116
I.1 FTIR spectroscopy.....	116
I.2 Conventional TGA.....	117
I.3 Temperature-modulated TGA (MT-TGA)	118
I.4 DSC measurement.....	120
I.5 TOPEM measurements.....	123
II. Non-isothermal crystallization	125
II.1 Critical cooling rate.....	125
II.2 Application of the three-phase model	133
II.3 Ozawa model.....	136
III. Isothermal crystallization.....	138
III.1 Equilibrium melting temperature T_m° using the Hoffman-Weeks method	138
III.2 Barandiarán and Colmenero's method	140
III.3 Kinetics investigation of the high-temperature crystalline form	142
III.4 Crystallization kinetics of PPeCE.....	146
III.5 Time-Temperature-Transformation diagrams	148
Conclusion.....	151
References	152
Chapter V – Molecular mobility of the amorphous phase	157
I. Glass transition kinetics of poly (lactic acid)	158
I.1. Vitrification function.....	159
I.2. Fragility index	160
I.3. Temperature fluctuation δT	162
I.4. Characteristic length ξ_α	164

I.5. Frequency dependence of the glass transition temperature.....	165
I.6 Comparison between calorimetric and dielectric relaxation spectroscopy experiments.....	167
II. Glass transition kinetics of the PCHs.....	167
II.1 Vitrification function.....	168
II.2 Fragility index	169
II.3 Characteristic length ξ_{α}	171
III. Towards a generalization of the temperature dependence of ξ_{α}?.....	177
Conclusion.....	181
Conclusions and prospects.....	186
Appendix 1: Table of acronyms and notations.....	190
Appendix 2: ^1H-NMR spectra	192
Scientific communications	194

Acknowledgments

En premier lieu je tiens à remercier ma directrice de thèse Allisson Saiter-Fourcin, pour sa réactivité, sa disponibilité et son suivi sans faille que ce soit sur le plan administratif ou scientifique, pour les opportunités et les collaborations dont j'ai pu bénéficier, pour m'avoir fait confiance et m'avoir donné beaucoup de liberté au cours de ces travaux de recherche.

J'aimerais à présent remercier ma co-encadrante de thèse Antonella Esposito pour son soutien constant, son apport scientifique pertinent et ses remarques enrichissantes, pour les sandwiches à la porchetta et le panpepato, le co-voiturage et les moments incroyables passés à Bologne et à Terni... Nous nous sommes rencontrés pour la première fois lors d'un forum des Masters où elle a donné envie à un étudiant de licence chimie de suivre un parcours en physique des matériaux, pour après deux stages ensemble et trois ans de thèse en arriver là, je pense qu'on peut dire que la boucle est bouclée. Allora ti ringrazio per quei momenti e nella speranza di crearne di nuovi !

Je suis très reconnaissant de l'aide financière apportée par la Région Normandie et le LabEX EMC³. Je tiens également à remercier le directeur du Groupe de Physique des Matériaux Xavier Sauvage pour m'avoir accueilli au sein du laboratoire.

Je tiens ensuite à exprimer ma reconnaissance envers mon jury de thèse et en particulier mes deux rapporteurs, Éric Leroy et Alice Mija, pour avoir accepté de rapporter ces travaux de thèse, pour leurs retours constructifs et les discussions que nous avons pu avoir pendant la soutenance. Je souhaite également remercier Franck Collas, pour avoir accepté le rôle d'examineur, pour son aide et sa réactivité en cas de pépin. Enfin je souhaite remercier le président du Jury, Denis Lourdin, pour la collaboration que nous avons pu avoir pendant la thèse, pour ses retours constructifs et pour avoir fourni ces fameux polyesters extraits de la cutine de tomate.

Vorrei ora ringraziare i collaboratori del Dipartimento d'Ingegneria Civile, Chimica, Ambientale e dei Materiali (DICAM) di Bologna, la Prof.ssa Nadia Lotti, la Dott.ssa Michelina Soccio e la Dott.ssa Giulia Guidotti per la loro accoglienza, per la sintesi dei PCHs et il loro aiuto nella comprensione dei vari meccanismi chimici. Vorrei anche ringraziare Gianfranco e gli altri dottorandi del DICAM per la loro accoglienza e le vivaci discussioni a pranzo.

I am deeply grateful to Jürgen E.K. Schawe for his advice, his helpful comments, his insight and all the discussions we had that were crucial for this work and definitely shaped me as a researcher.

Mes remerciements vont ensuite aux autres membres du département Systèmes Désordonnés et Polymères, Laurent Delbreilh, Nicolas Delpouve, Marie-Rose Garda, Éric Dontzoff et Clément

Demarest, pour leur aide et leur disponibilité dans tout ce qui était gestion du parc instrumental et ambiance pendant les pauses café. Je souhaite également remercier Éric Dargent et Valérie Dupray pour avoir accepté de faire partie de mon CSI et pour leur suivi au cours de ces trois années.

J'ai à présent une pensée particulière pour les doctorants du GPM passés et futurs, en commençant par Clément qui m'a initié à cette fabuleuse machine qu'est la Flash DSC, Alexandre pour sa formation express sur DSC/TGA, mes deux anciennes voisines de bureau Blandine et Tasnim pour leurs anecdotes, leur bonne humeur et les fabuleux gâteaux, Sanaa pour les pauses café et cette photo mémorable, Alexis pour les chouquettes, Loic pour les anecdotes incroyables et Florian que je n'aurai malheureusement connu que pour un court laps de temps. Je pense spécialement à mes anciens camarades de promo Yuri et J-B, que j'ai pu connaître pendant le Master avant que nous poursuivions ensemble en doctorat et à la team du deuxième étage, Yanis, Alexandre, Arnaud, Mehdi, Omar, Mohammed, Richel, pour toutes les parties de cartes, les mots inventés au SUTOM, les discussions philosophiques et les nombreux fous rires, que ce soit au labo ou en dehors. J'adresse également un grand merci à Jules, colocataire de bureau et demi-frère de thèse, embarqués ensemble dans cette folle aventure qu'est le doctorat en physique des matériaux, entre sessions de brainstorming au tableau sur la notion de fragilité et sessions JDR du dimanche après-midi. Je pense également à la team du premier, Aïssatou, Matteo, Onkar, Christian, Luis, Samba et Sélia qui trouvera j'espère le temps de lire Dune après notre soutenance.

Je tiens à remercier tous les étudiants avec qui j'ai travaillé et que j'ai eu l'opportunité d'encadrer de près ou de loin dans leurs divers stages et projets de recherche, notamment Yurley, Julien, Jeremy, Jason, Romane et surtout Marouane dont j'ai pu voir la transformation de jeune stagiaire M1 découvrant la vie de labo à doctorant deuxième année enseignant en astrophysique.

Pour finir je voudrais remercier et exprimer toute mon affection à mes amis de longue date et à ma famille, qui m'a toujours soutenu et que j'ai eu la joie de voir s'agrandir durant ces trois années de thèse.

Introduction

Polymers play an increasing role in manufacturing processes and their production keeps on growing, especially in the packaging industry, as rapid worldwide urbanization along with rising disposable income result in increased demand for packaged food and consumer goods [1]. Meanwhile, the decline of fossil



resources and the raise of collective awareness regarding the environmental impact of plastic waste encouraged industrials and researchers to look for possible alternatives to petroleum-based polymers with reduced carbon footprint and environmental risks. This endeavor is further supported by the legislation across the globe imposing strict regulations regarding the use of single-use plastics. For instance, the European Union (EU) recently published a directive restricting the commercialization of targeted single-use consumer goods when sustainable alternatives are available.

Bio-sourced and/or biodegradable polyesters stood out thanks to their easiness of production, versatility and barrier performances, and because the reactive compounds necessary for their synthesis can be extracted from biomass sources for mass production [2]. Polyesters can be obtained using solvent-free polycondensation processes and they offer tunable properties, which makes them appealing for a wide range of applications. Some studies also found that compostable and bio-based packages held the highest appeal to consumers [3]. Recently, poly (ethylene 2,5-furanoate) (2,5-PEF) attracted a lot of attention due to its promising mechanical and barrier properties, as well as to the fact that it can be obtained from renewable sources. Moreover, the properties of 2,5-PEF can be fine-tuned by changing the number of methylene groups in the repeating unit [4], by combining different amounts of 2,5- and 2,4-furandicarboxylic acid with different diols to form copolyesters [5], or in combination with amide functions [6]. At the Groupe de Physique des Matériaux (GPM), the PhD work carried out by Dr. Aurélie Bourdet (defense in March 2020) gave some insight on the molecular mobility of a series of bio-based polyesters with two main position isomers of furandicarboxylic acid (FDCA), that is to say 2,5-FDCA and 2,4-FDCA. She investigated the relationship between the microstructure and the physical properties of the homopolymers and copolymers based on both 2,5-FDCA and 2,4-FDCA combined with ethylene glycol, and evidenced the crucial role of isomerism in the resulting macroscopic properties [7]. Later on Dr. Clément Fosse (defense in December 2020) studied the establishment of the Rigid Amorphous Fraction (RAF) in 2,5-PEF and polyhydroxyalkanoates (PHA), another promising set of polyesters whose monomers can be produced by micro-organisms [8]. He also evidenced the effect of the alkyl chain length in the repeating unit of furan-based polyesters on

their molecular mobility and backbone flexibility, concluding that it is a key parameter governing the intermolecular interactions and the packing efficiency of the chains in the amorphous phase.

Through an increase in the R&D activities dedicated to the production of polymers from renewable resources, and in particular agricultural wastes, innovative synthesis paths were uncovered, leading to the obtention of original smart materials with potential applications for the packaging industry or in the bio-medical field. Two polyesters, or rather two series of polyesters, will be studied throughout this work. The first is a series of co-polyester based on hydroxy-fatty acids whose main component, the 9(10)-16 dihydroxyhexanedecanoic acid, could be extracted from the cutin of industrial tomato-peel wastes [9-10]. This part was realized in collaboration with Dr. Denis Lourdin, Research Director at the Institut National de Recherche pour l'Agriculture, l'Alimentation et l'Environnement (INRAE) in Nantes (France). The second is a series of poly (alkylene *trans*-1,4-cyclohexanedicarboxylate)s (PCHs), whose synthesis was realized at the Dipartimento di Ingegneria Civile, Chimica, Ambientale e dei Materiali (DICAM) in Bologna (Italy). The acidic component used for their synthesis, the *trans*-1,4-cyclohexanedicarboxylic acid, can be derived from bio-based terephthalic acid, which in turn can be obtained from limonene (terpene mostly found in citrus peels) [11, 12].

As newly synthesized polyesters, two challenges arise, i.e. limited quantity of material available and a lack of calorimetric data regarding these systems. This PhD thesis will therefore focus on the thermal characterization of the aforementioned series of polyesters based on either hydroxy-fatty acids or *trans*-1,4-cyclohexanedicarboxylic acid, in order to understand the intrinsic relationship between chemical structure and microstructure, which is essential for the control of the macroscopic properties, through the variation of two parameters, e.g. the crosslinking density and the length of the alkyl chain in the backbone of the repeating unit. The relevance of using specific calorimetric techniques for the investigation of these materials will be developed as well.

The chapters of this manuscript are organized as follows:

Chapter I gives an overview of the crystallization kinetics, and brushes over several models used for the interpretation of the crystallization kinetics, the description of the glassy state, and the parameters allowing the description and quantification of the relaxation of the amorphous phase (fictive temperature, fragility index, aging process...). This chapter also gives an overview of the main characteristics, advantages and uses of polyesters.

Chapter II is divided in two sections. The first section introduces the polyesters studied in this work, that is to say the co-polyesters extracted from tomato-peel agro-industrial waste products and the

poly (alkylene *trans*-1,4-cyclohexanedicarboxylate) (PCHs), but also the poly (L-lactic acid) (PLA), which served as a “model” material. The second section of this chapter introduces the experimental set-ups, techniques and protocols used throughout this work, and in particular the structural characterization and thermal analysis techniques.

Chapter III provides results on the crystallization kinetics of the co-polyesters synthesized from cutin-based monomers in an attempt to estimate the equilibrium melting enthalpy Δh_m° necessary for the calorimetric estimation of the crystalline fraction X_c . A protocol for the in-situ polymerization of the monomers is presented, whose objective was to assess the impact of the crosslinking density, and therefore of the average chain length between crosslink junctions, on the molecular mobility of these materials.

Chapter IV explores the crystallization kinetics of PCHs and a special attention is paid to their respective glass forming-ability (GFA). Isothermal crystallization analyses were carried out to construct the Time-Temperature-Transformation (TTT) diagrams and identify the different crystalline structures formed in different cooling conditions. The crystallization kinetics measured under isothermal and non-isothermal conditions will be discussed according to the methods proposed by Avrami and Ozawa.

Finally, Chapter V focuses on the relaxation dynamics of the amorphous phase of PCHs through the concept of Cooperative Rearranging Regions (CRR) introduced by Adam and Gibbs [13]. The fragility indices were estimated, and the temperature dependence of the characteristic length was assessed.

Appendix 1 provides a table with the acronyms and notations used throughout the thesis. Appendix 2 shows the ^1H -NMR spectra of the PCHs.

This research work was financially supported by the Normandy region (France) and conducted at the laboratory Groupe de Physique des Matériaux (GPM, UMR CNRS 6634), University of Rouen Normandie. The materials of interest are issued from collaborations with the Institut National de Recherche pour l'Agriculture, l'Alimentation et l'Environnement (INRAE, UR1268 BIA), Nantes (France), and the Dipartimento di Ingegneria Civile, Chimica, Ambientale e dei Materiali (DICAM), Bologna (Italy).

References

- [1] « <https://www.openpr.com/news/3574199/biopolymers-market-to-see-incredible-growth-during-2024-2031>, consulted on the 08/07/24 ».
- [2] X. Zhang, B. H. Tan, et Z. Li, « Biodegradable polyester shape memory polymers: Recent advances in design, material properties and applications », *Materials Science and Engineering: C*, vol. 92, p. 1061-1074, nov. 2018, doi: 10.1016/j.msec.2017.11.008.
- [3] D. Taufik, M. J. Reinders, K. Molenveld, et M. C. Onwezen, « The paradox between the environmental appeal of bio-based plastic packaging for consumers and their disposal behaviour », *Science of The Total Environment*, vol. 705, p. 135820, févr. 2020, doi: 10.1016/j.scitotenv.2019.135820.
- [4] D. G. Papageorgiou *et al.*, « Fast Crystallization and Melting Behavior of a Long-Spaced Aliphatic Furandicarboxylate Biobased Polyester, Poly(dodecylene 2,5-furanoate) », *Ind. Eng. Chem. Res.*, vol. 55, n° 18, p. 5315-5326, mai 2016, doi: 10.1021/acs.iecr.6b00811.
- [5] S. Thiyagarajan *et al.*, « Synthesis and Thermal Properties of Bio-Based Copolyesters from the Mixtures of 2,5- and 2,4-Furandicarboxylic Acid with Different Diols », *ACS Sustainable Chem. Eng.*, vol. 7, n° 22, p. 18505-18516, nov. 2019, doi: 10.1021/acssuschemeng.9b04463.
- [6] L. Papadopoulos *et al.*, « Unlocking the potential of furan-based poly(ester amide)s: an investigation of crystallization, molecular dynamics and degradation kinetics of novel poly(ester amide)s based on renewable poly(propylene furanoate) », *Polym. Chem.*, vol. 12, n° 38, p. 5518-5534, 2021, doi: 10.1039/D1PY00713K.
- [7] « Aurélie Bourdet. Relationship between the structure and the physical properties of polymers based on furandicarboxylic acid obtained from biomass. Materials Science [cond-mat.mtrl-sci]. Normandie Université, 2020. English. (NNT : 2020NORMR113). (tel-03376525) ».
- [8] « Clément Fosse. Understanding the role of the rigid amorphous fraction in polyesters. Material chemistry. Normandie Université, 2020. English. (NNT : 2020NORMR064). (tel-03934777) ».
- [9] M. Marc *et al.*, « Bioinspired co-polyesters of hydroxy-fatty acids extracted from tomato peel agro-wastes and glycerol with tunable mechanical, thermal and barrier properties », *Industrial Crops and Products*, vol. 170, p. 113718, oct. 2021, doi: 10.1016/j.indcrop.2021.113718.
- [10] M. Marc *et al.*, « From Tomato Pomaces Biorefinery to Biobased Shape-Memory Semicrystalline Polyester Networks », *ACS Sustainable Chem. Eng.*, vol. 12, n° 6, p. 2191-2202, févr. 2024, doi: 10.1021/acssuschemeng.3c05713.
- [11] M. Colonna *et al.*, « Synthesis and radiocarbon evidence of terephthalate polyesters completely prepared from renewable resources », *Green Chem.*, vol. 13, n° 9, p. 2543, 2011, doi: 10.1039/c1gc15400a.
- [12] G. Guidotti, M. Soccio, V. Siracusa, M. Gazzano, A. Munari, et N. Lotti, « Novel Random Copolymers of Poly(butylene 1,4-cyclohexane dicarboxylate) with Outstanding Barrier Properties for Green and Sustainable Packaging: Content and Length of Aliphatic Side Chains as Efficient Tools to Tailor the Material's Final Performance », *Polymers*, vol. 10, n° 8, Art. n° 8, août 2018, doi: 10.3390/polym10080866.
- [13] G. Adam et J. H. Gibbs, « On the Temperature Dependence of Cooperative Relaxation Properties in Glass-Forming Liquids », *The Journal of Chemical Physics*, vol. 43, n° 1, p. 139-146, juill. 1965, doi: 10.1063/1.1696442.

Chapter I - State of the art

Content

I. Crystallization kinetics	18
I.1. Three-phase model.....	18
I.2. Nucleation process	20
I.3. Hoffman-Lauritzen theory.....	23
I.4. Isothermal and non-isothermal crystallization	24
I.5. Crystalline polymorphism.....	26
I.6. Melting	27
II. The glassy state	28
II.1. Amorphization upon cooling	28
II.2. The glass transition.....	29
II.3. Physical aging	37
III. Polyesters: a class of polyvalent polymers.....	39
III.1. Development of bio-sourced and biodegradable polyesters.....	39
III.2. Diol length variation and odd-even effect.....	41
III.3. Fields of application.....	44
References	46

I. Crystallization kinetics

I.1 Three-phase model

Polymers are composed of long macromolecular chains entangled with each other in random coils [1]. Crystallization occurs when polymer chains partially align to form locally ordered regions (crystallites), which can grow radially into lamellae and eventually turn into bigger structures called spherulites, as represented in **Figure I.1**. Due to the entanglements, polymers cannot fully crystallize and form instead semi-crystalline microstructures made of crystalline domains (the crystalline phase) embedded in a disordered amorphous environment. The two-phase model provides the simplest way of describing the complex microstructure formed in semi-crystalline materials. In this model, the sum of the crystalline and the amorphous fractions, respectively X_c and X_{am} , is equal to one:

$$X_c + X_{am} = 1 \quad Eq.1$$

These fractions can be quantified using different experimental techniques, such as Differential Scanning Calorimetry (DSC) [2], Fourier Transform Infrared Spectroscopy (FTIR) [3], Dielectric Relaxation Spectroscopy (DRS) [4] or X-ray diffraction (XRD) [5] among others. Calorimetry in particular can inform on the presence of a residual amorphous phase, which is detected as a heat capacity step at the glass transition temperature T_g , i.e. the temperature at which the glassy, rigid amorphous domains turn into a rubbery or liquid-like state with higher molecular mobility. On the other hand, the crystalline domains turn from the solid to the liquid state at the melting temperature T_m . Depending on the perfection of chain folding and on the distribution of lamellae's thickness, melting will take place on a more or less extended temperature range, and at relatively high or low melting temperatures.

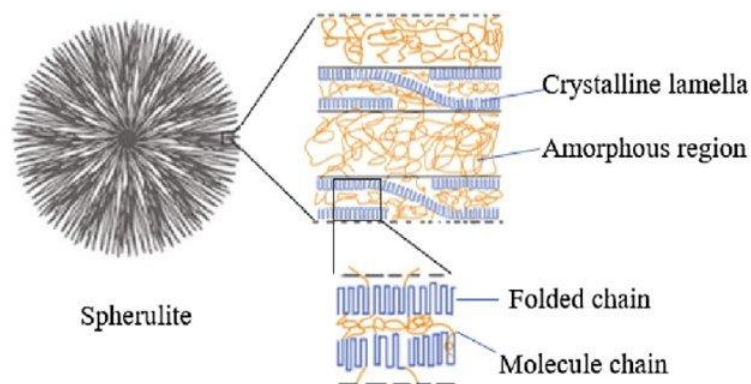


Figure I.1. Schematic representation of crystalline lamellae growing into a spherulite [from Wang et al. [6]].

The two-phase model is appealing due to its simplicity; however, it generally does not accurately describe the microstructure, especially when the crystalline content is high, and often diverges from unity. A better description is provided by the three-phase model, in which an additional “phase” is introduced, the Rigid Amorphous Fraction (RAF) [7]. This fraction acts as an interphase between the crystalline and the unconfined amorphous domains (referred to as the Mobile Amorphous Fraction, MAF) as represented in **Figure I.2**. RAF mobility is hindered due to its proximity to the crystals; consequently, the RAF does not undergo glass transition in the same temperature range as the MAF [8]. The relative amount of crystalline, rigid amorphous, and mobile amorphous fractions depend on the thermal history [9], including the crystallization temperature [10] and the cooling rates used to form the microstructure [11].

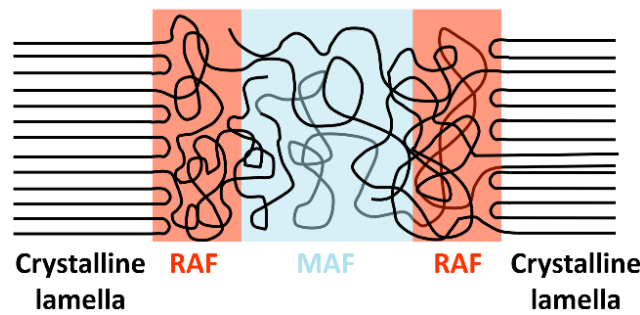


Figure I.2. Schematic representation of the three-phase model.

The mobile amorphous fraction X_{MAF} can be estimated by measuring the specific heat capacity step Δc_p at T_g with calorimetry:

$$X_{MAF} = \frac{\Delta c_p}{\Delta c_p^0} \quad \text{Eq. 2}$$

where Δc_p^0 is the specific heat capacity step at T_g for the same material in its fully amorphous state.

The crystalline fraction X_c can be estimated by calorimetric measurements according to **Eq. 3**:

$$X_c = \frac{\Delta h_m - \sum \Delta h_{cc}}{\Delta h_m^0} \quad \text{Eq. 3}$$

where Δh_m is the melting enthalpy normalized by mass, Δh_{cc} is the cold-crystallization enthalpy, and Δh_m^0 is the theoretical melting enthalpy of a fully crystalline material. This value can generally be found in handbooks for the most common polymers, and experimental procedures were developed to access Δh_m^0 for relatively new materials [12].

I.2 Nucleation process

The crystallization kinetics are generally described by the Classical Nucleation Theory (CNT), which considers two stages, i.e. nucleation followed by crystal growth. Nucleation can be activated via different mechanisms (homogeneous, heterogeneous, self-nucleation) and consists in the formation of clusters with the same degree of order as the final crystal. Cluster formation is associated to the Gibbs energy ΔG_n which has two contributions, the first related to the molecular aggregation, and the second to the surface tension. Assuming a spherical shape of the clusters, ΔG_n can be expressed as:

$$\Delta G_n = -\frac{4}{3}\pi r^3 \Delta g + 4\pi r^2 \gamma \quad \text{Eq. 4}$$

where Δg represents the variation of Gibbs free energy per volume unit, γ is the interfacial energy per area unit, and r is the cluster radius. These two opposing contributions (thermodynamic and surface tension driving forces) result in the existence of a critical size of the nuclei r^* [13]. When the volumetric contribution becomes prevalent, the formation of nuclei becomes energetically favorable; this condition defines the critical radius r^* and the associated energy barrier ΔG_n^* expressed as:

$$r^* = \frac{2\gamma}{\Delta g} \quad \text{Eq. 5}$$

$$\Delta G_n^* = \frac{16\pi\gamma^3}{3(\Delta g)^2} \quad \text{Eq. 6}$$

A double condition ($r > r^*$ and $\Delta G_n^* < 0$) should therefore be respected for a cluster to grow beyond its critical size into a crystal. In case of melt crystallization, the energy barrier ΔG_n^* decreases when the supercooling ΔT (defined as $\Delta T = T_m^\circ - T_c$ with T_m° the thermodynamic equilibrium melting temperature) increases, since supercooling acts as a driving force for cluster formation. According to equilibrium thermodynamics, it all depends on the difference in Gibbs free energy between the liquid and the solid state, ΔG_c . This quantity can be interpreted as the thermodynamic driving force for structure formation [14], and depends on the supercooling ΔT as shown in **Figure 1.3**.

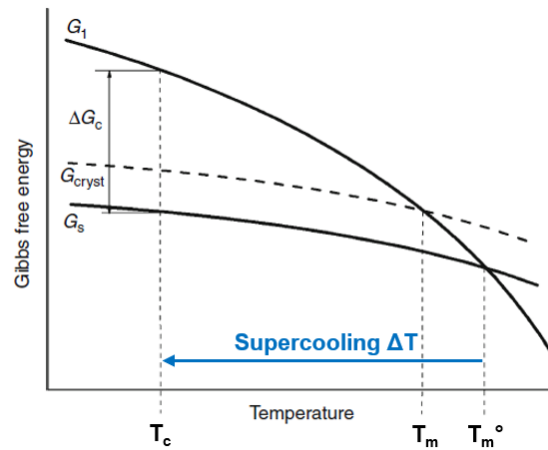


Figure I.3. Scheme of the Gibbs free energy as a function of temperature, illustrating melting, crystallization and supercooling (adapted from Schawe et al [14]).

ΔG_n is related to ΔG_c through Eq.7 [14]:

$$\Delta G_n(T) = \frac{C_\sigma}{\Delta G_c(T)^\kappa} \quad \text{Eq.7}$$

where C_σ is a parameter depending on the Gibbs free surface enthalpy and the geometry of the growing phase, and κ is an integer. In particular, $\kappa = 1$ if the crystallization process is driven by crystal growth, and $\kappa = 2$ if the crystallization process is determined by nucleation. From a thermodynamic point of view, crystallization is favored when the temperature of the supercooled liquid decreases because of a higher driving force. However, from a kinetic point of view, crystallization is hindered due to the increased viscosity. The highest crystallization rate is therefore reached when the positive contribution representative of supercooling equalizes the negative contribution originating from molecular motions.

In a supposedly homogeneous liquid, no nuclei are present. Homogeneous nucleation consists in the stochastic formation of supercritical nuclei. On the other hand, heterogeneous nucleation occurs on preferential sites such as impurities, where the energetic barrier is reduced and the development of clusters is favored [13]. At a given temperature, the time $t(T)$ needed to crystallize a given portion x of the supercooled liquid can be calculated as:

$$t(T) = \left(\frac{3 \ln(1-x)}{\pi I(T)u(T)^3} \right)^{\frac{1}{4}} \quad \text{Eq.8}$$

where $I(T)$ and $u(T)$ is the nucleation and crystal growth rate respectively.

In case of homogeneous nucleation, the homogeneous nucleation rate $I_{hom}(T)$ and the crystal growth rate $u(T)$ are calculated as:

$$I_{hom}(T) = \frac{A_v}{\eta(T)} \exp\left(-\frac{16\pi}{3k_B T} \frac{\gamma^3}{\Delta g_{l-x}(T)^2}\right) \quad Eq. 9$$

$$u(T) = \frac{k_B}{3\pi a_0^2} \frac{T}{\eta(T)} \left(1 - \exp\left(\frac{n}{k_B} \frac{\Delta g_{l-x}(T)}{T}\right)\right) \quad Eq. 10$$

where A_v is a pre-exponential factor, $\Delta g_{l-x}(T)$ is the difference in volume-specific free energy between the liquid and crystalline states, γ is the energy at the interface between the liquid and the crystal surfaces, a_0 is the average atomic diameter, n is the average atomic volume, and $\eta(T)$ is the temperature-dependent equilibrium viscosity [15].

In case of heterogeneous nucleation, $I_{het}(T)$ is calculated as follows:

$$I_{het}(T) = \frac{A_v}{\eta(T)} \exp\left(-S(\theta) \frac{16\pi}{3k_B T} \frac{\gamma^3}{\Delta g_{l-x}(T)^2}\right) \quad Eq. 11$$

where $S(\theta)$ corresponds to a wetting angle θ between the formed nuclei and their substrate surface:

$$S(\theta) = \frac{1}{4} (2 + \cos(\theta))(1 - \cos(\theta))^2 \quad Eq. 12$$

The temperature dependence of the homogeneous and heterogeneous nucleation rates is represented in **Figure I.4**:



Figure I.4. Temperature dependence of the nucleation rate and its two contributions, i.e. molecular mobility and thermodynamic driving force.

1.3 Hoffman-Lauritzen theory

The theory proposed by Hoffman and Lauritzen (HL) gives a reasonable description of the temperature dependence of polymer crystallization from both the glassy and the molten state [16]. The crystal growth rate G of a linear polymer at a specific crystallization temperature T_c is expressed as [17]:

$$G = G_0 \exp\left[\frac{-U^*}{R(T_c - T_\infty)}\right] \exp\left[\frac{-K_g}{T_c(\Delta T)f}\right] \quad \text{Eq. 13}$$

where G_0 is a pre-exponential factor, U^* is the activation energy characterizing molecular diffusion across the interfacial boundary between the melt and the growing crystal, $T_\infty = T_g - 30$ K is the temperature below which all the motions associated with viscous flow cease, K_g is a nucleation constant, ΔT is the degree of supercooling, and $f = 2 T_c (T_m^0 + T_c)$ is a correction factor accounting for the change in heat of fusion and close to unity at high temperatures [16]. The first exponential term represents the contribution of diffusion to the growth rate, while the second exponential term is related to the contribution of diffusion to the nucleation process. A common approximation of the growth rate G sets it close to the inverse of the half time of crystallization ($G \approx 1 / t_{1/2}$) [17].

Two types of crystallization behavior (regime I and regime II) have been observed in polymers, leading to different expressions for the nucleation rate parameter K_g :

$$K_{gI} = \frac{4b\sigma\sigma_e T_m^0}{\Delta h_f k_B} \quad \text{regime I} \quad \text{Eq. 14}$$

$$K_{gII} = \frac{2b\sigma\sigma_e T_m^0}{\Delta h_f k_B} \quad \text{regime II} \quad \text{Eq. 15}$$

where b represents the layer thickness, σ the lateral surface energy, σ_e the fold surface free energy, Δh_f the heat of fusion per volume unit, and k_B the Boltzmann constant. Regime I corresponds to sequential nucleation (a single nucleus completes one layer of crystal thickness before the formation of another nucleus) and regime II corresponds to the simultaneous formation of several nuclei.

The HL model is broadly accepted, however recent findings highlighted some deviations from the HL predictions [18]. These deviations were imputed on “unconventional crystallization” activated through other mechanisms, such as cross-nucleation [19] and memory effects [20]. Some authors also proposed the existence of mesomorphic layers prior to the appearance of the first crystallites as part of a multi-step process passing over intermediate states [21].

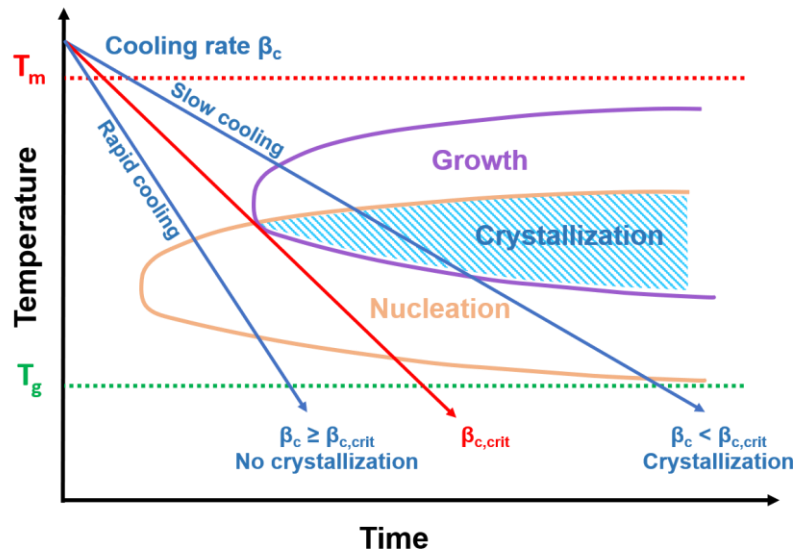


Figure I.5. Schematic representation of the temperature dependence of the nucleation and growth processes.

Figure I.5 represents the temperature dependence of the nucleation and growth processes. Crystallization can only occur when the regions corresponding to the two processes overlap (blue hatched area). Depending on the polymer, the nucleation and growth processes are more or less disjointed, which leads to different ability to crystallize and, by extension, to form a glass. The glass-forming ability (GFA) is also related to the critical cooling rate ($\beta_{c,crit}$) needed to avoid crystallization. Indeed, the lower $\beta_{c,crit}$, the higher the GFA.

I.4 Isothermal and non-isothermal crystallization

The kinetics of thermally activated crystallization is generally assessed using calorimetric approaches under either isothermal or non-isothermal conditions. The relative crystallinity degree defining the degree of conversion is noted α_T under non-isothermal conditions and α_t under isothermal conditions, and is evaluated as [22]:

$$\alpha_T = \frac{\Delta H_T}{\Delta H_{Total}} = \frac{\int_{T_0}^T \left(\frac{dH}{dT}\right) dT}{\int_{T_0}^{T_\infty} \left(\frac{dH}{dT}\right) dT} \quad Eq. 16$$

where dH is the heat released in an infinitesimally small temperature interval dT , and T_0 , T and T_∞ are the onset temperature, an arbitrary temperature in the selected temperature range, and the

endset temperature, respectively. To obtain the expression in isothermal conditions, the temperature T is replaced by the time t .

I.4.1. Johnson-Mehl-Avrami-Kolmogorov equation

In order to accurately simulate the crystallization curve under isothermal conditions (α_t vs time), Avrami proposed a theory based on the so-called extended volume [22]. A simplified form of kinetic equation based on Avrami's theory is the Johnson-Mehl-Avrami-Kolmogorov (JMAK) equation:

$$\alpha_t = 1 - \exp[-K(t_c - t_0)^n] \quad \text{Eq. 17}$$

where α_t is the crystallinity degree under isothermal conditions, K is the temperature-dependent rate constant, n is the Avrami exponent, t_c is the crystallization time, and t_0 is the induction time. The incorporation of t_0 into the JMAK equation gives more reasonable results for the parameters n and K , as shown by Lorenzo et al. [23]. The exponent n is generally an integer giving information on the nucleation process (Table I.1).

Table I.1. Relation between Avrami exponent n and nucleation process.

Growth	Nucleation	
	Heterogeneous	Homogeneous
Three dimensions (3D)	$n = 3$	$n = 4$
Two dimensions (2D)	$n = 2$	$n = 3$
One dimension (1D)	$n = 1$	$n = 2$

I.4.2. Ozawa model

The JMAK equation is based on some assumptions that are not always fulfilled [24, 25], leading to the development of other models such as the modified Avrami equation [26] or the Šesták-Berggren approach to isothermal crystallization [24, 27]. To this day, the majority of the crystallization kinetics experiences are actually performed under non-isothermal conditions [28]. Later on, Ozawa extended the JMAK model to account for crystallization occurring under non-isothermal conditions [29]:

$$\alpha = 1 - \exp\left[\frac{-X(T)}{|\beta_c|^m}\right] \quad \text{Eq. 18}$$

where $|\beta_c|$ is the cooling rate, $X(T)$ is the heating or cooling crystallization function, and m is the exponent related to the crystal nucleation mechanism. Linearization of **Eq. 18** gives:

$$\log[-\ln(1 - \alpha)] = \ln(X(T)) - m \log |\beta_c| \quad \text{Eq. 19}$$

Sometimes the requirements to use these models are not met experimentally, or calculations yield a too large number of parameters difficult to interpret. Other methods were proposed to analyze the kinetic parameters of polymer crystallization [30,31]. Recently, Vyazovkin et al. proposed a review discussing the applicability of the Avrami and Arrhenius equations to non-isothermal crystallization [28]. Model-free kinetics analysis can also be performed using an advanced iso-conversional method for non-isothermal crystallization from the melt [17]. The advanced non-linear iso-conversional method (NLN) based on Vyazovkin's equations [28, 32-34] allows the obtention of the effective activation energy for crystallization as a function of the degree of conversion α without any assumption on the reaction mechanism [18].

1.5 Crystalline polymorphism

Polymorphism is the ability of a material to crystallize in two or more crystalline phases with distinct arrangements and/or conformations of the molecules (or molecular segments) in the crystal lattice. Polymorphism can have a major impact on mechanical [35] and barrier properties [36], as well as photoluminescence [37] and membrane performance [38]. This characteristic is found in many systems, such as metallic alloys [39], liquid crystals [40] and many polymers [41] including poly (lactic acid) (PLA) [42]. Sometimes, a high-temperature peak is associated to the main crystalline form, and the presence of an additional low-temperature peak is related to some mesophase [31].

Different crystalline forms can be obtained with different processing conditions, annealing temperatures [43], and stretching at high draw-ratio and high temperature, as in hot-drawing of melt or solution to produce spun fibers [42], or cooling from the molten state with different cooling rates [44]. In general, this leads to the formation of a crystalline phase with defects, which reorganizes as molecular mobility is facilitated, i.e. upon heating, as in the case of PLA, whose imperfect α' crystalline form turns into the α form upon heating [45, 46].

I.6 Melting

I.6.1 Equilibrium melting temperature

The equilibrium melting temperature T_m^0 corresponds to the theoretical melting temperature of perfect crystals with infinite thickness. Different methods have been proposed for the calculation of T_m^0 . One of the most popular is the Hoffman-Weeks extrapolative method, which is based on the variation of the melting temperature T_m with lamellar thickness, itself dependent on the isothermal crystallization temperature T_c [47]. This theory is based on two assumptions: the thickening coefficient is independent of T_c and the lateral dimensions of the crystalline lamellae must be significantly higher than their thickness. The equation used in the Hoffman-Weeks theory is:

$$T_m = T_m^0 \left(1 - \frac{1}{\beta}\right) + \frac{T_c}{\beta} \quad \text{Eq. 20}$$

where T_m is the melting temperature measured after the isothermal crystallization at T_c and $\beta = d_c/d_c^*$ is the thickening coefficient, equal to the ratio of thicknesses of the grown crystallites d_c to the initial crystalline structures d_c^* . The melting temperatures T_m are converted into lamellae thickness d_c by the Gibbs-Thomson equation:

$$T_m(d_c) = T_m^0 \left(1 - \frac{2\sigma}{\Delta h_m} \frac{1}{d_c}\right) \quad \text{Eq. 21}$$

where T_m^0 is the equilibrium melting temperature, σ is the molar surface free energy of the crystalline lamellae in the final stabilized state, Δh_m is the specific heat of fusion, and d_z is the length of a repeating unit in the unit cell [48, 49].

I.6.2. Equilibrium melting enthalpy

The equilibrium melting enthalpy Δh_m^0 corresponds to the theoretical melting enthalpy of a fully crystalline material. Different methods were proposed to assess this thermodynamic parameter, such as Baur's method, extrapolation to infinite crystal thickness, Flory model for solution-grown crystals, or extrapolation to crystal density [42]. One issue is that different methods often yield different values, e.g. the Δh_m^0 associated to the α -form of the semi-crystalline PLA ranges from 81 J g⁻¹ to 135 J g⁻¹ depending of the method employed [42]. Fosse et al. proposed a protocol relying on Fast Scanning

Calorimetry (FSC), supposing a two-phase semi-crystalline microstructure with a negligible amount of RAF [12].

II. The glassy state

II.1 Amorphization upon cooling

The cooling rate is an important parameter for microstructure, in particular during the solidification of the relaxed melt and the development of specific interactions leading to the formation of supramolecular structures [50, 51]. These structures are responsible for the material's final properties, and therefore the cooling rate is a crucial parameter in many applications, from industrial processing to microbiology [52]. In polymer physics, and more generally in glass physics, the relaxational behavior of glass-forming liquids upon cooling gives precious information on the physical state of the glass.

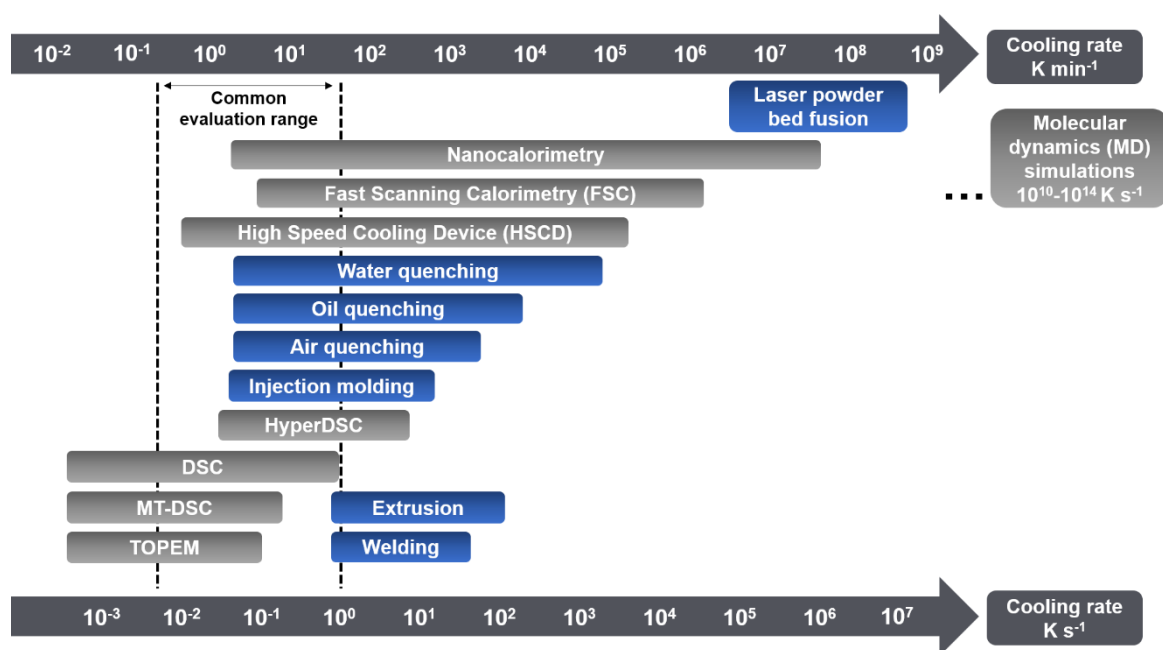


Figure I.6. Typical range of cooling rates achievable with different processing and characterization techniques for different materials including polymers [44, 53-67].

Controlling the cooling rate is a major issue, in particular for industrial processing. Indeed, processing techniques such as injection molding or extrusion can involve high cooling rates, with major impact on the polymer microstructure and final properties, with fast cooling producing more amorphous materials, increased transparency and elongation at break [68] and is also beneficial in terms of

production rate in comparison with slow cooling. **Figure I.6** presents the typical range of cooling rates associated to different processing and characterization techniques.

The critical cooling rate $\beta_{c,crit}$ corresponds to the minimum cooling rate needed to suppress the crystallization process upon cooling, as shown in **Figure I.5**. Vitrification can lead to the formation of two types of glasses, one with nuclei that can grow during subsequent heating (self-doped glass), and one without nuclei (homogeneous glass) [69]. The critical cooling rate is inherently related to a material's ability to crystallize and its GFA (see **Section I.3**). While the chemical nature of the glass-forming liquid is a major determinant (in general metallic alloys will have higher critical cooling rates than polymers), small composition changes can actually make a difference from a polymer to another [70]. The critical cooling rate can be assessed experimentally using differential scanning calorimetry (DSC) for low cooling rates (0.2 to 50 K min⁻¹) and fast scanning calorimetry (FSC) for higher cooling rates (up to 4.10⁴ K s⁻¹). A new experimental apparatus further extended the window for cooling rates up to 10⁶ K s⁻¹ [49, 71]. Recently, the use of molecular dynamics simulations allowed to probe molecular dynamics at the picosecond timescale. While the cooling rate gap between the experiments (up to 10⁶ K s⁻¹) and the simulations (around 10¹² K s⁻¹) is still wide, some fundamental properties (fictive temperature, relaxation enthalpy...) can be well extrapolated [60, 72].

In the literature it is possible to find several ways to estimate the critical cooling rates based on the degree of supercooling, such as the Barandiarán and Colmenero (BC) method [73]:

$$\beta_{c,crit} = \exp\left(A - \frac{B}{(T_m^0 - T_c)^2}\right) \quad \text{Eq. 22}$$

where T_m^0 is the equilibrium melting temperature, T_c is the crystallization temperature, A and B are material constants.

II.2 The glass transition

A basic explanation of vitrification was given by Tammann about 100 years ago in his famous book on glasses and the glass transition [74], where he proposed to consider glasses as undercooled solidified melts. Later on, Jones and Simon proposed a significant extension of this definition, stating that glasses are kinetically frozen-in and thermodynamically non-equilibrium states of the liquid [75]. In 2017, Zanatto et al. added to the general definition the notion of glass transition, stating that glasses spontaneously relax towards the supercooled liquid state and ultimately crystallize in the limit of infinite time [76]. Even though a lot of progress has been made along the years, a general

understanding of glass physics and in particular the mechanisms of glass transition is still one of the most challenging issues in soft matter physics [77].

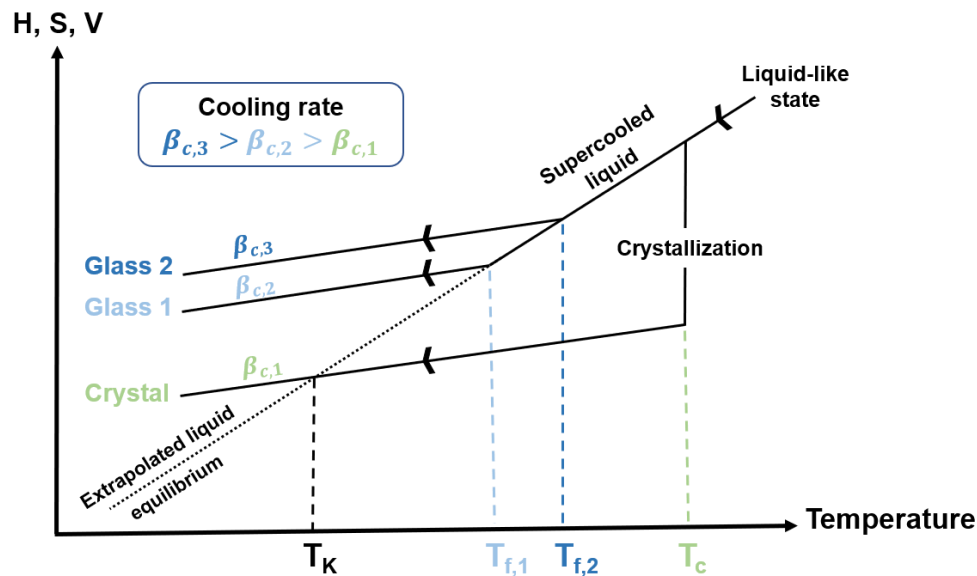


Figure I.7. Dependence of the thermodynamic properties of a glass-forming liquid on temperature.

When a glass-forming liquid is cooled down from the melt at a sufficiently high rate to bypass crystallization, it reaches the supercooled liquid state as represented in **Figure I.7**. Molecular dynamics progressively slow down as temperature decreases, and the supercooled liquid gets denser and more viscous. The characteristic time needed by the molecules to regain equilibrium after external perturbation corresponds to the relaxation time τ . As temperature is further decreased, the supercooled liquid does not have enough time to relax, it falls out of equilibrium, and undergoes vitrification. This transition is associated to a change from a rubbery to a glassy state with no long-range order, and is referred to as the glass transition, a time-dependent and reversible process which exhibits the characteristics of a kinetic transition. Even though the glass transition occurs on a more or less large temperature range, it is generally associated to a single glass transition temperature T_g , conventionally defined as the temperature at which the glass has a relaxation time $\tau = 100$ s (dynamical definition) or a viscosity $\eta = 10^{12}$ Pa s⁻¹ (rheological definition). The temperature T_g depends on intrinsic parameters of the material (chain flexibility, chemical functions, polarity, molar mass...), but also on the analytical technique used to measure it (calorimetry, volumetric analysis, rheology...) as well as on the experimental conditions set for the measurement (time scale, scanning rates, pressure, frequency...), and the previous thermomechanical history and thermodynamic state [78].

As a result, the concept of fictive temperature T_f was developed by Tool [79] as a way to better characterize the thermodynamic state attained by a glass after a given thermal protocol [80, 81]. The fictive temperature depends only on the cooling rate previously used to form the glass, and is independent of the heating rate used for its measurement [82]. The use of T_f is therefore more fundamental because it removes the time dependence of the measurement, leaving only the time dependence of the sample thermal history [78]. As illustrated in **Figure I.7**, T_f corresponds to the intersection of the investigated property (e.g. enthalpy H , specific volume V or entropy S) extrapolated from the low-temperature glass line, with the liquid equilibrium line extrapolated from the high-temperature liquid-like state. The faster the cooling, the less time is allotted to molecules to retain equilibrium, and the glass-forming liquid will fall out of equilibrium faster, thus resulting in higher T_f .

The Kauzmann temperature T_K is considered as a thermodynamic ideal glass transition temperature, for which the configurational entropy ΔS_C is nil, with $\Delta S_C = S_{\text{Liquid}} - S_{\text{Crystal}}$. Below T_K the configurational entropy becomes negative, leading to an infringement of the third law of thermodynamics. This infringement, known as the Kauzmann paradox, is still debated to this day [83, 84].

II.2.1. Fragility concept

There are important differences in the way liquids relax as they approach the glass transition, with rapid or slow variation in dynamic quantities under moderate temperature changes [85]. At high temperature, liquids exhibit a simple Arrhenius behavior of the structural relaxation time $\tau(T)$, as represented in **Figure I.8**. Upon cooling, when the system reaches the crossover region, the high-temperature Arrhenian relaxation splits into the main α relaxation process and other local relaxation processes (β , γ ...). The α relaxation process corresponds to the conformational changes of the polymer backbone, whereas the secondary relaxations concern the vibration or rotation of lateral segments or groups of atoms. The relaxation time related to the dynamic α -relaxation increases much faster than the Arrhenius law, causing a deviation from the expected behavior [86]. This deviation is characterized by a dramatic increase of the apparent activation energy giving rise to a super-Arrhenius behavior:

$$\tau(T) = \tau_0 \exp\left(\frac{\Delta E_\alpha(T)}{RT}\right) \quad \text{Eq. 23}$$

where τ_0 is the limiting high-temperature relaxing time or pre-exponential factor, R the universal gas constant, T is the temperature, and E_α is the apparent activation energy, which is associated to the structural relaxation and shear viscosity in the glass transition region [87]. For local relaxations, the relaxation time follows a simple Arrhenius behavior with $\Delta E_\alpha(T) = \text{const}$. Unfortunately, **Eq. 23** is not

directly applicable, since the temperature dependence of $\Delta E_a(T)$ is not always known. An alternative equation is therefore used in the form of a Vogel-Fulcher-Tammann (VFT) equation [88-90]:

$$\tau(T) = \tau_0 \exp\left(\frac{D T_v}{T - T_v}\right) \quad \text{Eq. 24}$$

The strength parameter D can be taken as a measure of the deviation from the Arrhenius behavior, and is related to the steepness of the variation of the relaxation time as a function of temperature. The non-Arrhenius behavior is considered by introducing the Vogel temperature T_v as an extrapolated temperature for an infinite relaxation time. This divergence may be taken as indication of an ideal glass transition, that would occur at a temperature T_v below the glass transition temperature T_g . This condition, though, is not reached for dynamical reasons. In general, T_v is found to be approximately 40 K below T_g [91].

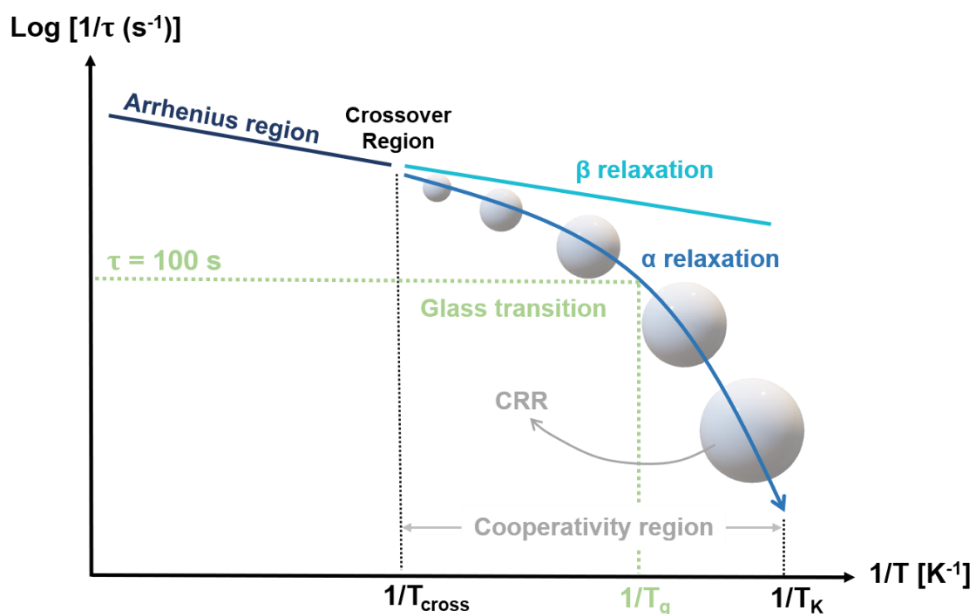


Figure I.8. Schematic representation of the relaxations and cooperative processes typical of a glass-forming liquid as a function of temperature. White spheres represent the Cooperative Rearranging Regions (CRR).

This deviation from the Arrhenius behavior differs from one liquid to another as their dynamics decelerate upon cooling towards the glass transition. To describe this deceleration, Angell introduced the concept of fragility, which is a kinetic property but closely correlated with various thermodynamics quantities, such as the width of the glass transition and the change in heat capacity at the glass transition [87]. The fragility index m is defined as follows:

$$m = \frac{d(\log \tau)}{d\left(\frac{T_g}{T}\right)}_{T=T_g} \quad \text{Eq. 25}$$

Depending on the thermal sensitivity of the physical relaxation during the glass transition, the fragility index m will be small for strong glass-forming liquids, and large for fragile glass-forming liquids, as represented in **Figure I.9**. Fragile glasses exhibit a marked non-linear behavior with a dramatic increase in τ (or η) over a limited temperature interval once the supercooled liquid approaches T_g . It was found that liquids with non-directional bonding and a heterogeneous distribution of interactions would typically have a fragile behavior [85]. Overall, fragile liquids belong to the category of weakly interacting ionic and van der Waals systems, while strong liquids are typically networking glass-formers such as SiO_2 or GeO_2 [92], whose short-range order is mostly unaffected by temperature change [82].

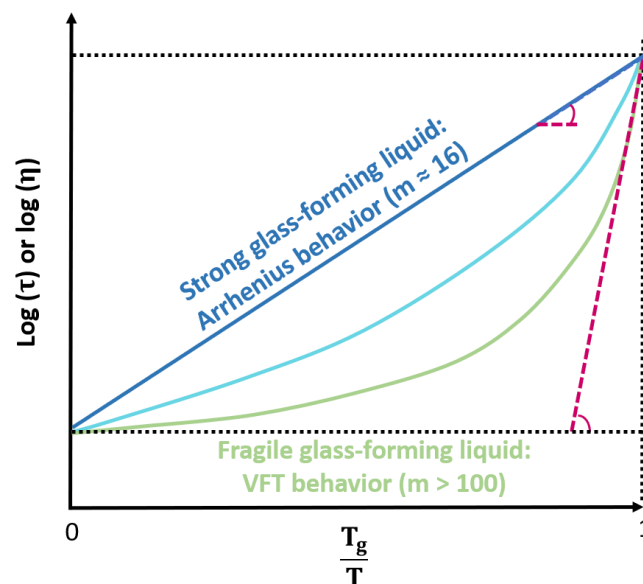


Figure I.9. Schematic illustration of the strong and fragile behaviors according to Angell's fragility concept.

Correlations between the fragility index and the material's properties have been thoroughly investigated, and relationships between m , T_g , structural features and elastic properties have been established in some cases, showing that various physical properties can actually influence the molecular relaxations and the fragility [93]. One striking point is that many polymers have a fragile behavior with a much steeper temperature dependence of their structural relaxation in comparison with smaller molecules, and the mechanisms behind this unusually high fragility in polymers are still unknown [94].

The relationship between m and the chemical structure of polymer repeating units was also investigated, with Yildirim et al. [85] showing the predominance of the spatial distribution of chain rigidity on the liquid relaxation properties over other structural aspects. Ngai et al. [95] highlighted the possible influence of the structural unit's symmetry on the fragility of polymers, with symmetric units leading to a stronger polymer due to symmetric units having lower intermolecular coupling than asymmetric ones. By studying the influence of molecular weight on fast dynamics and fragility, Ding et al. confirmed that polymers with symmetric structural units appear to be less fragile than polymers with asymmetric structural units. For asymmetrically substituted polymers (rather fragile), an increase in molecular weight leads to an increase in fragility, whereas for symmetrically substituted or non-substituted polymers (relatively strong), the symmetry of the chemical structure results in a distribution of configurational energies being rather independent of the chain length [96]. An explanation for this observation would be that asymmetric units lead to a strong broadening of the distribution. As a result, fragility should increase with molecular weight in polymers with asymmetric structural units [96].

Kunal et al. proposed an approach to understand the role of chemical structure in segmental dynamics, stating that polymers with flexible backbones and no side groups are the strongest [97]. This approach was extended by Novikov et al. who argued that polymers tend to be more fragile as the flexibility of their side groups becomes different from that of the backbone, as shown in **Figure I.10**:

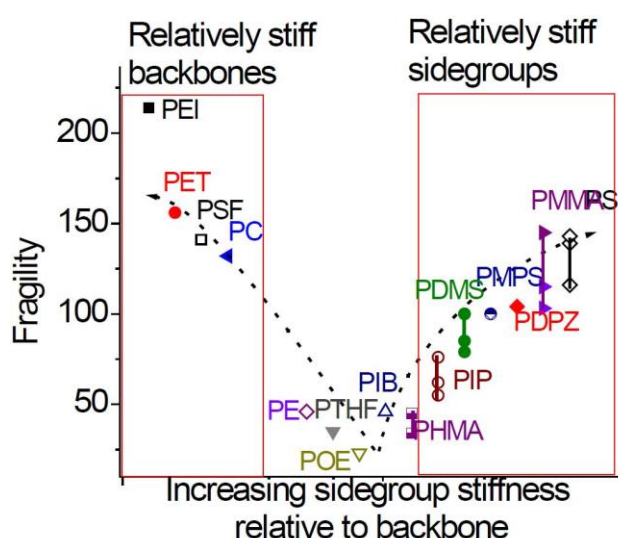


Figure I.10. Schematic presentation of polymers classification based on the relative flexibility of the side groups and backbone (Figure from Novikov et al. [98]).

II.2.2. Cooperativity

The viscous slowdown depends on the molecular or atomic rearrangements in the deeply supercooled melt, which are usually described by spatially and temporally fluctuating associations of particles. Depending on the selected material and characterization method, these associations are referred to as Medium Range Order (MRO) correlation regions [99, 100], dynamic heterogeneities [101], or spatial heterogeneities [102], but all of them describe spatio-temporal domains in which the molecular or atomic mobility is not homogeneous [101, 103] and drastically changes during the vitrification process [99, 104].

Different models have been proposed to understand the vitrification process, such as the string-like cooperative rearrangement model [77, 105], the Mode-Coupling Theory (MCT) [106-108] or the Adam and Gibbs model based on the configurational entropy of supercooled liquids [109]. In a supercooled liquid, the free volume available to the individual moiety (which often corresponds to the repeating unit in the case of a polymer) is considerably reduced. As a result, the α -relaxation process is cooperative in nature: a relaxing unit can move only if a certain number of neighboring units move as well, thus forming a Cooperative Rearranging Region (CRR). Adam and Gibbs defined a CRR as the smallest subsystem in which relaxing units can rearrange cooperatively (changing their configuration within the CRR) without affecting their neighbors upon a sufficient thermal fluctuation. Cooperativity in dynamics is often evaluated as the size of the CRR (ξ_α), or as the number of relaxing units contained in a CRR (N_α). The limit to the Adam-Gibbs model is that it cannot quantitatively predict the temperature dependence of cooperativity if the temperature profile of configurational entropy is not known [77].

To overcome this limitation, Donth developed an approach based on thermodynamics and calorimetric measurements. If a CRR is described as a system with a fluctuating temperature (Von Laue approach), its average size can be estimated based on the analysis of the shape of the thermal relaxation spectrum measured by calorimetry [110]. The CRR volume V_α can be calculated with Eq. 26:

$$V_\alpha = \frac{k_B}{\rho} \left(\frac{T_\alpha}{\delta T} \right)^2 \left(\frac{1}{c_{p,g}} - \frac{1}{c_{p,l}} \right) \quad \text{Eq. 26}$$

where k_B is the Boltzmann constant, ρ is the density, T_α is the dynamic glass transition temperature, $c_{p,g}$ and $c_{p,l}$ are the specific heat capacities of the glass and of the supercooled liquid respectively measured at T_α , and δT represents the temperature fluctuation. The temperature fluctuation δT is

obtained from the width of the thermal relaxation spectrum. The soundness of the inclusion of δT in **Eq. 26** has been widely discussed [110, 111]. From the cooperative volume V_α assumed as a sphere, the characteristic length ξ_α of a CRR can be determined with **Eq. 27**:

$$\xi_\alpha = \left(\frac{6}{\pi} V_\alpha \right)^{\frac{1}{3}} \quad \text{Eq. 27}$$

The number of relaxing units in a CRR can be obtained via **Eq. 28**:

$$N_\alpha = \frac{N_A V_\alpha \rho}{M_0} \quad \text{Eq. 28}$$

where N_A is the Avogadro number and M_0 is the mass of the moiety identified as the relaxing unit. The most direct method to assess the degree of cooperativity of molecular motions is from the broadening of the relaxation spectrum [95]. A broad glass transition can be characteristic of an heterogeneous amorphous phase with small cooperativity lengths and large temperature fluctuation δT [77]. Moreover, connectivity imposes additional restrictions on molecular motions, so that a larger number of structural units should be involved. Consequently, polymers are expected to have larger molecular cooperativity than non-polymeric materials [86].

In the 90s and early 2000s, heat capacity spectroscopy allowed to probe segmental dynamics near the crossover region [112-116], and attempts at finding a correlation between cooperativity at T_g and fragility were made. Unfortunately, no universal trends have been found so far, probably because of the complex interactions between macromolecular segments [77].

In recent years, there has been a renewed interest in the investigation of cooperative processes thanks to the improvement of experimental techniques such as X-ray Positron Correlation Spectroscopy (XPCS) [117, 118], Electron Correlation Microscopy (ECM) [119], Atomic Force Microscopy [120], Neutron Spin Echo (NSE) spectroscopy [111], as well as by simulation [77]. The development of Fast Scanning Calorimetry (FSC) with high time resolution [121, 122] and of the spectroscopy of heat capacity over a wide frequency range [123, 124] also provides a deeper insight into the kinetics of the glass transition [125-127]. Recent insights showed that the cooperative motions affect the kinetics of the glass transition (e.g. the fragility index) [128] but also other properties, such as thermal expansion [129] and microhardness [130]. On the other hand, the CRR size (and to a larger extent the segmental relaxation) is impacted by crystallization [131-133], causing a broadening of the relaxation spectrum and a shift to lower frequencies.

CRR are also impacted by free volume, when the segmental chains do not fully occupy the specific volume due to packing inefficiencies and hindered chain mobility (which is typical of polymers). The unoccupied volume is continuously redistributed as a result of thermally stimulated random segmental motions [134]. Comparisons between the free volume estimated using PALS and the cooperative volume V_{α} estimated by Donth's approach revealed that the appearance of open-volume defects leads to a significant decrease of V_{α} in As–Se chalcogenide glasses [135]. The same behavior was observed for a polymeric glass former, PLA [136].

The extension of Donth's approach allowed the investigation of the CRR size on a large frequency window using a combination of Dielectric Relaxation Spectroscopy and Modulated Temperature DSC (MT-DSC) [137] or Broadband Heat Capacity Spectroscopy [138]. The use of these experimental techniques is however limited to amorphous polymers unable to crystallize. Indeed, materials (and in particular polymers) with fast crystallization kinetics are challenging to analyze as their microstructure evolves during measurement, which makes the probing of amorphous phase mobility (without the impact of crystallization) difficult. One way to circumvent this issue would be to use Fast Scanning Calorimetry, as will be shown in the Experimental section.

II.3 Physical aging

In the previous sections we underlined the main characteristics of the α -relaxation in glass-forming liquids, as well as the increase of the CRR size associated to the α -relaxation upon cooling. When the glass-forming liquid is cooled down below its T_g another phenomenon takes place: physical aging.

Such phenomenon is related to the structural relaxation processes undergone by the amorphous phase when the material is maintained at an aging temperature (T_{ag}) below its T_g . Physical aging occurs in all types of materials (thermoplastic polymers [139], thermosets [140, 141], chalcogenide glasses [142, 143], pharmaceutical compounds [144]), whether they are fully amorphous or semi-crystalline with a residual amorphous phase. This phenomenon can significantly affect the macroscopic behavior, including barrier and mechanical properties [140, 145, 146].

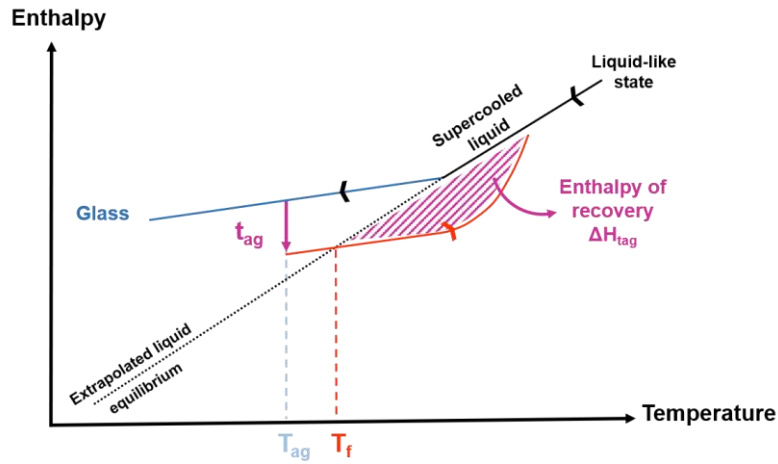


Figure I.11. Schematic illustration of the temperature dependence of the enthalpy of a glass-forming liquid upon physical aging.

When the cooling rate is too high for a glass-forming liquid to remain in an equilibrium state, the glass formed is intrinsically out-of-equilibrium, i.e. its thermodynamic properties (specific volume, enthalpy, and entropy) are higher than what they would have been in the corresponding equilibrium state (liquid equilibrium extrapolated to low temperatures) (**Figure I.11**). This thermodynamic excess initiates a progressive relaxation process towards equilibrium. The kinetics of physical aging can be investigated using calorimetric analysis, assessing the enthalpy of recovery $\Delta H(T_{ag}, t_{ag})$ associated with physical aging for a given time (t_{ag}) spent in isothermal conditions (T_{ag}) at a temperature below T_g . The enthalpy of recovery is calculated by integrating the difference between the scans recorded on an aged and successively rejuvenated samples, following **Eq. 29**:

$$\Delta H(T_{ag}, t_{ag}) = \int_{T_1}^{T_2} [c_{p,a}(T) - c_{p,r}(T)] dT \quad \text{Eq. 29}$$

where $c_{p,a}(T)$ and $c_{p,r}(T)$ correspond to the specific heat capacities of the aged and rejuvenated sample respectively, and T_1 and T_2 are arbitrary temperatures below and above T_g . For an infinite aging time, it is assumed that the thermodynamic equilibrium is reached. The expected enthalpy of recovery can then be estimated according to **Eq. 30**:

$$\Delta H_{\infty} = \Delta c_{p,(T_{g\,mid})} (T_{g\,mid} - T_{ag}) \quad \text{Eq. 30}$$

where $T_{g\,mid}$ is the glass transition temperature taken at half-eight of the glass transition step, and $\Delta c_p(T_{g\,mid})$ is the change in specific heat capacity extrapolated at $T_{g\,mid}$. On the curves recorded by calorimetry, physical aging appears as an endothermic peak superimposed to the specific heat capacity step at T_g as seen in **Figure I.12**:

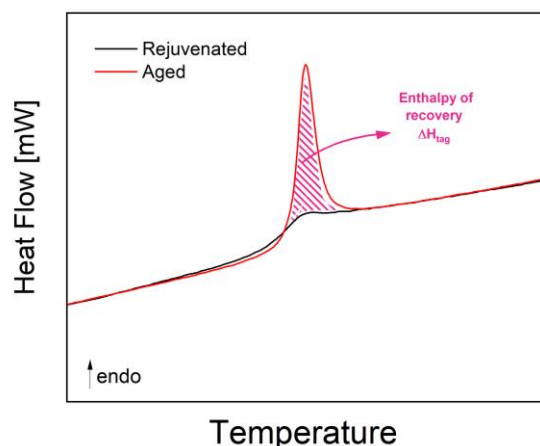


Figure I.12. DSC heat flows recorded upon heating on a rejuvenated (black) and aged (red) sample as a function of temperature. The purple dashed area represents the overshoot superimposed to the heat capacity step used to estimate the enthalpy of recovery associated with physical aging.

As stated before, physical aging is a natural and reversible process and, in this regard, differs from chemical aging, which affects covalent bonding. Chemical aging is a form of degradation which can occur to polymers in service under external factors such as temperature, oxidative gasses, UV light, humidity, radiations or mechanical stress [147]. These degradation processes can impact performance in numerous fields such as civil construction [140] or medicine [148], with potential repercussions on consumers' health and safety. This is why researchers and industrials have been focusing on developing high-performing and environmentally friendly polymers.

III. Polyesters: a class of polyvalent polymers

III.1 Development of bio-sourced and biodegradable polyesters

During the last decades there has been a growing interest in developing bio-polyesters from renewable resources due to the limits of fossil fuel reserves, the rise of petrochemicals' price, and the emission of greenhouse gasses [149]. Indeed, developing new bio-based materials is considered as a strategic approach to limit environmental concerns while keep on meeting the current demand for polymers and composites [150]. Bio-based materials have the advantage of being environmentally friendly and adaptable to a large range of applications, which explains that their production capacities have tripled from 5.2 million tons in 2015 to nearly 17 million tons in 2020 [151].

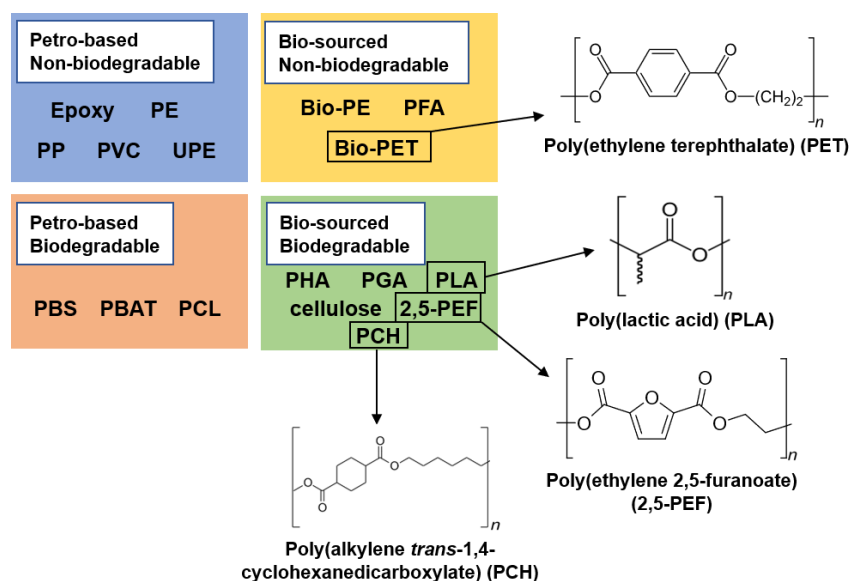


Figure I.13. Classification of common polymers depending on their sourcing and degradation behavior (non-exhaustive list).

Chen et al. published a review of present and future prospects for bio-sourced plastics, and their possible biological sources [152]. Another review on recent developments and future prospects on bio-based polyesters derived from renewable resources was proposed by Zia et al [149]. Polyesters have been attracting much attention because of their low immunogenicity, the easiness of their production, the possibility of obtaining a controlled chemical composition, and thus a quite high chemical versatility [153]. Depending on the crystallization and processing conditions, polyesters can develop complex microstructures with the formation of different polymorphs having a major effect on the structure-physical property relationship [154]. Polyesters are among the earliest and most extensively investigated biodegradable soft materials, as they are easily available from biomass sources for mass production [155]. They can be obtained using solvent-free polycondensation processes, and they offer tunable properties which make them appealing for a wide range of applications. Bio-sourced polyesters can be derived from starch, cellulose, fatty acids, sugars and proteins, natural essences, vegetal oils, or lignin [149]. Some of the monomers can be produced by microbial fermentation eventually combined with chemical polymerization [152] like polyhydroxyalkanoate (PHA) and PLA [152, 156]. In Figure I.13 one may notice the presence of bio-poly (ethylene terephthalate) (bio-PET); new synthesis pathways allow terephthalate polyesters to be completely synthesized from renewable resources, starting from bio-limonene for dimethyl terephthalate and bio-succinic acid for butanediol [157].

Biodegradable polyesters are also subject to extensive academic and industrial research, as recycling is energy-consuming and relies on infrastructures that are not always accessible everywhere, whereas composting allows a relatively easy and low-requirement disposal of polymer waste [158]. Moreover, the biodegradable character of some polymers attracted recent attention in light of the disintegration of plastic debris into microplastics, their dispersion in oceans and freshwater sources [159], and their accumulation in the organs of living beings. A review on the different routes accessible for biopolymer degradation is proposed by Nair et al. [160].

A polymer is considered biodegradable if it can be decomposed into carbon derivatives, inorganic compounds and water without toxic residues. Poly (ϵ -caprolactone) (PCL) and poly (butylene succinate) (PBS) are among the most common biodegradable polyesters. The latter has good processability and flexibility, however like PLA it suffers from brittleness [161]. Recently, poly (alkylene 2,5-furanoate) (PEF) and poly (alkylene 1,4-*trans*-cyclohexanedicarboxylate) (PCH) attracted a lot of attention due to the fact that their mechanical and barrier properties can be fine-tuned by changing the number of methylene groups in the repeating unit [17, 162].

III.2 Diol length variation and odd-even effect

Controlling the length of the linear aliphatic moiety within the repeating unit can help fine-tuning the macroscopic properties of a polyester, in particular its mechanical properties, going from a typical thermoplastic behavior for short lengths to a more elastomeric behavior [163]. Moreover, a peculiar behavior referred to as the odd-even effect has been observed, consisting in a variation of properties depending on the number of methylene groups (n_{CH_2}) contained in the linear aliphatic moiety of a polyester's repeating unit, which may be controlled through the choice of a suitable diol for the reaction with an acid. These properties include strain at break [164], birefringence [165], melting and crystallization temperatures [164, 166], and crystalline structure [164, 167].

Historically, odd-numbered polyesters were often discarded because of their poor properties compared to their even-numbered counterparts, or because of difficulties related to synthesis [168]. Nonetheless, recent synthesis routes allowed the production of 1,3-propanediol (1,3-PD) from renewable resources, and polyesters containing 1,3-propanediol (1,3-PD) such as poly (propylene terephthalate) (PPT) have actually shown excellent properties [168].

It seems therefore essential to define the dependence of a polyester's thermal properties on the length of the aliphatic segment within the repeating unit. In the following, two series of polyesters will be

considered as an example: poly (alkylene 2,5-furanoate)s (containing an aromatic acidic moiety) and poly (alkylene trans-1,4-cyclohexanedicarboxylate)s (containing an alicyclic acidic moiety).

III.2.1. Poly (alkylene 2,5-furanoate)s

Poly (alkylene 2,5-furanoate)s are synthesized starting from 2,5-furandicarboxylic acid (2,5-FDCA), which can be derived from 5-(hydroxymethyl)furfural (HMF). Even though HMF is employed as the starting compound for many furanic derivatives [169], poly (alkylene 2,5-furanoate)s have attracted most of the attention due to their interesting mechanical and barrier properties. Indeed, their properties can be fine-tuned by synthesizing copolyesters of 2,5- and 2,4-furandicarboxylic acid with different diols [170], i.e. by playing on position isomerism [171] or on the diol length, which can be varied from two (poly (ethylene 2,5-furandicarboxylate), 2,5-PEF [172]) to six (poly (hexamethylene 2,5-furandicarboxylate), PHF) [18] or even twelve (poly (dodecylene 2,5-furanoate), PDoF) [17] methylene units. However, polyfuranoates synthesized with long diols ($n_{CH_2} > 4$) are in general less studied than poly (ethylene furanoate) (PEF, $n_{CH_2} = 2$), poly (trimethylene furanoate) (PTF, $n_{CH_2} = 3$) and poly (butylene furanoate) (PBF, $n_{CH_2} = 4$) [18].

Toledano et al. showed that hydrogen bonding is present in both the crystalline and amorphous fractions of poly (trimethylene 2,5-furandicarboxylate) (PTF), and its rearrangement can be considered as a significant driving force for crystallization of poly (alkylene 2,5-furanoate)s [173]. Recently, Giudotti et al. found that poly (pentamethylene furanoate) (PPEF) manifested outstanding barrier and mechanical properties related to the formation of a specific 2D-ordered structure [174]. Martinez-Tong et al. attributed this behavior to possible interchain interactions between furan rings [51]. Comparison between 2,5-PEF and its chemical analogue PET showed that 2,5-PEF presents larger free volume and less RAF formation, however both polymers have similar characteristic length ξ_α [175]. Burgess et al. measured a larger fractional free volume (FFV) in poly(ethylene furanoate) (PEF) than in poly(ethylene terephthalate) (PET), and a higher oxygen permeability in PET than in PEF [176], concluding that a smaller FFV is not necessarily correlated with improved barrier properties. Other studies suggested that the higher barrier performance of 2,5-PEF could be related to the formation of compact helical structures stabilized by the π - π interactions of the furan rings within the amorphous fraction [177].

III.2.2. Poly (alkylene *trans*-1,4-cyclohexanedicarboxylate)s

Polyesters containing cyclohexane moieties have been known since 1950s, but due to the difficult conditions required for their synthesis, they had not been commercially available until recently [178]. PCHs have the advantage of being completely aliphatic, therefore they do not absorb UV light and suffer less from photo-induced degradation compared to other polyester such as PBT [178]. Bio-based PCHs can be synthesized with 1,4-butanediol derived from succinic acid or corn [157, 179] and cyclohexane dicarboxylic acid (CHDA) which can be derived from bio-based terephthalic acid obtained from limonene, a terpene found in citrus skin [157].

CHDA is a cyclic aliphatic compound that can undergo an isomerization reaction between the chair and boat conformations, as represented in **Figure I.14**. The conformational isomerism of the cyclohexane ring plays a major role in crystallization tendencies, with the crystallization temperature recorded on cooling that decreases along with the *trans* content [178]. Indeed, the *trans* conformation is more stable in the chair spatial conformation, whereas the *cis* conformation is found to be more stable in the boat spatial conformation, and therefore *cis* conformation hinders crystallization. Even though the crystallization temperature and the crystalline content X_c are dependent on the *cis/trans* ratio, the nature of the crystalline phase does not seem to be impacted [162]. For poly (butylene cyclohexane dicarboxylate), PBCE, Celli et al. found that the *trans* conformation favors crystal formation, with an increase in melting temperature and enthalpy following the increase in the *trans* content, whereas the *cis* isomers remain in the amorphous state and are rejected from the crystalline phase [180]. In this sense, the *cis* isomers act as defects as they hinder the formation of crystals, leading to a decrease in the crystallization rate [180]. When the *cis*-isomer content increases, gas permeability rises as well (higher values of Gas Transmission Rate, GTR) [162].

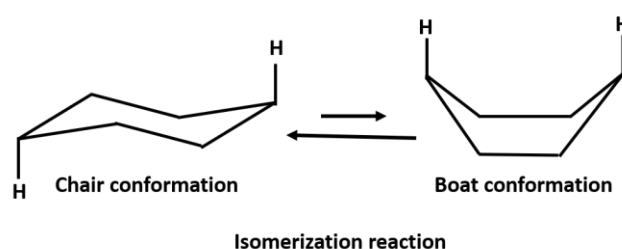


Figure I.14. Isomerization reaction between chair and boat conformations.

PCHs have outstanding barrier performance at ambient temperature, considering that they are above their glass transition temperature, i.e. in the rubbery state [162]. Their barrier properties are thus not attributable to the glassy state, which is associated to a reduced free volume compared to the

corresponding rubbery phase. Guidotti et al. related the barrier performance of PBCE copolymers to the ability of the polymer chains to develop a 2D-ordered structure akin to a mesophase, which hinders the passage of gaseous permeants [162]. A mesophase is a material fraction having a particular structure, whose development is attributed to the presence of mesogenic groups, such as the cyclohexane ring in combination with flexible aliphatic units [181]. The development of a mesophase would originate from a compact stacking of the cyclohexane rings in a chair conformation, which very efficiently hinders the passage of permeants. The formation of a mesophase generally occurs at the expense of the crystalline phase, and is favored by a situation of low crystallinity and high macromolecular mobility [181]. A mesophase is characterized by a different degree of molecular packing compared to the amorphous and the crystalline phases, which in turns has flexibilizing effects and thus improves the elongation at break [181]. This condition is seemingly due to the simultaneous presence in the polymer chain of relatively rigid units (the aliphatic cyclohexane ring) alternating with more flexible segments (the linear aliphatic moiety) [181], analogously to what happens in liquid crystals [162]. Dipole-dipole interactions also have a significant role in mesophase formation, and intermolecular hydrogen bonding has a great potential for ordering thermotropic liquid crystals, therefore stabilizing the mesophase [182-184].

In addition to the length of the linear aliphatic moiety present in the backbone of the repeating unit, the nature of the substituents or side chains can also impact the thermal and structural properties of a polymer. A change in the alkyl group from 1,4-butanediol to neopentyl glycol, for instance, does not alter the thermal stability [162]. However, it influences the order within the material, which in turns deeply affects the functional properties, mainly in terms of mechanical response and barrier performance [162].

III.3 Fields of application

III.3.1. Food packaging

Reviews on the opportunities offered by biodegradable polymers for sustainable food packaging were presented by Siracusa et al. [158] and Wu et al. [185]. In general, the microstructure has a strong impact on barrier properties, and thus chemical tuning can help improving barrier properties through the improvement of microstructure. For example, isomerism can deeply affect the barrier performance, with 2,4-PBF having better properties compared to 2,5-PBF thanks to interchain hydrogen bonds and reduced crystallization [171]. More generally, it is suggested that rigid amorphous fraction (RAF) [186], crystal morphology, polymorphism, an eventual block chain structure (block

composition) [187], free volume, the presence of impermeable fillers, polymer blending, multi-layer coextrusion, nanocomposites [188], coating, and vacuum deposition coating, may have an impact on the material final barrier properties [185].

The combination of a diacid with a glycol offers numerous advantages in terms of mechanical and barrier properties. In particular, the use of terephthalic acid (and more recently of furanoic acid) led to materials now commonly used at industrial scale, or with a strong appealing for it. Two PCH homopolymers, containing respectively three and four methylene groups in their repeating unit (PPCE and PBCE), were used in copolymer formulations with enhanced barrier performance and biodegradation ability [187]. Bioinspired co-polyesters obtained from hydroxy-fatty acids extracted from tomato peel agro-wastes and glycerol have also manifested tunable mechanical, thermal and barrier properties [189-191].

III.3.2. Biomedical

Zia et al. presented a few advances in polyester blends and composites with improved properties for biomedical applications, such as skin tissue engineering, guided bone regeneration and healing processes, drug delivery, and accelerated wound healing [149]. Polyester-based materials can also be used for ophthalmology and orthopedic applications [192].

Shape memory polymers (SMP) belong to a class of smart materials that are able to change from one shape to another when exposed to a specific environmental trigger (temperature, light...). They include surgical alloys that possess varying degrees of biotoxicity, which limits their applications. For this reason, many research efforts have been done to develop bio-compatible and eco-friendly polymers with a variety of applications [155]. Biodegradable polyester-based SMPs are particularly interesting, as they operate *in vivo* and have a shape-changing ability that needs minimal invasive interventions [155]. Furthermore, the excellent biocompatibility and controllable degradation by simple hydrolysis in aqueous environments, which is the case of body fluids, make polyesters particularly suitable for clinical use [155].

PLA, poly (glycolic acid) (PGA), PCL and their copolymers, just to mention a few, have been extensively researched as synthetic biomaterials for sutures, plates and fixtures for fracture consolidation, scaffolds for cell transplantation and tissue growth [49, 155], dental implants, stents, bone screws, pins and vascular grafts [193]. PLA can also be used as a vector for drug delivery as part of cancer treatments [194] and for gene delivery [153]. PCHs, and in particular PBCE copolymers, could also be tailored for biomedical applications [195, 196].

References

- [1] P. J. Flory, « Statistical thermodynamics of random networks », *Proc. R. Soc. Lond. A*, vol. 351, n° 1666, p. 351-380, nov. 1976, doi: 10.1098/rspa.1976.0146.
- [2] M. Arnoult, E. Dargent, et J. F. Mano, « Mobile amorphous phase fragility in semi-crystalline polymers: Comparison of PET and PLLA », *Polymer*, vol. 48, n° 4, p. 1012-1019, févr. 2007, doi: 10.1016/j.polymer.2006.12.053.
- [3] L. D'Esposito et J. L. Koenig, « Application of fourier transform infrared spectroscopy to the study of semicrystalline polymers: Poly(ethylene terephthalate) », *J. Polym. Sci. Polym. Phys. Ed.*, vol. 14, n° 10, p. 1731-1741, oct. 1976, doi: 10.1002/pol.1976.180141001.
- [4] T. A. Ezquerro, F. Liu, R. H. Boyd, et B. S. Hsiao, « Crystallization of poly(aryl ether ketone) polymers as revealed by time domain dielectric spectroscopy », *Polymer*, vol. 38, n° 23, p. 5793-5800, nov. 1997, doi: 10.1016/S0032-3861(97)00129-8.
- [5] N. S. Murthy et H. Minor, « General procedure for evaluating amorphous scattering and crystallinity from X-ray diffraction scans of semicrystalline polymers », *Polymer*, vol. 31, n° 6, p. 996-1002, juin 1990, doi: 10.1016/0032-3861(90)90243-R.
- [6] A. Wang, C. Chen, L. Liao, J. Qian, F.-G. Yuan, et N. Zhang, « Enhanced β -Phase in Direct Ink Writing PVDF Thin Films by Intercalation of Graphene », *J Inorg Organomet Polym*, vol. 30, n° 5, p. 1497-1502, mai 2020, doi: 10.1007/s10904-019-01310-0.
- [7] W. Chen et B. Wunderlich, « Nanophase separation of small and large molecules », *Macromol. Chem. Phys.*, vol. 200, n° 2, p. 283-311, févr. 1999, doi: 10.1002/(SICI)1521-3935(19990201)200:2<283::AID-MACP283>3.0.CO;2-6.
- [8] J. Pak, M. Pyda, et B. Wunderlich, « Rigid Amorphous Fractions and Glass Transitions in Poly(oxy-2,6-dimethyl-1,4-phenylene) », *Macromolecules*, vol. 36, n° 2, p. 495-499, janv. 2003, doi: 10.1021/ma021487u.
- [9] A. Esposito, N. Delpouve, V. Causin, A. Dhotel, L. Delbreilh, et E. Dargent, « From a Three-Phase Model to a Continuous Description of Molecular Mobility in Semicrystalline Poly(hydroxybutyrate- co - hydroxyvalerate) », *Macromolecules*, vol. 49, n° 13, p. 4850-4861, juill. 2016, doi: 10.1021/acs.macromol.6b00384.
- [10] M. C. Righetti et E. Tombari, « Crystalline, mobile amorphous and rigid amorphous fractions in poly(L-lactic acid) by TMDSC », *Thermochimica Acta*, vol. 522, n° 1-2, p. 118-127, août 2011, doi: 10.1016/j.tca.2010.12.024.
- [11] D. Heidrich et M. Gehde, « The 3-Phase Structure of Polyesters (PBT, PET) after Isothermal and Non-Isothermal Crystallization », *Polymers*, vol. 14, n° 4, p. 793, févr. 2022, doi: 10.3390/polym14040793.
- [12] C. Fosse *et al.*, « Determination of the equilibrium enthalpy of melting of two-phase semi-crystalline polymers by fast scanning calorimetry », *Thermochimica Acta*, vol. 677, p. 67-78, juill. 2019, doi: 10.1016/j.tca.2019.03.035.
- [13] T. A. Mukhametzyanov, R. A. Andrianov, D. N. Bolmatenkov, M. I. Yagofarov, B. N. Solomonov, et C. Schick, « Nucleation and crystallization of deeply supercooled benzocaine, a rapidly crystallizing organic compound: A Fast scanning calorimetry investigation », *Thermochimica Acta*, vol. 730, p. 179613, déc. 2023, doi: 10.1016/j.tca.2023.179613.
- [14] J. E. K. Schawe, « The Gibbs free energy difference between a supercooled melt and the crystalline phase of polymers: A new approach », *J Therm Anal Calorim*, vol. 120, n° 2, p. 1417-1425, mai 2015, doi: 10.1007/s10973-015-4453-z.
- [15] M. Frey *et al.*, « Determining and modelling a complete time-temperature-transformation diagram for a Pt-based metallic glass former through combination of conventional and fast scanning calorimetry », *Scripta Materialia*, vol. 215, p. 114710, juill. 2022, doi: 10.1016/j.scriptamat.2022.114710.
- [16] J. D. Hoffman, G. T. Davis, et J. I. Lauritzen, « The Rate of Crystallization of Linear Polymers with Chain Folding », in *Treatise on Solid State Chemistry*, N. B. Hannay, Éd., Boston, MA: Springer US, 1976, p. 497-614. doi: 10.1007/978-1-4684-2664-9_7.
- [17] D. G. Papageorgiou *et al.*, « Fast Crystallization and Melting Behavior of a Long-Spaced Aliphatic Furandicarboxylate Biobased Polyester, Poly(dodecylene 2,5-furanoate) », *Ind. Eng. Chem. Res.*, vol. 55, n° 18, p. 5315-5326, mai 2016, doi: 10.1021/acs.iecr.6b00811.

- [18] N. Guigo, G. Z. Papageorgiou, N. Pouloupoulou, D. N. Bikiaris, et N. Sbirrazzuoli, « Kinetics and mechanism of nonisothermal crystallization of biobased poly(hexamethylene 2,5-furan dicarboxylate) », *Polymer*, vol. 285, p. 126366, oct. 2023, doi: 10.1016/j.polymer.2023.126366.
- [19] D. Cavallo, L. Gardella, G. Portale, A. J. Müller, et G. C. Alfonso, « On cross- and self-nucleation in seeded crystallization of isotactic poly(1-butene) », *Polymer*, vol. 54, n° 17, p. 4637-4644, août 2013, doi: 10.1016/j.polymer.2013.06.051.
- [20] B. O. Reid *et al.*, « Strong Memory Effect of Crystallization above the Equilibrium Melting Point of Random Copolymers », *Macromolecules*, vol. 46, n° 16, p. 6485-6497, août 2013, doi: 10.1021/ma400839d.
- [21] G. Strobl, « From the melt via mesomorphic and granular crystalline layers to lamellar crystallites: A major route followed in polymer crystallization? », *The European Physical Journal E*, vol. 3, n° 2, p. 165-183, oct. 2000, doi: 10.1007/s101890070030.
- [22] M. A. Arshad, « A novel kinetic approach to crystallization mechanisms in polymers », *Polymer Engineering & Sci*, vol. 61, n° 5, p. 1502-1517, mai 2021, doi: 10.1002/pen.25670.
- [23] A. T. Lorenzo, M. L. Arnal, J. Albuerno, et A. J. Müller, « DSC isothermal polymer crystallization kinetics measurements and the use of the Avrami equation to fit the data: Guidelines to avoid common problems », *Polymer Testing*, vol. 26, n° 2, p. 222-231, avr. 2007, doi: 10.1016/j.polymertesting.2006.10.005.
- [24] M. A. Arshad et A. Maaroufi, « Relationship between Johnson–Mehl–Avrami and Šesták–Berggren models in the kinetics of crystallization in amorphous materials », *Journal of Non-Crystalline Solids*, vol. 413, p. 53-58, avr. 2015, doi: 10.1016/j.jnoncrysol.2015.01.012.
- [25] M. L. Di Lorenzo et C. Silvestre, « Non-isothermal crystallization of polymers », *Progress in Polymer Science*, vol. 24, n° 6, p. 917-950, août 1999, doi: 10.1016/S0079-6700(99)00019-2.
- [26] I. H. Hillier, « Modified avrami equation for the bulk crystallization kinetics of spherulitic polymers », *J. Polym. Sci. A Gen. Pap.*, vol. 3, n° 9, p. 3067-3078, sept. 1965, doi: 10.1002/pol.1965.100030902.
- [27] J. Sestak, *Science of heat and thermophysical studies: a generalized approach to thermal analysis*, Elsevier. 2005.
- [28] S. Vyazovkin et N. Sbirrazzuoli, « Nonisothermal Crystallization Kinetics by DSC: Practical Overview », *Processes*, vol. 11, n° 5, p. 1438, mai 2023, doi: 10.3390/pr11051438.
- [29] T. Ozawa, « Kinetics of non-isothermal crystallization », *Polymer*, vol. 12, n° 3, p. 150-158, mars 1971, doi: 10.1016/0032-3861(71)90041-3.
- [30] X. Li, M. Zou, L. Lei, et L. Xi, « Non-Isothermal Crystallization Kinetics of Poly(ethylene glycol) and Poly(ethylene glycol)-B-Poly(ϵ -caprolactone) by Flash DSC Analysis », *Polymers*, vol. 13, n° 21, p. 3713, oct. 2021, doi: 10.3390/polym13213713.
- [31] J. E. K. Schawe, « Cooling rate dependence of the crystallinity at nonisothermal crystallization of polymers: A phenomenological model », *J of Applied Polymer Sci*, vol. 133, n° 6, p. app.42977, févr. 2016, doi: 10.1002/app.42977.
- [32] S. Vyazovkin, « Evaluation of activation energy of thermally stimulated solid-state reactions under arbitrary variation of temperature », *J. Comput. Chem.*, vol. 18, n° 3, p. 393-402, 1997.
- [33] S. Vyazovkin, « Modification of the integral isoconversional method to account for variation in the activation energy », *J. Comput. Chem.*, vol. 22, n° 2, p. 178-183, 2001.
- [34] N. Sbirrazzuoli, « Determination of pre-exponential factors and of the mathematical functions $f(\alpha)$ or $G(\alpha)$ that describe the reaction mechanism in a model-free way », *Thermochimica Acta*, vol. 564, p. 59-69, juill. 2013, doi: 10.1016/j.tca.2013.04.015.
- [35] C. D'Aniello, P. Rizzo, et G. Guerra, « Polymorphism and mechanical properties of syndiotactic polystyrene films », *Polymer*, vol. 46, n° 25, p. 11435-11441, nov. 2005, doi: 10.1016/j.polymer.2005.09.052.
- [36] M. Cocca, M. L. D. Lorenzo, M. Malinconico, et V. Frezza, « Influence of crystal polymorphism on mechanical and barrier properties of poly(l-lactic acid) », *European Polymer Journal*, vol. 47, n° 5, p. 1073-1080, mai 2011, doi: 10.1016/j.eurpolymj.2011.02.009.
- [37] M. Li *et al.*, « Impact of polymorphism on the optoelectronic properties of a low-bandgap semiconducting polymer », *Nat Commun*, vol. 10, n° 1, p. 2867, juin 2019, doi: 10.1038/s41467-019-10519-z.
- [38] Z. Cui, N. T. Hassankiadeh, Y. Zhuang, E. Drioli, et Y. M. Lee, « Crystalline polymorphism in poly(vinylidene fluoride) membranes », *Progress in Polymer Science*, vol. 51, p. 94-126, déc. 2015, doi: 10.1016/j.progpolymsci.2015.07.007.
- [39] J. E. K. Schawe, S. Pogatscher, et J. F. Löffler, « Thermodynamics of polymorphism in a bulk metallic glass: Heat capacity measurements by fast differential scanning calorimetry », *Thermochimica Acta*, vol. 685, p. 178518, mars 2020, doi: 10.1016/j.tca.2020.178518.
- [40] H. Sackmann et D. Demus, « The Polymorphism of Liquid Crystals », *Molecular Crystals*, vol. 2, n° 1-2, p. 81-102, déc. 1966, doi: 10.1080/15421406608083062.

- [41] P. Corradini et G. Guerra, « Polymorphism in polymers », in *Macromolecules: Synthesis, Order and Advanced Properties*, vol. 100/1, in *Advances in Polymer Science*, vol. 100/1. , Berlin/Heidelberg: Springer-Verlag, 1992, p. 183-217. doi: 10.1007/BFb0051637.
- [42] S. Saeidlou, M. A. Huneault, H. Li, et C. B. Park, « Poly(lactic acid) crystallization », *Progress in Polymer Science*, vol. 37, n° 12, p. 1657-1677, déc. 2012, doi: 10.1016/j.progpolymsci.2012.07.005.
- [43] R. Androsch, A. Toda, Y. Furushima, et C. Schick, « Insertion-Crystallization-Induced Low-Temperature Annealing Peaks in Melt-Crystallized Poly(L-Lactic Acid) », *Macromol. Chem. Phys.*, p. 2100177, juin 2021, doi: 10.1002/macp.202100177.
- [44] A. Gradys, P. Sajkiewicz, E. Zhuravlev, et C. Schick, « Kinetics of isothermal and non-isothermal crystallization of poly(vinylidene fluoride) by fast scanning calorimetry », *Polymer*, vol. 82, p. 40-48, janv. 2016, doi: 10.1016/j.polymer.2015.11.020.
- [45] P. Jariyasakoolroj *et al.*, « Isotropically small crystalline lamellae induced by high biaxial-stretching rate as a key microstructure for super-tough polylactide film », *Polymer*, vol. 68, p. 234-245, juin 2015, doi: 10.1016/j.polymer.2015.05.006.
- [46] T. Kawai *et al.*, « Crystallization and Melting Behavior of Poly(L-lactic Acid) », *Macromolecules*, vol. 40, n° 26, p. 9463-9469, déc. 2007, doi: 10.1021/ma070082c.
- [47] J. D. Hoffman et J. J. Weeks, « Melting process and the equilibrium melting temperature of polychlorotrifluoroethylene », *J. RES. NATL. BUR. STAN. SECT. A.*, vol. 66A, n° 1, p. 13, janv. 1962, doi: 10.6028/jres.066A.003.
- [48] T. Konishi, K. Nishida, et T. Kanaya, « Crystallization of Isotactic Polypropylene from Prequenched Mesomorphic Phase », *Macromolecules*, vol. 39, n° 23, p. 8035-8040, nov. 2006, doi: 10.1021/ma060191b.
- [49] A. Wurm *et al.*, « Crystallization and Homogeneous Nucleation Kinetics of Poly(ϵ -caprolactone) (PCL) with Different Molar Masses », *Macromolecules*, vol. 45, n° 9, p. 3816-3828, mai 2012, doi: 10.1021/ma300363b.
- [50] D. Mileva, R. Androsch, E. Zhuravlev, et C. Schick, « Morphology of mesophase and crystals of polyamide 6 prepared in a fast scanning chip calorimeter », *Polymer*, vol. 53, n° 18, Art. n° 18, août 2012, doi: 10.1016/j.polymer.2012.06.045.
- [51] D. E. Martínez-Tong *et al.*, « Evidence of Nanostructure Development from the Molecular Dynamics of Poly(pentamethylene 2,5-furanoate) », *Macromolecules*, vol. 53, n° 23, p. 10526-10537, déc. 2020, doi: 10.1021/acs.macromol.0c02297.
- [52] F. Dumont, P.-A. Marechal, et P. Gervais, « Cell Size and Water Permeability as Determining Factors for Cell Viability after Freezing at Different Cooling Rates », *Appl Environ Microbiol*, vol. 70, n° 1, p. 268-272, janv. 2004, doi: 10.1128/AEM.70.1.268-272.2004.
- [53] S. A. Adamovsky, A. A. Minakov, et C. Schick, « Scanning microcalorimetry at high cooling rate », *Thermochimica Acta*, vol. 403, n° 1, p. 55-63, juin 2003, doi: 10.1016/S0040-6031(03)00182-5.
- [54] A. Bardelcik, C. P. Salisbury, S. Winkler, M. A. Wells, et M. J. Worswick, « Effect of cooling rate on the high strain rate properties of boron steel », *International Journal of Impact Engineering*, vol. 37, n° 6, p. 694-702, juin 2010, doi: 10.1016/j.ijimpeng.2009.05.009.
- [55] A. Buczek et T. Telejko, « Investigation of heat transfer coefficient during quenching in various cooling agents », *International Journal of Heat and Fluid Flow*, vol. 44, p. 358-364, déc. 2013, doi: 10.1016/j.ijheatfluidflow.2013.07.004.
- [56] E. Carmeli, D. Cavallo, et D. Tranchida, « Instrument for mimicking fast cooling conditions of polymers: Design and case studies on polypropylene », *Polymer Testing*, vol. 97, p. 107164, mai 2021, doi: 10.1016/j.polymertesting.2021.107164.
- [57] T. Han *et al.*, « Effect of cooling rate on microstructure and mechanical properties of AlCrFe2Ni2 medium entropy alloy fabricated by laser powder bed fusion », *Journal of Materials Research and Technology*, vol. 25, p. 4063-4073, juill. 2023, doi: 10.1016/j.jmrt.2023.06.241.
- [58] H. Hyer *et al.*, « Understanding the Laser Powder Bed Fusion of AlSi10Mg Alloy », *Metallogr. Microstruct. Anal.*, vol. 9, n° 4, p. 484-502, août 2020, doi: 10.1007/s13632-020-00659-w.
- [59] M. R. Kamal et D. Kalyon, « Heat transfer and microstructure in extrusion blowmolding », *Polymer Engineering & Sci*, vol. 23, n° 9, p. 503-509, juin 1983, doi: 10.1002/pen.760230905.
- [60] X. Li *et al.*, « Cooling rate effects in sodium silicate glasses: Bridging the gap between molecular dynamics simulations and experiments », *The Journal of Chemical Physics*, vol. 147, n° 7, p. 074501, août 2017, doi: 10.1063/1.4998611.
- [61] A. A. Minakov et C. Schick, « Dynamics of the temperature distribution in ultra-fast thin-film calorimeter sensors », *Thermochimica Acta*, vol. 603, p. 205-217, mars 2015, doi: 10.1016/j.tca.2014.05.030.

- [62] T. F. J. Pijpers, V. B. F. Mathot, B. Goderis, R. L. Scherrenberg, et E. W. van der Vegte, « High-Speed Calorimetry for the Study of the Kinetics of (De)vitrification, Crystallization, and Melting of Macromolecules », *Macromolecules*, vol. 35, n° 9, p. 3601-3613, avr. 2002, doi: 10.1021/ma011122u.
- [63] K. Poorhaydari, B. M. Patchett, et D. G. Ivey, « Estimation of cooling rate in the welding of plates with intermediate thickness », *Welding Journal*, vol. 84, p. 149-s, oct. 2005.
- [64] J. E. Seppala et K. D. Migler, « Infrared thermography of welding zones produced by polymer extrusion additive manufacturing », *Additive Manufacturing*, vol. 12, p. 71-76, oct. 2016, doi: 10.1016/j.addma.2016.06.007.
- [65] Y. Shen, Y. Li, C. Chen, et H.-L. Tsai, « 3D printing of large, complex metallic glass structures », *Materials & Design*, vol. 117, p. 213-222, mars 2017, doi: 10.1016/j.matdes.2016.12.087.
- [66] A. Suplicz, F. Szabo, et J. G. Kovacs, « Injection molding of ceramic filled polypropylene: The effect of thermal conductivity and cooling rate on crystallinity », *Thermochimica Acta*, vol. 574, p. 145-150, déc. 2013, doi: 10.1016/j.tca.2013.10.005.
- [67] G. Vanden Poel et V. B. F. Mathot, « High performance differential scanning calorimetry (HPer DSC): A powerful analytical tool for the study of the metastability of polymers », *Thermochimica Acta*, vol. 461, n° 1-2, p. 107-121, sept. 2007, doi: 10.1016/j.tca.2007.04.009.
- [68] N. Herrera, A. M. Salaberria, A. P. Mathew, et K. Oksman, « Plasticized polylactic acid nanocomposite films with cellulose and chitin nanocrystals prepared using extrusion and compression molding with two cooling rates: Effects on mechanical, thermal and optical properties », *Composites Part A: Applied Science and Manufacturing*, vol. 83, p. 89-97, avr. 2016, doi: 10.1016/j.compositesa.2015.05.024.
- [69] J. E. K. Schawe et J. F. Löffler, « Kinetics of structure formation in the vicinity of the glass transition », *Acta Materialia*, vol. 226, p. 117630, mars 2022, doi: 10.1016/j.actamat.2022.117630.
- [70] H. Janeschitz-Kriegl, G. Eder, M. Stadlbauer, et E. Ratajski, « A Thermodynamic Frame for the Kinetics of Polymer Crystallization under Processing Conditions », *Monatshefte für Chemie*, vol. 136, n° 7, p. 1119-1137, juill. 2005, doi: 10.1007/s00706-005-0328-5.
- [71] E. Zhuravlev, J. W. P. Schmelzer, B. Wunderlich, et C. Schick, « Kinetics of nucleation and crystallization in poly(ϵ -caprolactone) (PCL) », *Polymer*, vol. 52, n° 9, p. 1983-1997, avr. 2011, doi: 10.1016/j.polymer.2011.03.013.
- [72] M. Diaeddine *et al.*, « Assessing the consequences of position isomerism on the glass-forming behavior of 2,4- and 2,5-PEF by Molecular Dynamics and Fast Scanning Calorimetry », under preparation.
- [73] J. M. Barandiarán et J. Colmenero, « Continuous cooling approximation for the formation of a glass », *Journal of Non-Crystalline Solids*, vol. 46, n° 3, p. 277-287, déc. 1981, doi: 10.1016/0022-3093(81)90006-5.
- [74] G. Tammann, *Der glaszustand*. Leipzig: L. Voss, 1933.
- [75] G. O. Jones et F. E. Simon, « Qu'est-ce qu'un verre? », *Endeavour*, vol. 8, p. 175-181, 1949.
- [76] E. D. Zanotto et J. C. Mauro, « The glassy state of matter: Its definition and ultimate fate », *Journal of Non-Crystalline Solids*, vol. 471, p. 490-495, sept. 2017, doi: 10.1016/j.jnoncrysol.2017.05.019.
- [77] A. Sato et T. Sasaki, « Cooperativity of dynamics in supercooled polymeric materials and its temperature dependence predicted from a surface controlled model », *European Polymer Journal*, vol. 99, p. 485-494, févr. 2018, doi: 10.1016/j.eurpolymj.2018.01.003.
- [78] R. B. Cassel, « Physical Aging and Fragility of Amorphous Polyethylene Terephthalate », *TA Instruments Applications Brief TA299*.
- [79] « Tool AQ. Relation between inelastic deformability and thermal expansion of glass in its annealing range. *J Am Ceram Soc.* 1946;29:240–53. ».
- [80] A. Dhotel, B. Rijal, L. Delbreilh, E. Dargent, et A. Saiter, « Combining Flash DSC, DSC and broadband dielectric spectroscopy to determine fragility », *J Therm Anal Calorim*, vol. 121, n° 1, Art. n° 1, juill. 2015, doi: 10.1007/s10973-015-4650-9.
- [81] A. A. Abate, D. Cangialosi, et S. Napolitano, « High throughput optimization procedure to characterize vitrification kinetics », *Thermochimica Acta*, vol. 707, p. 179084, janv. 2022, doi: 10.1016/j.tca.2021.179084.
- [82] F. Spieckermann, I. Steffny, X. Bian, S. Ketov, M. Stoica, et J. Eckert, « Fast and direct determination of fragility in metallic glasses using chip calorimetry », *Heliyon*, vol. 5, n° 3, Art. n° 3, mars 2019, doi: 10.1016/j.heliyon.2019.e01334.
- [83] J. C. Martinez-Garcia, S. J. Rzoska, A. Drzozd-Rzoska, J. Martinez-Garcia, et J. C. Mauro, « Divergent dynamics and the Kauzmann temperature in glass forming systems », *Sci Rep*, vol. 4, n° 1, p. 5160, juin 2014, doi: 10.1038/srep05160.

- [84] A. A. El Banna et G. B. McKenna, « Challenging the Kauzmann paradox using an ultra-stable perfluoropolymer glass with a fictive temperature below the dynamic VFT temperature », *Sci Rep*, vol. 13, n° 1, p. 4224, mars 2023, doi: 10.1038/s41598-023-31074-0.
- [85] C. Yildirim, J.-Y. Raty, et M. Micoulaut, « Revealing the role of molecular rigidity on the fragility evolution of glass-forming liquids », *Nat Commun*, vol. 7, n° 1, Art. n° 1, avr. 2016, doi: 10.1038/ncomms11086.
- [86] L. Hong, V. N. Novikov, et A. P. Sokolov, « Is there a connection between fragility of glass forming systems and dynamic heterogeneity/cooperativity? », *Journal of Non-Crystalline Solids*, vol. 357, n° 2, p. 351-356, janv. 2011, doi: 10.1016/j.jnoncrysol.2010.06.071.
- [87] Q. Zheng, J. C. Mauro, et Y. Yue, « Reconciling calorimetric and kinetic fragilities of glass-forming liquids », *Journal of Non-Crystalline Solids*, vol. 456, p. 95-100, janv. 2017, doi: 10.1016/j.jnoncrysol.2016.11.014.
- [88] « H. Vogel, *Phys. Z.* 22, 645 (1921) ».
- [89] « G. S. Fulcher, *J. Am. Ceram. Soc.* 8, 339 (1925) ».
- [90] « G. Tammann and W. Hesse, *Z. Anorg. Allg. Chem.* 156, 245 (1926) ».
- [91] Friedrich Kremer et Andreas Schönhals, « Broadband Dielectric Spectroscopy », in *Broadband Dielectric Spectroscopy*, Springer., p. 99-101.
- [92] « Mattsson, J.; Bergman, R.; Jacobsson, P.; Börjesson, L. *Phys. Rev. Lett.* 2003, 90, 075702-1 ».
- [93] M. Gao et J. H. Perepezko, « Separating β relaxation from α relaxation in fragile metallic glasses based on ultrafast flash differential scanning calorimetry », *Phys. Rev. Materials*, vol. 4, n° 2, p. 025602, févr. 2020, doi: 10.1103/PhysRevMaterials.4.025602.
- [94] C. Dalle-Ferrier *et al.*, « Why many polymers are so fragile: A new perspective », *The Journal of Chemical Physics*, vol. 145, n° 15, Art. n° 15, oct. 2016, doi: 10.1063/1.4964362.
- [95] K. L. Ngai et C. M. Roland, « Chemical structure and intermolecular cooperativity: dielectric relaxation results », *Macromolecules*, vol. 26, n° 25, p. 6824-6830, déc. 1993, doi: 10.1021/ma00077a019.
- [96] Y. Ding, V. N. Novikov, A. P. Sokolov, C. Dalle-Ferrier, C. Alba-Simionesco, et B. Frick, « Influence of Molecular Weight on Fast Dynamics and Fragility of Polymers », *Macromolecules*, vol. 37, n° 24, Art. n° 24, nov. 2004, doi: 10.1021/ma0492420.
- [97] K. Kunal, C. G. Robertson, S. Pawlus, S. F. Hahn, et A. P. Sokolov, « Role of Chemical Structure in Fragility of Polymers: A Qualitative Picture », *Macromolecules*, vol. 41, n° 19, p. 7232-7238, oct. 2008, doi: 10.1021/ma801155c.
- [98] V. N. Novikov et A. P. Sokolov, « Temperature Dependence of Structural Relaxation in Glass-Forming Liquids and Polymers », *Entropy*, vol. 24, n° 8, p. 1101, août 2022, doi: 10.3390/e24081101.
- [99] C. W. Ryu et T. Egami, « Medium-range atomic correlation in simple liquids. I. Distinction from short-range order », *Phys. Rev. E*, vol. 104, n° 6, p. 064109, déc. 2021, doi: 10.1103/PhysRevE.104.064109.
- [100] S. S. Sørensen, C. A. N. Biscio, M. Bauchy, L. Fajstrup, et M. M. Smedskjaer, « Revealing hidden medium-range order in amorphous materials using topological data analysis », *Sci. Adv.*, vol. 6, n° 37, p. eabc2320, sept. 2020, doi: 10.1126/sciadv.abc2320.
- [101] X. Wang, W.-S. Xu, H. Zhang, et J. F. Douglas, « Universal nature of dynamic heterogeneity in glass-forming liquids: A comparative study of metallic and polymeric glass-forming liquids », *The Journal of Chemical Physics*, vol. 151, n° 18, p. 184503, nov. 2019, doi: 10.1063/1.5125641.
- [102] P. G. Debenedetti et F. H. Stillinger, « Supercooled liquids and the glass transition », *Nature*, vol. 410, n° 6825, p. 259-267, mars 2001, doi: 10.1038/35065704.
- [103] L. Alzate-Vargas, N. Onofrio, et A. Strachan, « Universality in Spatio-Temporal High-Mobility Domains Across the Glass Transition from Bulk Polymers to Single Chains », *Macromolecules*, vol. 53, n° 21, p. 9375-9385, nov. 2020, doi: 10.1021/acs.macromol.0c00853.
- [104] Y. Nie, X. Ye, Z. Zhou, W. Yang, et L. Tao, « Intrinsic correlations between dynamic heterogeneity and conformational transition in polymers during glass transition », *The Journal of Chemical Physics*, vol. 141, n° 7, p. 074901, août 2014, doi: 10.1063/1.4892757.
- [105] T. Salez, J. Salez, K. Dalnoki-Veress, E. Raphaël, et J. A. Forrest, « Cooperative strings and glassy interfaces », *Proc. Natl. Acad. Sci. U.S.A.*, vol. 112, n° 27, p. 8227-8231, juill. 2015, doi: 10.1073/pnas.1503133112.
- [106] A. P. Sokolov, « Why the Glass Transition Is Still Interesting », *Science*, vol. 273, n° 5282, p. 1675-1676, sept. 1996, doi: 10.1126/science.273.5282.1675.
- [107] W. Götze, « The essentials of the mode-coupling theory for glassy dynamics », *Condensed Matter Physics*, vol. 1, n° 4(16), p. 873-904, 1998.
- [108] W. Götze, « Recent tests of the mode-coupling theory for glassy dynamics », *J. Phys.: Condens. Matter*, vol. 11, n° 10A, p. A1-A45, mars 1999, doi: 10.1088/0953-8984/11/10A/002.

- [109] G. Adam et J. H. Gibbs, « On the Temperature Dependence of Cooperative Relaxation Properties in Glass-Forming Liquids », *The Journal of Chemical Physics*, vol. 43, n° 1, p. 139-146, juill. 1965, doi: 10.1063/1.1696442.
- [110] E. Donth, « The size of cooperatively rearranging regions at the glass transition », *Journal of Non-Crystalline Solids*, vol. 53, n° 3, p. 325-330, déc. 1982, doi: 10.1016/0022-3093(82)90089-8.
- [111] Y. Z. Chua, R. Zorn, J. W. P. Schmelzer, C. Schick, O. Holderer, et M. Zamponi, « Determination of Cooperativity Length in a Glass-Forming Polymer », *ACS Phys. Chem Au*, vol. 3, n° 2, p. 172-180, mars 2023, doi: 10.1021/acspchemau.2c00057.
- [112] M. Beiner, H. Huth, et K. Schröter, « Crossover region of dynamic glass transition: general trends and individual aspects », *Journal of Non-Crystalline Solids*, vol. 279, n° 2-3, p. 126-135, févr. 2001, doi: 10.1016/S0022-3093(00)00409-9.
- [113] S. Kahle, E. Hempel, M. Beiner, R. Unger, K. Schröter, et E. Donth, « Confirmation of a calorimetric peculiarity in the crossover region of glass transition in poly(n-hexyl methacrylate) by differential scanning calorimetry », *Journal of Molecular Structure*, vol. 479, n° 2-3, p. 149-162, avr. 1999, doi: 10.1016/S0022-2860(98)00866-7.
- [114] S. Kahle, K. Schröter, E. Hempel, et E. Donth, « Calorimetric indications of a cooperativity onset in the crossover region of dynamic glass transition for benzoin isobutylether », *The Journal of Chemical Physics*, vol. 111, n° 14, p. 6462-6470, oct. 1999, doi: 10.1063/1.479942.
- [115] S. Kahle *et al.*, « Glass-Transition Cooperativity Onset in a Series of Random Copolymers Poly(n -butyl methacrylate- *stat* -styrene) », *Macromolecules*, vol. 30, n° 23, p. 7214-7223, nov. 1997, doi: 10.1021/ma961933b.
- [116] H. Huth, M. Beiner, S. Weyer, M. Merzlyakov, C. Schick, et E. Donth, « Glass transition cooperativity from heat capacity spectroscopy—temperature dependence and experimental uncertainties », *Thermochimica Acta*, vol. 377, n° 1-2, p. 113-124, oct. 2001, doi: 10.1016/S0040-6031(01)00546-9.
- [117] B. Ruta *et al.*, « Revealing the fast atomic motion of network glasses », *Nat Commun*, vol. 5, n° 1, p. 3939, mai 2014, doi: 10.1038/ncomms4939.
- [118] S. Hechler *et al.*, « Microscopic evidence of the connection between liquid-liquid transition and dynamical crossover in an ultraviscous metallic glass former », *Phys. Rev. Materials*, vol. 2, n° 8, p. 085603, août 2018, doi: 10.1103/PhysRevMaterials.2.085603.
- [119] P. Zhang, J. J. Maldonis, Z. Liu, J. Schroers, et P. M. Voyles, « Spatially heterogeneous dynamics in a metallic glass forming liquid imaged by electron correlation microscopy », *Nat Commun*, vol. 9, n° 1, p. 1129, mars 2018, doi: 10.1038/s41467-018-03604-2.
- [120] M. Gao et J. H. Perepezko, « Mapping the Viscoelastic Heterogeneity at the Nanoscale in Metallic Glasses by Static Force Spectroscopy », *Nano Lett.*, vol. 20, n° 10, p. 7558-7565, oct. 2020, doi: 10.1021/acs.nanolett.0c03026.
- [121] E. Zhuravlev et C. Schick, « Fast scanning power compensated differential scanning nano-calorimeter: 1. The device », *Thermochimica Acta*, vol. 505, n° 1-2, p. 1-13, juin 2010, doi: 10.1016/j.tca.2010.03.019.
- [122] V. Mathot *et al.*, « The Flash DSC 1, a power compensation twin-type, chip-based fast scanning calorimeter (FSC): First findings on polymers », *Thermochimica Acta*, vol. 522, n° 1-2, Art. n° 1-2, août 2011, doi: 10.1016/j.tca.2011.02.031.
- [123] H. Huth, A. A. Minakov, et C. Schick, « Differential AC-chip calorimeter for glass transition measurements in ultrathin films », *J Polym Sci B Polym Phys*, vol. 44, n° 20, p. 2996-3005, oct. 2006, doi: 10.1002/polb.20921.
- [124] E. Shoifet, Y. Z. Chua, H. Huth, et C. Schick, « High frequency alternating current chip nano calorimeter with laser heating », *Review of Scientific Instruments*, vol. 84, n° 7, p. 073903, juill. 2013, doi: 10.1063/1.4812349.
- [125] J. E. K. Schawe, « Vitrification in a wide cooling rate range: The relations between cooling rate, relaxation time, transition width, and fragility », *The Journal of Chemical Physics*, vol. 141, n° 18, p. 184905, nov. 2014, doi: 10.1063/1.4900961.
- [126] X. Monnier, S. Marina, X. Lopez de Pariza, H. Sardón, J. Martin, et D. Cangialosi, « Physical Aging Behavior of a Glassy Polyether », *Polymers*, vol. 13, n° 6, p. 954, mars 2021, doi: 10.3390/polym13060954.
- [127] X. Monnier, N. Delpouve, et A. Saiter-Fourcin, « Distinct dynamics of structural relaxation in the amorphous phase of poly(L -lactic acid) revealed by quiescent crystallization », *Soft Matter*, vol. 16, n° 13, p. 3224-3233, 2020, doi: 10.1039/C9SM02541C.
- [128] Y. Shi *et al.*, « Revealing the relationship between liquid fragility and medium-range order in silicate glasses », *Nat Commun*, vol. 14, n° 1, p. 13, janv. 2023, doi: 10.1038/s41467-022-35711-6.

- [129] A. Firlus, M. Stoica, S. Michalik, R. E. Schäublin, et J. F. Löffler, « Atomic structure evolution related to the Invar effect in Fe-based bulk metallic glasses », *Nat Commun*, vol. 13, n° 1, p. 1082, févr. 2022, doi: 10.1038/s41467-022-28650-9.
- [130] K. Nomoto *et al.*, « Medium-range order dictates local hardness in bulk metallic glasses », *Materials Today*, vol. 44, p. 48-57, avr. 2021, doi: 10.1016/j.mattod.2020.10.032.
- [131] « Ngai, K. L.; Roland, C. M. *Macromolecules* 1993, 26, 6824. ».
- [132] J. A. S. Puente, B. Rijal, L. Delbreilh, K. Fatyeyeva, A. Saiter, et E. Dargent, « Segmental mobility and glass transition of poly(ethylene-vinyl acetate) copolymers: Is there a continuum in the dynamic glass transitions from PVAc to PE? », *Polymer*, vol. 76, p. 213-219, oct. 2015, doi: 10.1016/j.polymer.2015.09.007.
- [133] J. C. Coburn et R. H. Boyd, « Dielectric relaxation in poly(ethylene terephthalate) », *Macromolecules*, vol. 19, n° 8, p. 2238-2245, août 1986, doi: 10.1021/ma00162a021.
- [134] K. A. Iyer, « Chain mobility, secondary relaxation, and oxygen transport in terephthalate copolyesters with rigid and flexible cyclic diols », *Polymer*, vol. 129, p. 117-126, oct. 2017, doi: 10.1016/j.polymer.2017.09.049.
- [135] A. Saiter, J.-M. Saiter, R. Golovchak, M. Shpotyuk, et O. Shpotyuk, « Cooperative rearranging region size and free volume in As–Se glasses », *J. Phys.: Condens. Matter*, vol. 21, n° 7, p. 075105, févr. 2009, doi: 10.1088/0953-8984/21/7/075105.
- [136] N. Varol *et al.*, « Amorphous rigidification and cooperativity drop in semi-crystalline plasticized polylactide », *Polymer*, vol. 194, p. 122373, avr. 2020, doi: 10.1016/j.polymer.2020.122373.
- [137] A. Saiter, L. Delbreilh, H. Couderc, K. Arabeche, A. Schönhals, et J.-M. Saiter, « Temperature dependence of the characteristic length scale for glassy dynamics: Combination of dielectric and specific heat spectroscopy », *Phys. Rev. E*, vol. 81, n° 4, p. 041805, avr. 2010, doi: 10.1103/PhysRevE.81.041805.
- [138] Y. Z. Chua *et al.*, « Glass transition cooperativity from broad band heat capacity spectroscopy », *Colloid Polym Sci*, vol. 292, n° 8, p. 1893-1904, août 2014, doi: 10.1007/s00396-014-3280-2.
- [139] X. Monnier, A. Saiter, et E. Dargent, « Physical aging in PLA through standard DSC and fast scanning calorimetry investigations », *Thermochemica Acta*, vol. 648, p. 13-22, févr. 2017, doi: 10.1016/j.tca.2016.12.006.
- [140] B. Quelennec *et al.*, « Effect of physical and chemical ageing on barrier properties of epoxy coating », *Construction and Building Materials*, vol. 409, p. 133908, déc. 2023, doi: 10.1016/j.conbuildmat.2023.133908.
- [141] S. Oumnas, B. Quelennec, E. Richaud, A. Duthoit, N. Delpouve, et L. Delbreilh, « Post-curing and structural relaxation of epoxy networks during early stages of aging for civil engineering applications », *Applied Research*, vol. 2, n° 6, p. e202200090, déc. 2023, doi: 10.1002/appl.202200090.
- [142] A. Morvan, N. Delpouve, A. Vella, et A. Saiter-Fourcin, « Physical aging of selenium glass: Assessing the double mechanism of equilibration and the crystallization process », *Journal of Non-Crystalline Solids*, vol. 570, p. 121013, oct. 2021, doi: 10.1016/j.jnoncrysol.2021.121013.
- [143] A. Morvan, L. Calvez, A. Vella, et A. Saiter-Fourcin, « Physical aging of the 62.5GeS₂-12.5Sb₂S₃-25CsCl chalcogenide glass: Assessing the mechanisms of equilibration and crystallization », *Journal of Non-Crystalline Solids*, vol. 598, p. 121955, déc. 2022, doi: 10.1016/j.jnoncrysol.2022.121955.
- [144] A. Drogoń, M. Skotnicki, A. Skotnicka, et M. Pyda, « Physical Ageing of Amorphous Indapamide Characterised by Differential Scanning Calorimetry », *Pharmaceutics*, vol. 12, n° 9, p. 800, août 2020, doi: 10.3390/pharmaceutics12090800.
- [145] P. Pan, B. Zhu, et Y. Inoue, « Enthalpy Relaxation and Embrittlement of Poly(L-lactide) during Physical Aging », *Macromolecules*, vol. 40, n° 26, p. 9664-9671, déc. 2007, doi: 10.1021/ma071737c.
- [146] S. K. Burgess, C. R. Mubarak, R. M. Kriegel, et W. J. Koros, « Physical aging in amorphous poly(ethylene furanoate): Enthalpic recovery, density, and oxygen transport considerations », *J. Polym. Sci. Part B: Polym. Phys.*, vol. 53, n° 6, p. 389-399, mars 2015, doi: 10.1002/polb.23648.
- [147] R. Tian, K. Li, Y. Lin, C. Lu, et X. Duan, « Characterization Techniques of Polymer Aging: From Beginning to End », *Chem. Rev.*, vol. 123, n° 6, p. 3007-3088, mars 2023, doi: 10.1021/acs.chemrev.2c00750.
- [148] R. M. Baena-Nogueras, E. González-Mazo, et P. A. Lara-Martín, « Degradation kinetics of pharmaceuticals and personal care products in surface waters: photolysis vs biodegradation », *Science of The Total Environment*, vol. 590-591, p. 643-654, juill. 2017, doi: 10.1016/j.scitotenv.2017.03.015.
- [149] K. M. Zia, A. Noreen, M. Zuber, S. Tabasum, et M. Mujahid, « Recent developments and future prospects on bio-based polyesters derived from renewable resources: A review », *International Journal of Biological Macromolecules*, vol. 82, p. 1028-1040, janv. 2016, doi: 10.1016/j.ijbiomac.2015.10.040.
- [150] T. Garrison, A. Murawski, et R. Quirino, « Bio-Based Polymers with Potential for Biodegradability », *Polymers*, vol. 8, n° 7, p. 262, juill. 2016, doi: 10.3390/polym8070262.

- [151] F. Aeschelmann et M. Carus, « Biobased Building Blocks and Polymers in the World: Capacities, Production, and Applications—Status Quo and Trends Towards 2020 », *Industrial Biotechnology*, vol. 11, n° 3, p. 154-159, juin 2015, doi: 10.1089/ind.2015.28999.fae.
- [152] G.-Q. Chen et M. K. Patel, « Plastics Derived from Biological Sources: Present and Future: A Technical and Environmental Review », *Chem. Rev.*, vol. 112, n° 4, p. 2082-2099, avr. 2012, doi: 10.1021/cr200162d.
- [153] C.-K. Chen, P.-K. Huang, W.-C. Law, C.-H. Chu, N.-T. Chen, et L.-W. Lo, « Biodegradable Polymers for Gene-Delivery Applications », *IJN*, vol. Volume 15, p. 2131-2150, mars 2020, doi: 10.2147/IJN.S222419.
- [154] Y. Zheng et P. Pan, « Crystallization of biodegradable and biobased polyesters: Polymorphism, cocrystallization, and structure-property relationship », *Progress in Polymer Science*, vol. 109, p. 101291, oct. 2020, doi: 10.1016/j.progpolymsci.2020.101291.
- [155] X. Zhang, B. H. Tan, et Z. Li, « Biodegradable polyester shape memory polymers: Recent advances in design, material properties and applications », *Materials Science and Engineering: C*, vol. 92, p. 1061-1074, nov. 2018, doi: 10.1016/j.msec.2017.11.008.
- [156] Y. Wang et G.-Q. Chen, « Polyhydroxyalkanoates: Sustainability, Production, and Industrialization », in *Sustainable Polymers from Biomass*, C. Tang et C. Y. Ryu, Éd., Weinheim, Germany: Wiley-VCH Verlag GmbH & Co. KGaA, 2017, p. 11-33. doi: 10.1002/9783527340200.ch2.
- [157] M. Colonna *et al.*, « Synthesis and radiocarbon evidence of terephthalate polyesters completely prepared from renewable resources », *Green Chem.*, vol. 13, n° 9, p. 2543, 2011, doi: 10.1039/c1gc15400a.
- [158] V. Siracusa, P. Rocculi, S. Romani, et M. D. Rosa, « Biodegradable polymers for food packaging: a review », *Trends in Food Science & Technology*, vol. 19, n° 12, p. 634-643, déc. 2008, doi: 10.1016/j.tifs.2008.07.003.
- [159] A. R. Bagheri, C. Laforsch, A. Greiner, et S. Agarwal, « Fate of So-Called Biodegradable Polymers in Seawater and Freshwater », *Global Challenges*, vol. 1, n° 4, p. 1700048, juill. 2017, doi: 10.1002/gch2.201700048.
- [160] L. S. Nair et C. T. Laurencin, « Biodegradable polymers as biomaterials », *Progress in Polymer Science*, vol. 32, n° 8-9, p. 762-798, août 2007, doi: 10.1016/j.progpolymsci.2007.05.017.
- [161] S. A. Rafiqah *et al.*, « A Review on Properties and Application of Bio-Based Poly(Butylene Succinate) », *Polymers*, vol. 13, n° 9, p. 1436, avr. 2021, doi: 10.3390/polym13091436.
- [162] G. Guidotti, M. Soccio, V. Siracusa, M. Gazzano, A. Munari, et N. Lotti, « Novel Random Copolymers of Poly(butylene 1,4-cyclohexane dicarboxylate) with Outstanding Barrier Properties for Green and Sustainable Packaging: Content and Length of Aliphatic Side Chains as Efficient Tools to Tailor the Material's Final Performance », *Polymers*, vol. 10, n° 8, Art. n° 8, août 2018, doi: 10.3390/polym10080866.
- [163] A. Larrañaga et E. Lizundia, « A review on the thermomechanical properties and biodegradation behaviour of polyesters », *European Polymer Journal*, vol. 121, p. 109296, déc. 2019, doi: 10.1016/j.eurpolymj.2019.109296.
- [164] C. Zhou *et al.*, « Biobased long-chain aliphatic polyesters of 1,12-dodecanedioic acid with a variety of diols: Odd-even effect and mechanical properties », *Materials Today Communications*, vol. 19, p. 450-458, juin 2019, doi: 10.1016/j.mtcomm.2019.05.005.
- [165] N. Kumar, S. Chaudhary, P. Singh, K. B. Thapa, et D. Kumar, « Electro-optical odd-even effect of APAPA liquid crystal molecules studied under the influence of an extraneous electric field (THz): A theoretical approach », *Journal of Molecular Liquids*, vol. 318, p. 114254, nov. 2020, doi: 10.1016/j.molliq.2020.114254.
- [166] G. Fredi, D. Rigotti, D. N. Bikiaris, et A. Dorigato, « Tuning thermo-mechanical properties of poly(lactic acid) films through blending with bioderived poly(alkylene furanoate)s with different alkyl chain length for sustainable packaging », *Polymer*, vol. 218, p. 123527, mars 2021, doi: 10.1016/j.polymer.2021.123527.
- [167] I. Flores *et al.*, « Unexpected Structural Properties in the Saturation Region of the Odd–Even Effects in Aliphatic Polyethers: Influence of Crystallization Conditions », *Macromolecules*, p. acs.macromol.1c02235, janv. 2022, doi: 10.1021/acs.macromol.1c02235.
- [168] D. N. Bikiaris, G. Z. Papageorgiou, D. J. Giliopoulos, et C. A. Stergiou, « Correlation between Chemical and Solid-State Structures and Enzymatic Hydrolysis in Novel Biodegradable Polyesters. The Case of Poly (propylene alkanedicarboxylate) s », *Macromolecular Bioscience*, vol. 8, n° 8, p. 728-740, août 2008, doi: 10.1002/mabi.200800035.
- [169] M. Annatelli *et al.*, « Beyond 2,5-furandicarboxylic acid: *status quo*, environmental assessment, and blind spots of furanic monomers for bio-based polymers », *Green Chem.*, p. 10.1039/D4GC00784K, 2024, doi: 10.1039/D4GC00784K.
- [170] S. Thiyagarajan *et al.*, « Synthesis and Thermal Properties of Bio-Based Copolyesters from the Mixtures of 2,5- and 2,4-Furandicarboxylic Acid with Different Diols », *ACS Sustainable Chem. Eng.*, vol. 7, n° 22, p. 18505-18516, nov. 2019, doi: 10.1021/acssuschemeng.9b04463.

- [171] E. Bianchi, M. Soccio, V. Siracusa, M. Gazzano, S. Thiyagarajan, et N. Lotti, « Poly(butylene 2,4-furanoate), an Added Member to the Class of Smart Furan-Based Polyesters for Sustainable Packaging: Structural Isomerism as a Key to Tune the Final Properties », *ACS Sustainable Chem. Eng.*, vol. 9, n° 35, p. 11937-11949, sept. 2021, doi: 10.1021/acssuschemeng.1c04104.
- [172] D. Kourtidou, M. Grigora, L. Papadopoulos, D. Tzetzis, D. N. Bikiaris, et K. Chrissafis, « Crystallization kinetics and nanomechanical behavior of biobased poly(ethylene 2,5-furandicarboxylate) reinforced with carbon nanotubes », *Polymer Composites*, vol. 44, n° 1, p. 632-649, janv. 2023, doi: 10.1002/pc.27124.
- [173] O. Toledano *et al.*, « Study of the Crystal Structure and Hydrogen Bonding during Cold Crystallization of Poly(trimethylene 2,5-furandicarboxylate) », *Macromolecules*, vol. 57, n° 5, p. 2218-2229, mars 2024, doi: 10.1021/acs.macromol.3c02471.
- [174] G. Guidotti *et al.*, « Evidence of a 2D-Ordered Structure in Biobased Poly(pentamethylene furanoate) Responsible for Its Outstanding Barrier and Mechanical Properties », *ACS Sustainable Chem. Eng.*, vol. 7, n° 21, p. 17863-17871, nov. 2019, doi: 10.1021/acssuschemeng.9b04407.
- [175] A. Codou, M. Moncel, J. G. van Berkel, N. Guigo, et N. Sbirrazzuoli, « Glass transition dynamics and cooperativity length of poly(ethylene 2,5-furandicarboxylate) compared to poly(ethylene terephthalate) », *Phys. Chem. Chem. Phys.*, vol. 18, n° 25, Art. n° 25, 2016, doi: 10.1039/C6CP01227B.
- [176] S. K. Burgess, G. B. Wenz, R. M. Kriegel, et W. J. Koros, « Penetrant transport in semicrystalline poly(ethylene furanoate) », *Polymer*, vol. 98, p. 305-310, août 2016, doi: 10.1016/j.polymer.2016.06.046.
- [177] G. Papamokos, T. Dimitriadis, D. N. Bikiaris, G. Z. Papageorgiou, et G. Floudas, « Chain Conformation, Molecular Dynamics, and Thermal Properties of Poly(*n* -methylene 2,5-furanoates) as a Function of Methylene Unit Sequence Length », *Macromolecules*, vol. 52, n° 17, p. 6533-6546, sept. 2019, doi: 10.1021/acs.macromol.9b01320.
- [178] D. J. Brunelle et T. Jang, « Optimization of poly(1,4-cyclohexylidene cyclohexane-1,4-dicarboxylate) (PCCD) preparation for increased crystallinity », *Polymer*, vol. 47, n° 11, p. 4094-4104, mai 2006, doi: 10.1016/j.polymer.2006.02.070.
- [179] L. Genovese, N. Lotti, M. Gazzano, L. Finelli, et A. Munari, « New eco-friendly random copolyesters based on poly(propylene cyclohexanedicarboxylate): Structure-properties relationships », *Express Polym. Lett.*, vol. 9, n° 11, Art. n° 11, 2015, doi: 10.3144/expresspolymlett.2015.88.
- [180] A. Celli, P. Marchese, S. Sullalti, C. Berti, et G. Barbioli, « Eco-friendly Poly(butylene 1,4-cyclohexanedicarboxylate): Relationships Between Stereochemistry and Crystallization Behavior », *Macromol. Chemistry & Physics*, vol. 212, n° 14, p. 1524-1534, juill. 2011, doi: 10.1002/macp.201100052.
- [181] G. Guidotti *et al.*, « Chemical Modification of Poly(butylene trans-1,4-cyclohexanedicarboxylate) by Camphor: A New Example of Bio-Based Polyesters for Sustainable Food Packaging », *Polymers*, vol. 13, n° 16, p. 2707, août 2021, doi: 10.3390/polym13162707.
- [182] T. Kato et J. M. J. Frechet, « A new approach to mesophase stabilization through hydrogen bonding molecular interactions in binary mixtures », *J. Am. Chem. Soc.*, vol. 111, n° 22, p. 8533-8534, oct. 1989, doi: 10.1021/ja00204a044.
- [183] R. I. Gearba *et al.*, « Tailoring Discotic Mesophases: Columnar Order Enforced with Hydrogen Bonds », *Advanced Materials*, vol. 15, n° 19, p. 1614-1618, oct. 2003, doi: 10.1002/adma.200305137.
- [184] L. Veltri *et al.*, « Mesophase Tuning in Discotic Dimers π -Conjugated Ionic Liquid Crystals through Supramolecular Interactions and the Thermal History », *Crystal Growth & Design*, vol. 16, n° 10, p. 5646-5656, oct. 2016, doi: 10.1021/acs.cgd.6b00441.
- [185] F. Wu, M. Misra, et A. K. Mohanty, « Challenges and new opportunities on barrier performance of biodegradable polymers for sustainable packaging », *Progress in Polymer Science*, vol. 117, p. 101395, juin 2021, doi: 10.1016/j.progpolymsci.2021.101395.
- [186] M. Safandowska, C. Makarewicz, A. Rozanski, et R. Idczak, « Barrier Properties of Semicrystalline Polylactide: The Role of the Density of the Amorphous Regions », *Macromolecules*, vol. 55, n° 22, p. 10077-10089, nov. 2022, doi: 10.1021/acs.macromol.2c01490.
- [187] L. Genovese *et al.*, « Gas permeability, mechanical behaviour and compostability of fully-aliphatic biobased multiblock poly(ester urethane)s », *RSC Adv.*, vol. 6, n° 60, p. 55331-55342, 2016, doi: 10.1039/C6RA08882A.
- [188] M. K. Patel, F. Hansson, O. Pitkänen, S. Geng, et K. Oksman, « Biopolymer Blends of Poly(lactic acid) and Poly(hydroxybutyrate) and Their Functionalization with Glycerol Triacetate and Chitin Nanocrystals for Food Packaging Applications », *ACS Appl. Polym. Mater.*, vol. 4, n° 9, p. 6592-6601, sept. 2022, doi: 10.1021/acsp.2c00967.

- [189] M. Marc *et al.*, « Bioinspired co-polyesters of hydroxy-fatty acids extracted from tomato peel agro-wastes and glycerol with tunable mechanical, thermal and barrier properties », *Industrial Crops and Products*, vol. 170, p. 113718, oct. 2021, doi: 10.1016/j.indcrop.2021.113718.
- [190] M. Marc *et al.*, « From Tomato Pomaces Biorefinery to Biobased Shape-Memory Semicrystalline Polyester Networks », *ACS Sustainable Chem. Eng.*, vol. 12, n° 6, p. 2191-2202, févr. 2024, doi: 10.1021/acssuschemeng.3c05713.
- [191] E. Ruffini *et al.*, « Crosslinked Polyesters as Fully Biobased Coatings with Cutin Monomer from Tomato Peel Wastes », *Polymers*, vol. 16, n° 5, p. 682, mars 2024, doi: 10.3390/polym16050682.
- [192] R. N. Darie-Niță, M. Râpă, et S. Frackowiak, « Special Features of Polyester-Based Materials for Medical Applications », *Polymers*, vol. 14, n° 5, p. 951, févr. 2022, doi: 10.3390/polym14050951.
- [193] A.-C. Albertsson et I. K. Varma, « Recent Developments in Ring Opening Polymerization of Lactones for Biomedical Applications », *Biomacromolecules*, vol. 4, n° 6, p. 1466-1486, nov. 2003, doi: 10.1021/bm034247a.
- [194] C. K. Williams, « Synthesis of functionalized biodegradable polyesters », *Chem. Soc. Rev.*, vol. 36, n° 10, p. 1573, 2007, doi: 10.1039/b614342n.
- [195] M. Gigli, N. Lotti, M. Vercellino, L. Visai, et A. Munari, « Novel ether-linkages containing aliphatic copolyesters of poly(butylene 1,4-cyclohexanedicarboxylate) as promising candidates for biomedical applications », *Materials Science and Engineering: C*, vol. 34, p. 86-97, janv. 2014, doi: 10.1016/j.msec.2013.08.013.
- [196] F. Morena *et al.*, « Unpatterned Bioactive Poly(Butylene 1,4-Cyclohexanedicarboxylate)-Based Film Fast Induced Neuronal-Like Differentiation of Human Bone Marrow-Mesenchymal Stem Cells », *IJMS*, vol. 21, n° 23, p. 9274, déc. 2020, doi: 10.3390/ijms21239274.

Chapter II - Materials and methods

Content

I. Materials.....	58
I.1. Poly (lactic acid) (PLA).....	58
I.2. Poly (alkylene <i>trans</i>-1,4-cyclohexanedicarboxylate)s.....	58
I.3. Co-polyesters of hydroxy-fatty acids	61
II. Experimental techniques.....	63
II.1. Structural characterization.....	63
II.1.1. Nuclear Magnetic Resonance Spectroscopy (NMR).....	63
II.1.2. Gel Permeation Chromatography (GPC)	64
II.1.3. Wide Angle X-ray diffraction (WAXD).....	64
II.1.4. Polarized Optical Microscopy (POM).....	66
II.1.5. Fourier transform infrared spectroscopy (FTIR).....	66
II.2. Thermal analysis.....	67
II.2.1. Thermogravimetric Analysis (TGA).....	67
II.2.2. Modulated temperature TGA (MT-TGA)	67
II.2.3. Differential Scanning Calorimetry (DSC).....	69
II.2.4. Modulated temperature DSC (MT-DSC).....	71
II.2.5. Stochastically-modulated DSC (TOPEM)	73
II.2.6. Fast Scanning Calorimetry (FSC).....	74
II.2.7. Correction procedures for FSC analyses.....	77
References.....	80

This second chapter presents the materials investigated in this work, a description of the experimental techniques, and all the details about the experimental set-ups and thermal protocols used for the investigations.

I. Materials

I.1. Poly (lactic acid) (PLA)

Pellets of poly (lactic acid) (PLA) with 95.7% L and 4.3% D isomer contents (grade PLA4042D), and an average molecular weight \overline{M}_w of 188,000 g mol⁻¹ were purchased from NatureWorks. PLA has a density ρ of 1.25 g cm⁻³ and the molar mass of its repeating unit M_0 is 72 g mol⁻¹. The pellets were oven-dried (12 h at 60 °C), hot-pressed (3 min at 200 °C under 2 tons) and quenched in water to obtain amorphous films with a controlled thickness of about 200 μ m to ease further sample preparation. The chemical structure of the repeating unit is presented in **Figure II.1**:

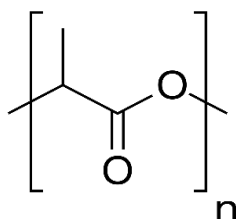


Figure II.1. Repeating unit PLA.

I.2. Poly (alkylene *trans*-1,4-cyclohexanedicarboxylate)s

The poly (alkylene *trans*-1,4-cyclohexanedicarboxylate)s (PCHs) were synthesized at the Dipartimento di Ingegneria Civile, Chimica, Ambientale e dei Materiali (DICAM) in Bologna (Italy), via a two-step melt polycondensation procedure which is a solvent free method*. It consists in the esterification reaction between a bifunctional acid (*trans*-1,4-cyclohexanedicarboxylic acid, CHDA) and a bifunctional glycol (from 1,3-propanol to 1,6-hexanol) to form dimers, as represented in **Figure II.2**. The four homopolymers synthesized in this work differ by their glycol subunits, as it contains linear alkyl groups of different lengths, from three (PPCE) to six (PHCE) methylene groups.

*PCHs synthesis was realized in collaboration with Dr. Giulia GUIDOTTI, Dr. Michelina SOCCIO and Pr. Nadia LOTTI, during an Erasmus exchange in Bologna from October to December 2022. Structural characterizations including Nuclear Magnetic Resonance (NMR) and Gel Permeation Chromatography (GPC) were performed as well.

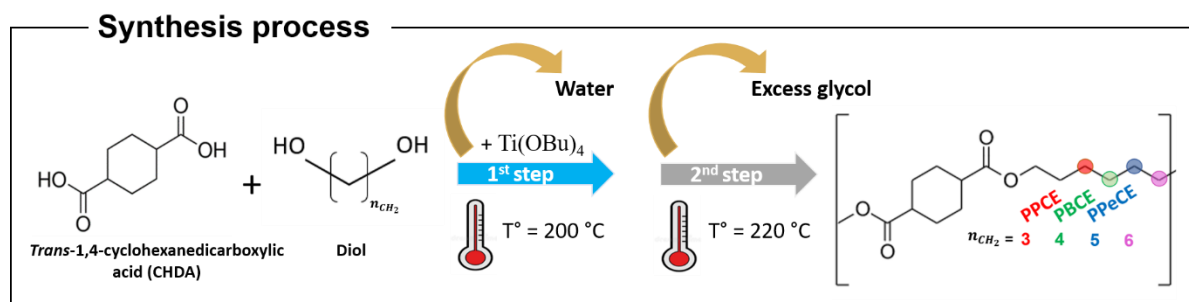


Figure II.2. Two-step melt polycondensation for the synthesis of the four PCH homopolymers.

Trans-1,4-cyclohexanedicarboxylic acid (95%, *cis* 5 mol %) (CHDA) was purchased from Fluorochem (Hadfield, UK). 1,3-Propanediol (PD) (98%) was purchased from Carbosynth, 1,4-Butanediol (BD) (99%) was purchased from Sigma-Aldrich, 1,5-Pentanediol (PeD) (97%) was purchased from Fluka Chemika, 1,6-Hexanediol (HD) (>97%) was purchased from TCI, and Ti(OBu)₄ (TBT) was purchased from Sigma-Aldrich.

During the first stage, the reagents and the catalyst are put in a glass reactor under stirring (about 50 rpm) and continuously flushed with 50 mL min⁻¹ of N₂ (**Figure II.3.a**). For x mol of diacid, 2x mol of glycol are used to favor esterification and diacid dissolution. TBT is a catalyst whose function is to increase the reaction rate. The glass reactor is placed in a thermostated oil bath and connected to a six-bulb condenser to prevent reagents evaporation. The reactor is then heated to 190 °C (**Figure II.4**), the temperature being continuously monitored via a temperature controller. At the end of this stage, a translucent liquid is obtained made of short polymeric chains.

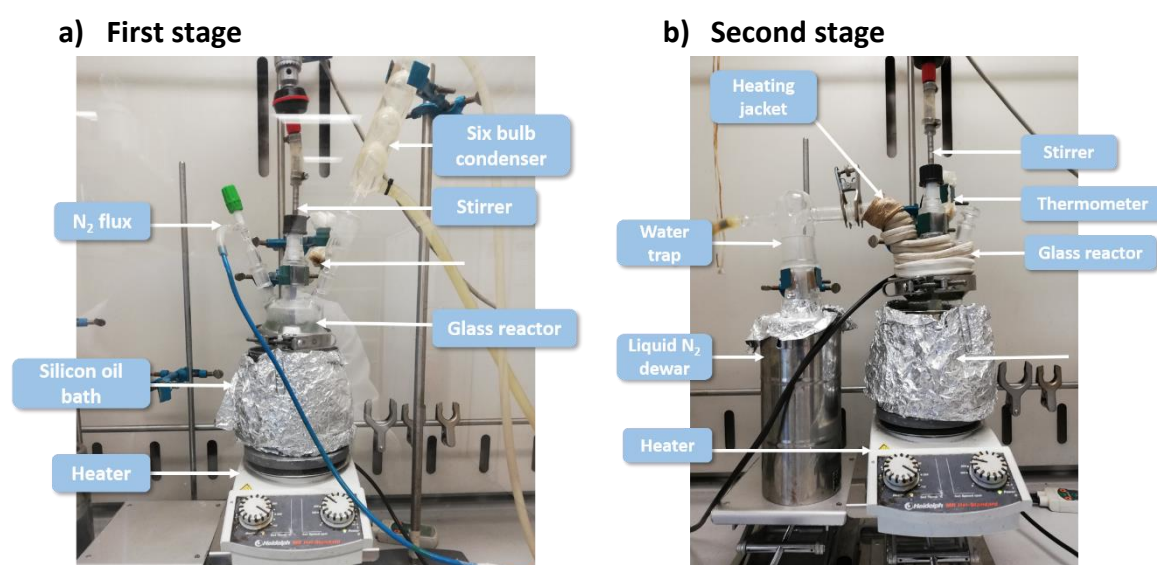


Figure II.3. Experimental set-up corresponding to **a)** first stage and **b)** second stage of the synthesis of PCHs.

For second stage, the nitrogen flow is removed and a water trap device is added, connecting the glass reactor to vacuum (**Figure II.3.b**). The trap is put in a container filled with liquid nitrogen, so that the excess diol condenses and is not extracted by the vacuum pump. A heating jacket is added around the glass reactor and the trap junction to favor water distillation and shift the reaction equilibrium towards the formation of the desired product. Then stirring is increased to 100 rpm and the temperature is also increased from 190 °C to 200 °C to remove the excess of glycol that did not react. The torque value is constantly monitored, which is an indication of the material resistance to stirring. Then vacuum is progressively increased through the opening of two valves. When it reaches its maximum (pressure at 6.10^{-2} mbar), the temperature is further increased from 200 °C to 210 °C to promote transesterification reactions and help removing the excess of glycol. The reaction is considered complete when there is no longer distillation and the torque reaches a maximum constant value.

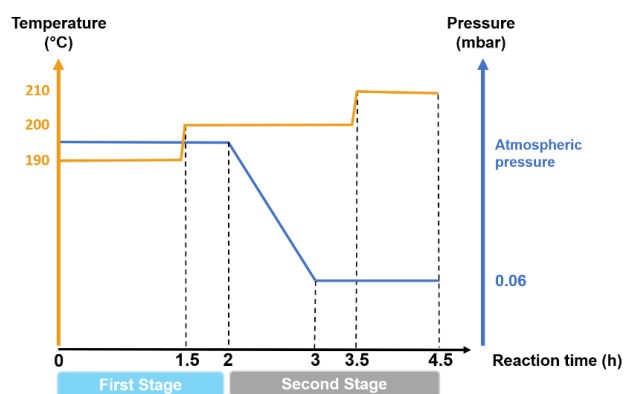


Figure II.4. Temperature and pressure parameters during synthesis of PCHs.

The *cis/trans* isomer ratio of *trans*-1,4-cyclohexanedicarboxylate influences the crystallization temperature of the final polymer, indeed T_c on cooling decreases along with the *trans* content. Isomerization of *trans*-1,4-cyclohexanedicarboxylate can occur during the polymerization process and is enhanced with temperature, time and catalyst amount, so these variables should be minimized to prepare PCHs polymers with high T_c . However, these same variables also control the increase in molecular weight, and so a compromise between the best conditions for high T_c and those for high molecular weights \overline{M}_w must be made [1].

After the synthesis, about 8 g of product is collected. The polymer is then put inside the reactor and dissolved with chloroform (CHCl_3) under stirring. For the purification process, a beaker is filled with 400 mL of methanol. The dissolved polymer is then injected with a pipette in the methanol, leading to the removal of catalyst, oligomers and impurities. All the polymers were purified by precipitation in cold methanol. After purification and precipitation, the samples were dried under vacuum (1 h at 0.1

mbar) and molded with a hot press to obtain thin films (two with the purified samples, one with the non-purified samples for comparison purposes). All films appear pellucid, with thicknesses between 100 and 200 μm .

The chemical structures and *cis/trans* ratios were determined by Nuclear Magnetic Resonance spectroscopy ($^1\text{H-NMR}$). The weight-average molecular weight (\overline{M}_w) and number-average molecular weight (\overline{M}_n) were determined using Gel Permeation Chromatography (GPC). Thermal stability was investigated with thermogravimetric analysis (TGA) under N_2 . The $^1\text{H-NMR}$ spectra with proton assignment can be found in **Appendix 2**. The data issued from molecular characterizations is reported in **Table II.1**. The degree of polymerization DP_n corresponds to the molecular weight divided by the molar mass of the repeating unit M_0 , and dispersity \mathcal{D} is the ratio $\overline{M}_w / \overline{M}_n$.

Table II.1. Data issued from the molecular characterizations of the four PCHs using refractive index detector. M_0 , \overline{M}_n and \overline{M}_w are expressed in g mol^{-1} .

Sample	M_0	\overline{M}_n	\overline{M}_w	\mathcal{D}	DP_n	<i>cis</i> [%]
PPCE	212	62 462	96 657	1.5	295	6.6
PBCE	226	68 703	93 382	1.4	304	5.5
PPeCE	240	57 855	83 592	1.4	241	5.4
PHCE	254	$38\,666 \pm 1141^*$	$58\,734 \pm 160^*$	$1.5 \pm 0.1^*$	152	9.4

*these values correspond to the average of two tries, the uncertainty is calculated as the deviation from the mean value. The percentage of *cis*-isomer is expressed as *cis* [%].

Prior to characterization, all the PCHs were stored under vacuum in a desiccator in the presence of phosphorus pentoxide (P_2O_5) to reduce the exposure to humidity.

1.3. Co-polyesters of hydroxy-fatty acids

Bioinspired co-polyesters of hydroxy-fatty acids were obtained from tomato peel agro-wastes using a solvent-free and catalyst-free polycondensation [2]. Two materials are studied, first the purified cutin monomer (light yellow powder) containing about 95 % non-polymerized 9(10)-16-dihydroxyhexadecenoic acid, and 5 % dicarboxylic fatty acids (the composition and an illustration of the materials can be found in **Figure II.5** and **Figure II.6.a**)[†]. In the following, the purified cutin

[†]The synthesis of the purified CM and the polyester network was realized at the Institut National de Recherche pour l'Agriculture, l'Alimentation et l'Environnement (INRAE) in Nantes (more details about the synthesis and The chemical characterizations can be found in Marc et al. [3]). The materials were provided by DR Denis LOURDIN as part of a collaboration between GPM and INRAE.

monomer will be referred to as “purified CM”. The bulk polycondensation of purified CM extract at 150 °C for 24 h results in the second studied material, a weakly cross-linked polyester network (dark amber film represented in **Figure II.6.b**) with an estimated average number of 80 repeating units between nodes [3] which will be later referred to as “polyester network”.

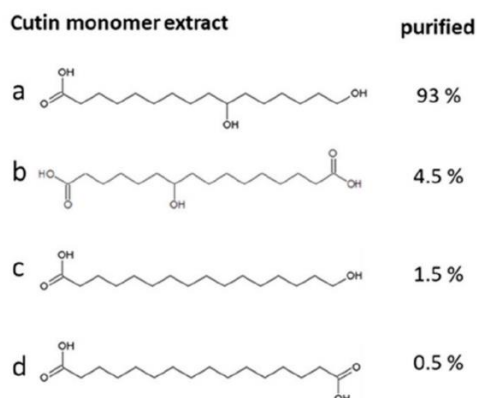


Figure II.5. Lipid compositions (% of fatty acids of the cutin monomers after purification). **a**) 9(10)-16-dihydroxyhexadecanoic acid; **b**) 10-hydroxyhexadecanoic acid; **c**) 16-hydroxydecanoic acid; **d**) hexadecenoic acid (figure extracted from Marc et al [3]).

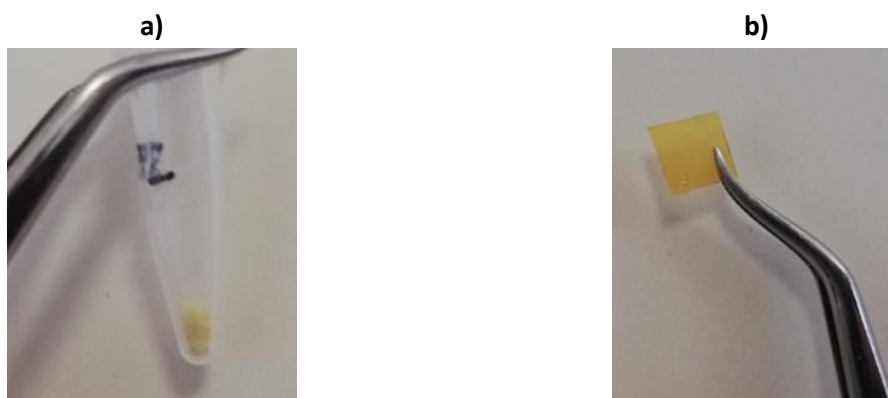


Figure II.6. **a**) Purified CM (light yellow powder) and **b**) polyester network (film).

In-situ polymerization at 150 °C of the purified CM at the nanoscale using Fast Scanning Calorimetry (FSC) for 40 and 600 s resulted in two materials referred to as “purified CM_40s” and “purified CM_600s” respectively, as shown in **Figure II.7**.

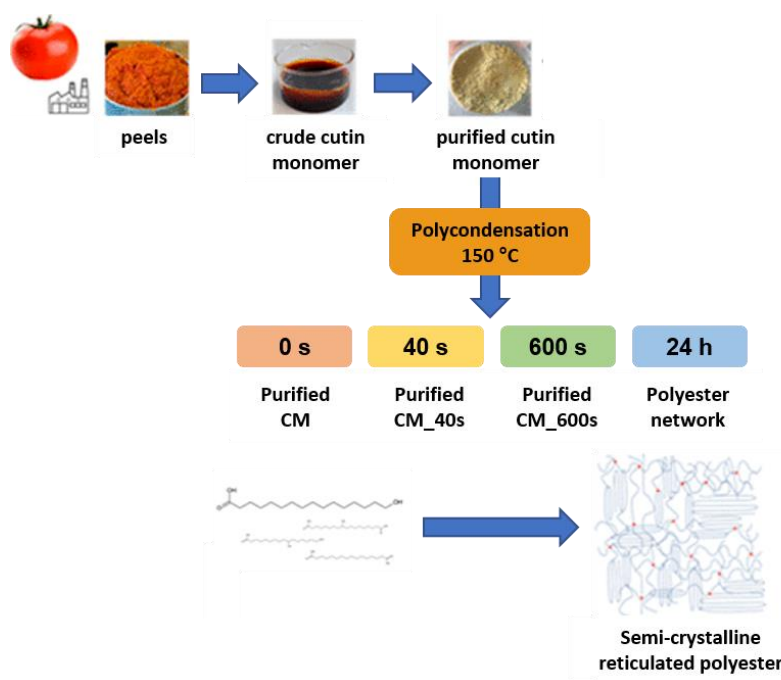


Figure II.7. Solvent- and catalyst-free polycondensation of tomato cutin extract (adapted from Marc et al. [3]). The color code (red for the purified CM, orange for the purified CM_40s, green for the purified CM_600s and blue for the polyester network) will be used throughout **Chapter III**.

II. Experimental techniques

II.1. Structural characterization

II.1.1. Nuclear Magnetic Resonance Spectroscopy (NMR)

Nuclear Magnetic Resonance spectroscopy (NMR) gives information on the chemical structure of the molecules and their chemical environment thanks to the magnetic properties of selected atomic nuclei. The intramolecular magnetic field surrounding any given atom in a molecule has a different resonance frequency, which in turn can be related to the electronic structure of the molecule.

Hydrogen Nuclear Magnetic Resonance Spectroscopy ($^1\text{H-NMR}$) was performed using a Variant XL-400MHz NMR spectrometer (Palo Alto, CA, USA) at room temperature (relaxation time = 0 s, acquisition time = 1 s, 100 repetitions). The PCHs were first dissolved by introducing about 15 mg of sample in 1 mL of deuterated chloroform CDCl_3 containing 0.03 % tetramethylsilane (TMS) as internal reference. The RMN spectra were then used to check the polymer chemical structure and calculate the *cis* content.

II.1.2. Gel Permeation Chromatography (GPC)

Gel Permeation Chromatography (GPC) is a separation method used in analytical chemistry to estimate the average molecular weight of a polymer. About 2 mg of polymer is dissolved in CHCl_3 , a small amount of polymer solution is then injected into a column packed with porous resin with a large distribution of pore sizes. The smaller the molecule, the longer will be the pathway taken through the resin, and the longer the retention time, as indicated in **Figure II.8**. GPC gives access to the weight-average molecular weight (\overline{M}_w) and number-average molecular weight (\overline{M}_n), from which the dispersity \mathcal{D} and the degree of polymerization DP_n can be calculated. PCHs characteristics are reported in **Table II. 1**.

GPC analysis was performed at 30 °C using an HPLC 1100 chromatograph (Agilent Technologies, Santa Clara, USA) equipped with an analytical PLgel 5 mm MiniMIX-C column (300 mm length and 7.80 mm width) and a refractive index detector. A chloroform solution was used as eluent with a flow of 0.3 mL min^{-1} flow and sample concentrations of about 0.1 mg mL^{-1} were applied. The calibration curve was obtained using polystyrene standards with a molecular weight range of 800-100,000 g mol^{-1} .

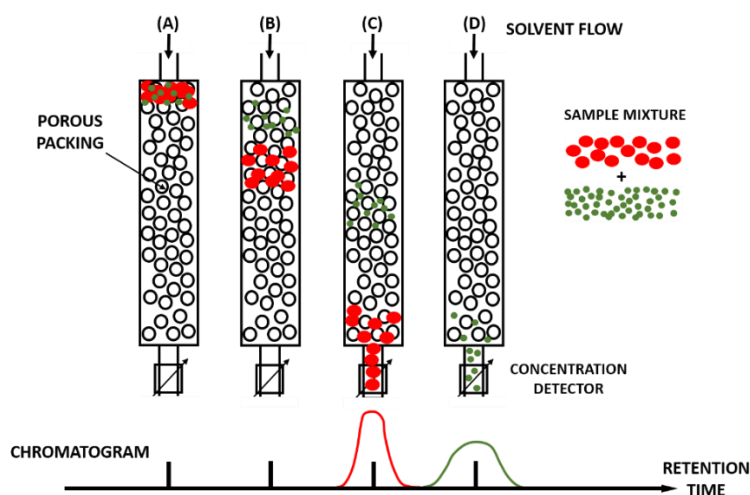


Figure II.8. Schematic representation of GPC principle based on steric exclusion.

II.1.3. Wide Angle X-ray diffraction (WAXD)

Wide Angle X-ray diffraction (WAXD) is a non-destructive analytical technique used to investigate the spatial arrangement of materials with specific ordered structures. In polymer science, this technique allows the detection and quantification of crystalline fractions in semi-crystalline microstructures. As depicted in **Figure II.9**, the basic principle of WAXD relies on hitting the sample with X-ray beams and

measuring the intensity of the diffracted rays as a function of the scattered angle 2θ with a detector. The X-rays are either diffracted or scattered to different angles after elastic interactions with regular or irregular arrangements, i.e. crystalline domains or amorphous matrix. The presence of crystalline domains results in high intensity diffraction peaks that can be analyzed with the Bragg's law [4]:

$$d = \frac{n\lambda}{2 \sin(\theta)} \quad \text{Eq. 1}$$

where d is the crystalline interplanar distance, n is an integer, λ is the X-ray wavelength and θ is the Bragg's angle. The crystallinity X_c is determined as the ratio between the areas below the crystalline diffraction peaks and the total area below the WAXD spectrum. Diffracted peaks are fitted with Gaussian functions that can be used to estimate the average size of the crystalline domains l_c following Scherrer's equation [5]:

$$l_c = \frac{K \lambda}{\beta \cos \theta} \quad \text{Eq. 2}$$

where K is a dimensionless shape factor and β is the Full Width at Half Maximum (FWHM) of the selected crystalline peak.

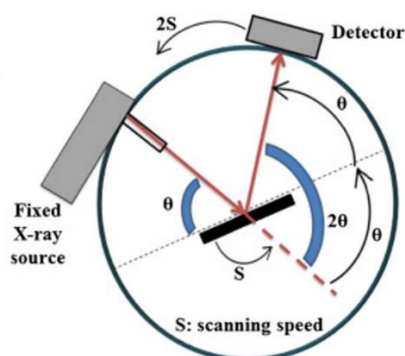


Figure II.9. Schematic representation of a WAXD set-up with a Bragg-Brentano $\theta:2\theta$ geometry (figure from Bishnoi et al. [6]).

In this work, WAXD measurements of PCHs were performed on a Bruker D8 X-ray diffractometer with a cobalt source ($\lambda_{Co} = 0.179$ nm) within the angular range $2\theta = 5 - 40^\circ$ and a scanning step of $0.03^\circ/s$. WAXD patterns were recorded as a function of temperature from ambient temperature to 180°C with a step of 10°C under vacuum and a heating rate of 2 K min^{-1} between two consecutive steps. WAXD measurements of the co-polyesters of hydroxy-fatty acids were performed on a Bruker D8 Advance X-ray diffractometer with a copper source ($\lambda_{Cu} = 0.154$ nm) at ambient temperature within the angular

range $2\theta = 5 - 40^\circ$ and a scanning step of $0.04^\circ/\text{s}$. Crystalline fraction X_c was estimated using the integrated Diffract EVA software.

II.1.4. Polarized Optical Microscopy (POM)

Polarized Optical Microscopy (POM) is a technique allowing the observation of anisotropic structures at the micro-scale. It relies on two polarizing filters: the first one (polarizer) is placed between the light source and the sample, and the second one (analyzer) is placed between the sample and the eyepiece or camera. The emitted light goes through the filters which restrict the electro-magnetic field vectors to a single plane, creating polarized light. As a result, when birefringent samples (such as semi-crystalline polymers) are placed in the light's pathway, the restricted electro-magnetic field vectors passing through the material are transmitted according to many different perpendicular planes, and only the vectors parallel to the polarization direction of the analyzer can be visualized in the eyepiece or by the camera.

In this work, POM observations were performed using a universal Nikon EPI-illuminator with Nikon M plan lenses (x2.5; x5; x10; x20) connected to a Nikon DS-Fi2 camera, either in transmission or reflection mode. A sample piece was placed between two glass slides, then heated onto a Mettler Toledo HS82 Hot Stage to $T_m + 20^\circ\text{C}$ and annealed for 3 min. A gentle pressure was then applied to the upper glass to squeeze the melt into a thin film before cooling to ambient temperature at 2 K min^{-1} . The hot stage is placed underneath the lenses for in-situ observations in different temperature conditions.

II.1.5. Fourier transform infrared spectroscopy (FTIR)

Fourier Transform Infrared spectroscopy (FTIR) is a non-destructive technique that gives information on the chemical composition and the conformation of molecular materials. The vibrational frequencies of different chemical bonds are evidenced through absorption or transmission peaks, and can be related to functional groups. Two FTIR modes can be used: transmission mode or Attenuated Total Reflectance (ATR). Transmission mode consists in an infrared beam traversing the sample to a detector, which records the transmitted energy depending on the wavenumber ν (cm^{-1}). An intensity spectrum is thus generated giving the absorption (A) or transmission ($T = 1 - A$) as a function of the wavenumber. Using ATR mode, the incident beam is reflected within the sample with a specific angle before and after detection.

FTIR spectra were collected in air at room temperature on a Thermo Scientific Nicolet iS10 spectrometer equipped with a diamond crystal in ATR mode. Absorbance spectra were obtained collecting 32 scans with a resolution of 8 cm^{-1} and an acquisition time of 29 s. A blank scan was recorded prior to recording the sample scan to correct for atmospheric CO_2 and H_2O contributions. Absorbance spectra were then normalized using the peak at 1715 cm^{-1} corresponding to the double -C=O bonding taken as a reference.

II.2. Thermal analysis

II.2.1. Thermogravimetric Analysis (TGA)

Thermogravimetric Analysis (TGA) allows a continuous monitoring of the mass evolution of a material sample as a function of time and temperature under controlled conditions [7]. TGA can be performed either in isothermal conditions (the sample is held at a specific temperature T for a specific time t) or for most cases in non-isothermal conditions (the sample is heated with a linear variation of temperature). TGA is used to estimate the thermal stability and evidence thermochemical phenomena such as oxidation, decomposition in a single or multiple step, volatilization, desorption, etc. In non-isothermal kinetic analysis, the temperature (T) is related to the heating rate (β_h) through **Eq. 3**:

$$T = T_0 + \beta_h t \quad \text{Eq. 3}$$

where T_0 is the starting temperature. In this work, TGA measurements were performed on a TGA Discovery (TA Instruments). Temperature calibration was realized using the Curie point of a Nickel standard. Mass calibration was performed using reference platinum pans of known mass. About 5 mg of sample were deposited onto 100 μL platinum pan. The samples were then heated from room temperature up to $600\text{ }^\circ\text{C}$ at 10 K min^{-1} with a constant N_2 gas flow of 25 mL min^{-1} .

II.2.2. Modulated temperature TGA (MT-TGA)

Modulated temperature TGA (MT-TGA) is based on a method proposed by Flynn and Ozawa [7, 8] and provides information on the kinetic parameters associated to mass loss, such as the activation energy E associated to the thermal reaction [9]. The extent of reaction (conversion) α ranges from 0 to 1. The reaction rate is defined as:

$$\frac{d\alpha}{dt} = k f(\alpha) \quad \text{Eq. 4}$$

with $f(\alpha)$ the kinetic reaction function, and k a parameter that depends on temperature variations, and that can be expressed with an Arrhenius equation:

$$k = A \exp\left(\frac{-E}{RT}\right) \quad \text{Eq. 5}$$

where A is a pre-exponential factor, E is the activation energy, and R is the universal gas constant. The combination of **Eq. 4** and **5** gives:

$$\frac{d\alpha}{dt} = A \exp\left(\frac{-E}{RT}\right) f(\alpha) \quad \text{Eq. 6}$$

When a sinusoidal temperature modulation is superimposed to the underlying heating rate, **Eq. 6** can be evaluated as the ratio for adjacent peaks (p) and valleys (v) of the periodic rate of reaction **[9]**:

$$\frac{\frac{d\alpha_p}{dt}}{\frac{d\alpha_v}{dt}} = \frac{A f(\alpha_p) \exp\left(\frac{-E}{RT_p}\right)}{A f(\alpha_v) \exp\left(\frac{-E}{RT_v}\right)} \quad \text{Eq. 7}$$

If the reacted fraction has few variations between adjacent half cycles, the value of $f(\alpha_p)$ is close to $f(\alpha_v)$ and their ratio approaches one. The activation energy is then defined as:

$$E = R \ln\left(\frac{d\alpha_p}{d\alpha_v}\right) \frac{T_p T_v}{T_p - T_v} \quad \text{Eq. 8}$$

In this kind of experiment, the modulated temperature is defined by an average temperature T , an amplitude A , and a period (or frequency). The parameters T_p and T_v in **Eq. 8** can therefore be replaced with $T+A$ and $T-A$ respectively, and T_p-T_v becomes $2A$. **Eq. 8** is further simplified by introducing the parameter L , which is defined as the difference between the maximum and minimum value for the $\ln(d\alpha)$ envelope, with $L = \ln(d\alpha_p) - \ln(d\alpha_v) = \ln(d\alpha_p / d\alpha_v)$:

$$E = R \frac{(T^2 - A^2) L}{2A} \quad \text{Eq. 9}$$

The calculation of the activation energy E using **Eq. 9** does not require to know the kinetic function, i.e. **Eq. 9** is “model free”.

In this work, MT-TGA measurements were performed using the same apparatus as for conventional TGA measurements. The samples were heated from room temperature up to 600 °C at 2 K min⁻¹ with a sinusoidal amplitude modulation of ± 5 K and a period of 200 s under a gas flow of 25 mL min⁻¹ of nitrogen.

II.2.3. Differential Scanning Calorimetry (DSC)

Differential Scanning Calorimetry (DSC) measures the heat flows associated to physical and chemical transitions as a function of time and temperature in a controlled atmosphere. These phase transitions can involve e.g. crystallization, glass transition, oxidation or melting, and they are either endothermic (heat is absorbed by the sample during transition) or exothermic (heat is released). This technique is qualified as “differential” because it relies on the quantification of the difference between the heat amount required to increase the temperature of a sample, and the response of an inert reference subjected to the same temperature program. From this difference, the apparatus determines the heat flow associated as a function of time and temperature. Two kinds of DSC systems are available: heat-flux and power-compensated DSC. In heat-flux calorimeters, the sample and the reference are located in the same furnace (as illustrated in **Figure II.10**), whereas in power-compensated DSC they are placed in separate furnaces.

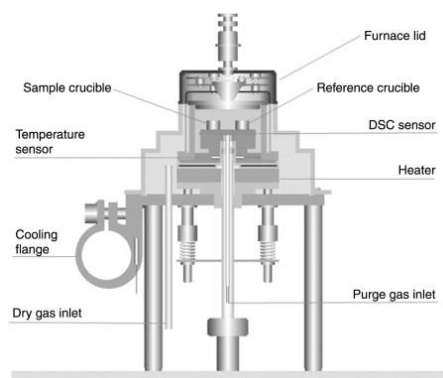


Figure II.10. Schematic representation of heat-flux DSC furnace [credits to Mettler-Toledo].

With conventional DSC, a linear temperature ramp is applied to the sample and the reference (see **Eq. 3**). The heat flow Φ resulting from the heat transfer Q is expressed as follows:

$$\Phi = \frac{dQ}{dt} = m c_p \beta + f(t, T) \quad \text{Eq. 10}$$

where m is the sample mass, c_p is the specific heat capacity, and $f(t, T)$ is the function associated to kinetic reactions. The first term corresponds to the sensible heat and is related to reversing events (glass transition, melting...), which involve heat capacity changes. The second term is the latent heat, which refers to non-reversing events involving chemical reaction or transformations (crystallization, oxidation...). As a result, **Eq. 10** can be rewritten as:

$$\Phi = \Phi_{rev} + \Phi_{non-rev} \quad \text{Eq. 11}$$

In heat-flux calorimeters, the sample and the reference are placed in the same furnace. The heat flow Φ_s absorbed or released by the sample is given by:

$$\Phi_s = \frac{T_s - T_{furnace}}{R_{th}} \quad \text{Eq. 12}$$

where T_s and $T_{furnace}$ are the temperatures of the sample and the furnace respectively, and R_{th} is the thermal resistance of the sensor. Similarly, the heat flow absorbed or released by the reference is given by:

$$\Phi_r = \frac{T_r - T_{furnace}}{R_{th}} \quad \text{Eq. 13}$$

The DSC signal of the heat flow Φ is given by the difference between the sample and the reference heat flows:

$$\Phi = \Phi_s - \Phi_r = \frac{T_s - T_r}{R_{th}} \quad \text{Eq. 14}$$

In order for the heat to flow from the furnace to the reference crucible, a temperature difference ΔT is applied by increasing the furnace temperature $T_{furnace}$ at the beginning of the dynamic segment. The time difference between $T_{furnace}$ and T_r is referred as the time constant τ_0 . ΔT is then given by:

$$\Delta T = \beta_h \tau_0 \quad \text{Eq. 15}$$

with β_h the heating rate. Within the time constant τ_0 the apparatus automatically adapts the furnace temperature to the heating rate set in the method.

In this work, DSC experiments were performed on a heat-flux DSC 3+ calorimeter (Mettler Toledo) equipped with a FRS 6+ sensor. Temperature, enthalpy and τ_0 calibrations were performed using zinc, indium and water as standards. The samples were placed in 40 μL sealed aluminum pans. The

experiments were performed with scanning rates between 5 and 30 K min⁻¹ under a constant 50 mL min⁻¹ nitrogen flow rate.

II.2.4. Modulated temperature DSC (MT-DSC)

As seen in the previous section, conventional DSC is used to obtain the heat flow exchanged between a sample and its environment as a function of temperature and time, highlighting possible thermal reactions such as glass transition, crystallization, oxidation and melting to name just a few. Sometimes these reactions occur within the same temperature range, leading to overlapping effects on the measured heat flow. As a consequence, these phenomena cannot be distinguished from each other, since the heat flow is the algebraic sum of the reversing heat flow Φ_{rev} and the non-reversing heat flow $\Phi_{non-rev}$. One way to deconvolute these two terms would be to use different scanning rate β_1 and β_2 , giving respectively:

$$\Phi_1 = \frac{dQ}{dt} = C_p \beta_1 + f(t, T) \quad Eq. 16$$

$$\Phi_2 = \frac{dQ}{dt} = C_p \beta_2 + f(t, T) \quad Eq. 17$$

From the combination of **Eq. 16** and **17** the heat capacity can be obtained as:

$$C_p = \frac{\Phi_2 - \Phi_1}{\beta_2 - \beta_1} \quad Eq. 18$$

However, this procedure involves at least two measurements using the same experimental conditions (sample and crucible mass, baseline), which is time consuming and often leads to uncertainties. In 1993, Reading proposed to superimpose a sinusoidal temperature oscillation to the linear ramp in order to dissociate the reversing and non-reversing events **[10]**:

$$T = T_0 + \beta t + A \sin(\omega t) \quad Eq. 19$$

where A is the modulation amplitude and ω is the angular frequency of the temperature modulation associated to the period of oscillation $p = 2\pi / \omega$. The modulated heat flow Φ becomes:

$$\Phi = \frac{dQ}{dt} = C_p^* (\beta + A \omega \cos(\omega t)) \quad Eq. 20$$

with C_p^* the complex heat capacity defined as:

$$C_p^* = \frac{A_{HF}}{A_\beta} \quad Eq. 21$$

where A_{HF} and A_β are the amplitudes of the heat flow and of the heating rate modulation, respectively. From C_p^* the two apparent heat capacity components, C_p' (in-phase component) and C_p'' (out-of-phase component), can be obtained with the deconvolution procedure proposed by Lacey et al. [11]:

$$C_p' = |C_p^*| \cos \varphi \quad Eq. 22$$

$$C_p'' = |C_p^*| \sin \varphi \quad Eq. 23$$

where φ is the phase lag between the response function (total heat flow) and the modulated temperature. The phase lag φ is defined as:

$$\varphi = \varphi_{sample} + \varphi_{exp} \quad Eq. 24$$

where φ_{sample} is the phase lag due to the sample itself, and φ_{exp} is the experimental phase lag related to furnace asymmetry and heat transfers occurring within the apparatus. The total phase lag φ can be corrected with baseline adjustment by selecting areas in which no thermal event occurs (typically before and after glass transition) and setting φ_{exp} as zero. This procedure is nowadays automatically realized by the manufacturer software, so from now on φ_{sample} will be referred as φ .

MT-DSC experiments were performed on a Thermal Analysis instrument (TA DSC Q2000). To prevent any oxidative degradation, nitrogen atmosphere was used for all measurements with a constant gas flow of 50 mL min⁻¹. The instrument was calibrated in heat flow and temperature with water and indium standards. The specific heat capacity was measured by applying the calibration carried out with a sapphire as a reference. A sample mass of about 5 mg was inserted in a T_{ZERO} aluminum pan. The optimal conditions to perform specific heat capacity measurements can be obtained by using different modes: heat-only, heat-iso and heat-cool [12].

In this work, the measurements were performed using the heat-cool modulation parameters recommended by Rijal et al. [12] (oscillation amplitude $A = \pm 1$ K, heating rate $\beta_h = 0.5$ K min⁻¹ and oscillation period $p = 60$ s), the temperature range scanned being adjusted to the glass transition of each material.

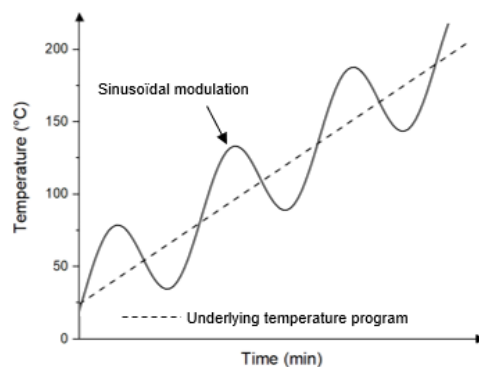


Figure II.11. Temperature program with a superimposed sinusoidal temperature modulation.

II.2.5. Stochastically-modulated DSC (TOPEM)

Stochastically-modulated DSC is based on the same principle as MT-DSC, i.e. it uses a temperature modulation superimposed to the linear variation in order to obtain the contributions Φ_{rev} and $\Phi_{non-rev}$, as well as the complex heat capacity and the in-phase and out-of-phase components [13]. However, unlike MT-DSC, the temperature oscillation $\delta T(t)$ is stochastic rather than periodic (**Figure II.12**).

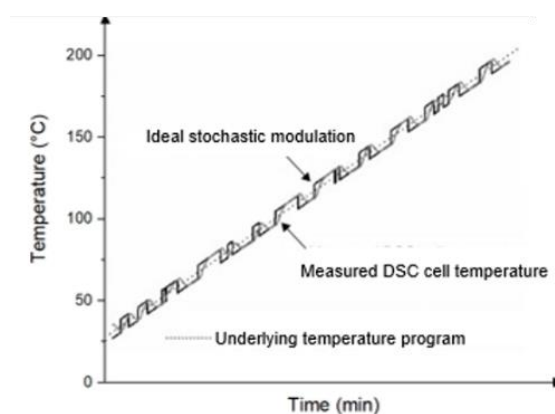


Figure II.12. Temperature program with a stochastic temperature modulation.

A different mathematical approach is used for TOPEM in comparison with MT-DSC. The as-measured heat flow is first analyzed depending on its correlation to the heating rate:

$$\Phi = \Phi_{corr} + \Phi_{non-corr} \quad Eq. 25$$

where Φ_{corr} and $\Phi_{non-corr}$ are the correlated and non-correlated heat flows, respectively. The first term can be divided into instrumental and sample contributions, noted $\Phi_{instrument}$ and Φ_{rev} . With $\Phi_{non-corr}$ rewritten as the non-reversing heat flow $\Phi_{non-rev}$ Eq. 25 becomes:

$$\Phi = \Phi_{instrument} + \Phi_{rev} + \Phi_{non-rev} \quad Eq. 26$$

The non-reversing heat flow $\Phi_{non-rev}$ is directly obtained from the non-correlated heat flow. Usually, with both conventional and modulated-temperature DSC, $\Phi_{instrument}$ is subtracted from the signal using an additional blank curve during calibration; however, for TOPEM the correlated heat flow related to the instrument is directly separated from the sample contribution, giving the reversing heat flow Φ_{rev} . The normalization of Φ_{rev} by the underlying scanning rate and the sample mass gives the quasi-static heat capacity extrapolated to zero frequency $C_{p,0}$. Thanks to the stochastic temperature modulation, the complex heat capacity C_p^* can be calculated for any frequency within the 5-200 mHz window with a single measurement.

TOPEM characterizations were performed on a DSC 3+ apparatus (Mettler-Toledo) equipped with an FRS 6+ sensor. Temperature, enthalpy and thermal lag calibrations were performed using zinc, indium and water standards. Between 3 mg and 10 mg of sample were inserted in 40 μ L hermetically sealed aluminum crucibles. The experiments were performed under nitrogen (50 mL min⁻¹ flow rate) with a pulse height ΔT of ± 0.05 K (when investigating crystallization and melting) or ± 0.5 K (when recording glass transition), and pulse widths Δt between 15-30 s for normal measurements and 15-200 s for frequency evaluation. A reference measurement using sapphire with the same modulation parameters was also performed to correct the phase lag ϕ . An extrapolation to zero frequency was realized to obtain the quasi-static heat capacity. No blank measurement with empty crucible was performed as it can corrupt the dynamics of the measurement signals [14].

II.2.6. Fast Scanning Calorimetry (FSC)

As stated before, DSC is commonly used to study the crystallization and melting behavior of polymers. However, the cooling rate associated to polymer processing techniques (e.g. injection molding, extrusion, film blowing) is typically much larger than the maximum rate achievable by conventional DSC. It is therefore difficult to use DSC to correctly simulate the actual processing conditions [15].

Fast Scanning Calorimetry (FSC) is a powerful tool to probe the molecular dynamics of a large range of materials, with high sensitivity and temperature resolution [16]. The available scanning rates can be

very high (up to $50\,000\text{ K s}^{-1}$ on heating and $40\,000\text{ K s}^{-1}$ on cooling with the Flash DSC 2+ from Mettler Toledo) and therefore offer the possibility to inhibit and/or shift thermal events such as crystallization, separating close-lying thermal effects thanks to a short time constant. FSC is also particularly useful to quench materials with poor glass-forming ability (GFA), such as pharmaceutical compounds or metallic alloys, and investigate their thermal properties and relaxation process *in situ* [17-19].

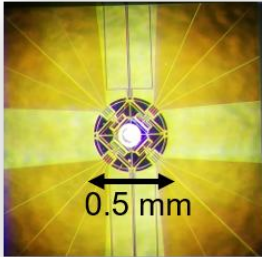
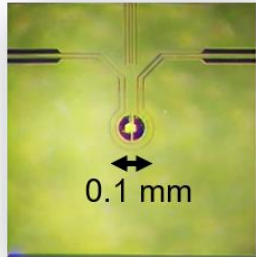
The apparatus used is a power-compensated calorimeter (see **Figure II.13**) in which the sample is deposited onto a twin-chip sensor embedded in a ceramic support based on MEMS (Micro-Electro-Mechanical Systems) technology. Each sensor consists of two identical square silicon membranes mounted on a silicon frame. They act as separate furnaces (one for the sample, one for the reference), similar to the crucibles in conventional DSC. The reference side is left empty. The characteristics of the two sensors available with Flash DSC 2+, Multi STAR UFS1 (Ultra-Fast Sensor) and UFH1 (Ultra-Fast Heating Sensor), are reported in **Table II.2**. The calorimeter has a double-layered film structure, composed of a silicon nitride film and a silicon oxide dielectric film [15]. The center of the calorimeter film is the temperature control area, with a diameter of about 0.5 mm (UFS1 sensors) or 0.1 mm (UFH1 sensors).



Figure II.13. Flash DSC 2+ apparatus (credits to Mettler-Toledo).

A variation of temperature is applied to both furnaces. The apparatus measures the difference in the energy required to keep both sides (sample and reference) at the same temperature throughout the experiment. In case of endothermic transition, the energy absorbed by the sample is compensated by an increased energy input in the sample furnace to maintain the temperature balance. Because this energy input (under the assumption of a perfectly symmetric measuring system) is equivalent in magnitude to the energy absorbed during the transition, recording the balancing energy gives a direct measurement of the energy of the observed transition.

Table II.2. Principal characteristics of the UFS1 and UFH1 MEMS sensors.

Sensor	UFS1	UFH1
Sample furnace (only the central area where the sample is deposited gets heated)		
Thermocouples (whole sensor)	16	4
Time constant	1 ms	≈ 0.2 ms
Temperature range	-95 to 420 °C	-95 to 1 000 °C
Typical range of cooling rates	0.1 to 4 000 K s ⁻¹	0.1 to 40 000 K s ⁻¹
Typical range of heating rates	0.1 to 40 000 K s ⁻¹	0.1 to 50 000 K s ⁻¹

Analogously to conventional DSC, FSC measures the total heat flow as a function of temperature and time.

$$\Phi = \frac{dQ}{dt} = m c_p \beta + f(t, T) \quad \text{Eq. 27}$$

As seen from **Eq. 27**, the use of large sample masses and scanning rates increases the heat flow and improves measurement sensibility. However, the major inconvenience related to large sample masses and rates is the temperature gradient which builds up in the sample during the measurement (thermal lag ΔT_{lag}). For quality improvement, it is advised to use large sample masses associated to low scanning rates, and small sample masses with higher rates [20]. As a result, using FSC requires to make a compromise between resolution (separation of thermal events) and sensitivity (magnitude of each thermal event), which depends on the scanning rate.

In all experiments, the sensor support temperature (T_{ss}) of the Flash-DSC was set to -95 °C using a Huber intracooler TC100. The FSC samples were prepared by cutting the polymer films into small pieces under a stereomicroscope and transferring them using a paint brush hair onto the center of the active zone of a previously conditioned and temperature-corrected Multi STAR UFS1 or UFH1 sensor.

To prevent water condensation and oxidation, the apparatus was continuously flushed under 60 mL min⁻¹ of Argon throughout the experiments. Reproducibility was checked by comparing the same thermal cycles at the start and end of each measurement series.

II.2.7. Correction procedures for FSC analyses

II.2.7.a. Thermal lag

Polymers are materials with low thermal conductivity, therefore a thermal lag ΔT_{lag} is likely to be observed with high scanning rates (typically higher than $1\,000\text{ K s}^{-1}$) and large sample thicknesses (more than $10\ \mu\text{m}$). The thermal lag ΔT_{lag} influences the experimental results causing significant shifts of the recorded phenomena to higher temperatures [21]. To keep the thermal lag within an acceptable range, if the scanning rate has to be increased, the sample mass has to be reduced (from the typical milligram level for conventional DSC down to the microgram or nanogram level for FSC) [16]. Schawe proposed two corrections accounting for sample thickness (static thermal lag ΔT_s) and high scanning rate (dynamic thermal lag ΔT_D) [21]. ΔT_s corresponds to a third of the difference in the onset melting temperatures of a reference piece of Indium placed over the sample, with respect to another piece of similar size positioned directly on the reference chip sensor. ΔT_D is estimated as a half of the difference in the glass transition temperatures measured upon heating and cooling at the same scanning rate, as shown in Figure II.14.

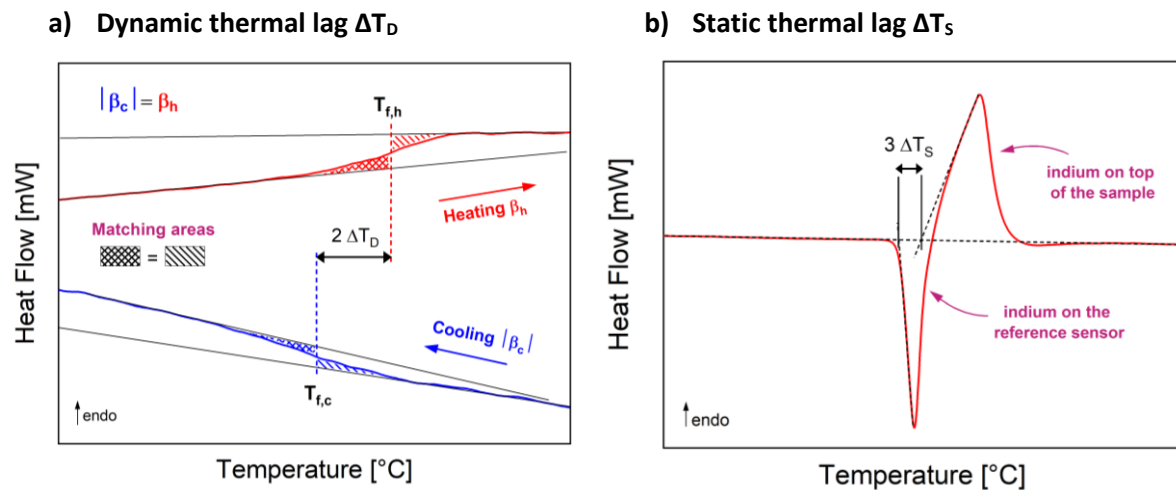


Figure II.14. a) Estimation of the dynamic thermal lag ΔT_D from the difference in fictive temperature T_f upon heating and cooling with $\beta_h = |\beta_c|$; b) Estimation of the static thermal lag ΔT_s from the third of the difference in the onset melting temperature of a piece of a reference substance (Indium) placed on top of the sample, with respect to another piece of similar size placed on the reference sensor, with a heating rate β_h .

II.2.7.b. Smearing effects

In addition to thermal lags, smearing effects can cause a broadening and a shift to higher (upon heating) or lower (upon cooling) temperatures of the observed thermal events. A thorough investigation of the temperature dependence of thermal events requires to correct the smearing due to thermal inertia. The corrected heat flow Φ_m° can be obtained with the following equation [22]:

$$\Phi_m^\circ = \Phi_m + \tau_0 \frac{d(\Phi_m)}{dt} \quad \text{Eq. 28}$$

where Φ_m is the measured heat flow and τ_0 is a time constant, that for glass transition can be calculated as:

$$\tau_0 = \frac{T_{f,h} - T_{f,c}}{2\beta} \quad \text{Eq. 29}$$

where $T_{f,h}$ and $T_{f,c}$ are the limiting fictive temperatures measured respectively upon heating and cooling on the as-measured heat flow curves (**Figure II.14.a**), and $\beta = \beta_h = |\beta_c|$ is the scanning rate. Because τ is proportional to the total heat capacity, and thus to sample mass, the effect of thermal inertia is diminished by conducting FSC measurements on smaller masses and at slower heating rates. However, such conditions may not be suitable for low enthalpy processes [22]. A compromise must then be made between measurement sensitivity (high mass or high scanning rate) and low thermal inertia [23]. The estimation of the fictive temperature T_f can be done using Moynihan's method [24]:

$$\int_{T_f}^{T_2} (c_{p,l} - c_{p,g}) dT = \int_{T_1}^{T_2} (c_p - c_{p,g}) dT \quad \text{Eq. 30}$$

where T_1 and T_2 are arbitrary temperatures above and below the glass transition respectively, c_p is the specific heat capacity of the sample, $c_{p,l}$ and $c_{p,g}$ are the extrapolated lines representing the heat capacity of the sample in the liquid and glassy states, respectively. A schematic representation of the procedure used to estimate T_f is presented in **Figure II.15**.

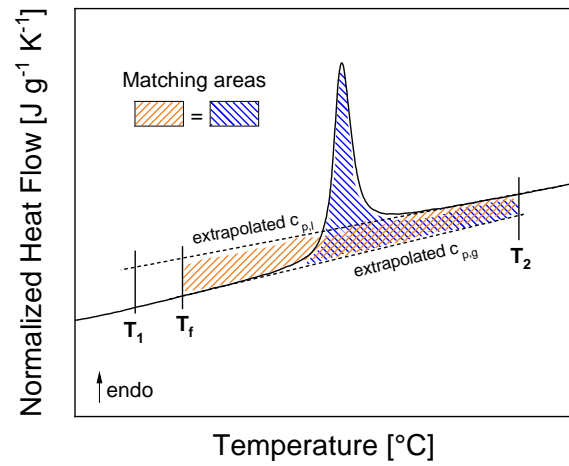


Figure II.15. Estimation of the fictive temperature T_f with Moynihan's method. Dashed lines correspond to the specific heat capacity in the glassy and in the liquid states extrapolated through the glass transition.

References

- [1] D. J. Brunelle et T. Jang, « Optimization of poly(1,4-cyclohexylidene cyclohexane-1,4-dicarboxylate) (PCCD) preparation for increased crystallinity », *Polymer*, vol. 47, n° 11, p. 4094-4104, mai 2006, doi: 10.1016/j.polymer.2006.02.070.
- [2] M. Marc *et al.*, « Bioinspired co-polyesters of hydroxy-fatty acids extracted from tomato peel agro-wastes and glycerol with tunable mechanical, thermal and barrier properties », *Industrial Crops and Products*, vol. 170, p. 113718, oct. 2021, doi: 10.1016/j.indcrop.2021.113718.
- [3] M. Marc *et al.*, « From Tomato Pomaces Biorefinery to Biobased Shape-Memory Semicrystalline Polyester Networks », *ACS Sustainable Chem. Eng.*, vol. 12, n° 6, p. 2191-2202, févr. 2024, doi: 10.1021/acssuschemeng.3c05713.
- [4] « The reflection of X-rays by crystals », *Proc. R. Soc. Lond. A*, vol. 88, n° 605, p. 428-438, juill. 1913, doi: 10.1098/rspa.1913.0040.
- [5] P. Scherrer, « Bestimmung der Grösse und der inneren Struktur von Kolloidteilchen mittels Röntgenstrahlen, Nachrichten von der Gesellschaft der Wissenschaften, Göttingen », 1918, p. 98-100.
- [6] A. Bishnoi, S. Kumar, et N. Joshi, « Wide-Angle X-ray Diffraction (WXR) », in *Microscopy Methods in Nanomaterials Characterization*, Elsevier, 2017, p. 313-337. doi: 10.1016/B978-0-323-46141-2.00009-2.
- [7] T. Ozawa, « A New Method of Analyzing Thermogravimetric Data », *Bulletin of the Chemical Society of Japan*, vol. 38, n° 11, p. 1881-1886, nov. 1965, doi: 10.1246/bcsj.38.1881.
- [8] J. H. Flynn, « THE HISTORICAL DEVELOPMENT OF APPLIED NONISOTHERMAL KINETICS », in *Thermal Analysis*, Elsevier, 1969, p. 1111-1126. doi: 10.1016/B978-0-12-395734-4.50035-7.
- [9] R. L. Blaine et B. K. Hahn, « Obtaining Kinetic Parameters by Modulated Thermogravimetry », *Journal of Thermal Analysis and Calorimetry*, vol. 54, n° 2, p. 695-704, 1998, doi: 10.1023/A:1010171315715.
- [10] M. Reading, A. Luget, et R. Wilson, « Modulated differential scanning calorimetry », *Thermochimica Acta*, vol. 238, p. 295-307, juin 1994, doi: 10.1016/S0040-6031(94)85215-4.
- [11] Lacey, A.A.; Price, D.M.; Reading, M. *Basic Theory and Practice for Modulated Temperature Differential Scanning Calorimetry (MTDSC)*. In: Reading, M.; Hourston, D.J. (eds.). *Modulated Temperature Differential Scanning Calorimetry - Theoretical and Practical Applications in Polymer Characterisation*. Springer, Dordrecht, 2006.
- [12] B. Rijal, L. Delbreilh, J.-M. Saiter, A. Schönhals, et A. Saiter, « Quasi-isothermal and heat-cool protocols from MT-DSC: Influence on the values extracted for the cooperativity length calculation », *J Therm Anal Calorim*, vol. 121, n° 1, p. 381-388, juill. 2015, doi: 10.1007/s10973-015-4671-4.
- [13] J. E. K. Schawe, T. Hütter, C. Heitz, I. Alig, et D. Lellinger, « Stochastic temperature modulation: A new technique in temperature-modulated DSC », *Thermochimica Acta*, vol. 446, n° 1-2, p. 147-155, juill. 2006, doi: 10.1016/j.tca.2006.01.031.
- [14] J. E. K. Schawe, S. Pogatscher, et J. F. Löffler, « Thermodynamics of polymorphism in a bulk metallic glass: Heat capacity measurements by fast differential scanning calorimetry », *Thermochimica Acta*, vol. 685, p. 178518, mars 2020, doi: 10.1016/j.tca.2020.178518.
- [15] X. Li, M. Zou, L. Lei, et L. Xi, « Non-Isothermal Crystallization Kinetics of Poly(ethylene glycol) and Poly(ethylene glycol)-B-Poly(ϵ -caprolactone) by Flash DSC Analysis », *Polymers*, vol. 13, n° 21, p. 3713, oct. 2021, doi: 10.3390/polym13213713.
- [16] V. Mathot *et al.*, « The Flash DSC 1, a power compensation twin-type, chip-based fast scanning calorimeter (FSC): First findings on polymers », *Thermochimica Acta*, vol. 522, n° 1-2, p. 36-45, août 2011, doi: 10.1016/j.tca.2011.02.031.
- [17] J. Q. Wang, Y. Shen, J. H. Perepezko, et M. D. Ediger, « Increasing the kinetic stability of bulk metallic glasses », *Acta Materialia*, vol. 104, p. 25-32, févr. 2016, doi: 10.1016/j.actamat.2015.11.048.
- [18] X. Monnier, N. Delpouve, et A. Saiter-Fourcin, « Distinct dynamics of structural relaxation in the amorphous phase of poly(L-lactic acid) revealed by quiescent crystallization », *Soft Matter*, vol. 16, n° 13, p. 3224-3233, 2020, doi: 10.1039/C9SM02541C.
- [19] R. Pilar, P. Honcová, G. Schulz, C. Schick, et J. Málek, « Enthalpy relaxation of selenium observed by fast scanning calorimetry », *Thermochimica Acta*, vol. 603, p. 142-148, mars 2015, doi: 10.1016/j.tca.2014.09.026.
- [20] « J. Schawe, "Practical aspects of the Flash DSC 1: Sample preparation for measurements of polymers. Mettler Toledo Thermal Analysis UserCom. 2012;36:17-24. http://ch.mt.com/ch/en/home/supportive_content/usercom/TA_UserCom36.html." ».

-
- [21] J. E. K. Schawe, « Measurement of the thermal glass transition of polystyrene in a cooling rate range of more than six decades », *Thermochimica Acta*, vol. 603, p. 128-134, mars 2015, doi: 10.1016/j.tca.2014.05.025.
- [22] S. Vyazovkin et N. Sbirrazzuoli, « Nonisothermal Crystallization Kinetics by DSC: Practical Overview », *Processes*, vol. 11, n° 5, p. 1438, mai 2023, doi: 10.3390/pr11051438.
- [23] J. E. K. Schawe, « Vitrification in a wide cooling rate range: The relations between cooling rate, relaxation time, transition width, and fragility », *The Journal of Chemical Physics*, vol. 141, n° 18, p. 184905, nov. 2014, doi: 10.1063/1.4900961.
- [24] C. T. Moynihan, A. J. Easteal, M. A. Bolt, et J. Tucker, « Dependence of the Fictive Temperature of Glass on Cooling Rate », *J American Ceramic Society*, vol. 59, n° 1-2, Art. n° 1-2, janv. 1976, doi: 10.1111/j.1151-2916.1976.tb09376.x.

Chapter III - Crystallization kinetics of co-polyesters obtained from tomato peel agro-wastes

Content

I. First thermal analysis of the monomer and polyester network	85
II. Cooling-rate dependence of the crystallization process	90
III. Isothermal crystallization kinetics of the polyester network.....	93
III.1 Thermal protocol	93
III.2 Estimation of the equilibrium melting enthalpy Δh_m° of the polyester network.....	95
III.3 Application of the Avrami model for isothermal crystallization	97
IV. Effect of polymerization on the crystallization kinetics.....	99
IV.1 Thermal protocol.....	99
IV.2 FSC measurements	101
IV.3 Application of the Avrami model for isothermal crystallization	104
IV.4 Equilibrium melting enthalpy Δh_m°	105
Conclusion	110
References	111

This third chapter focuses on the crystallization kinetics in non-isothermal and isothermal conditions of a co-polyester (referred to as “polyester network”) synthesized from a purified cutin monomer (referred to as “purified CM”) consisting in hydroxy-fatty acids extracted from tomato peel agro-wastes. This work was realized in collaboration with the Institut National de Recherche pour l'Agriculture, l'Alimentation et l'Environnement (INRAE) in Nantes. Bio-sourced co-polyesters obtained from agricultural waste recently raised interest thanks to their eco-friendliness and interesting barrier and mechanical properties, making them appealing for packaging applications [1]. The functional properties of these co-polyesters can be tailored through the control over the chemical structure, and a better understanding of the relationship between microstructure and macroscopic properties requires a precise knowledge of the crystallinity degree X_c and of the crystallization kinetics.

The need for biomass valorization and the quest for sustainable materials are two major sources of focus in the industrial and research communities. Among all possible high-performance polymers, polyesters have attracted a lot of attention because of their low immunogenicity, their easiness of production, and their tunable properties, that make them appealing for a wide range of applications. They can be synthesized using solvent-free and catalyst-free procedures, and can be biodegraded in controlled environments. Their microstructure can also be fine-tuned to improve their barrier and mechanical properties. It is common knowledge that the crystallinity X_c has a major impact on the mechanical properties of a polymer. Assessing the crystallization ability of a material is therefore essential, since it affects several macroscopic properties including stiffness, strength, chemical resistance, thermal stability, material morphology and gas permeability [2, 3], which are all important for processability, applicability, and biodegradability of the final material [4].

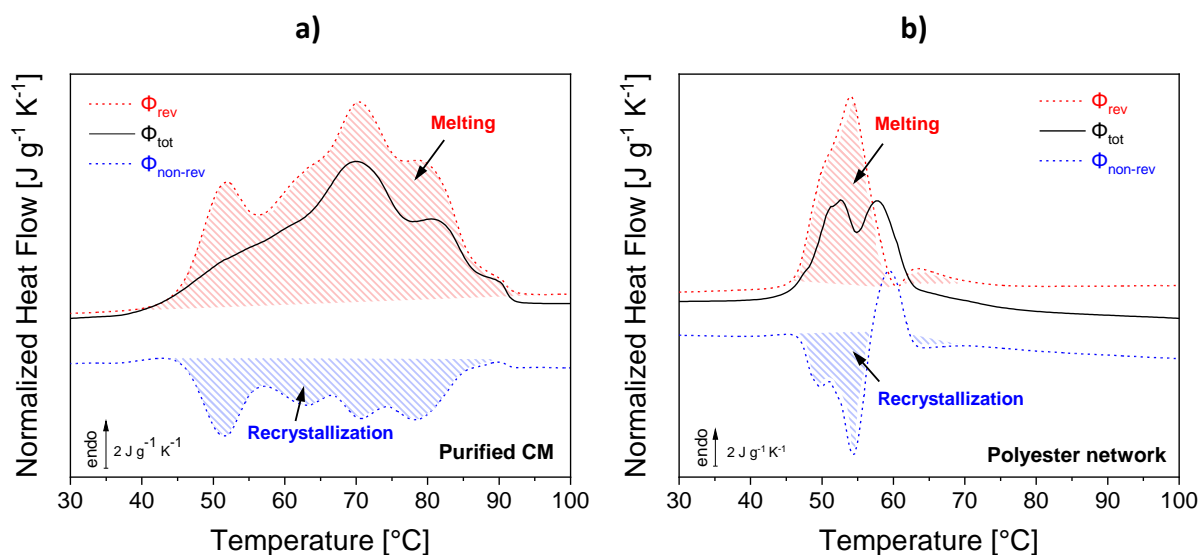
High X_c generally results in harder, stiffer and less ductile mechanical behavior [5]. Therefore, predictions require a precise knowledge of the crystallinity X_c . The estimation of X_c can be done by calorimetry, through the ratio of the melting enthalpy Δh_m and the equilibrium melting enthalpy Δh_m° corresponding to the melting of a fully crystallized polymer (which is never achieved due to chain entanglements). For common polymers, the values of Δh_m° related to the different crystalline phases are eventually reported in handbooks, but for relatively new materials this parameter is not always available. The estimation of the equilibrium melting enthalpy for organic compounds can be achieved through models relying on physicochemical and structural parameters, group contribution methods, or molecular dynamics [6, 7]. Recently, Cebe et al. [8] and Fosse et al. [9] proposed a calorimetric method to estimate Δh_m° relying on Fast Scanning Calorimetry (FSC) for polymers that crystallize rapidly and cannot be fully amorphized using the cooling rates associated with conventional Differential Scanning Calorimetry (DSC). Bio-based co-polyesters of hydroxy-fatty acids have interesting barrier and mechanical properties, which make them appealing for food packaging applications [1]. The polymerization of the monomers extracted from cutin produces loosely crosslinked semi-crystalline networks, whose thermal and mechanical properties are expected to depend on the crosslinking density. As a result, it is important to assess the consequences of polymerization (for different reaction times) on the microstructure and therefore on the macroscopic properties.

In the following, the methodology proposed by Cebe et al. [8] and Fosse et al. [9] will be used in the attempt to estimate the value of Δh_m° of the cutin monomers in their initial state (after extraction and purification) in order to estimate its crystalline content. The purified cutin monomer (purified CM) is

then polymerized in bulk for 24 h, and *in situ* for shorter times (from 40 s to 600 s) using FSC nanoscale sample, to assess the impact of crosslinking on the thermal behavior.

I. Preliminary thermal analyses of the monomers and of the polyester networks

Preliminary thermal characterizations of the prepolymers (purified CM) and the crosslinked polyester networks were done by TOPEM. As mentioned in **Chapter II (Section II.2.5)**, TOPEM enables the separation of partially or entirely overlapping thermal events, such as crystallization and melting. The total heat flow Φ_{tot} corresponds to the signal measured with conventional DSC, and is the algebraic sum of two components, the reversing heat flow Φ_{rev} and the non-reversing heat flow $\Phi_{non-rev}$. The first term is related to thermal events involving heat capacity changes, whereas the latter is related to kinetic events. From Φ_{rev} the quasi-static heat capacity $c_{p,0}$ can be derived using an extrapolation to zero frequency. TOPEM measurements consisted in heating segments from ambient temperature ($T = 20\text{ }^{\circ}\text{C}$) to $100\text{ }^{\circ}\text{C}$ with a heating rate of 2 K min^{-1} , then an isothermal holding at $100\text{ }^{\circ}\text{C}$ for 2 minutes, followed by cooling from $100\text{ }^{\circ}\text{C}$ to $-60\text{ }^{\circ}\text{C}$ at 2 K min^{-1} , and finally a second heating scan from $-60\text{ }^{\circ}\text{C}$ up to $100\text{ }^{\circ}\text{C}$ at the same rate. The reversing, non-reversing, and total heat flows recorded during the first heating ramp, the cooling segment, and the second heating ramp are represented in **Figure III.1**.



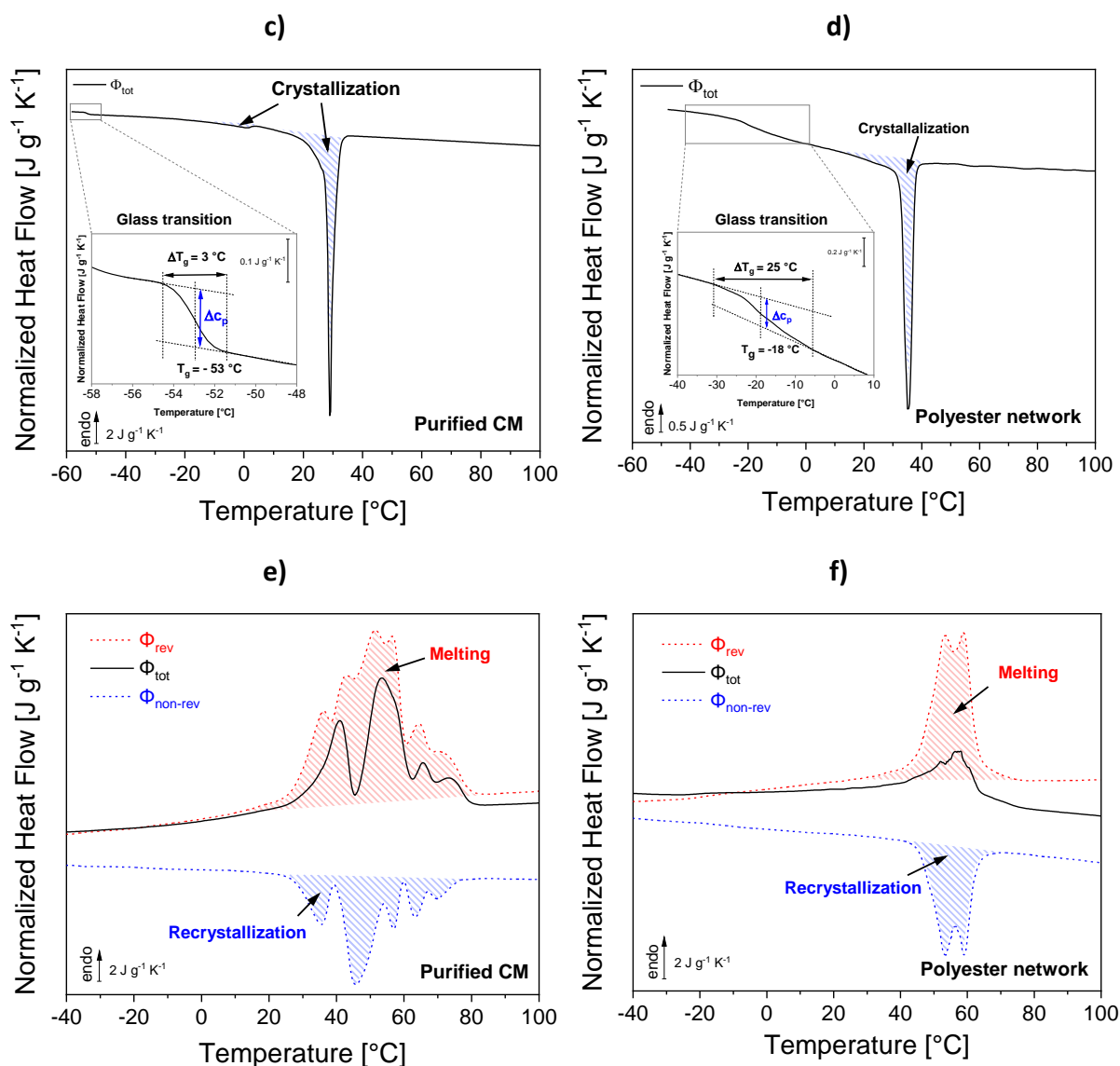


Figure III.1. Normalized total heat flow (black), reversing heat flow (red) and non-reversing heat flow (blue) measured during the first heating ramp for **a)** purified CM and **b)** polyester network with a heating rate of 2 K min^{-1} . The hatched areas indicate the melting (red) and recrystallization (blue) processes. Normalized total heat flow obtained for **c)** purified CM and **d)** polyester network upon cooling at 2 K min^{-1} . The insets show a magnification of the glass transition, with ΔT_g indicating the broadness of the glass transition. Normalized total heat flow (black), reversing heat flow (red) and non-reversing heat flow (blue) recorded during the second heating ramp for **e)** purified CM and **f)** polyester network with a heating rate of 2 K min^{-1} . The hatched areas indicate the melting (red) and recrystallization (blue) processes.

Different melting behaviors are observed for the purified CM and the polyester network. The thermal parameters extracted from the heating and cooling curves in **Figure III.1** are presented in **Table III.1**. The purified CM shows a very complex endothermic peak, with several shoulders from 40°C to 92°C in the reversing heat flow, whereas the polyester network has a main melting peak spread from 46°C to 60°C , followed by another smaller endothermic peak on the high-temperature side. In both cases,

melting and recrystallization occur simultaneously, as shown by the hatched areas. Recording complex melting peaks made of several endotherms is not unusual for fatty acids due to the existence of different polymorphs (mostly α , β' and β forms) [10]. Each polymorphic form yields different crystal structures with different thermodynamic stabilities, which means that they potentially have different lifetimes within a crystal matrix. The general tendency suggests a greater stability going from α to β' to β [11].

The low-temperature melting endotherm is generally associated with the melting of the least stable phase α and of the sub- α modification [11], the intermediate temperature endotherms are associated to the β' form or its submodifications, and the endotherm observed at the highest temperature is generally attributed to the most stable polymorph β [12]. The respective melting temperatures associated to these polymorphs were found to depend on the fatty acid chain length; the longer the chain, the harder it gets to separate two adjacent melting peaks [13].

Table III.1: Glass transition temperature (T_g), specific heat capacity step measured at T_g (Δc_p), temperature range of the melting process (ΔT_m), melting enthalpy (Δh_m) measured on the total (Φ_{tot}) and reversing (Φ_{rev}) heat flow, crystallization temperature (T_c) and crystallization enthalpy measured upon cooling (Δh_c) on the non-reversing heat flow.

Sample		T_g [°C]	Δc_p [J g ⁻¹ K ⁻¹]	ΔT_m [°C]	Δh_m [J g ⁻¹] Φ_{tot}	Δh_m [J g ⁻¹] Φ_{rev}	T_c [°C]	Δh_c [J g ⁻¹]
Purified CM	1 st heating	/	/	40-92	155 ± 3	218 ± 5	/	/
	Cooling	-53 ± 1	0.19	/	/	/	28.8	57 ± 2
	2 nd heating	/	/	26-80	87 ± 5	156 ± 5	/	/
Polyester Network	1 st heating	/	/	46-74	74 ± 2	92 ± 2	/	/
	Cooling	-18 ± 1	0.15	/	/	/	35.3	37 ± 2
	2 nd heating	-22 ± 1	0.14	33-76	40 ± 5	94 ± 5	/	/

The exothermic crystallization peak recorded upon cooling is very sharp for both materials, and is located at a slightly higher temperature for the polyester network. A secondary crystallization peak is noticeable at about 0 °C for the purified CM. A low value of T_g is obtained for both materials, resulting from a relatively high molecular mobility due to the long methylene sequences. A gap of about 35 °C is observed between the glass transition measured upon cooling for the semi-crystalline purified CM and the polyester network, likely due to the crosslinking nodes present in the polyester, as evidenced by Marc et al. [1]. In addition to a change in T_g , the width of the glass transition differs as well. This broadening can be quantified by ΔT_g (defined as $T_{g,max} - T_{g,min}$). For purified CM, the width of the

glass transition ΔT_g is only 3 °C, whereas for the polyester network it reaches 25 °C, which is a sign of increased heterogeneity in the relaxation times associated within the amorphous phase upon cooling. Since the purified CM seems to be more crystallized than the polyester network, this increase in dynamic heterogeneity cannot be imputed on a higher crystallized fraction, but is most likely due to structural effects, in particular to the topological change associated with crosslinking. The values of melting enthalpy differ as well between the purified CM and the polyester network, with larger Δh_m obtained for the purified CM during both the first and the second heating ramps. It appears that crosslinking affects the melting enthalpy which is nearly twice as high for the purified CM compared to the polyester network. A significant decrease in melting enthalpy is observed when comparing the first and the second heating ramps (155 vs. 87 J g⁻¹ for the purified CM, 74 vs. 40 J g⁻¹ in the case of the polyester network). Finally, the melting enthalpy measured for the polyester network during the first and second heating ramps based on Φ_{tot} are close to the values previously obtained by Marc et al. [1].

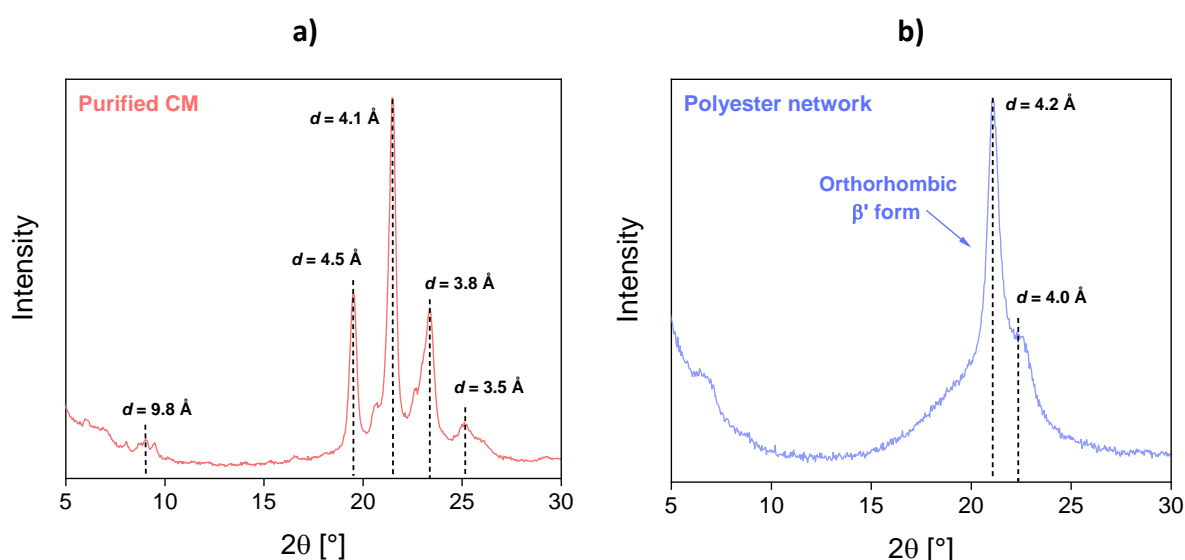


Figure III.2. X-ray patterns recorded at 30 °C for **a)** the purified CM and **b)** the polyester network after a long storage. Low-angle deviation is due to partial cutting of the incident beam.

Figure III.2 shows the XRD patterns recorded for the purified CM and the polyester network after a long storage (about four years) at ambient temperature. The polyester network is in an orthorhombic β' polymorphic form, with two peaks at 21.1 ° ($d = 4.2 \text{ \AA}$) and 22.3 ° ($d = 4.0 \text{ \AA}$). The presence of a Lorentzian peak's tail in the XRD spectrum of the polyester network could account for the presence of a paracrystalline phase [14]. More peaks are visible in the XRD pattern of the purified CM. The same orthorhombic β' polymorphic form is observed through the peaks located at 21.6 ° ($d = 4.1 \text{ \AA}$) and 23.4 ° ($d = 3.8 \text{ \AA}$). An additional peak at 9 ° ($d = 9.8 \text{ \AA}$) is visible, which could indicate a longitudinal

organization of the chains, as suggested by Marc et al. [1]. Additional peaks at 19.5° ($d = 4.5 \text{ \AA}$) and 25.2° ($d = 3.5 \text{ \AA}$) are observed, revealing the presence of a triclinic packing characteristic of the β form [7]. Interestingly, thermal analysis and X-ray diffraction patterns show a coexistence of β and β' -forms in the purified CM, but only the orthorhombic form β' is observed for the polyester network, indicating that the relative stability of the β and β' -form seems to be dependent on the crosslinking density.

The microstructure of these polyesters was observed under Polarized Optical Microscopy (POM) in an attempt at getting more information about the nucleation and growth process. Each sample was pressed under a cover slip and heated to the melt at 100°C , held for 5 minutes, then cooled down to 25°C with the same cooling rate used for TOPEM measurements (2 K min^{-1}). Only the purified CM is shown here, since no spherulites were observed for the polyester network.

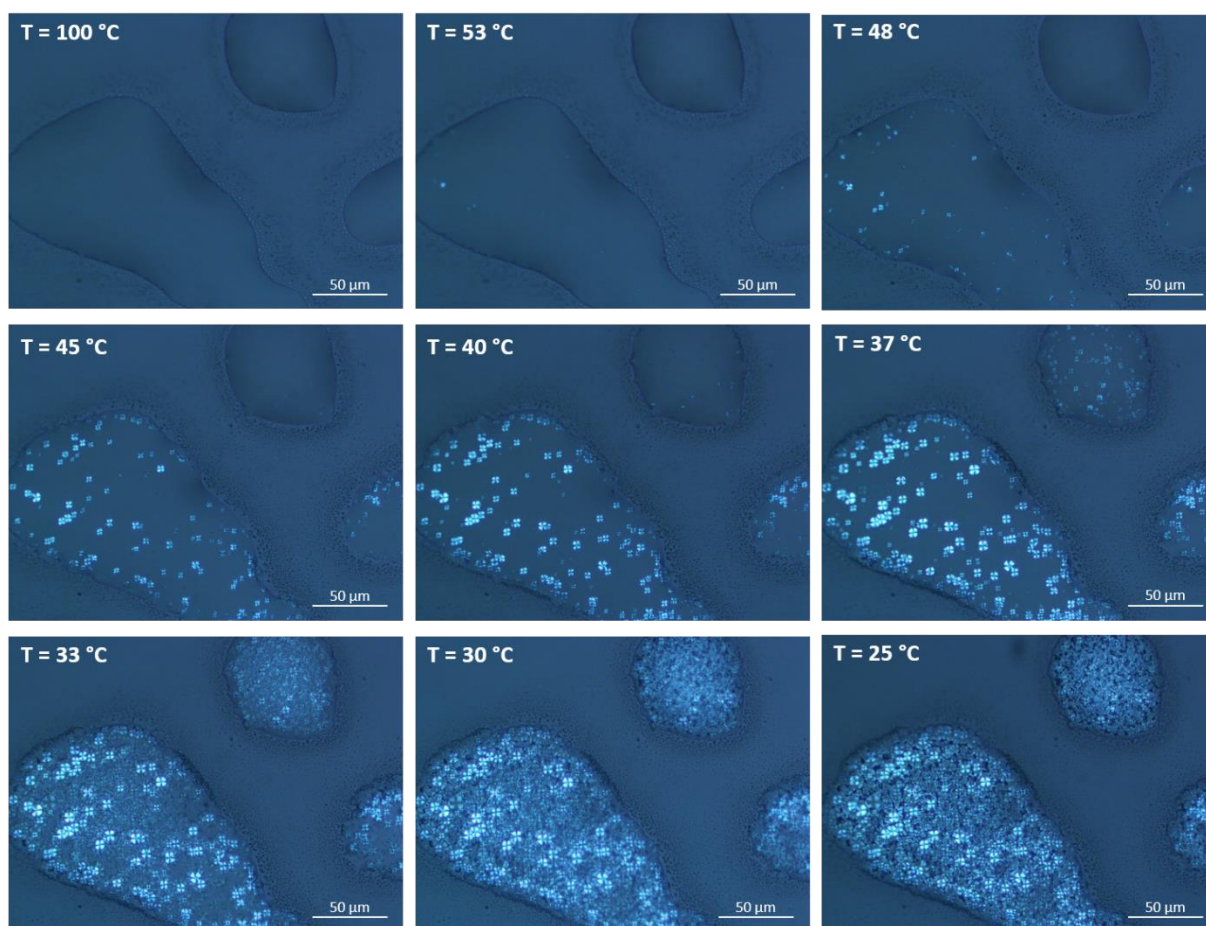


Figure III.3. Micrographs of the purified CM recorded under polarized light during cooling at 2 K min^{-1} from 100°C down to 25°C .

Figure III.3 depicts the crystallization of the purified CM upon cooling at 2 K min^{-1} from $100 \text{ }^\circ\text{C}$ to $25 \text{ }^\circ\text{C}$ (the observations reported here were made at specific temperatures). At $53 \text{ }^\circ\text{C}$ sporadic nucleation occurs, and as the temperature decreases, these early nuclei grow in a radial fashion to form microsized particles. At $33 \text{ }^\circ\text{C}$ a spontaneous and very rapidly space-filling secondary nucleation and growth occurs until the temperature reaches $25 \text{ }^\circ\text{C}$. These small secondary structures grow so fast and are so space-filling that they get to surround and almost mask the particles formed during the earlier stages of crystallization [11]. The resulting microstructure consists of a large number of small crystalline structures whose diameter does not exceed $8 \text{ }\mu\text{m}$. **Figure III.4** shows the micrograph recorded once the cooling ramp is completed and after microstructure stabilization. Star-shaped structures are visible with a large size distribution, supposedly connected in a vast crystal network stabilized by van der Waals forces [15].

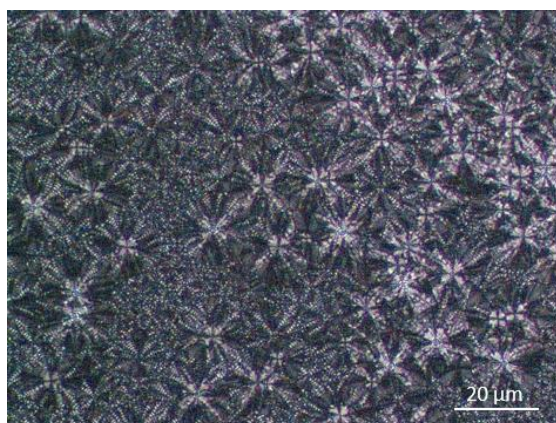


Figure III.4. Micrograph with a magnification of $\times 20$ obtained on the purified CM at $25 \text{ }^\circ\text{C}$ after cooling from $100 \text{ }^\circ\text{C}$ at 2 K min^{-1} .

II. Cooling-rate dependence of the crystallization process

The functional properties of crystal networks formed out of macromolecular materials depend on the processing conditions and in particular on the cooling rate, and it has been also observed in systems such as milk fat and lard [15]. FSC allows to cool down materials at extremely high rates (in the order of 10^4 K s^{-1}). **Figure III.5** compares the normalized heat flows recorded upon cooling at 0.03 K s^{-1} with TOPEM (**Figures III.1.c** and **III.1.d**) with the normalized heat flows measured at different rates (β_c from 30 K s^{-1} to $5\,000 \text{ K s}^{-1}$) with FSC for the purified CM and the polyester network. The exothermic crystallization peak recorded at low cooling rates is very sharp. When the cooling rate increases, the crystallization is shifted to lower temperatures and the peak spreads, possibly due to a change from

heterogeneous to homogeneous (sporadic) nucleation. Moreover, at intermediate cooling rates, a double contribution to the crystallization exotherm can be observed for both the monomer and the polyester, which could be related to the formation of different polymorphs.

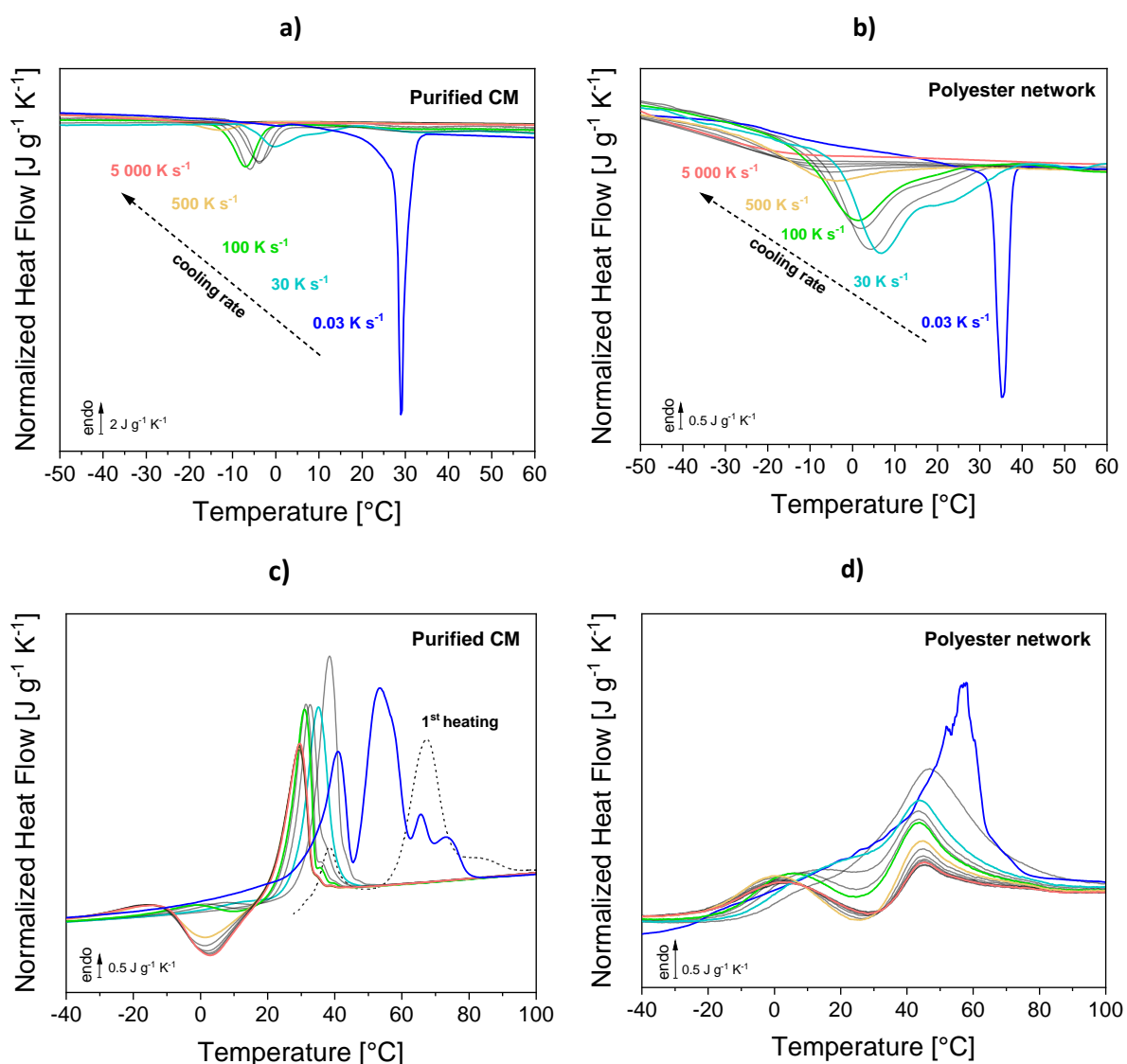


Figure III.5. Normalized heat flows recorded upon cooling at different rates from 0.03 K s⁻¹ (TOPEM) up to 5 000 K s⁻¹ (FSC) for **a**) purified CM and **b**) polyester network. Normalized heat flows recorded upon subsequent heating at 0.03 K s⁻¹ (TOPEM) and 1 000 K s⁻¹ (FSC) for **c**) purified CM and **d**) polyester network. The dashed curve was measured during the first heating ramp without prior thermal treatment.

The cooling-rate dependences of the crystallization, cold crystallization and melting temperatures are shown in **Figure III.6**. For cooling rates higher than 2 000 K s⁻¹ no change in cold crystallization and melting temperatures is observed for the polyester network, and a self-doped glass (SDG) is formed upon cooling according to the classification proposed by Schawe and Löffler [16]. No change in melting

and cold crystallization temperature is observed above $2\,000\text{ K s}^{-1}$ for the purified CM, while crystallization is observed upon cooling at rates as high as $5\,000\text{ K s}^{-1}$. At even higher cooling rates, the crystallization exothermic peak merges into the glass transition and is no longer visible. As the cooling rate decreases, crystallization occurs; this happens for cooling rates below $4\,000\text{ K s}^{-1}$ for the purified CM, and below $1\,000\text{ K s}^{-1}$ for the polyester network, whose crystallization ability is hindered by the crosslinking nodes [1]. An increase in T_c is also observed at lower cooling, however no change in the melting temperature is noted for intermediate cooling rates (between $4\,000$ and $1\,000\text{ K s}^{-1}$ for the purified CM, and between $1\,000$ and 300 K s^{-1} for the polyester network). Below these intermediate cooling rates, a constant increase in the melting temperature is observed.

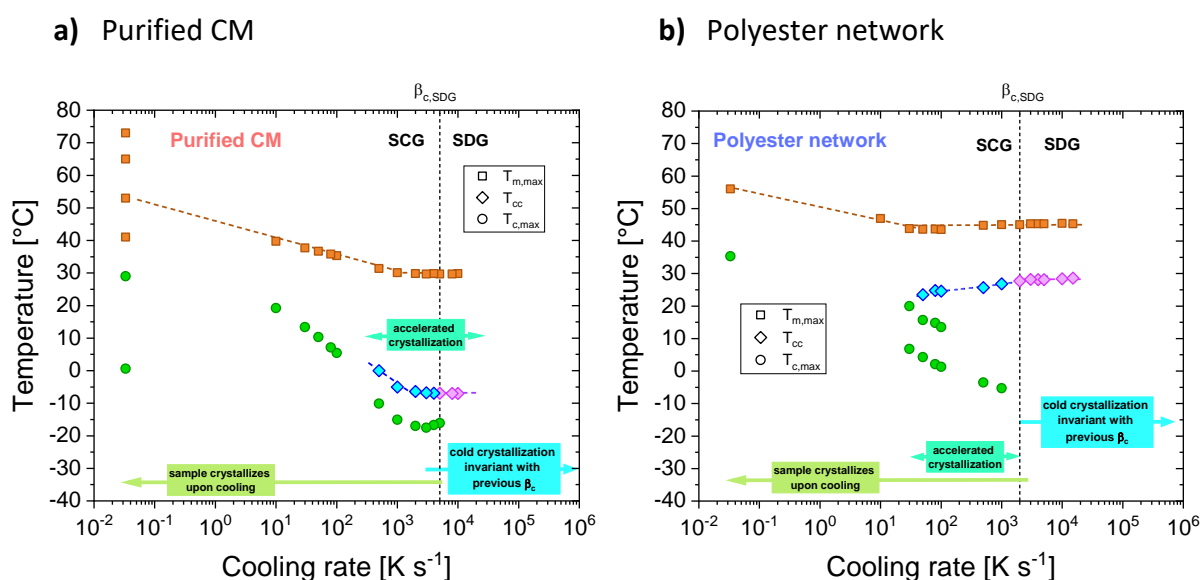


Figure III.6. Cooling-rate dependences of the crystallization temperature for **a)** the purified CM and **b)** the polyester network. The melting temperatures (T_m) are represented by orange squares, the crystallization temperatures (T_c) are represented by green circles, and the cold-crystallization temperatures (T_{cc}) are represented by blue diamonds in case of semi-crystalline glass (SCG), and by purple diamonds in case of self-doped glass (SDG). The experimental data at 0.03 K s^{-1} (2 K min^{-1}) is extracted from the TOPEM curves represented in **Figure III.1**. The dashed lines are guides to the eye.

To investigate the crystalline structures formed upon fast cooling, X-ray diffraction patterns were recorded after liquid N_2 cooling for the purified CM and the polyester network, as shown in **Figure III.7**. For both the samples, fast cooling from the melt results in the formation of the metastable α -form. Then a polymorphic transformation occurs as the samples are stored for a certain time at ambient temperature, with transformations from the unstable α -phase to the more stable β and β' -

phases as seen from the DRX spectra in **Figure III.2**. The polymorphic α -to- β' transformation was found to occur within 7 days of storage at ambient temperature [1,15].

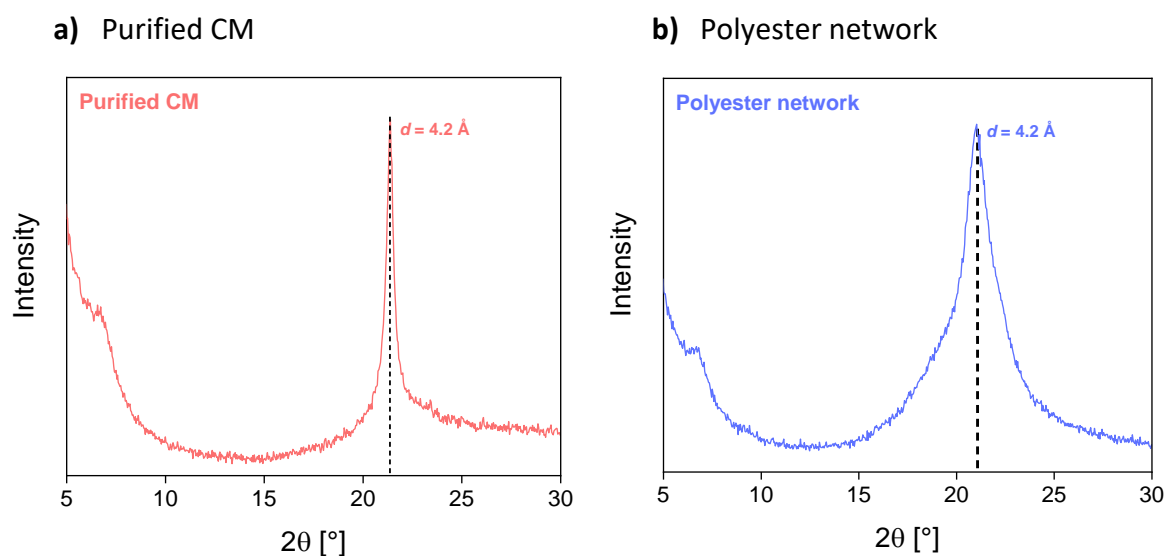


Figure III.7. XRD spectra recorded at 30 °C for **a)** the purified CM and **b)** the polyester network after liquid N₂ cooling from the molten state to -196 °C.

III. Isothermal crystallization kinetics of the polyester network

III.1 Thermal protocol

The procedure proposed by Cebe and al. [8] and Fosse et al. [9] relies on a linear regression of the normalized melting enthalpy against the specific heat capacity for different crystallization fractions assuming a two-phase model. This requires the absence of rigid amorphous fraction (RAF), whose formation depends on the temperature at which the material crystallizes [17]. When the temperature chosen for isothermal crystallization is too low, the decreased chain mobility leads to the formation of imperfect crystals with a significant coupling with the neighboring amorphous phase, and therefore a certain amount of RAF. On the opposite, a high crystallization temperature results in a reduced coupling between phases but suffers from a competition between crystallization and melting.

From the cooling-rate dependence of T_m and T_c (see **Figure III.6**), a temperature of 20 °C is chosen for isothermal crystallization. The second reason of this choice is that previous mechanical investigations showed that the mechanical behavior of the polyester network at ambient temperature is determined

by its semi-crystalline structure [1]. During storage, a number of post-crystallization processes occur that can affect properties such as hardness, which often noticeably increases because of sintering, a phenomenon related to the formation of solid bridges between crystals to form a network [18].

FSC experiments were performed on a Flash DSC 2+ (Mettler-Toledo) with conditioned and calibrated UFH1 sensors under a continuous argon flow of 60 mL min^{-1} . The sample mass was estimated at about 20 ng through the comparison of the heat capacity baseline recorded upon heating at $5\,000 \text{ K s}^{-1}$ with FSC in the glassy and molten state, and the specific heat capacity baseline recorded with TOPEM at 2 K min^{-1} . The polyester network is first heated to $T_m + 50 \text{ }^\circ\text{C}$ to erase thermal history, then quenched to the selected isothermal crystallization temperature T_c at $5\,000 \text{ K s}^{-1}$. The sample undergoes crystallization for a given time (t_c) in isothermal conditions (T_c) according to the protocol in **Figure III.8**. More details about the crystallization protocol are given in Fosse et al. [9].

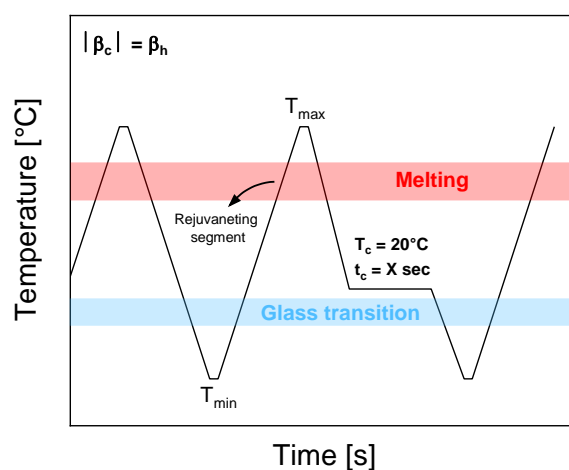


Figure III.8. Thermal protocol used for isothermal crystallization. The sample is first heated to $T_{max} = T_m + 50^\circ\text{C}$ to erase thermal history, then it is quenched to the crystallization temperature T_c and held isothermally for a defined time t_c . After isothermal crystallization, the sample is quenched down to $T_{min} = T_g - 50 \text{ }^\circ\text{C}$ and finally heated up to T_{max} . The same heating and cooling rates are applied with $|\beta_c| = \beta_h = 5\,000 \text{ K s}^{-1}$.

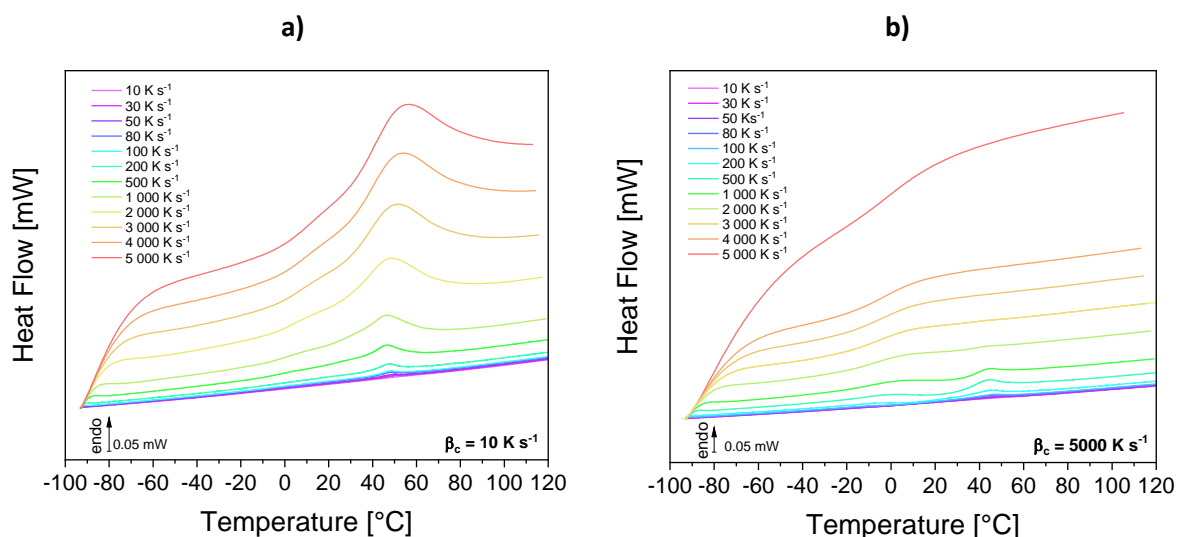


Figure III.9. Heat flow curves measured with different heating rates from $-90\text{ }^{\circ}\text{C}$ to $120\text{ }^{\circ}\text{C}$ following a previous cooling from $120\text{ }^{\circ}\text{C}$ to $-90\text{ }^{\circ}\text{C}$ at **a)** 10 K s^{-1} and **b)** 5000 K s^{-1} .

The scanning rate of 5000 K s^{-1} chosen for the thermal protocol in **Figure III.8** prevents crystallization upon cooling and cold crystallization upon heating. **Figure III.9.a** shows the heat flow measured following a cooling scan at 10 K s^{-1} . Neither a change in the endothermic melting peak nor any reorganization are notable, suggesting the formation of a single and well-defined crystalline form upon cooling at 10 K s^{-1} . In **Figure III.9.b** the heating curves measured after a cooling at 5000 K s^{-1} show the presence of cold crystallization at $20\text{ }^{\circ}\text{C}$ followed by melting at heating rates up to 4000 K s^{-1} . For heating rates higher than 4000 K s^{-1} , neither cold crystallization nor melting are visible anymore. When the heating rate is too high, the nuclei are either suppressed or do not have time to grow. The polyester network undergoes cold crystallization for heating rates lower than 3000 K s^{-1} after cooling at 5000 K s^{-1} . No melting is observed for heating rates higher than 2000 K s^{-1} .

III.2 Estimation of the melting enthalpy Δh_m° of the polyester network

From **Figure III.10**, the melting enthalpy Δh_m° (calculated by the linear regression to $\Delta c_p = 0\text{ J g}^{-1}\text{ K}^{-1}$) reaches a value of $77 \pm 10\text{ J g}^{-1}$ for the polyester network. The uncertainty is mainly due to the arbitrary baseline used to integrate the melting peak, as well as to the mass estimation. Because the thermal protocol is similar to the one employed for the X-ray diffraction measurements after quench from the melt by liquid nitrogen, it seems reasonable to assume that the crystals formed correspond to the metastable α -crystals with a hexagonal packing.

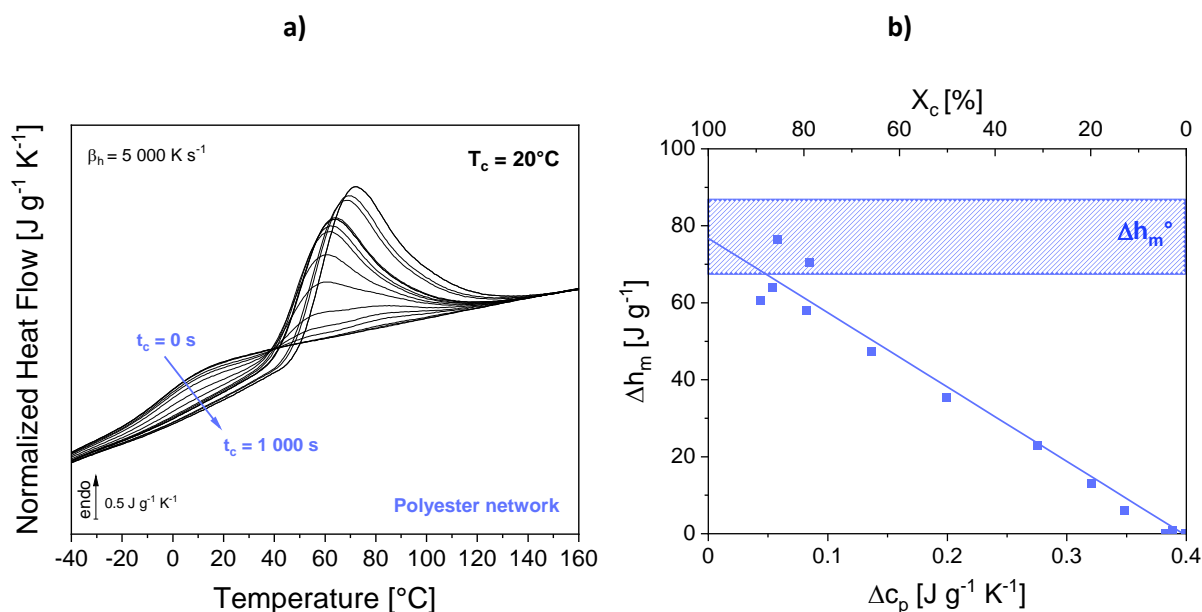


Figure III.10. **a)** Normalized heat flows measured upon heating at $5\,000 \text{ K s}^{-1}$ after isothermal crystallization at 20°C for increasing durations (t_c from 0 to 1 000 s); **b)** Melting enthalpy Δh_m plotted against the specific heat capacity Δc_p normalized by the sample mass and the heating rate for the polyester network crystallized for different crystallization times t_c at a crystallization temperature $T_c = 20^{\circ}\text{C}$. A linear regression (solid line) to $\Delta c_p = 0 \text{ J g}^{-1} \text{K}^{-1}$ ($X_c = 100\%$) gives the equilibrium melting enthalpy Δh_m° corresponding to a theoretically fully crystallized material under the assumption of a two-phase model [8, 9]. The hatched area represents an uncertainty of $\pm 10 \text{ J g}^{-1}$ for the estimation of Δh_m° .

Fosse et al. evidenced that for some samples the choice of T_c could have a significant influence on the estimation of Δh_m° , especially the ones that are prone to polymorphism, as in the case of PLLA [9].

Figure III.11 shows the same experimental protocol performed at a crystallization temperature $T_c = 40^{\circ}\text{C}$.

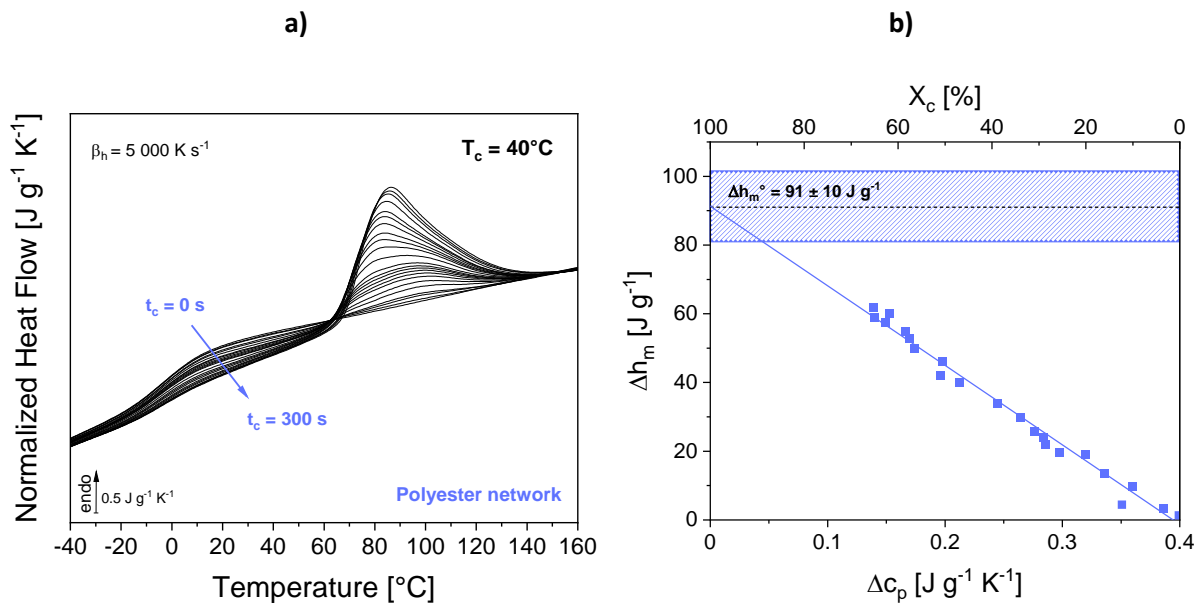


Figure III.11. **a)** Normalized heat flows measured upon heating at 5 000 K s⁻¹ after isothermal crystallization at 40 °C for increasing durations (t_c from 0 to 300 s); **b)** Melting enthalpy Δh_m plotted against the specific heat capacity Δc_p normalized by the sample mass and the heating rate for the polyester network crystallized for different crystallization times t_c at a crystallization temperature $T_c = 40$ °C. A linear regression (solid line) to $\Delta c_p = 0$ J g⁻¹ K⁻¹ ($X_c = 100\%$) gives the equilibrium melting enthalpy Δh_m^o corresponding to a theoretically fully crystallized material under the assumption of a two-phase model [8, 9]. The hatched area represents an uncertainty of ± 10 J g⁻¹ for the estimation of Δh_m^o .

The experimental data acquired for a crystallization temperature of 40 °C are shown in **Figure III.11**. The melting peaks have a similar shape as before, but are shifted to higher temperatures in comparison with the melting peaks obtained after crystallization at 20 °C. A value of Δh_m^o reaching 91 ± 10 J g⁻¹ is obtained, which is higher than the previous values reported after isothermal crystallization at 20 °C, suggesting that different crystalline phases are formed at these two temperatures. Since the formation of the α -phase has been evidenced from the XRD pattern, it is possible that crystallizing at 40 °C results in the formation of the two polymorphs α and β' . To better understand these results, the isothermal crystallization kinetics will be investigated using Avrami's model [19].

III.3 Application of the Avrami model for isothermal crystallization

Isothermal crystallization kinetics are analyzed with the Avrami equation [19]:

$$\alpha(t) = 1 - \exp(-k(t - t_0)^n) \quad \text{Eq. 1}$$

where $\alpha(t)$ is the relative crystalline fraction already transformed at time t , n is the Avrami index, k is the crystallization rate constant, and t_0 is the induction time at which crystallization starts. This

equation is based on the assumption that the nucleation rate is constant and that growth is linear (constant growth rate) [20]. In the logarithmic form, Eq. 1 becomes:

$$\text{Log}[-\ln(1 - \alpha)] = \text{Log}(k) + n \text{Log}(t - t_0) \quad \text{Eq. 2}$$

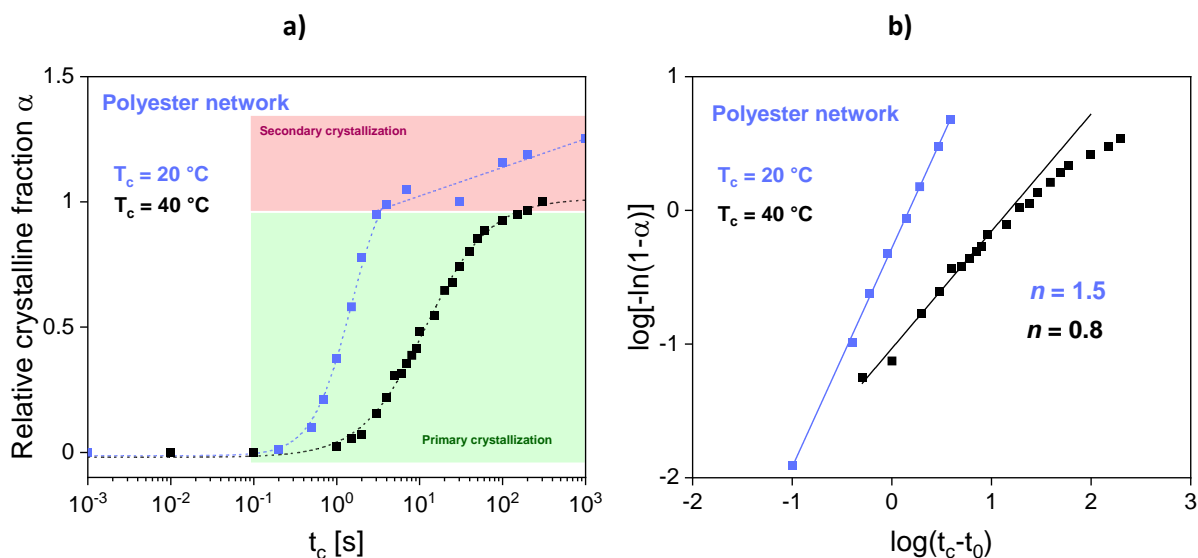


Figure III.12. a) Dependence of the relative crystalline fraction α of the polyester network as a function of the isothermal crystallization time t_c during isothermal crystallization at 20°C (blue squares) and 40°C (black squares); the lines are guide for the eye; b) Avrami plots for the polyester network; the lines correspond to the fitting of the experimental data with Eq. 2.

The increase of the relative fraction α with the crystallization time follows a typical sigmoidal shape and progresses more rapidly for $T_c = 20^\circ\text{C}$ than 40°C , as shown in **Figure III.12.a**. The curve obtained for an isothermal crystallization at 20°C reveals two crystallization modes. The first primary crystallization is associated to a rapid increase of the relative crystalline fraction (initial crystal growth), and is followed by secondary crystallization, which is characterized by a linear increase of the relative crystalline fraction α with respect to time in logarithm scale (crystal thickening). A similar behavior was observed in other polyesters, such as PLA [21] and PCL [22]. From the Avrami plot represented in **Figure III.12.b**, the dimensionality of crystal growth can be assessed, and the surprisingly low Avrami indices seem to suggest a one-dimension growth. Unfortunately, the crystals formed by the polyester network could not be observed with POM because of its inability to flow, which would have been helpful to explain such results.

In the following, the effect of polymerization on the crystallization kinetics will be investigated. To this purpose, the results obtained for the polyester network (which was polymerized in bulk for 24 h at 150

°C) will be compared to those obtained for the purified CM after polymerization at the nanoscale for various times ranging from 0 to 600 s.

IV. Effect of polymerization on the crystallization kinetics

As stated before, it seems important to investigate the effect of polymerization on the crystallization kinetics of these systems. The polyester network was obtained after baking at 150 °C for 24 h, resulting in an increase in molar mass M_n , as well as branching and crosslinking due to the reacted acid and hydroxyl functions, forming in the end a complex topology [1]. In the following section all the samples have the same chemical composition but the variation of the polymerization time results in a change of topology (difference in M_n , branching and crosslinking density). Because the impact of M_n and of the crosslinking density on the crystallization kinetics cannot be differentiated, both will be referred to under the term “polymerization” to simplify the analysis.

IV.1 Thermal protocol

The heating and cooling rates were selected to prevent crystallization upon cooling and cold crystallization upon heating. In light of the results obtained in **Section II** on this chapter, a scanning rate of 10 000 K s⁻¹ was chosen for the purified CM. For comparative purposes, identical scanning rates would have been preferred. However, cold crystallization is prevalent at 5 000 K s⁻¹ for the purified CM, and the signal did not allow to clearly visualize the glass transition in the case of polyester network at 10 000 K s⁻¹. FSC was performed with conditioned and calibrated UFH1 sensor under a continuous argon flow of 60 mL min⁻¹. A mass of about 11 ng of purified CM was estimated using the same procedure as the polyester network. The samples were first heated up to $T_m + 50$ °C to erase thermal history, then quenched down to the isothermal crystallization temperature T_c at 10 000 K s⁻¹. They were subjected to crystallization for a given time (t_c) in isothermal conditions (T_c) following the thermal protocol described in **Figure III.13**. After the crystallization procedure (**Figure III.13.a**), the purified CM sample was polymerized at 150°C for a given time (t_{pol}) *in situ* (**Figure III.13.b**).

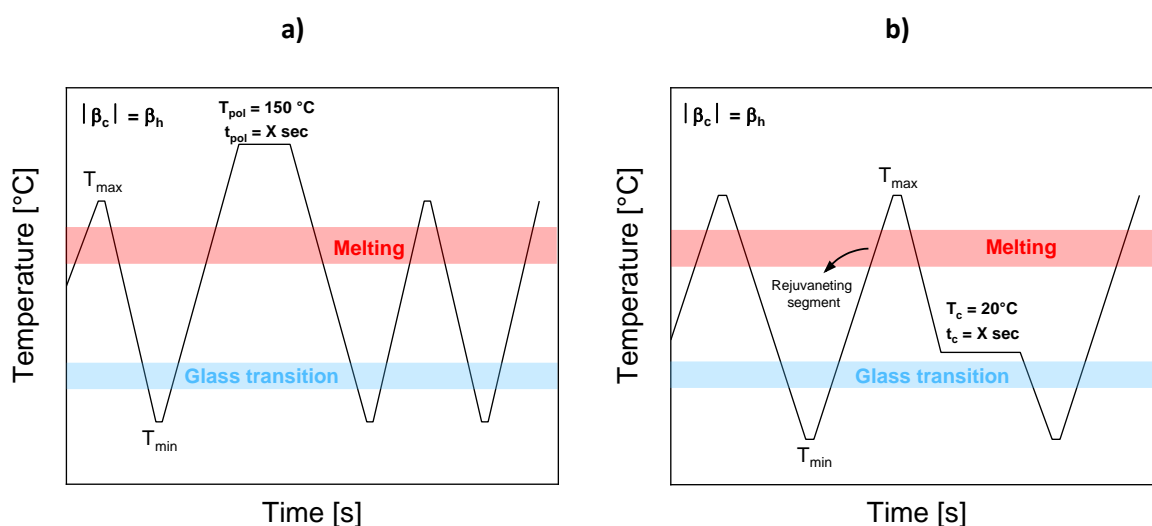


Figure III.13. **a)** Thermal protocol used for *in situ* polymerization at 150 °C for polymerization times $t_{pol} = 0, 40$ and 600 s; **b)** Thermal protocols used for isothermal crystallization. The sample was first heated at $T_{max} = T_m + 50$ °C to erase thermal history, then quenched down to the crystallization temperature T_c and held in isothermal conditions for a defined time t_c . After isothermal crystallization, the sample was quenched down to $T_{min} = T_g - 50$ °C and finally heated to T_{max} . The same heating and cooling rates were applied with $|\beta_c| = \beta_h = 10\,000$ K s⁻¹.

The polymerization process at 150 °C was performed *in situ* in the Flash DSC apparatus on the UFH1 sensor containing the purified CM sample for 40 s and 600 s, as shown in **Figure III.14**. A decrease in the measured heat flow is observed as the polymerization time increases. Even though polycondensation involves some water evaporation, the mass loss due to the release of H₂O molecules (18 g mol⁻¹ each) is neglectable in comparison with the mass of cutin monomer (288 g mol⁻¹ for the main component, 9(10)-16-dihydroxyhexadecanoic acid), and could only be accounted for about 6% of the total sample mass. In Marc et al. [1], a very small weight loss (less than 0.5%) was observed below 100°C, which was attributed to moisture evaporation, and thermal degradation was found to occur above 300°C. By comparing the different curves, a reduction of the heat flow of about 65 % is observed, which seems to suggest that some degradation evidenced as a mass loss potentially occurred during the isotherms at 150°C. This mass loss was considered for further calculation of the melting enthalpy and the specific heat capacity.

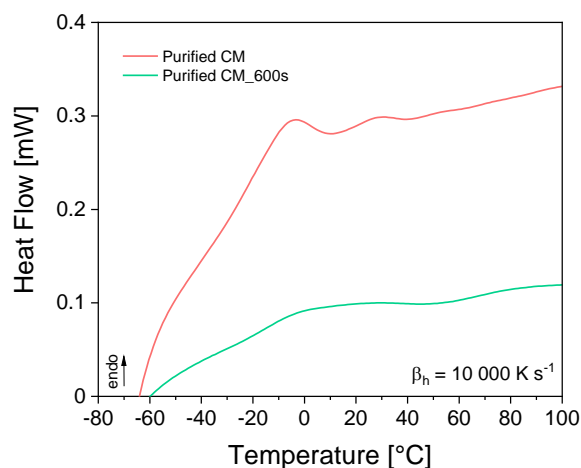


Figure III.14. Heat flows measured upon heating at $10\,000\text{ K s}^{-1}$ for the purified CM (red curve) and after polymerization for 600 s (purified CM_600s, green curve).

IV.2 FSC measurements

Figure III.15 shows the normalized heat flows recorded for the purified CM after polymerization at $150\text{ }^{\circ}\text{C}$ for 0 s, 40 s and 600 s, and for the polyester network following different times of isothermal crystallization at $20\text{ }^{\circ}\text{C}$. The main melting peak increases from $40\text{--}60\text{ }^{\circ}\text{C}$ for the purified CM to $60\text{--}70\text{ }^{\circ}\text{C}$ for the polyester network. Concerning the purified CM, additional phenomena are observed, such as cold crystallization and additional endothermic peaks resulting from the formation of nuclei upon cooling. However, the melting enthalpy resulting from this cold crystallization is neglectable in comparison with the melting of the crystals formed at $20\text{ }^{\circ}\text{C}$. For each isothermal crystallization, specific heat capacity c_p and melting enthalpy Δh_m are estimated based on the curves of the subsequent heating.

A shift of the melting endotherm towards high temperatures is observed for crystallization times above one second. A partially semi-crystalline structure is obtained for short crystallization times, whereas the final semi-crystalline structure is obtained for long crystallization times.

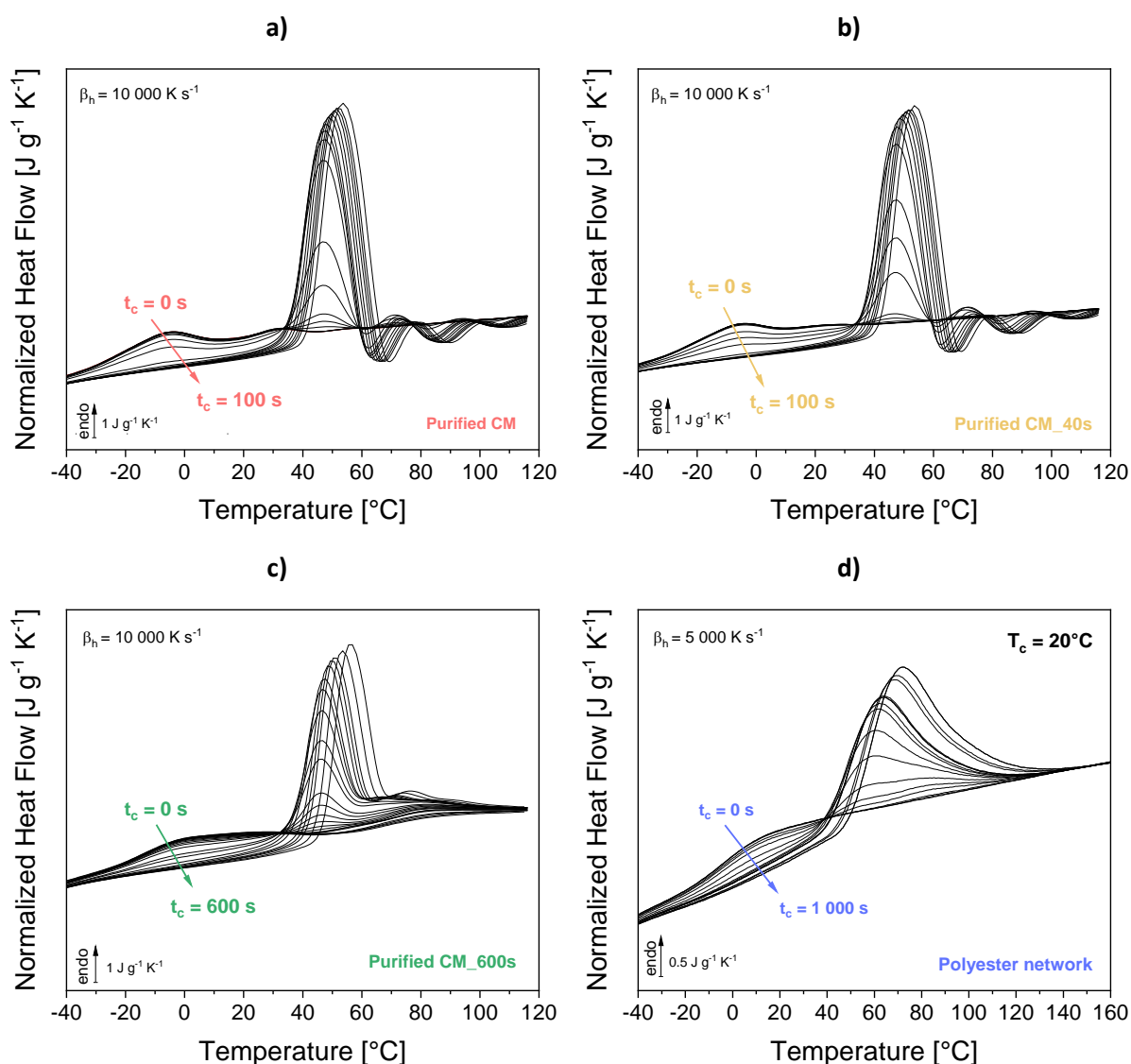


Figure III.15. Normalized heat flows measured upon heating at $10\,000\text{ K s}^{-1}$ for **a)** purified CM **b)** purified CM_40s **c)** purified CM_600s, and at $5\,000\text{ K s}^{-1}$ for **d)** the polyester network after crystallization at 20°C from 0 s to 1 000 s.

The glass transition temperature T_g remains largely unaffected by crystallization, confirming that low coupling is generated between the crystalline and the amorphous phases. However, as the crystallized fraction grows and Δc_p diminishes, for long crystallization times the glass transition is not visible anymore; this is observed for both the purified CM and the sample polymerized during 40 and 600 s. The effect of polymerization is clearly visible in **Figure III.16**, where the normalized heat flows measured after no crystallization and a crystallization of 100 s are reported for all the considered samples. During polymerization, the end functions of the purified CM react, resulting in longer chains (increase in the molar mass M_n); since the diacid compounds and esterified monomers in the system can react to form crosslinking nodes, the amorphous phase gets increasingly constrained by the change

in topology, and molecular mobility decreases. This results in an increase of the glass transition temperature, from $-16\text{ }^{\circ}\text{C}$ and $-15\text{ }^{\circ}\text{C}$ for the purified CM and purified CM_40 s respectively, to $-9\text{ }^{\circ}\text{C}$ and $0\text{ }^{\circ}\text{C}$ for the purified CM_600s and the polyester network respectively. The shape of the curve in the melting temperature range is impacted as well, and the broadness of the melting peak increases with t_{pol} .

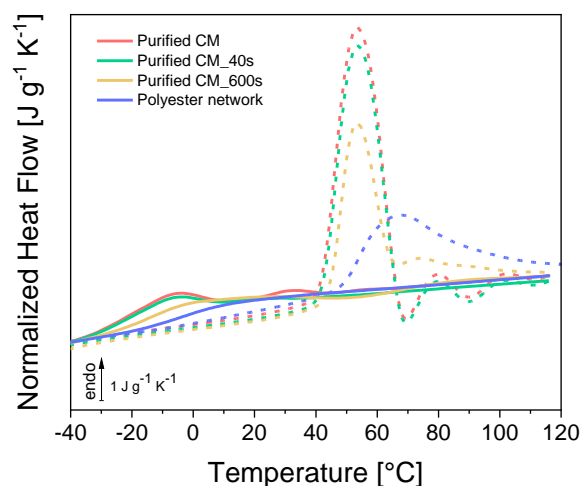


Figure III.16. Normalized heat flows measured upon heating at $10,000\text{ K s}^{-1}$ for the purified CM (red curves), purified CM_40s (green curve), and purified CM_600s (orange curve), and at $5,000\text{ K s}^{-1}$ for the polyester network (blue curve). The solid lines correspond to the heating ramp performed right after quenching from the melt. The dotted lines are the signals measured after crystallization at $20\text{ }^{\circ}\text{C}$ for 100 s.

The decrease in Δc_p with the increasing crystallization time is represented on **Figure III.17**. No major difference is observed between the purified CM and its polymerized counterpart (purified CM_40s), both showing a sharp drop in Δc_p after about 0.5 s. After polymerization (purified CM_600s), the Δc_p drop is shifted to 1 s. Crystallization is hindered in the weakly crosslinked polyester network, with a decrease in Δc_p starting at 0.5 s until reaching a constant value after a crystallization time of 10 s.

For the purified CM and purified CM_40s, the amorphous phase gets constrained to the point that no heat capacity step is observed in the temperature range of the glass transition. This result corroborates the observation made by POM, showing that crystallization leads to a high density of tightly packed spherulites.

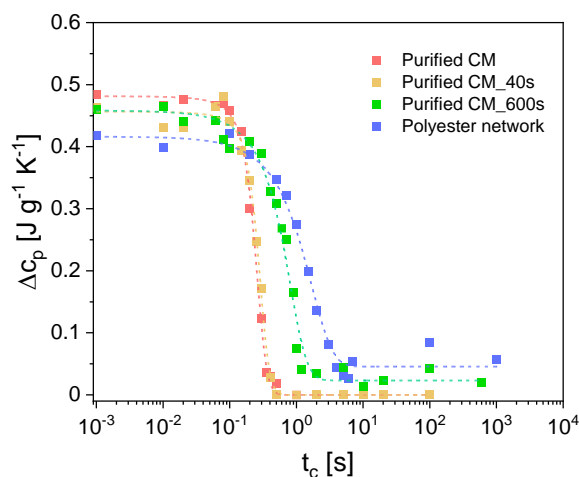


Figure III.17. Change in specific heat capacity step at the glass transition as a function of the crystallization time t_c varying from 10^{-3} s up to 10^3 s. The dashed lines are a guide for the eye.

IV.3 Application of the Avrami model for isothermal crystallization

The evolution of the normalized crystallized fraction α with the isothermal crystallization time is plotted in **Figure III.18.a**. When the molar mass increases, the curves are shifted to longer times, likely due to the branched chains and the reticulation nodes inhibiting the crystallization by hindering the motions of the macromolecular chains and segments. **Figure III.18.b** shows the Avrami plots obtained as explained in **Section III** for the purified CM with different polymerization times, and for the polyester network. If the assumption is made of a time independent transition rate k and Avrami exponent n , one could expect that the $\log[-\ln(1-\alpha)]$ as a function of $\log(t - t_0)$ dependencies is linear. However, the experimental results are clearly non-linear at early stages of crystallization. A possible explanation is that time-dependent effects kick in at the early stages of crystallization and as the system approaches the steady-state regime, as suggested by Gradys et al. [23].

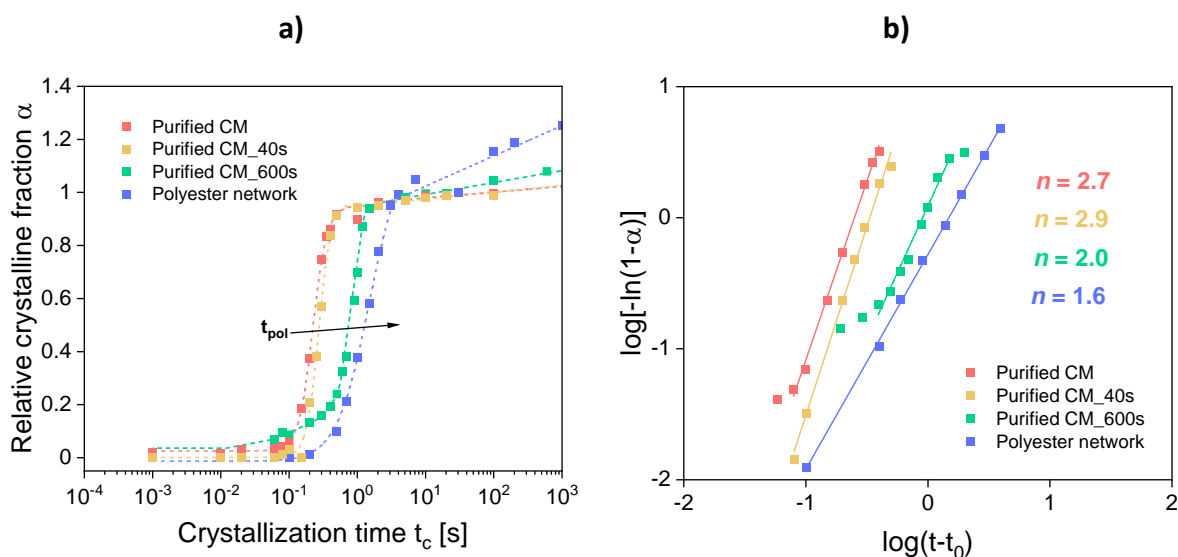


Figure III.18. **a)** Evolution of the relative crystalline fraction α as a function of the isothermal crystallization time t_c ; the lines are guide for the eye; **b)** Avrami plots obtained for the purified CM, purified CM_40s, purified CM_600s, and for the polyester network; the lines represent the fitting of the experimental data with Eq. 2.

The Avrami exponent n is used to somehow characterize the nucleation mode of the crystalline domains. Here, the n values range from about 3 for the purified CM in both its initial state and after polymerization at 150 °C for 40 s (purified CM_40s), down to 2.0 for the *in-situ* crosslinked system after 600 s polymerization (purified CM_600s), and finally drops to 1.6 for the polyester network. These values are lower compared to the ones expected in case of homogeneous growth of the spherulitic nuclei ($n = 3$). As stated in **Chapter I**, the Avrami exponent depends on the nucleation mechanism and the dimensionality of growth of the crystalline fraction. Higher cooling rates result in higher degrees of undercooling ΔT , and therefore in a stronger driving force; it is consequently expected that a lower free energy barrier must be overcome for the nucleation process [15]. When the Avrami index n increases, the nucleation process is more sporadic and the dimensionality of growth is higher [15]. Values of 2.0 suggest that the growth is sporadic and spherical. Polymerization and crosslinking lead to longer induction times as a general trend, and a decrease in the nucleation driving force. Secondary nucleation is impacted as well, and seems to grow in intensity with t_{pol} . The melting enthalpy Δh_m° of the crystalline phase formed beforehand will be estimated in the following.

IV.4 Melting enthalpy Δh_m°

Figure III.19 shows the melting enthalpy as a function of the specific heat capacity for all the considered samples. No significant change is observed as a function of the polymerization time, at least not within

the experimental uncertainty. The values obtained for Δh_m^0 decrease from 102 J g^{-1} (purified CM) and 95 J g^{-1} (purified CM_40s) down to 84 J g^{-1} (purified CM_600s) and 77 J g^{-1} (polyester network).

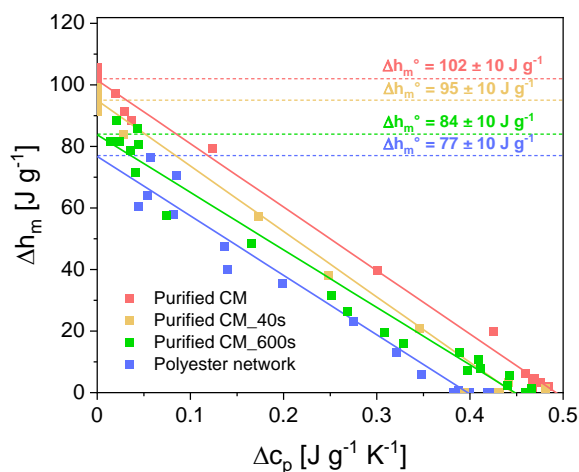


Figure III.19. Melting enthalpy Δh_m plotted against the specific heat capacity Δc_p normalized by the sample mass and the heating rate for the polyester network crystallized for different crystallization times t_c at a crystallization temperature $T_c = 20 \text{ }^\circ\text{C}$. The linear regression (solid line) to $\Delta c_p = 0 \text{ J g}^{-1} \text{ K}^{-1}$ ($X_c = 100\%$) gives the melting enthalpy Δh_m^0 , which corresponds to the melting enthalpy of a theoretically fully crystallized material under the assumption of a two-phase model [8-9].

X-ray diffraction patterns of the polyester network recorded at ambient temperature showed the formation of a hexagonal packing of the acyl chains (α polymorphic form) after rapid cooling from the melt [1]. However, after seven days of storage at room temperature, the sample was found to be in an orthorhombic β' sub-cell. Moreover, the thermogram recorded with TOPEM showed a broad endotherm with a melting enthalpy Δh_m of 92 J g^{-1} , higher than the theoretical value of Δh_m^0 estimated by FSC measurements. To better understand the inconsistency of these results, the melting enthalpy Δh_m^0 has also been estimated through the cross-comparison of XRD and DSC results. X_c can be estimated from XRD patterns using Eq. 3:

$$X_c = \frac{I_{cryst}}{I_{cryst} + I_{am}} \quad \text{Eq. 3}$$

where I_{cryst} is the integrated intensities of the crystalline diffraction peaks, and I_{am} is the integrated intensity of the amorphous halo. It is worth noting that this approach could underestimate the total crystalline volume fraction, due to the inability to separate overlapping peaks and correctly model the diffuse signal arising from the paracrystalline fractions (partially disordered crystals with short or medium-range order of the lattice) [14]. The data obtained by FSC and XRD could therefore differ, as

previously reported in the literature [5]. However, it can still be useful to get a rough estimation. X_c can also be estimated by calorimetry using **Eq. 4**:

$$X_c = \frac{\Delta h_m - \sum \Delta h_{cc}}{\Delta h_m^0} \quad \text{Eq. 4}$$

where Δh_m is the melting enthalpy, Δh_{cc} is the cold crystallization enthalpy, and Δh_m^0 corresponds to the melting enthalpy expected for a 100% crystalline material. In the absence of cold crystallization, inserting **Eq. 3** into **Eq. 4** Δh_m^0 provides the following equation:

$$\Delta h_m^0 = \frac{I_{cryst} + I_{am}}{I_{cryst}} \Delta h_m \quad \text{Eq. 5}$$

The crystallinity fraction was computed using the diffract EVA software. The polyester network in the β' -form has a crystallinity fraction of 78%. The enthalpy Δh_m associated to the melting of the β' crystals of the polyester network was estimated at 92 J g⁻¹, and using **Eq. 5** an extrapolated melting enthalpy of 118 J g⁻¹ is found for the β' -form. This could explain why a Δh_m^0 of 91 J g⁻¹ was estimated following a crystallization of the polyester network at 40 °C, seemingly due to a co-crystallization of the α and the β' phases at intermediate temperatures.

Concerning the β -phase, such procedure is not straightforward since the XRD spectrum revealed a co-existence of two crystalline phases for the purified CM, the β' and β -form. Gradys et al. [24] used the method developed by Turner-Jones [25] to estimate the content of one crystalline form in relation to another for polypropylene, however this method requires well separated α and β -peaks. Flores and al. [26] used the molar contribution function of Van Krevelen [27] to estimate the melting enthalpy Δh_m^0 of new aliphatic polyethers. By applying the Van Krevelen function to the saturated 9(10)-16-dihydroxyhexadecanoic acid, which is the major component of the purified CM (**Figure II.5**), Δh_m^0 would be:

$$\Delta h_m^0 = \frac{(\Delta h_{CH_2} n_{CH_2} + \Delta h_O n_O + \Delta h_{CH(OH)})}{M_i} \quad \text{Eq. 6}$$

In the repeating unit, there are 14 -CH₂- groups, 2 -OH- groups, one -C=O- group and one -CH(OH)- group. The molar mass M_i of the repeating unit is 288 g mol⁻¹. The estimation gives a value of 213 J g⁻¹ which may correspond to the most stable polymorph β and is close enough to the melting enthalpy of 208.2 J g⁻¹ for pure palmitic acid (same number of carbon as 9(10)-16-dihydroxyhexadecanoic acid) found by Cedeno et al. [28].

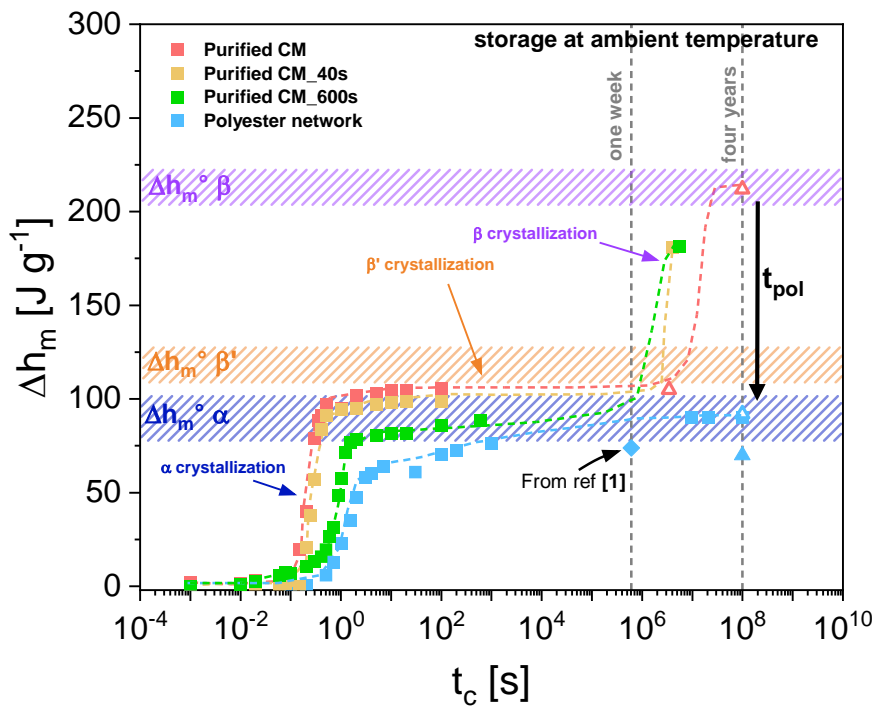


Figure III.20. Dependence of the melting enthalpy Δh_m on the crystallization time t_c at ambient temperature. The hatched areas represent the estimation of the extrapolated melting enthalpy Δh_m^0 for the α -form (dark blue), the β' -form (orange) and the β -form (purple). The square symbols represent the FSC experimental data. The full and empty triangles represent the total heat flow Φ_{tot} and reversing heat flow Φ_{rev} measured with TOPEM respectively. The dotted gray lines are added to indicate the storage time at ambient temperature before calorimetric measurements. Note that the four years indication is an approximation.

Figure III.20 shows the evolution of the total Δh_m with the crystallization time. Based on FSC and TOPEM results, it seems that both the purified CM and the polyester network initiates crystallization rapidly at ambient temperature under the α form (hexagonal packing) before further transforming into the β' form (orthorhombic packing).

The polyester network crystallizes under the orthorhombic β' form when annealed for a sufficiently long time, whereas in the purified CM different crystalline forms coexist, including the α and β' forms. Different metastable states are reached before the final transformation from the hexagonal to the orthorhombic crystalline phase. The literature reports that secondary crystallization can occur through different processes; it can be sometimes triggered by RAF relaxation [29], or proceed through cross-nucleation with the initial crystalline phase acting as a nucleation site for the secondary crystallization. POM experiments showed that this second mechanism is predominant in the case of the purified CM. The α crystals have a short lifetime, which was expected since they represent a metastable crystalline form, and rapidly convert into β' -crystals in the span of minutes. At the end of the preliminary stage of

crystallization, secondary crystallization occurs for the polyester network via a solid-solid transformation from the initial α -form (hexagonal packing) to the β' -form (orthorhombic packing). For all the samples crystallized at 20 °C, the mesophase forms as an intermediate transient stage within the path of transformation of the melt into β' -crystals, following Ostwald's rule of stages. With this crystallization pathway, the isotropic melt first converts into a Liquid Crystalline phase (LC-phase) before undergoing a monotropic transition into a more ordered crystal phase. Such crystallization pathway is not uncommon in aromatic polyesters, where the stiff aryl rings act as mesogenic units [30], or in other polymer with high flexibility such as polyethylene, for which it was shown that during the initial process of growth a crystal goes through thermodynamically stable and metastable states before transforming from the hexagonal to the orthorhombic phase [31]. *In-situ* optical microscopy and transmission electron microscopy also showed that the newly formed crystal acts as a nucleation center for secondary crystallization [31].

Conclusion

The co-polyesters of hydroxy fatty acids investigated in this work present complex rapidly-evolving microstructures depending on the processing conditions and the crosslinking density. Different ordered structures are formed depending on the crystallization temperature and the cooling rate. Long storage at ambient temperature results in the formation of β and β' -crystals. The formation of the stable β polymorph was observed for the purified CM but not for the co-polyester, possibly due to the crosslinking nodes and branched chains hindering the formation of a triclinic phase. High cooling rates ($> 100 \text{ K s}^{-1}$) lead to the formation of metastable α -crystals characterized by a hexagonal packing with an interplanar distance $d = 4.1 \text{ \AA}$. From a combination of calorimetry and X-ray diffraction, the melting enthalpy extrapolated to full crystallinity was estimated for the α -phase (77 J g^{-1}), the β' -phase (118 J g^{-1}), and the β polymorph (213 J g^{-1}).

Even though XRD, TOPEM and FSC results are in good agreement, the timescale related to the crystal stability in FSC samples (nanoscale samples) may differ from bulk samples. The same reasoning can be made regarding the effect of polymerization and crosslinking, for which the experimental data obtained after a nanoscale polymerization at $150 \text{ }^\circ\text{C}$ for 10 min (Purified CM_600 s) appear to be in the same order of magnitude to the ones obtained after bulk polymerization at $150 \text{ }^\circ\text{C}$ for 24 h (polyester network).

References

- [1] M. Marc *et al.*, "From Tomato Pomaces Biorefinery to Biobased Shape-Memory Semicrystalline Polyester Networks," *ACS Sustainable Chem. Eng.*, vol. 12, no. 6, pp. 2191–2202, Feb. 2024, doi: 10.1021/acssuschemeng.3c05713.
- [2] G. Fredi, D. Rigotti, D. N. Bikiaris, and A. Dorigato, "Tuning thermo-mechanical properties of poly(lactic acid) films through blending with bioderived poly(alkylene furanoate)s with different alkyl chain length for sustainable packaging," *Polymer*, vol. 218, p. 123527, Mar. 2021, doi: 10.1016/j.polymer.2021.123527.
- [3] G. Z. Papageorgiou, V. Tsanaktis, and D. N. Bikiaris, "Crystallization of poly(butylene-2,6-naphthalate-co-butylene adipate) copolymers: regulating crystal modification of the polymorphic parent homopolymers and biodegradation," *CrystEngComm*, vol. 16, no. 34, pp. 7963–7978, 2014, doi: 10.1039/C4CE00651H.
- [4] C. Berti, A. Celli, P. Marchese, E. Marianucci, G. Barbiroli, and F. D. Credico, "The effect of aliphatic chain length on thermal properties of poly(alkylene dicarboxylate)s," *e-Polymers*, vol. 7, no. 1, Dec. 2007, doi: 10.1515/epoly.2007.7.1.658.
- [5] M. Gigli *et al.*, "Biodegradable aliphatic copolyesters containing PEG-like sequences for sustainable food packaging applications," *Polymer Degradation and Stability*, vol. 105, pp. 96–106, Jul. 2014, doi: 10.1016/j.polymdegradstab.2014.04.006.
- [6] A. R. Katritzky, R. Jain, A. Lomaka, R. Petrukhin, U. Maran, and M. Karelson, "Perspective on the Relationship between Melting Points and Chemical Structure," *Crystal Growth & Design*, vol. 1, no. 4, pp. 261–265, Jul. 2001, doi: 10.1021/cg010009s.
- [7] C. Himawan, V. M. Starov, and A. G. F. Stapley, "Thermodynamic and kinetic aspects of fat crystallization," *Advances in Colloid and Interface Science*, vol. 122, no. 1–3, pp. 3–33, Sep. 2006, doi: 10.1016/j.cis.2006.06.016.
- [8] P. Cebe *et al.*, "Heat of fusion of polymer crystals by fast scanning calorimetry," *Polymer*, vol. 126, pp. 240–247, Sep. 2017, doi: 10.1016/j.polymer.2017.08.042.
- [9] C. Fosse *et al.*, "Determination of the equilibrium enthalpy of melting of two-phase semi-crystalline polymers by fast scanning calorimetry," *Thermochimica Acta*, vol. 677, pp. 67–78, Jul. 2019, doi: 10.1016/j.tca.2019.03.035.
- [10] K. Larsson *et al.*, "Classification of Glyceride Crystal Forms.," *Acta Chem. Scand.*, vol. 20, pp. 2255–2260, 1966, doi: 10.3891/acta.chem.scand.20-2255.
- [11] M. A. Rogers, D. Tang, L. Ahmadi, and A. G. Marangoni, "Fat Crystal Networks," in *Food Materials Science*, J. M. Aguilera and P. J. Lillford, Eds., New York, NY: Springer New York, 2008, pp. 369–414. doi: 10.1007/978-0-387-71947-4_17.
- [12] L. Hernqvist, *Crystallization and polymorphism of fats and fatty Acids*, Garti N, Sato K (eds), Marcel Dekker Inc, New York. 1988.
- [13] J. W. Hagemann and J. A. Rothfus, "Polymorphism and transformation energetics of saturated monoacid triglycerides from differential scanning calorimetry and theoretical modeling," *J Americ Oil Chem Soc*, vol. 60, no. 6, pp. 1123–1131, Jun. 1983, doi: 10.1007/BF02671340.
- [14] G. Fredi, A. Dorigato, M. Bortolotti, A. Pegoretti, and D. N. Bikiaris, "Mechanical and Functional Properties of Novel Biobased Poly(decylene-2,5-furanoate)/Carbon Nanotubes Nanocomposite Films," *Polymers*, vol. 12, no. 11, p. 2459, Oct. 2020, doi: 10.3390/polym12112459.
- [15] R. Campos, S. S. Narine, and A. G. Marangoni, "Effect of cooling rate on the structure and mechanical properties of milk fat and lard," *Food Research International*, vol. 35, no. 10, pp. 971–981, Jan. 2002, doi: 10.1016/S0963-9969(02)00159-X.
- [16] J. E. K. Schawe and J. F. Löffler, "Existence of multiple critical cooling rates which generate different types of monolithic metallic glass," *Nat Commun*, vol. 10, no. 1, p. 1337, Mar. 2019, doi: 10.1038/s41467-018-07930-3.
- [17] M. C. Righetti and E. Tombari, "Crystalline, mobile amorphous and rigid amorphous fractions in poly(L-lactic acid) by TMDSC," *Thermochimica Acta*, vol. 522, no. 1–2, pp. 118–127, Aug. 2011, doi: 10.1016/j.tca.2010.12.024.
- [18] N. Widlak, R. W. Hartel, and S. S. Narine, *Crystallization and solidification properties of lipids*. 2001.
- [19] M. Avrami, "Kinetics of Phase Change. I General Theory," *The Journal of Chemical Physics*, vol. 7, no. 12, pp. 1103–1112, Dec. 1939, doi: 10.1063/1.1750380.

- [20] A. T. Lorenzo, M. L. Arnal, J. Albuérne, and A. J. Müller, "DSC isothermal polymer crystallization kinetics measurements and the use of the Avrami equation to fit the data: Guidelines to avoid common problems," *Polymer Testing*, vol. 26, no. 2, pp. 222–231, Apr. 2007, doi: 10.1016/j.polymertesting.2006.10.005.
- [21] R. Androsch, A. Toda, Y. Furushima, and C. Schick, "Insertion-Crystallization-Induced Low-Temperature Annealing Peaks in Melt-Crystallized Poly(L-Lactic Acid)," *Macromol. Chem. Phys.*, p. 2100177, Jun. 2021, doi: 10.1002/macp.202100177.
- [22] E. Zhuravlev, J. W. P. Schmelzer, A. S. Abyzov, V. M. Fokin, R. Androsch, and C. Schick, "Experimental Test of Tammann's Nuclei Development Approach in Crystallization of Macromolecules," *Crystal Growth & Design*, vol. 15, no. 2, pp. 786–798, Feb. 2015, doi: 10.1021/cg501600s.
- [23] A. Gradys, P. Sajkiewicz, E. Zhuravlev, and C. Schick, "Kinetics of isothermal and non-isothermal crystallization of poly(vinylidene fluoride) by fast scanning calorimetry," *Polymer*, vol. 82, pp. 40–48, Jan. 2016, doi: 10.1016/j.polymer.2015.11.020.
- [24] A. Gradys *et al.*, "Crystallization of polypropylene at various cooling rates," *Materials Science and Engineering: A*, vol. 413–414, pp. 442–446, Dec. 2005, doi: 10.1016/j.msea.2005.08.167.
- [25] A. T. Jones, J. M. Aizlewood, and D. R. Beckett, "Crystalline forms of isotactic polypropylene," *Makromol. Chem.*, vol. 75, no. 1, pp. 134–158, Jan. 1964, doi: 10.1002/macp.1964.020750113.
- [26] I. Flores *et al.*, "Unexpected Structural Properties in the Saturation Region of the Odd–Even Effects in Aliphatic Polyethers: Influence of Crystallization Conditions," *Macromolecules*, p. acs.macromol.1c02235, Jan. 2022, doi: 10.1021/acs.macromol.1c02235.
- [27] D. W. Van Krevelen, *Chapter 5 - calorimetric properties*, 3rd ed. Elsevier: Amsterdam. in *Properties of Polymers*. 1997.
- [28] F. O. Cedeño, M. M. Prieto, A. Espina, and J. R. García, "Measurements of temperature and melting heat of some pure fatty acids and their binary and ternary mixtures by differential scanning calorimetry," *Thermochimica Acta*, vol. 369, no. 1–2, pp. 39–50, Mar. 2001, doi: 10.1016/S0040-6031(00)00752-8.
- [29] J. Chen *et al.*, "Structural evolutions of the amorphous fraction of polyethylene terephthalate during the secondary crystallization," *Polymer*, vol. 253, p. 124987, Jun. 2022, doi: 10.1016/j.polymer.2022.124987.
- [30] Q. Ding *et al.*, "Smectic liquid crystal Schlieren texture in rapidly cooled poly(butylene naphthalate)," *European Polymer Journal*, vol. 101, pp. 90–95, Apr. 2018, doi: 10.1016/j.eurpolymj.2018.02.010.
- [31] S. Rastogi and L. Kurelec, "Polymorphism in polymers; its implications for polymer crystallisation," *Journal of Materials Science*, vol. 35, no. 20, pp. 5121–5138, 2000, doi: 10.1023/A:1004844001714.

Chapter IV. Crystallization kinetics of a series of poly (alkylene *trans*-1,4-cyclohexanedicarboxylate)

Parts of this chapter are extracted from:

Hallavant, K.; Soccio, M.; Guidotti, G.; Lotti, N.; Esposito, A.; Saiter-Fourcin, A. Critical cooling rate of fast-crystallizing polyesters: the example of poly (alkylene *trans*-1,4-cyclohexanedicarboxylate) in *Polymers*, 16, 2792, **2024**, DOI: 10.3390/polym16192792

Content

I. Preliminary analyses	116
I.1 FTIR spectroscopy	116
I.2 Conventional TGA	117
I.3 Temperature-modulated TGA (MT-TGA).....	118
I.4 DSC measurement	120
I.5 TOPEM measurements	123
II. Non-isothermal crystallization.....	125
II.1 Critical cooling rate	125
II.2 Application of the three-phase model	133
II.3 Ozawa model	136
III. Isothermal crystallization	138
III.1 Equilibrium melting temperature T_m° using the Hoffman-Weeks method	138
III.2 Barandiarán and Colmenero's method	140
III.3 Kinetics investigation of the high-temperature crystalline form	142
III.4 Crystallization kinetics of PPeCE	146
III.5 Time-Temperature-Transformation diagrams	148
Conclusion	151
References	152

As mentioned in **Chapter III**, assessing the crystallization ability of a material is essential since it has consequences on macroscopic properties such as stiffness, strength, chemical resistance, thermal stability, material morphology and gas permeability [1, 2], which has to be considered for the evaluation of processability, applicability, and biodegradability of the material [3]. In **Chapter III** we investigated the influence of the crosslinking density on the crystallization ability of bio-sourced polyesters extracted from tomato peel cutin with potential applications for packaging.

This chapter presents the detailed thermal analysis of a series of thermoplastic polyesters with promising barrier properties, the poly (alkylene *trans*-1,4-cyclohexanedicarboxylate) (PCHs), using an association of calorimetric techniques (TOPEM, DSC, FSC) and structural characterization techniques (FTIR, XRD and POM). As reported in **Chapter I**, few works have been published on the PCHs, and up to date most information found in the literature concerns the first two polyesters of this series, i.e. PPCE ($n_{CH_2} = 3$), PBCE ($n_{CH_2} = 4$), and their copolyesters [4-8]. The influence of the alkyl chain length within the main structure of the repeating unit on the crystallization kinetics will be systematically investigated, and several procedures for kinetics analysis will be applied to get a deeper insight into the crystallization abilities of the PCHs. Important parameters such as the critical cooling rate $\beta_{c,crit}$, the equilibrium melting temperature T_m° and the nature of the polymorphs will be assessed.

I. Preliminary analyses

I.1 FTIR spectroscopy

The FTIR spectra in **Figure IV.1** show that all the PCHs present the characteristic bonds associated with polyesters, that is to say the C=O bond between 1720 and 1715 cm^{-1} , the C-O-C bond at 1040 cm^{-1} , and the C-O bond at 1160 cm^{-1} [9]. Some differences are notable (gray areas), and a zoom into these regions is proposed in **Figure IV.2**. On one hand, the length of the alkyl chain in the main structure of the repeating unit affects the peak located at 1040 cm^{-1} corresponding to the symmetrical and asymmetrical C-O-C stretching, whose intensity increases as the alkyl chain gets shorter. On the other hand, the absorption intensity of the peak located at 2900 cm^{-1} (stretching of C-H bond) increases as the alkyl chain gets longer. The C=O bond is affected by an odd-even effect, since it is shifted to higher wavenumbers for odd-numbered PCHs (1719 cm^{-1} for PPCE and 1718 cm^{-1} for PPeCE) in comparison with the even-numbered PCHs (1715 cm^{-1} for PBCE and 1716 cm^{-1} for PHCE).

The shape of the peaks located in the fingerprint between 1500 and 800 cm^{-1} vary as well depending on the considered sample. In particular, the peaks located between 1490 and 1430 cm^{-1} (CH_2 bending

region) could inform about the conformational changes of the methylene groups [10]. The four PCHs present a peak at 1452 cm^{-1} , however only the even-numbered PCHs manifest a peak at 1479 cm^{-1} .

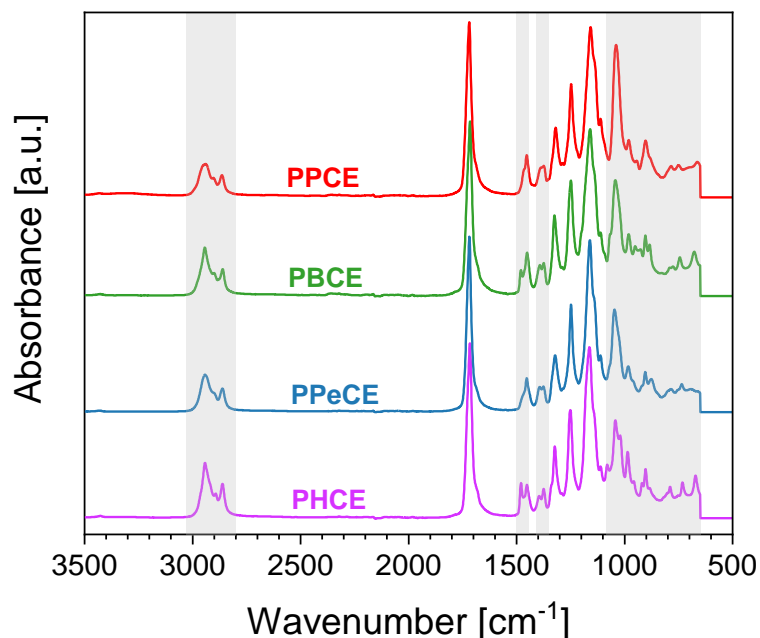


Figure IV.1. FTIR spectra of the as-synthesized PCHs. All spectra are normalized with respect to the carbonyl peak (1715 cm^{-1}).

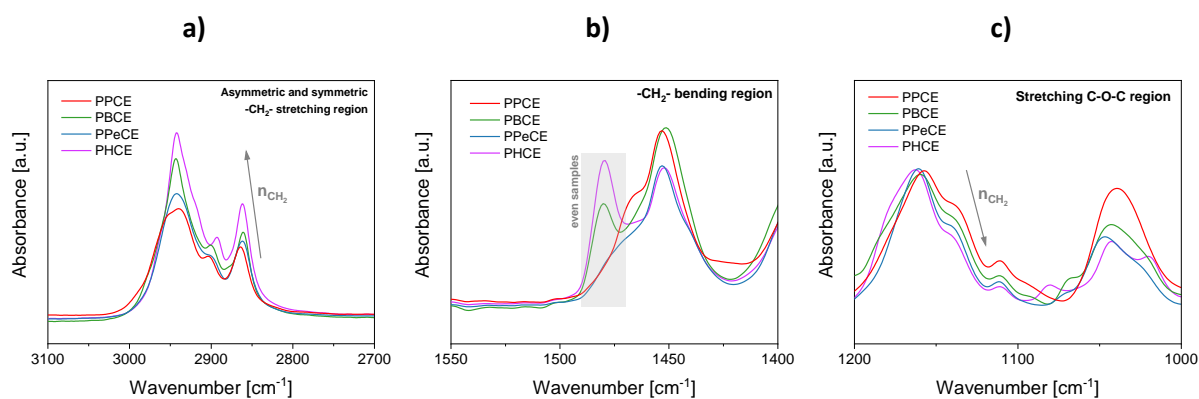


Figure IV.2. Close-up of the regions of interest; **a)** $3100\text{-}2700\text{ cm}^{-1}$, **b)** $1550\text{-}1400\text{ cm}^{-1}$ and **c)** $1200\text{-}1000\text{ cm}^{-1}$

I.2 Conventional TGA

Thermogravimetric analyses were carried out with a constant heating rate of 10 K min^{-1} under N_2 to check the thermal stability of the PCHs. The thermograms shown in **Figure IV.3** report no major difference in the degradation kinetics for the considered samples, since all of them degrade in a one-step process. The temperature corresponding to a 5% mass loss ($T_{5\%}$) (**Figure IV.3.a**) slightly increases

with the alkyl chain length, from 375 °C for PPCE to 387 °C for PHCE. The temperature corresponding to the maximum rate of degradation (T_{max}) (Figure IV.3.b) are similar. No mass loss occurs before 250 °C, suggesting that all the PCHs have a good thermal stability, better than PLA [11] but slightly lower than PET [12] and 2,5-PEF [13]. However, compared to other polyester with the same number of methylene groups ($n_{CH_2} = 3$), the derivative curve of the mass with respect to temperature shows a peak at 412 °C for PPCE, which is slightly higher than poly (propylene furanoate) (396 °C), poly (propylene terephthalate) (402 °C) or poly (propylene naphthalate) (407 °C) [14].

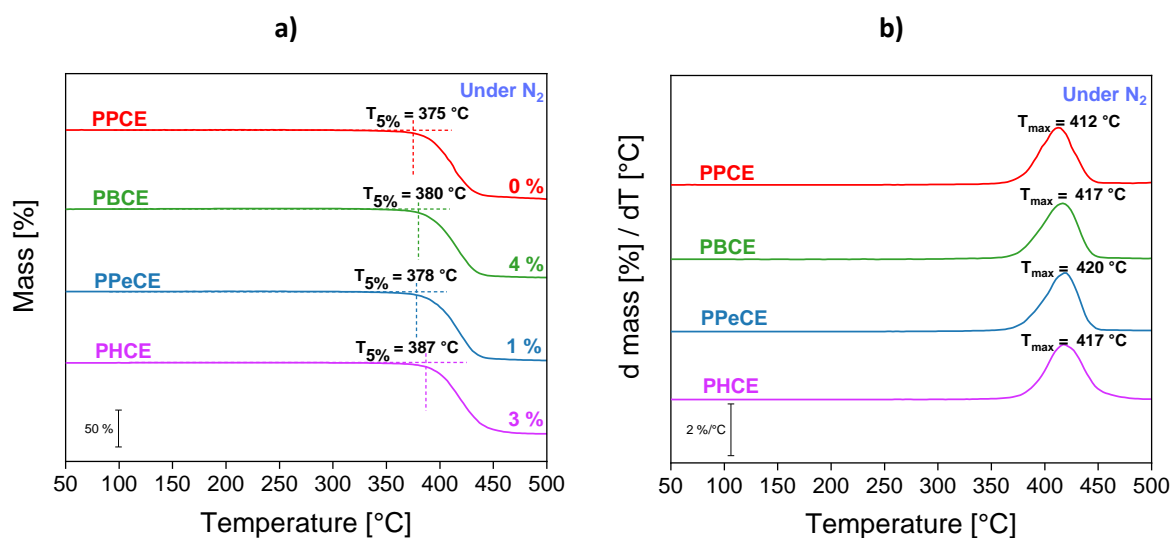


Figure IV.3. a) TGA curves of the PCHs measured at $\beta_h = 10 \text{ K min}^{-1}$ under N₂; b) First derivative of the mass with respect to temperature.

I.3 Temperature-modulated TGA (MT-TGA)

MT-TGA analyses can provide, with a single measurement, the activation energy E_a as a function of temperature, which may be interesting especially when the thermal degradation proceeds through different steps, with different mechanisms. Figure IV.4.a shows the degradation curves obtained for the PCHs under N₂. The temperature-derivative of the thermograms (DTG) are also plotted (Figure IV.4.b).

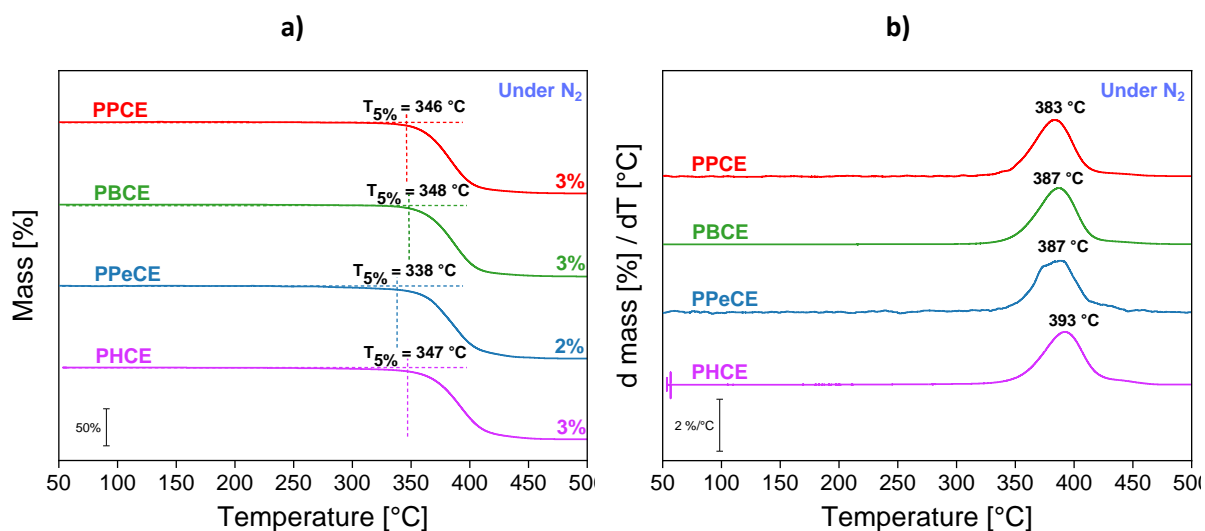


Figure IV.4. MT-TGA thermograms recorded with a constant heating rate of 2 K min⁻¹, amplitude of ± 5 K and a period of 200 s under N₂ with **a)** mass as a function of temperature; **b)** first derivative of the mass with respect to temperature. The temperatures corresponding to a mass loss of 5 % ($T_{5\%}$) are also added, as well as the percentage of residual mass after degradation.

The thermograms recorded under N₂ with MT-TGA are similar in shape with those recorded using TGA, however the degradation temperatures $T_{5\%}$ are lower of about 30-40 °C because of the lower heating rate (2 K min⁻¹ instead of 10 K min⁻¹).

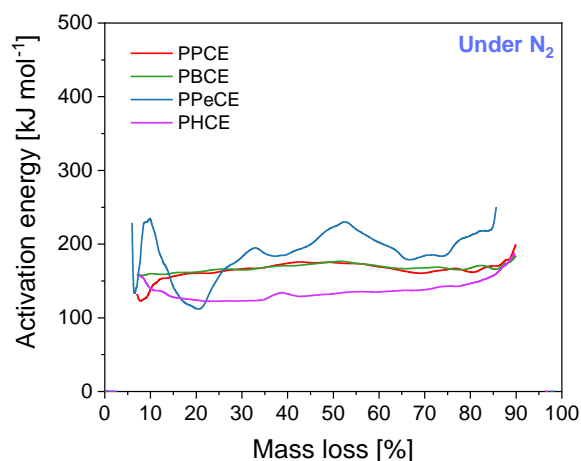


Figure IV.5. Activation energy E_a as a function of mass loss.

Figure IV.5 shows the activation energy associated with the degradation process under N₂ as a function of the recorded mass loss. **Table IV.1** report the average values of the activation energy E_a obtained with MT-TGA from **Figure IV.5**, with uncertainties estimated from the lower and upper bonds of the E_a fluctuations. The activation energy obtained for PHCE is lower compared to the other PCHs, possibly

due to the lower molar mass obtained at the end of the synthesis (see **Chapter II, Section I.1.2**). Compared to other polyesters, the values of E_a measured under N_2 are higher than PLA (110 kJ mol⁻¹ [15]) but lower than 2,5-PEF (195 kJ mol⁻¹ [13]) and PET (227 kJ mol⁻¹ [12]).

Table IV.1. Activation energy E_a measured under N_2 .

Sample	E_a (under N_2) [kJ mol ⁻¹]
PPCE	165 ± 10
PBCE	167 ± 10
PPeCE	170 ± 60
PHCE	133 ± 25

I.4 DSC measurement

Preliminary characterizations of the thermal behavior of each PCH were done by DSC through typical heating-cooling-heating ramps, with heating and cooling rates $\beta_h = |\beta_c| = 10 \text{ K min}^{-1}$. The first heating ramp brought the samples up to the melt, thus ensuring the best thermal contact with the bottom of the aluminum pan and erasing any previous thermal history. The subsequent cooling ramp allowed to compare the relative aptitude to crystallize when the four samples were cooled from the melt with the same cooling rate, providing the temperature range over which crystallization is expected to occur. The second heating ramp is used to get a glimpse on the microstructural differences induced on each sample due to their different chemical compositions, despite the common cooling conditions. A zoom into the glass transition temperature range is reported in the inset to each graph.

Upon cooling, the crystallization enthalpy (Δh_c) and the crystallization temperature measured at the peak (T_c) were obtained, and on the second heating scan the midpoint glass transition temperature (T_g), the melting range (ΔT_m) and the melting enthalpy Δh_m were estimated. The thermal characteristics of the four PCHs extracted from the thermograms recorded at 10 K min^{-1} with DSC (see **Figure IV.6**) are reported in **Table IV.2**.

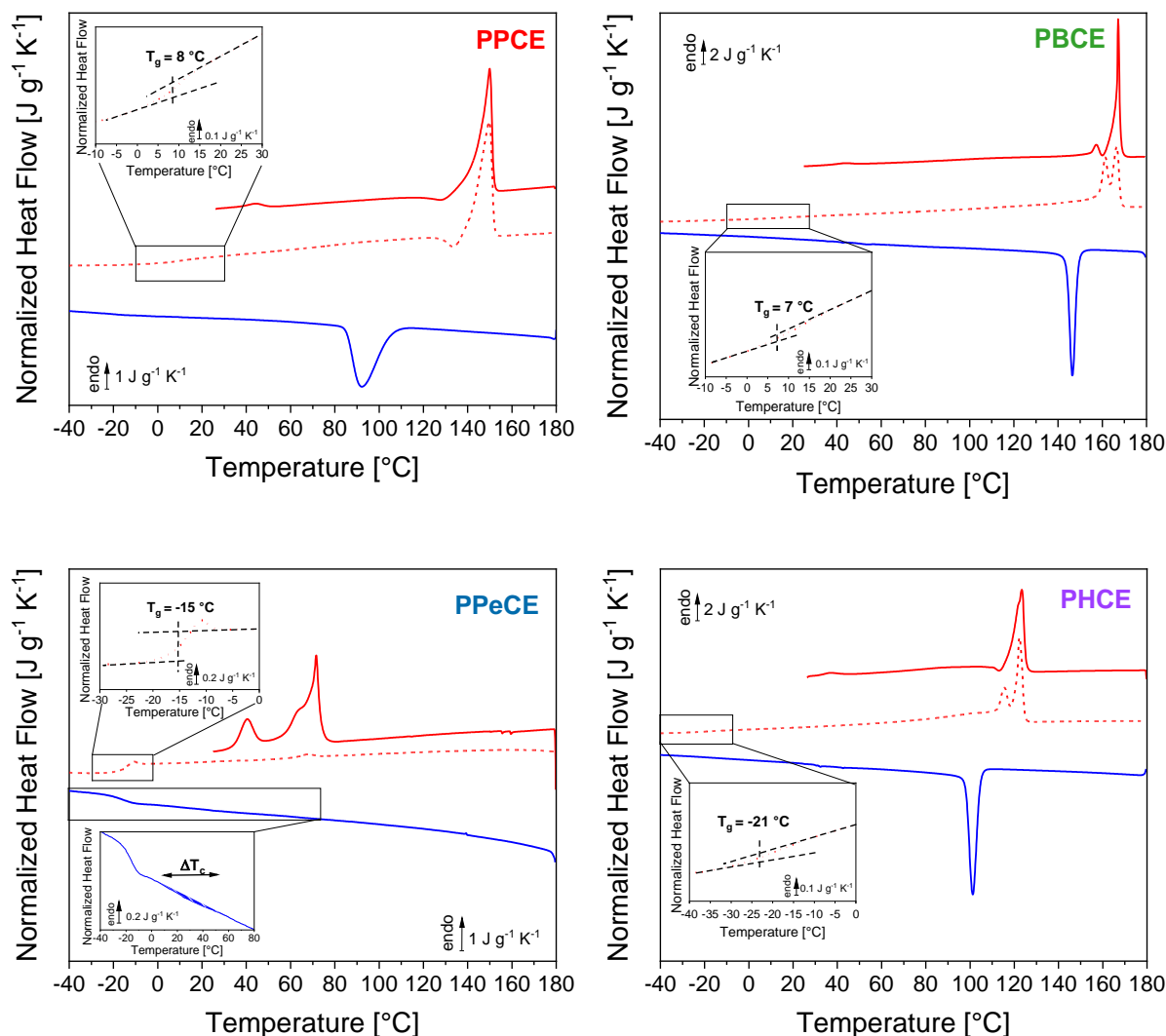


Figure IV.6. Thermal behavior recorded by DSC with cooling and heating rates $|\beta_c| = \beta_h = 10 \text{ K min}^{-1}$. The first heating (solid red line), the cooling (blue line) and the second heating (dashed red line) ramps are represented. A zoom into the glass transition temperature range is reported for each sample in the corresponding inset. For PPeCE, an additional inset zooms into the crystallization temperature range (dashed blue area). The curves are y -shifted for better visibility.

The melting and crystallization behaviors vary significantly from one sample to another. On the first heating ramp, a low-temperature endothermic peak is visible for all samples around 40°C , which is not seen on the second heating. Since the samples were prepared in the form of films by hot-pressing, this low endothermic peak could correspond to some relaxation of constrained macromolecular segments and/or to the melting of mesophases induced by processing. Concerning the crystallization upon cooling (blue curves), the even-numbered samples (PBCE and PHCE) are prone to a very rapid crystallization process and manifest a narrow exothermic peak at high temperature ($\Delta T_c < 10^{\circ}\text{C}$), whereas odd-numbered samples crystallize much slower. PPeCE ($n_{\text{CH}_2} = 5$), for instance, barely has the

time to start the process, and shows a wide crystallization peak (large ΔT_c) with a low intensity (Δh_c of 0.5 J g^{-1}). The glass transition temperature measured during the second heating scan decreases as the number of methylene groups introduced in the backbone increases, from about $8 \text{ }^\circ\text{C}$ for PPCE ($n_{CH_2} = 3$) to about $-21 \text{ }^\circ\text{C}$ for PHCE ($n_{CH_2} = 6$). Irrespective of the odd or even character of n_{CH_2} , the melting temperature generally decreases as the number of methylene groups increases. However, the lowest melting (and crystallization) temperature is observed for PPeCE ($n_{CH_2} = 5$). This particular behavior has been reported for other polymers containing five methylene groups in their backbone [16, 17], and could be due to some local polarization that builds up in odd-numbered polyesters, hindering the crystallization process, whereas in even-numbered polyesters the dipoles are aligned in opposite directions, allowing a more efficient chain folding and packing [18, 19]. NMR experiments conducted on flexible alkyl chains with mesogenic groups at either end showed that, for $n_{CH_2} = 5$, the alkyl chain is mostly in an all-*trans* conformation, except around the C-O single bonds, where it was found to be approximately *gauche* [18]. This *gauche* conformation forces the molecule to bend more with respect to an all-*trans* conformation, causing less efficient packing and therefore improving its glass-forming ability. A recent investigation on the crystal structure of PBCE confirms the all-*trans* conformation of its alkyl segments [8].

PPCE and PPeCE show one single endothermic peak (albeit very weak in the case of PPeCE) when PBCE and PHCE manifest double melting peaks. The presence of a double peak depends on the heating rate [20, 21] and is common among polyesters including polyhydroxyalkanoates [22, 23], poly (ethylene terephthalate) [24] or aliphatic polycarbonates [10]. Such phenomenon can have different causes, including the reorganization process occurring upon heating, the simultaneous melting and recrystallization of crystals with defects to improve crystal perfection, or the melting of different polymorphs.

Table IV.2. Thermal characteristics of the investigated PCHs extracted from the thermograms reported in **Figure IV.6**. T_g is taken as the mid-point glass transition, T_c is the crystallization temperature measured at the maximum of the exothermic peak, Δh_c is the crystallization enthalpy, ΔT_m is the melting temperature range, Δh_m is the melting enthalpy calculated as the algebraic area under the curve in the melting temperature range.

Sample	T_g [$^\circ\text{C}$]	T_c [$^\circ\text{C}$]	ΔT_c [$^\circ\text{C}$]	Δh_c [J g^{-1}]	ΔT_m	Δh_m [J g^{-1}]
PPCE	8 ± 2	92.2 ± 0.5	85-106	33 ± 1	136-160	32 ± 2
PBCE	7 ± 2	146.5 ± 0.5	144-150	39 ± 2	92-171	55 ± 5
PPeCE	-15 ± 1	25 ± 5	6-51	0.5 ± 0.1	60-76	0.6 ± 0.1
PHCE	-21 ± 2	101.3 ± 0.5	98-105	43 ± 3	50-129	57 ± 5

On a final note, a small exothermic peak occurs at $128 \text{ }^\circ\text{C}$ (first heating) and $134 \text{ }^\circ\text{C}$ (second heating) for PPCE, and $113 \text{ }^\circ\text{C}$ (first heating) for PHCE, right before melting that could be related to crystalline

reorganization. For a deeper understanding of the phenomena described above, modulated-temperature DSC is needed.

I.5 TOPEM measurements

As described in **Chapter II**, TOPEM allows the deconvolution between the non-reversing heat flow (related to kinetic events) and the reversing heat flow (related to heat capacity changes). This technique is convenient to distinguish overlapping thermal events.

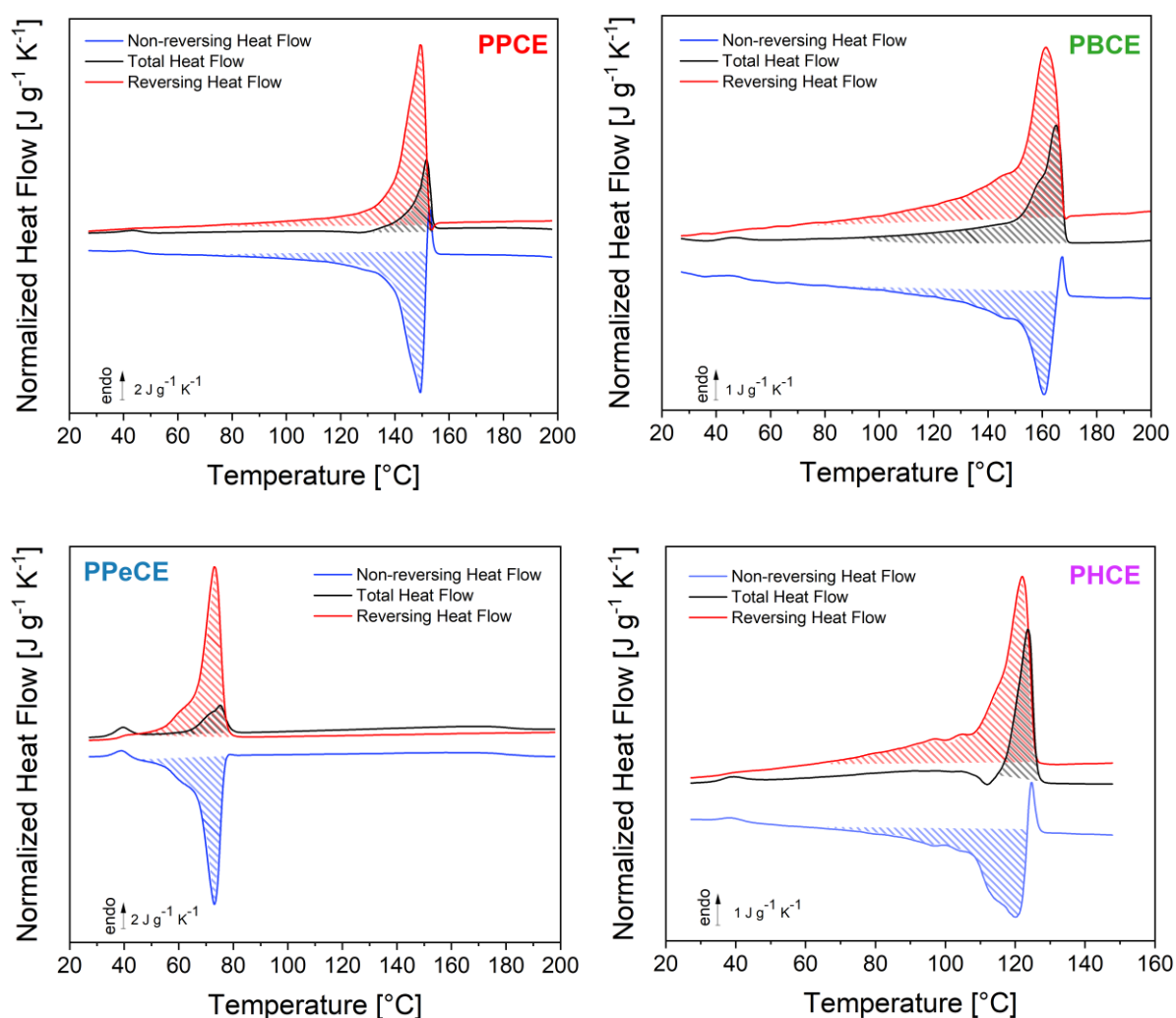
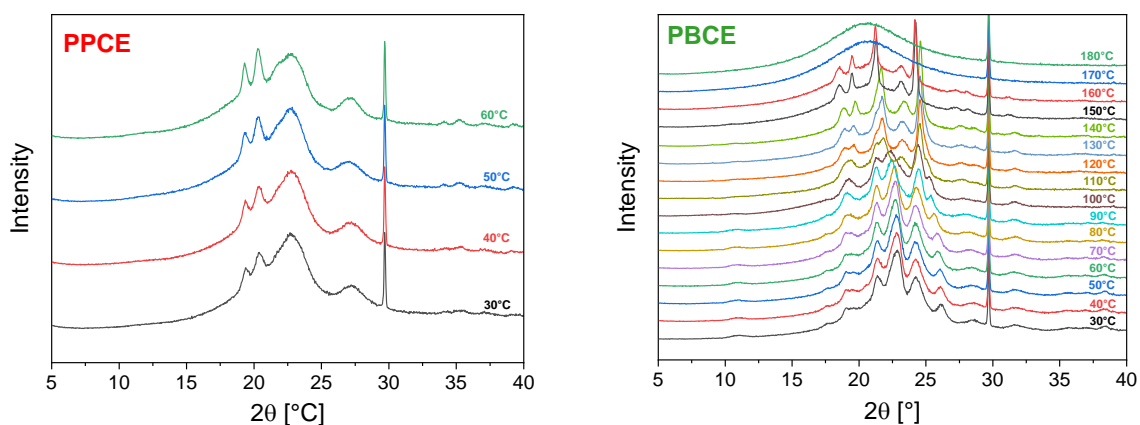


Figure IV.7. Reversing (red curve), non-reversing (blue curve) and total (black curve) normalized heat flows recorded with TOPEM upon heating at 2 K min^{-1} with a temperature modulation δT of 0.1 K and a period between 15 and 30 s . The total heat flow is obtained by addition of the reversing and non-reversing contributions. The dashed areas are added to highlight the melting (red and black areas) and the recrystallization processes (blue area).

From the thermograms in **Figure IV.7**, it appears that the complex melting peak observed using DSC is indeed related to a melting and recrystallization process. The low endothermic peak corresponds to the melting of original crystals that can either contain defects or are too small to form crystals with better ordering and larger dimensions (recrystallization). The high temperature endothermic peak corresponds to the melting of the newly recrystallized crystals. For all polyesters except PPCE, the melting process associated to crystalline reorganization occurs on a large temperature range, from 80 °C to 150 °C for PPCE, 100 °C to 170 °C for PBCE, and 20 °C to 120 °C for PHCE. The small endothermic peak observed on the DSC thermograms between 40 and 50 °C is also visible for all samples in the non-reversing contribution of the heat flow. Because it appears on the first heating scan, this endothermic contribution could be related to a relaxation process following the fabrication of polyester films by a hot-press. The endothermic peak around 50 °C has already been evidenced for PPCE [4] and PBCE [6], the former being explained as a pre-melting peak associated with the fusion of crystals with a poor degree of perfection, whereas for the latter Guidotti et al. raised the possibility of the formation of a 2D-structure akin to a mesophase for PBCE copolymers [6]. PBCE contains an even number of methylene units in the glycol moiety, and that could favor the formation of a smectic phase in a temperature range between T_g and T_m . X-ray diffraction spectra of the as-synthesized PCHs were recorded from ambient temperature to the melt every 10 °C upon heating at 2 K min⁻¹ and are presented in **Figure IV.8**. The X-ray spectra are different for all the PCHs, with odd-numbered samples having broader, less defined diffraction peaks in opposition to the even-numbered, whose peaks are narrower and well defined. A small peak is observed for the four PCHs at low angle corresponding to an interplanar distance of about 10 Å, and could be related to a longitudinal organization. However, no major change is observed in the spectra between 30 °C and 50 °C that could be related to the relaxation of a 2D-ordered phase.



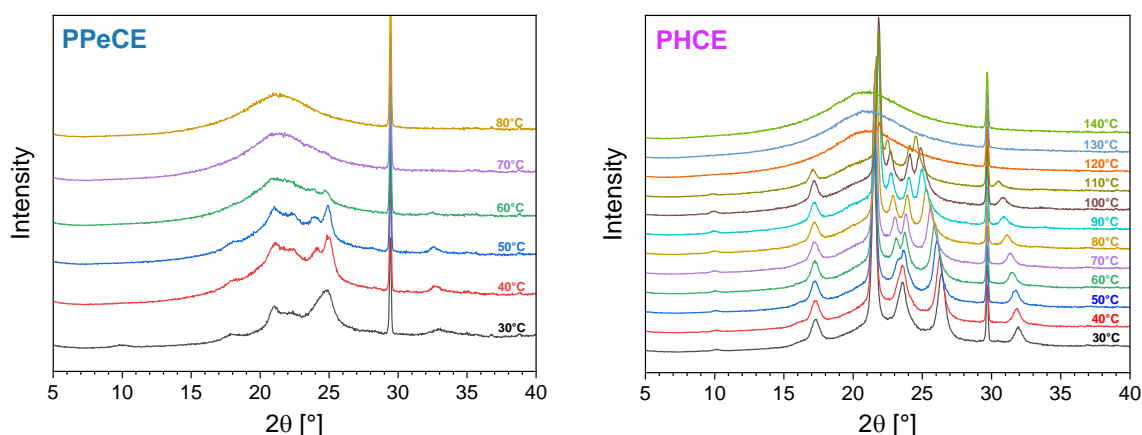


Figure IV.8. X-ray diffraction patterns recorded from 30 to 120 °C upon cooling in slow stepwise conditions (cooling at 2 K min⁻¹ followed by 20 min measurement), without prior thermal treatment. The diffraction peak at 30 °C is an artefact due to the chamber ensuring the temperature-control. Due to technical issue only the spectra up to 60 °C could be recorded for PPeCE.

From this first look into the thermal characterization of the PCHs, complex crystallization and melting behaviors were evidenced, with notable differences in terms of crystallization enthalpy and temperature, as well as melting enthalpy and temperature, depending on the alkyl chain length n_{CH_2} . Cooling from the melt at 10 K min⁻¹ is nearly enough to amorphize PPeCE, whereas the other PCHs keep their ability to crystallize even though PPeCE has the lowest *cis*-content (%) (**Table II.1** in **Chapter II**). Controlling the cooling rate and understanding its effect on the microstructure is essential, particularly for industrial processing. Indeed, processing techniques such as injection molding or extrusion can involve high cooling rates with a direct impact on the material final properties, with fast cooling producing more amorphous materials, increased transparency and elongation at break [25] in comparison with slow cooling. As evidenced in **Figure I.7** (**Chapter I**), the common cooling rates associated with TOPEM (0.02-2 K min⁻¹) and conventional DSC (5-100 K min⁻¹) cannot help with investigating what happens during and after quenching. FSC can successfully be used to better emulate the actual processing conditions for polymers, in association with DSC and TOPEM.

II. Non-isothermal crystallization

II.1 Critical cooling rate

As mentioned in **Chapter I** and **III**, Schawe and Löffler distinguished two types of glasses: the chemically homogeneous glass (CHG) only made of amorphous domains, and the self-doped glass (SDG) containing nuclei [26]. Two critical cooling rates are respectively associated with the formation of these

two types of glasses, that is to say $\beta_{c,CHG}$ and $\beta_{c,SDG}$, with $\beta_{c,CHG} > \beta_{c,SDG}$. Based on the preliminary results, a thermal protocol consisting in a series of successive cooling and heating ramps was designed for each PCH, with the purpose of evaluating their critical cooling rate $\beta_{c,SDG}$, i.e. the minimum cooling rate at which no crystallization is observed when the polymer is cooled down from the melt. The protocol consists in heating up each sample with a constant heating rate β_h to a temperature slightly above its melting, holding it to ensure that melting is complete, cooling it down through the glass transition to $-90\text{ }^\circ\text{C}$ at a constant cooling rate β_c , then heating it up again to check for any possible sign of crystals through melting. The protocol, whose temperature ranges and cooling rates were adjusted to each sample's thermal behavior (crystallization temperature T_c , glass transition temperature T_g , melting temperature range ΔT_m), is schematically represented in **Figure IV.9**. Five decades of cooling rates (from 2 K min^{-1} to 5000 K s^{-1}) were investigated to assess the critical cooling rates of PPCE, PBCE, PPeCE and PHCE. The normalized heat flows recorded during the cooling scans along with the normalized heat flows recorded during the following reheating scans are showed in **Figure IV.9**.

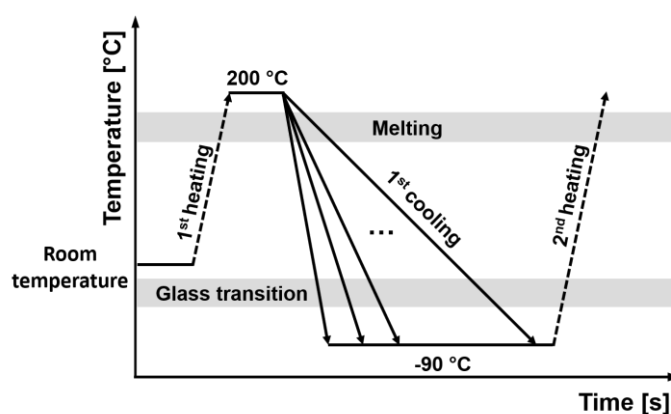
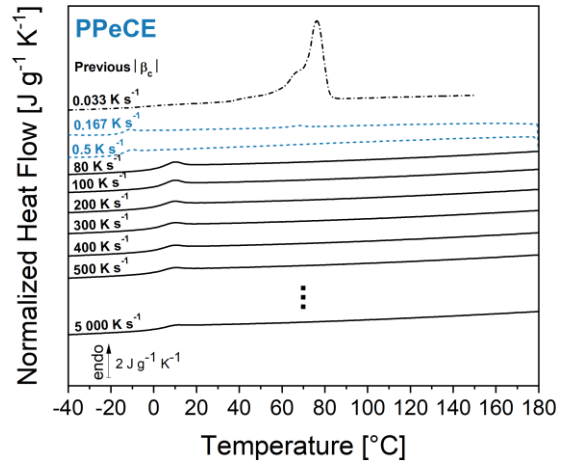
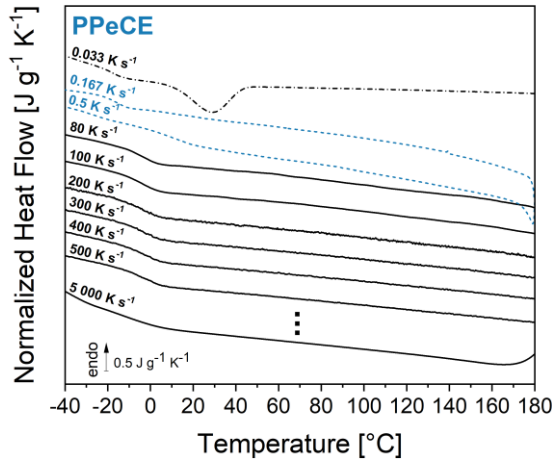
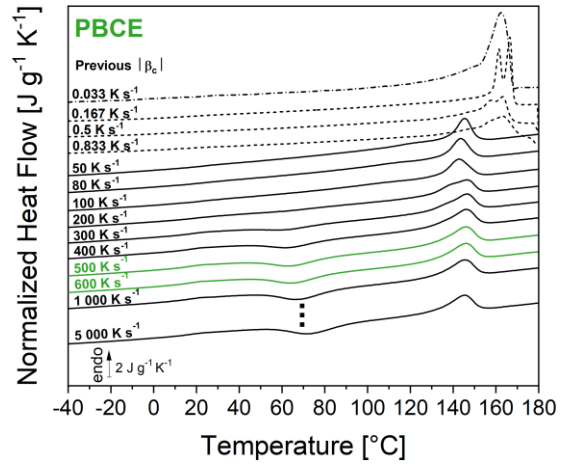
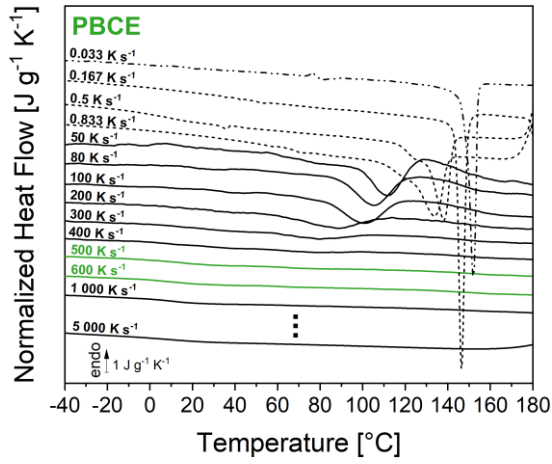
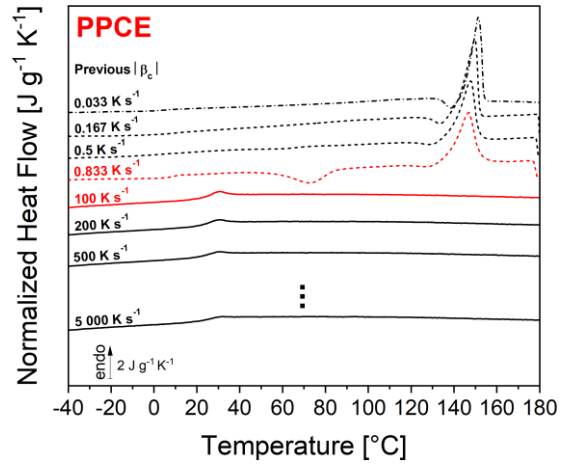
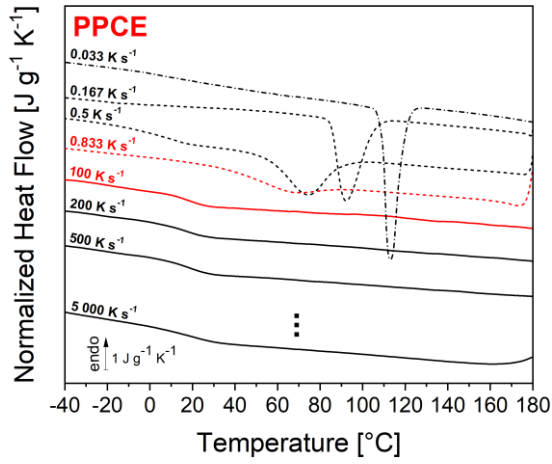


Figure IV.9. Thermal protocol used for calorimetric measurements aimed at estimating the critical cooling rate. A first heating is performed from room temperature to $200\text{ }^\circ\text{C}$, where the material is held for a certain time to erase thermal history (from 0.01 s with FSC to 5 min for DSC and TOPEM). Then the samples are cooled down to $-90\text{ }^\circ\text{C}$ at different rates depending on the calorimetric technique used, and are finally reheated to $200\text{ }^\circ\text{C}$.

Figure IV.10 (left column) reports the cooling ramps obtained for each PCH according to the thermal protocol presented in **Figure IV.9**. The cooling ramps recorded at the lowest cooling rates $|\beta_c| = 0.033\text{ K s}^{-1}$ were obtained by TOPEM (dashed-dotted lines). The cooling ramps plotted with dashed lines were obtained by conventional DSC. The cooling ramps recorded at the highest cooling rates were obtained by FSC (solid lines). A quick glance at the cooling curves confirms that PPeCE is the easiest to melt-quench, whereas PBCE is the most challenging. It is indeed necessary, at first, to check that no exothermal signals associated with crystallization are recorded during the cooling ramp. Based on this criterion, a threshold cooling rate could be identified for each PCH (left column, curves in colors). The

corresponding critical cooling rates would be somewhere between 0.833 K s^{-1} (50 K min^{-1}) and 100 K s^{-1} for PPCE, between 400 and 500 K s^{-1} for PBCE, between 0.167 K s^{-1} (10 K min^{-1}) and 0.5 K s^{-1} (30 K min^{-1}) for PPeCE, and between 100 and 200 K s^{-1} for PHCE. It is however necessary to double-check these values by considering the heating ramps recorded right after cooling. In **Figure IV.10** (right column), the heating ramps recorded by TOPEM and DSC were obtained with $\beta_h = |\beta_c|$, and all the heating ramps obtained by FSC were recorded at $\beta_h = 1000 \text{ K s}^{-1}$. The double-check consists in verifying that no endothermic signals associated with melting are recorded upon heating, or that the recorded enthalpy of melting is perfectly balanced by the enthalpy of cold crystallization (if cold crystallization occurs). Based on this additional criterion, the threshold cooling rate for melt-quenching can in some cases be readjusted (right column, curves in colors). About PPCE, for instance, **Figure IV.10** shows that (1) the slowest cooling rate leads to a fully crystallized sample (TOPEM), (2) a progressive increase in the cooling rate hinders the crystallization process and let appears cold crystallization (DSC curves), and (3) FSC allows to melt-quench the sample (no cold crystallization is observed during the subsequent heating ramp because of the higher heating rate with respect to DSC measurements). In the case of PBCE, it is worth noting that (1) only FSC is able to provide sufficiently high cooling rates for an efficient melt-quenching, (2) the range of cooling rates previously identified as critical (400 - 500 K s^{-1}) is sufficient to suppress the crystallization from the melt and cold crystallization occurs during the subsequent heating ramps, (3) a heating rate faster than 1000 K s^{-1} is required to suppress cold crystallization and any other possible melting-recrystallization process. Focusing on the heating ramps recorded after cooling at 300 , 400 , 500 and 600 K s^{-1} , one may notice that the peak of cold crystallization keeps on evolving, which confirms that vitrification is more and more efficient; the shape of the peak stabilizes between 500 and 600 K s^{-1} , which is therefore considered as a better estimation of the range within which the critical cooling rate is supposed to fall. PPeCE is easily quenched with conventional cooling rates. As for PHCE, based solely on the cooling ramps one may guess that the critical cooling rate is between 100 and 200 K s^{-1} (left column, curves in colors), however the heating ramps clearly show that a crystalline phase is formed for cooling rates up to 500 - 1000 K s^{-1} (right column, curves in colors).



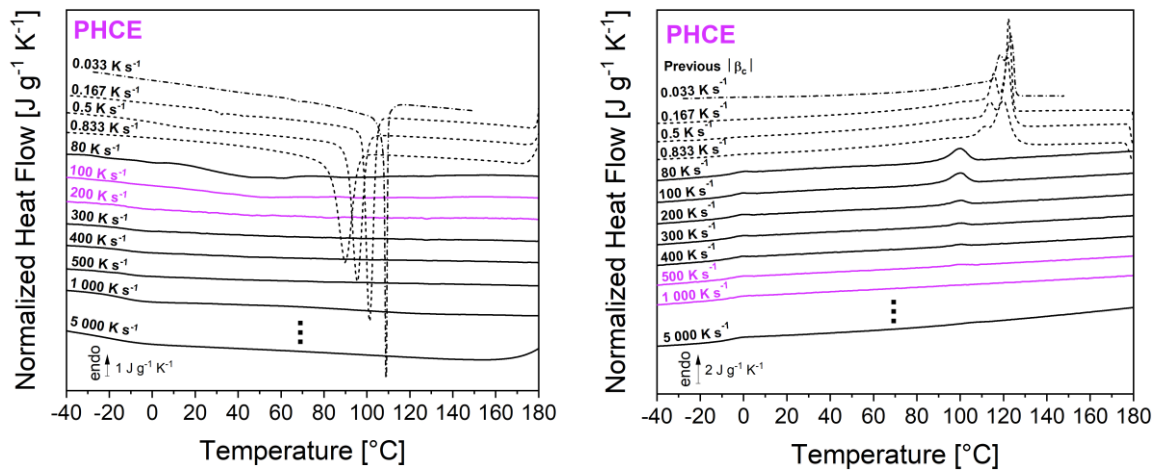


Figure IV.10. Normalized heat flows recorded upon cooling from the melt (left column) and during the subsequent heating ramp (right column). The curves at the lowest cooling rate $|\beta_c| = 0.033 \text{ K s}^{-1}$ (2 K min^{-1}) (dashed-dotted lines) were obtained by TOPEM. The curves plotted with dashed lines were obtained by conventional DSC. The curves at the highest cooling rates were obtained by FSC (solid lines). The heating ramps were obtained with $\beta_h = |\beta_c|$ (TOPEM and DSC) or $\beta_h = 1000 \text{ K s}^{-1}$ (FSC). The curves in colors highlight the range within which the critical cooling rate $|\beta_{c,SDG}|$ is supposed to fall based on either crystallization (left column) or subsequent melting (right column).

Of all the considered samples, PBCE is the only one being able to cold-crystallize despite the relatively high heating rates used in FSC experiments (1000 K s^{-1}) (**Figure IV.10**, right column). Such phenomenon can be triggered by the formation of nucleation pre-cursors upon cooling or upon heating with sufficient mobility. **Figure IV.11** illustrates the additional criterion to meet to make sure that a polymer able to cold-crystallize is completely vitrified during melt-quenching. **Figure IV.11.a** shows a selection of heating ramps recorded after cooling from the melt at different $|\beta_c|$. The additional criterion consists in calculating the enthalpy of cold crystallization Δh_{cc} and the enthalpy of melting Δh_m , and then verifying if they are perfectly balanced. For cooling rates below 100 K s^{-1} , no cold crystallization is observed during the subsequent heating. When faster cooling rates are used, cold crystallization occurs, and the associated enthalpy Δh_{cc} gradually increases until reaching a plateau (18 J g^{-1} for $|\beta_c| = 1000 \text{ K s}^{-1}$). On the other hand, the enthalpy of melting Δh_m decreases from 40 to 18 J g^{-1} as the cooling rate increases up to 100 K s^{-1} , and then stabilizes at 18 J g^{-1} as well. **Figure IV.11.b** reports the values of Δh_{cc} , Δh_m , and their algebraic difference $\Delta h_m - \Delta h_{cc}$, plotted against the cooling rate $|\beta_c|$ previously used for melt-quenching. With this additional criterion, the critical cooling rate $|\beta_{c,SDG}|$ for PBCE is rather estimated at about 3000 K s^{-1} (when $\Delta h_m - \Delta h_{cc} = 0$).

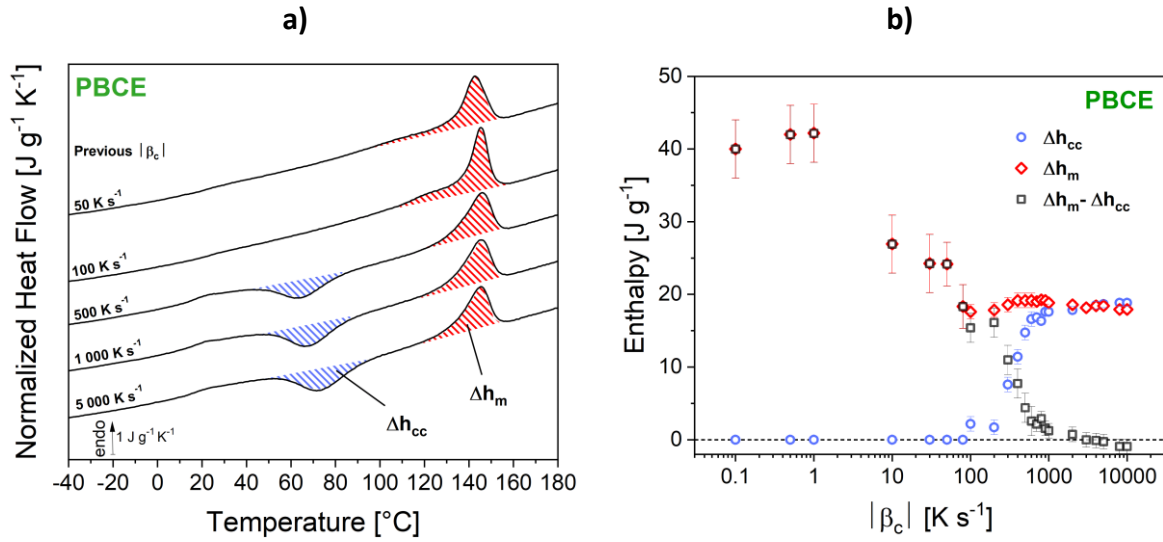


Figure IV.11. a) Calculation of the enthalpies of cold crystallization Δh_{cc} (blue-hatched areas) and melting Δh_m (red-hatched areas) for PBCE previously cooled down from the melt at different cooling rates $|\beta_c|$. **b)** Enthalpies of cold crystallization Δh_{cc} (blue circles) and melting Δh_m (red diamonds), along with their algebraic difference $\Delta h_m - \Delta h_{cc}$ (black squares) plotted against the cooling rate β_c previously used to attempt melt-quenching.

Based on the Johnson-Mehl-Avrami-Kolmogorov (JMAK) equation for isothermal crystallization, Schawe and Löffler proposed that the cooling-rate dependence of the cold-crystallization temperature (taken at the top of the cold crystallization peak) follows a power law [26]:

$$T_{cc} = T_1 + C[\beta_c - \beta_0]^\kappa \quad \text{Eq. 1}$$

where C and κ are empirical constants, T_1 is the minimum crystallization temperature during heating, and β_0 is the minimum cooling rate under which no cold crystallization happens during heating. **Figure IV.12** shows that, as the cooling rate increases, the cold crystallization temperature T_{cc} increases from 60 °C to 70 °C, suggesting a delay in the growth of the nuclei formed during previous cooling. Consequently, the melting temperature decreases from 163 °C to 145 °C because of the reduced dimensions of the crystal lamellae. The application of the power law in **Eq. 1** gives a cooling rate β_0 of 130 K s⁻¹ under which no cold crystallization occurs upon subsequent heating at 1 000 K s⁻¹.

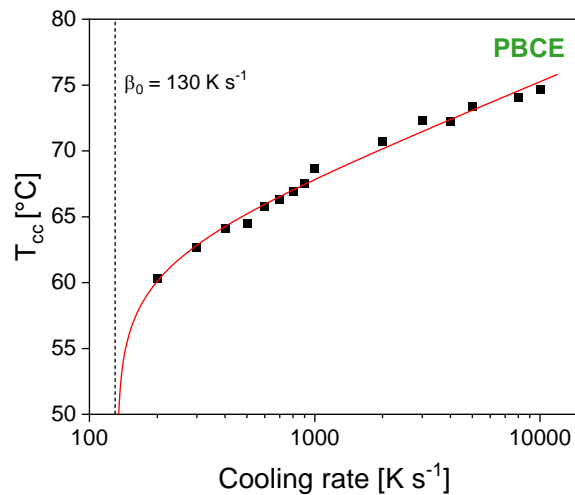


Figure IV.12. Cold-crystallization temperatures T_{cc} (black squares) measured upon heating at 1000 K s^{-1} following different cooling rates $|\beta_c|$. The red line represents the power law in **Eq. 1**.

Figure IV.13 shows the influence of the cooling rate on the crystallization temperature T_c (symbols), and more generally on the temperature range at which crystallization occurs (bars). Two phenomena are evidenced. The first observation is that, irrespective of n_{CH_2} , an increase in the cooling rate $|\beta_c|$ leads to a decrease in the crystallization temperature T_c and a broadening of the crystallization peak (increase in ΔT_{cc}), from less than $10 \text{ }^\circ\text{C}$ at the slowest cooling rates to more than $30 \text{ }^\circ\text{C}$ at the fastest cooling rates. The shift of T_c and the increase in ΔT_{cc} both prove that the observed transformation is controlled by nucleation; indeed, slow cooling enables the activation of the nuclei at higher temperature, whereas fast cooling retards and slows down the nucleation process [27]. Since the sample mass and thickness are sufficiently small (few tenths of ng), the broad crystallization peaks of the polyester are caused neither by thermal lag nor by smearing effects [20].

The second observation is that the odd-numbered polyesters are associated with larger crystallization peaks and lower crystallization temperatures in comparison with their even-numbered counterparts at the same cooling rate. It should also be mentioned that PBCE has recently been shown to crystallize in at least two polymorphic forms, α and β , with the α -form observed upon slow cooling, and the β -form generated with sufficiently fast cooling from the melt (however the explored range of cooling rates did not exceed 50 K min^{-1}) [8]. With this in mind, the shift of T_c from 80 to $150 \text{ }^\circ\text{C}$ could be interpreted as the progressive transformation of the metastable β -form into the more stable α -form as the undercooling ΔT gets reduced, with ΔT being the difference between the equilibrium melting temperature T_m^0 and the crystallization temperature T_c (**Chapter I, Section I.2**). One may also notice that both PBCE and PHCE have a double value of T_c at the lowest cooling rates. This could be due to the formation of a different crystalline phase upon cooling, considered that the polymorphic character

of PBCE has been mentioned before but so far, the literature reports no evidence of polymorphism for PHCE.

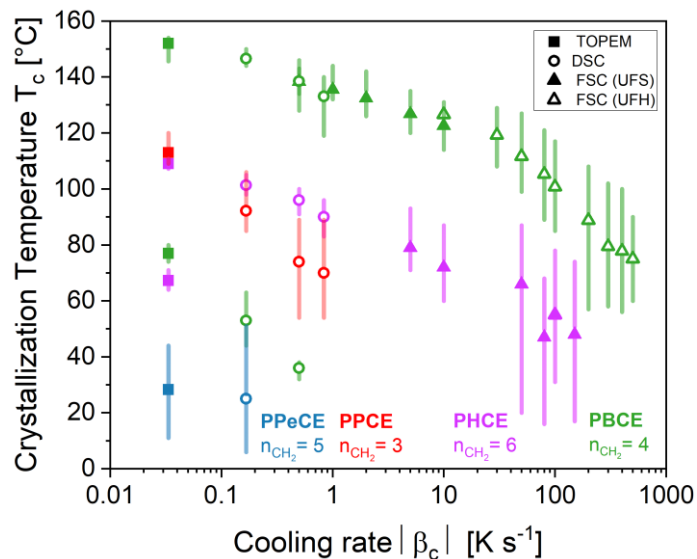


Figure IV.13. Crystallization temperatures T_c (symbols) and temperature ranges at which crystallization occurs ΔT_{cc} (bars) measured upon cooling from the melt at different cooling rates $|\beta_c|$. The bars represent the temperature range going from the onset ($T_{c,on}$) to the endset ($T_{c,end}$) of the crystallization peak.

Figure IV.14 shows a summary of the critical cooling rates $|\beta_{c,crit}|$ reported in the literature for common polymers and for a few other materials (silica, benzocaine, water). The critical cooling rates estimated in this work for PPCE, PBCE, PPeCE and PHCE are also reported for comparison purposes. As expected, the even-numbered PCHs (PBCE with $n_{CH_2} = 4$ and PHCE with $n_{CH_2} = 6$) require faster cooling rates to be effectively melt-quenched as compared to the odd-numbered PCHs (PPCE with $n_{CH_2} = 3$ and PPeCE with $n_{CH_2} = 5$). It also appears that, irrespective of the odd or even character of n_{CH_2} , the value of the critical cooling rate decreases as the length of the alkyl chain within the repeating unit increases, suggesting that the methylene groups act as defects for crystal formation. This observation cannot be extended to other systems, such as poly (ethylene terephthalate) (PET) and poly (butylene terephthalate) (PBT), for which an increase of n_{CH_2} from 2 to 4 leads to a four-decade decrease in $|\beta_{c,crit}|$. It is however interesting to see that PBCE has about the same critical cooling rate as its terephthalic counterpart PBT, regardless of the nature of the acidic component. Together with poly (ϵ -caprolactone) (PCL) they also show a propensity for cold crystallization [21, 28, 29].

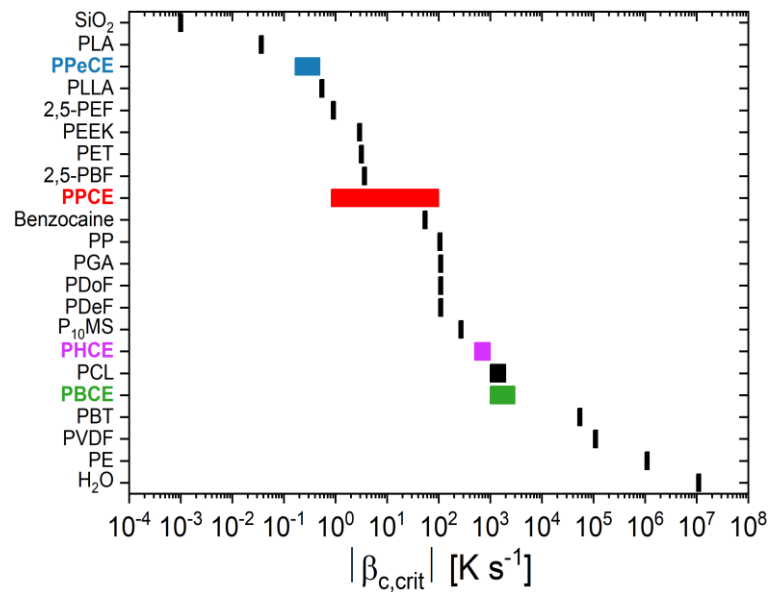


Figure IV.14. Values of critical cooling rates $|\beta_{c,crit}|$ issued from the literature [14, 20, 30-37] for common polymers as well as for a few other materials (silica, benzocaine, water). Full names can be found in **Appendix 1**.

The methodology developed here allowed to estimate the range of critical cooling rates of the four PCHs, but is rather time-consuming. Barandiarán and Colmenero [30] proposed a method relying on the degree of supercooling ΔT . The equilibrium melting temperature T_m° is commonly estimated using the Hoffman-Weeks extrapolative method [38], which will be applied later on.

II.2 Application of the three-phase model

To investigate the consequences of cooling rate on the microstructure, the three-phase model was applied to the cooling curves. This procedure cannot be done on the heating curves from **Figure IV.10** because of the small relaxation peak superimposed to the heat capacity step at the glass transition, which can appear as the heating rate used is far greater than the previous cooling rate ($|\beta_c| \ll \beta_h$). To circumvent this issue, a thermal protocol inspired by Heidrich et al. [28] was used, consisting in two different cooling rates: the first one β_{c_1} is used to cross the crystallization domain, whereas the second one β_{c_2} is used to cross the glass transition domain, and is equal to the subsequent heating rate β_h .

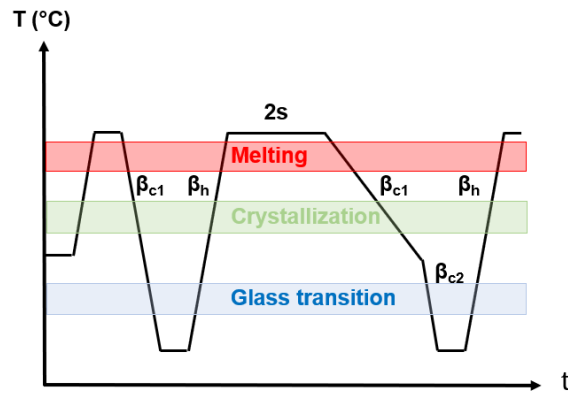
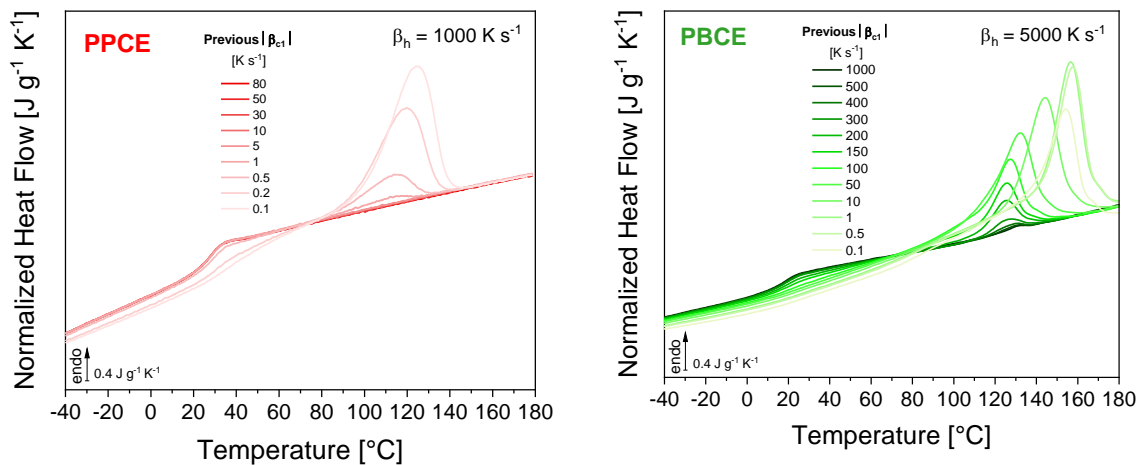


Figure IV.15. Thermal protocol for the quantification of the three fractions (crystalline, mobile amorphous and rigid amorphous) depending on the cooling rate.

Figure IV.16 shows the normalized heat flows recorded by FSC upon heating according to the thermal protocol in **Figure IV.15**. Each curve is used to measure the specific heat capacity step Δc_p and the melting enthalpy Δh_m . The Mobile Amorphous Fraction X_{MAF} , the Rigid Amorphous Fraction X_{RAF} and the Crystalline Fraction X_C are estimated using **Eq. 2** and **Eq. 3** presented in **Chapter I**, and the values for the melting enthalpy of fully crystalline material Δh_m° are the ones estimated by Fosse et al. [39] in a previous work.



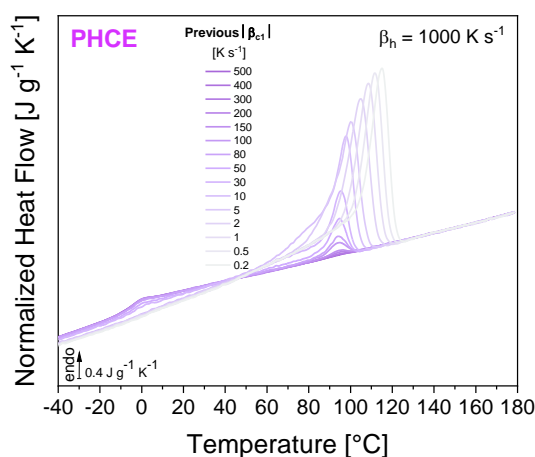


Figure IV.16. Normalized heat flows recorded upon heating at $\beta_h = 1\,000\text{ K s}^{-1}$ for PPCE and PHCE, and at $5\,000\text{ K s}^{-1}$ for PBCE in order to avoid cold crystallization, according to the thermal protocol in **Figure IV.15**. The cooling rates β_{c1} used to sweep through the crystallization zone are adapted to each material.

Figure IV.17 shows the cooling-rate dependence of the two amorphous fractions and of the crystalline fraction. DSC results (empty symbols) are consistent with FSC results (full symbols). Since PPeCE remains amorphous using the range of cooling rates associated with DSC, the DSC curves shown in **Figure IV.10** were used for the calculations. With an increase in the cooling rate, all the polyesters become fully amorphous, with a crystallization suppression occurring in the same range of cooling rates estimated from **Figure IV.13**. As the cooling rate decreases, X_{MAF} decreases whereas X_{RAF} and X_C increase. Interestingly, in the case of even-numbered polyesters, RAF formation precedes the formation of the crystalline phase. The same phenomenon has been previously observed after non-isothermal crystallization of PET and PBT [28]. As seen in **Figure IV.13**, with the increased cooling rate the crystallization is inhibited and shifted to lower temperatures, so that the macromolecular chains have enough time to fold. Lower T_c results in higher RAF contents, as observed for other polyesters [40]. Presumably the mobile amorphous fraction first converts into RAF, then the activation of secondary crystallization occurs at lower temperature. The participation of RAF in the crystallization process through lamellar perfection has been observed before [41]. RAF activation is expected to cause a shift in the crystallization kinetics, which can be investigated using the Ozawa model for non-isothermal crystallization. Non-isothermal crystallization evidenced the presence of RAF up to 40 % and 45 % for even-numbered samples, and not exceeding 15 % for their odd-numbered counterparts.

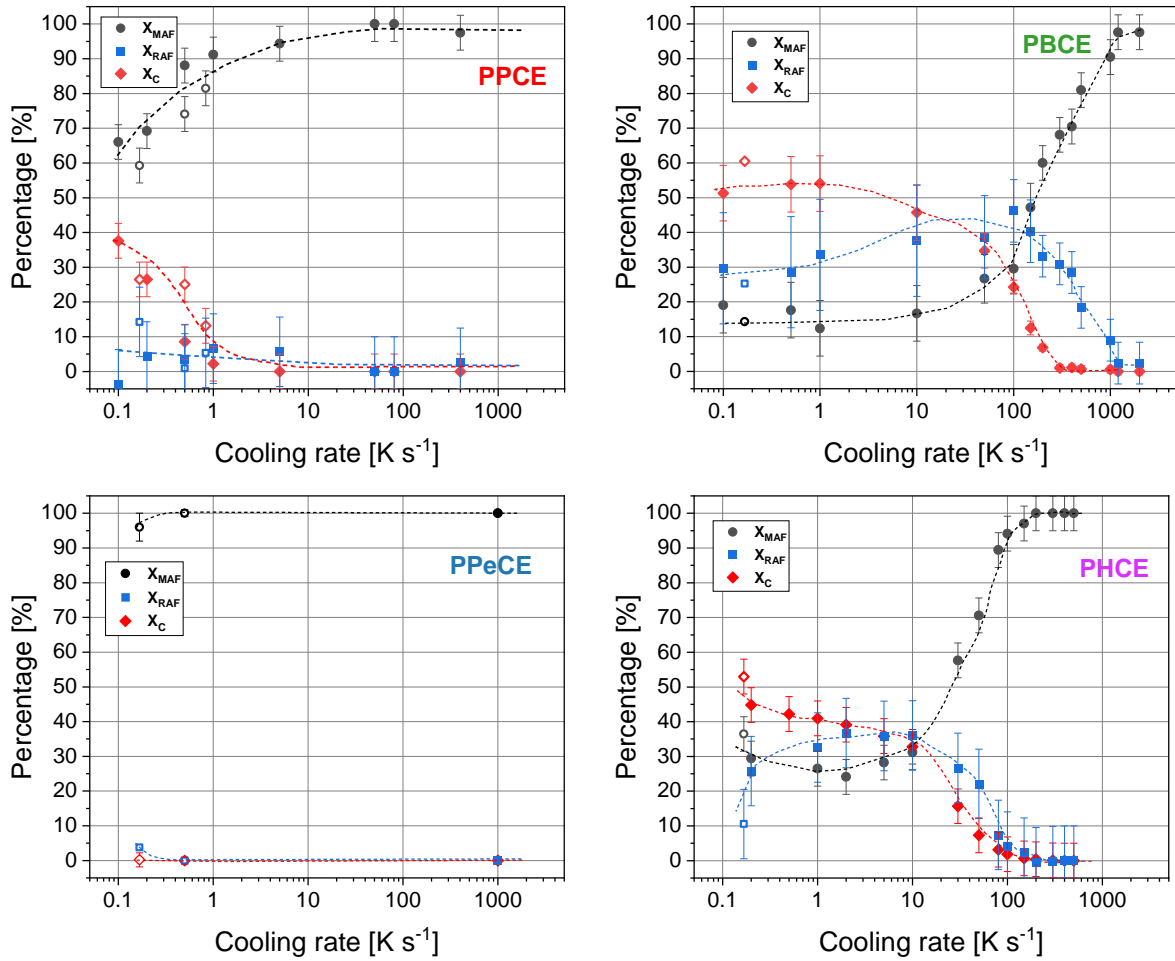


Figure IV.17. Mobile Amorphous Fraction X_{MAF} (black circles), Rigid Amorphous Fraction X_{RAF} (blue squares) and Crystalline Fraction X_C (red diamonds) as a function of the cooling rate. The filled and empty symbols correspond to FSC and DSC measurements, respectively.

II.3 Ozawa model

The temperature dependence of the relative crystalline fraction $\alpha(T)$ are determined from DSC and FSC measurements after melt-quenching with different cooling rates following the model developed by Ozawa for the investigation of crystallization under cooling at a constant rate [42]:

$$\alpha = 1 - \exp \left[\frac{-X(T)}{|\beta_c|^m} \right] \tag{Eq. 2}$$

where α is the relative crystalline fraction, $X(T)$ is the cooling function, $|\beta_c|$ is the cooling rate, and m is the Ozawa exponent. The high GFA associated to PPeCE makes it difficult to investigate the non-isothermal crystallization. The PPeCE case will then be investigated in more details later on, in isothermal conditions.

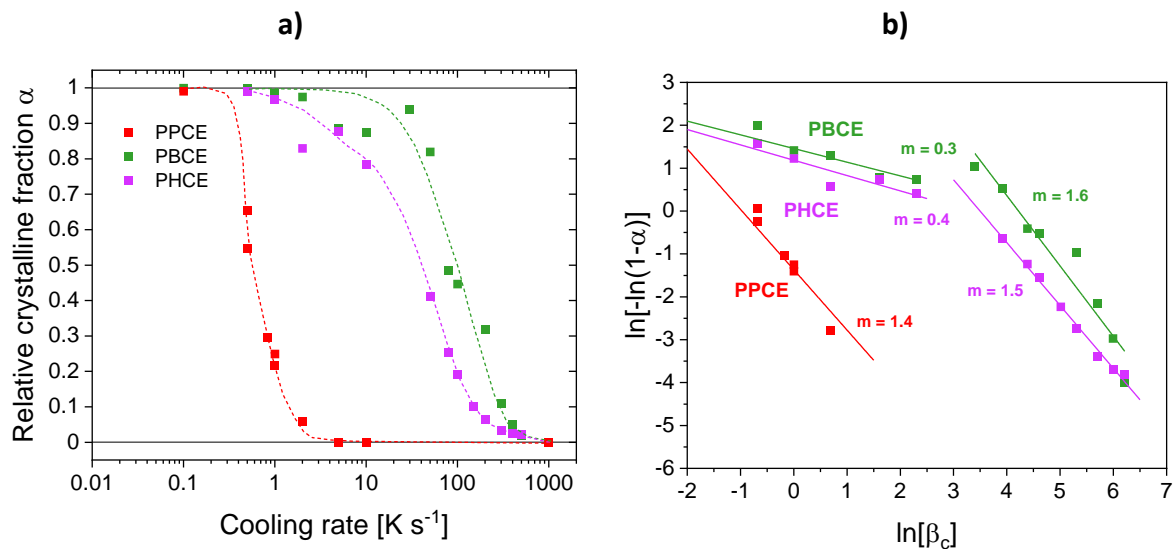


Figure IV.18. a) Cooling rate-dependence of the normalized crystalline fraction α ; b) Ozawa plots for non-isothermal crystallization.

Figure IV.18.a depicts the cooling-rate dependence of the relative crystalline fraction $\alpha(T)$ following the Ozawa model for a crystallization in non-isothermal conditions. As expected, the even-numbered polyesters (PBCE and PHCE) are characterized by faster crystallization kinetics in comparison with PPCE, with a first increase in the crystalline fraction occurring nearly two decades apart in terms of cooling rate. However, all the polyesters reach their highest crystalline fraction in the same range of cooling rates (between 0.1 and 1 K s^{-1}), suggesting a slow-down of the crystallization processes as the cooling rate decreases in the case of the even-numbered PCHs. The Ozawa plots represented in **Figure IV.18.b** evidence two tendencies, with an index m nearly constant (between 1.4 and 1.6) for PPCE and the even-numbered PCHs between 50 and 500 K s^{-1} , and an index m between 0.3 and 0.4 for the even-numbered PCHs associated to low cooling rates (between 10 and 0.5 K s^{-1}). The difference observed for the even-numbered PCHs correlates well with the increase in Rigid Amorphous Fraction previously observed in **Figure IV.17** with the decreasing cooling rate. Moreover, the estimated values are unusually low. For isothermal crystallization, Toda and al. [43] and Schawe et al. [44] proposed a mechanism explaining the appearance of non-linearity with the slowing down of crystalline growth caused by the inhibition of chain folding at the crystal growth front due to the presence of RAF; they used this mechanism to explain Avrami indices n below 2 , which could potentially be transposed to non-isothermal crystallization.

III. Isothermal crystallization

III.1 Equilibrium melting temperature T_m° using the Hoffman-Weeks method

The equilibrium melting temperature T_m° can be obtained by plotting the melting temperature T_m measured for samples crystallized to their maximum extent at different crystallization temperature T_c following the extrapolation method proposed by Hoffman and Weeks [38].

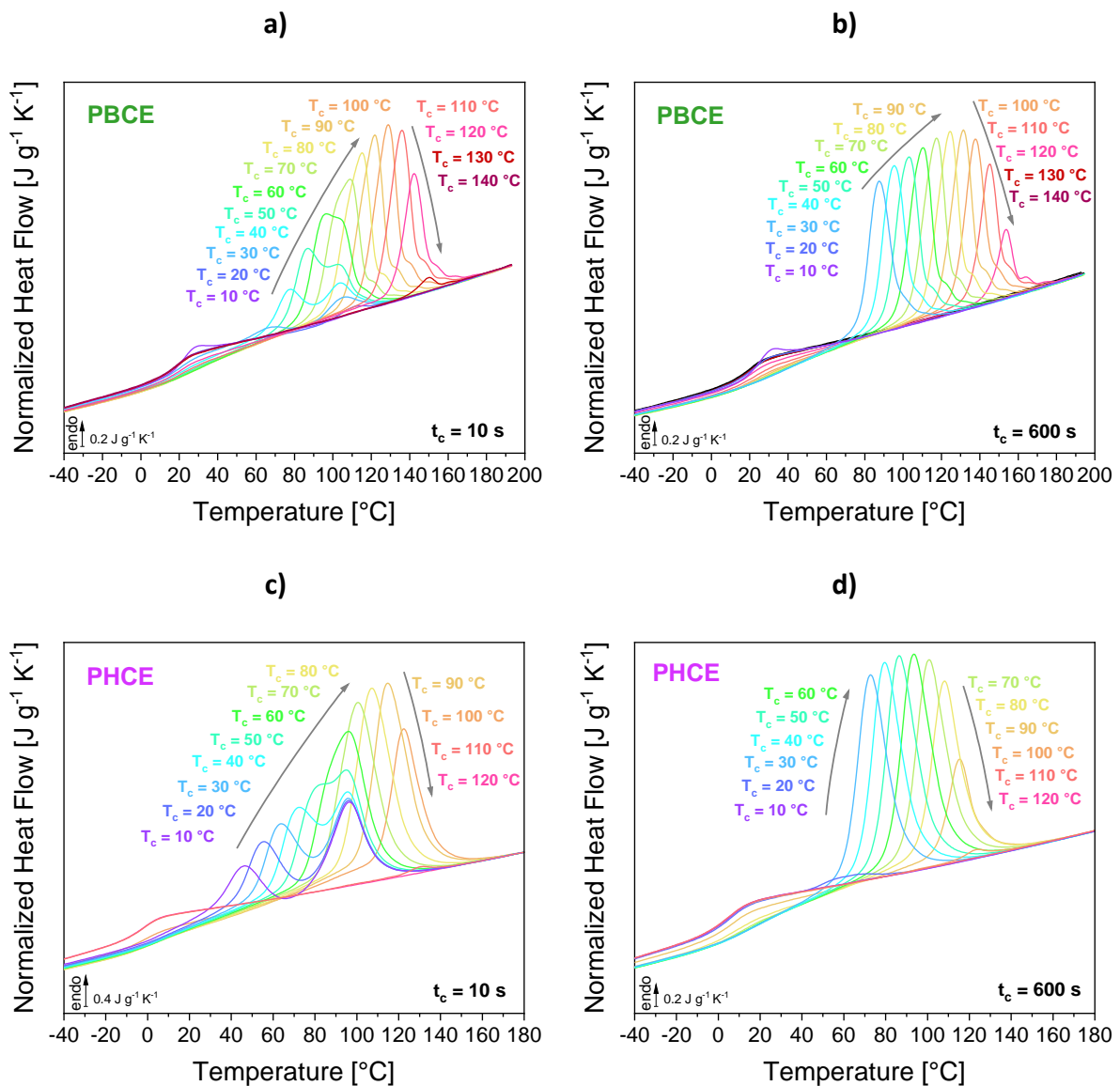


Figure IV.19. Normalized heat flows measured upon heating at 5 000 K s⁻¹ after isothermal crystallization at the indicated T_c for **a)** PBCE with $t_c = 10$ s, **b)** PBCE with $t_c = 600$ s, **c)** PHCE with $t_c = 10$ s, **d)** PHCE with $t_c = 600$ s.

The normalized heat flows measured upon heating after isothermal crystallization at various T_c for PBCE and PHCE are shown in **Figure IV.19**. An increase in T_c leads to an increase in the melting temperature, however depending on the crystallization time t_c different endotherms can be distinguished.

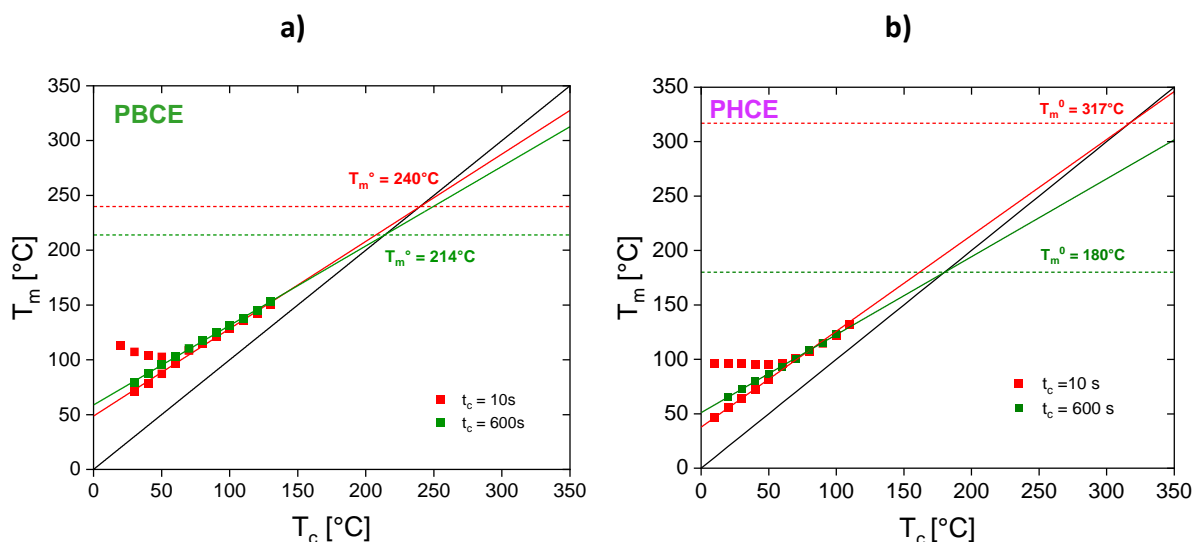


Figure IV.20. Melting temperatures T_m plotted against the crystallization temperatures T_c for **a)** PBCE and **b)** PHCE. The red and green squares correspond to a crystallization time t_c of 10 s and 600 s, respectively. The black line represents $T_m = T_c$, the dotted lines show the temperature corresponding to the intersection between the extrapolated experimental data and the $T_m = T_c$ curve.

Figure IV.20 shows the Hoffman-Weeks extrapolation for PBCE and PHCE. For short crystallization time (10 s) two melting peaks are visible, whereas a single melting peak is obtained for crystallization time reaching 600 s. As the crystallization time increases, the intersection corresponding to T_m° decreases from 240 °C to 214 °C for PBCE, and from 317 °C to 180 °C for PHCE. Strobl proposed a model for polymer crystallization that includes intermediate states between the amorphous phase and the crystal [45, 46]. This model predicts that the equilibrium melting temperature of the mesomorphic phase is located at a higher temperature with respect to the one of the crystalline phase. This would suggest that the crystallization pathway undergone by the even-numbered PCH from the isotropic melt to an ordered crystalline phase goes through intermediate transient stages. As mentioned in **Chapter III**, transitions from isotropic melt to liquid crystal (LC) phase and from LC to ordered crystals are not uncommon in aromatic polyesters with aryl rings acting as mesogenic units [47]. This could also be the case here especially considering that the cyclohexane moiety in the backbone of the PCH repeating unit is a mesogenic unit as well [6].

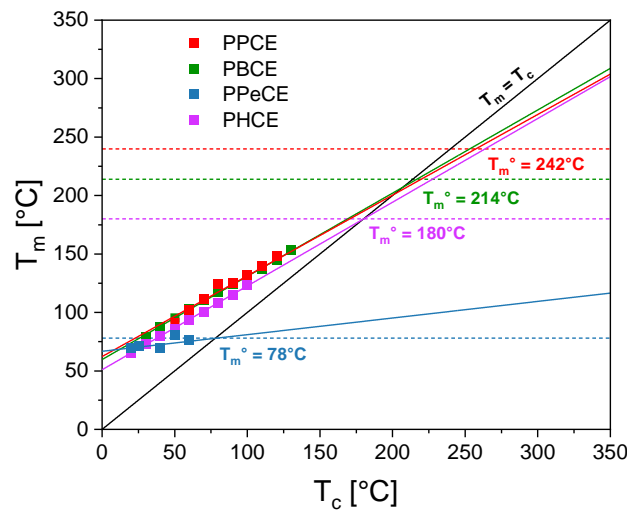


Figure IV.21. Melting temperature T_m plotted against the crystallization temperature T_c for the four PCHs. The black line represents $T_m = T_c$, the dotted lines show the temperature corresponding to the intersection between the extrapolated experimental data measured at $t_c = 600$ s and the $T_m = T_c$ curve.

From the intersections between the extrapolated experimental data and the $T_m = T_c$ straight line in **Figure IV.21**, a decrease in T_m° is observed from 242 °C (PPCE) to 78 °C (PPeCE). The temperature found for PBCE is however notably higher than the value of 182 °C found in the literature [48, 49]. PCHs with the shortest alkyl chain in the repeating unit have the highest T_m° , followed by PHCE and PPeCE. This decrease could be related to a lower packing density of the macromolecules in the crystal lattice [47]. For a series of aliphatic polyethers, Flores et al. evidenced a monotonic increase of T_m° with n_{CH_2} [19], however they investigated the series from $n_{CH_2} = 6$ to 12, and long aliphatic chains can eventually lead to a saturation effect [10].

III.2 Barandiarán and Colmenero's method

As explained before, the critical cooling rate is an important parameter for industrial processing. The experimental results presented so far allowed to estimate a range for $\beta_{c,crit}$ however no precise value can be provided unless performing a potentially large number of additional measurements with a dichotomic approach. A theoretical expression proposed by Barandiarán and Colmenero (BC) [30] (Eq. 22 in Chapter I) relates $\beta_{c,crit}$ to the degree of undercooling ΔT defined as the difference between the equilibrium melting temperature T_m° and the crystallization temperature T_c estimated in **Figure IV.13**.

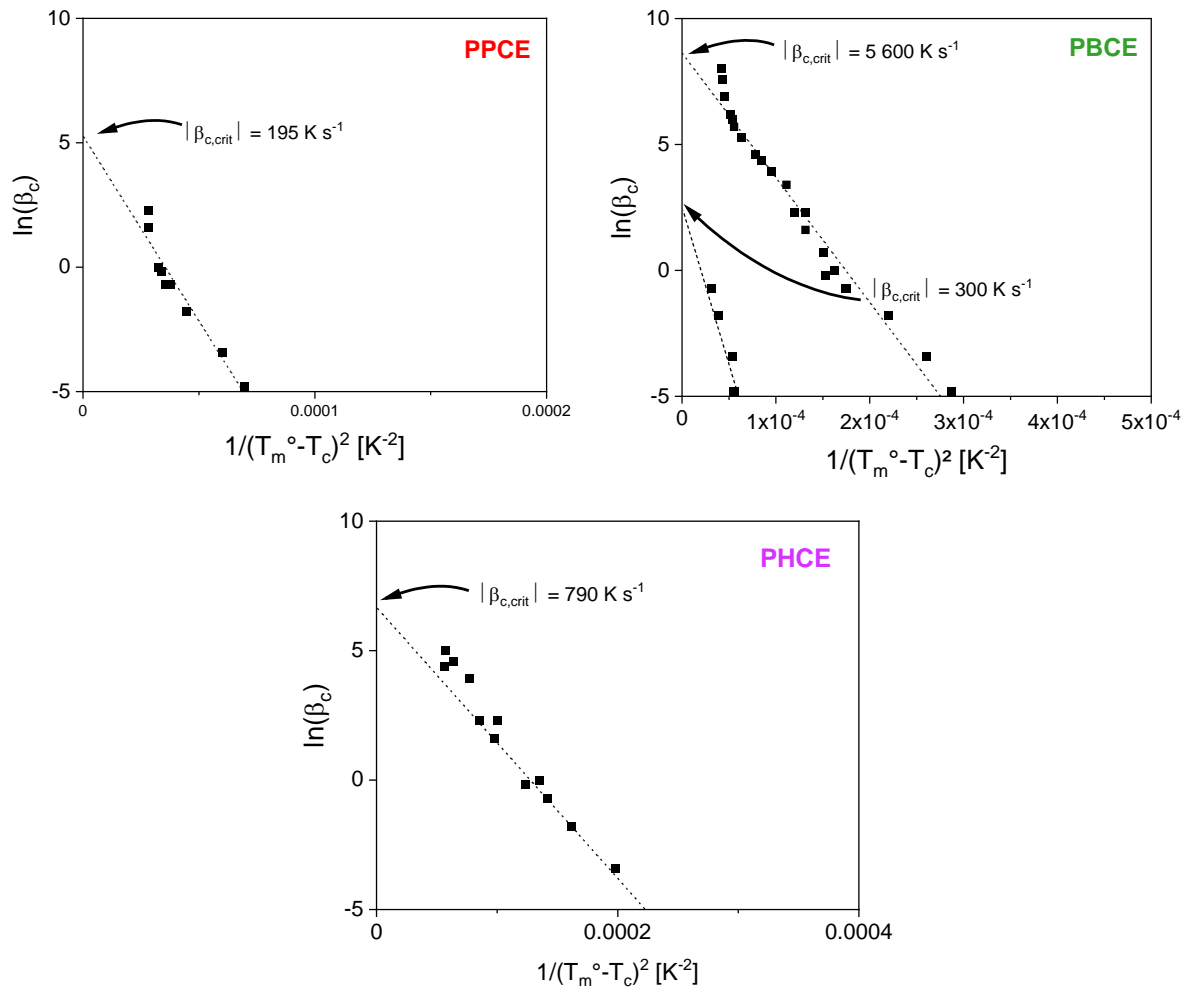


Figure IV.22. Estimation of the critical cooling rate based on the Barandiarán and Colmenero's method for PPCE, PBCE and PHCE.

It appears that the critical cooling rates estimated from the linear regression in **Figure IV.22** are overestimated in comparison with the previous values of critical cooling rate assessed experimentally in **Section II.1** for PPCE and PBCE. PPCE could not be investigated due to an insufficient amount of experimental data points. Two critical cooling rates are observed for PBCE, corresponding to the main crystallization at high temperature and a secondary crystallization at low temperature and slow cooling (**Figure IV.13**).

For PBCE, the Barandiarán and Colmenero's method gives a critical cooling rate of 1200 K s^{-1} with $T_m^\circ = 182 \text{ }^\circ\text{C}$ as reported in the literature [48, 49], which is closer to the critical cooling rate determined experimentally. This overestimation of the equilibrium melting temperature could be related to a crystallization time that is too short to form the stable crystalline phase, as mentioned before.

III.3 Kinetics investigation of the high-temperature crystalline form

Due to the fast crystallization kinetics observed upon cooling, only the crystalline phases formed at high temperature (HT crystalline form) can be investigated using DSC, except for PPeCE which can be amorphized with a cooling rate of 30 K min^{-1} . The same thermal protocol sketched in **Figure IV.23** was used and adapted to the cooling rates accessible with conventional DSC ($\beta_h = 30 \text{ K min}^{-1}$). **Figure IV.24** shows the heat flows measured during isothermal crystallization and the subsequent heating scan. The Avrami index obtained through the application of JMAK equation for the different crystallization temperatures is reported in **Table IV.3**.

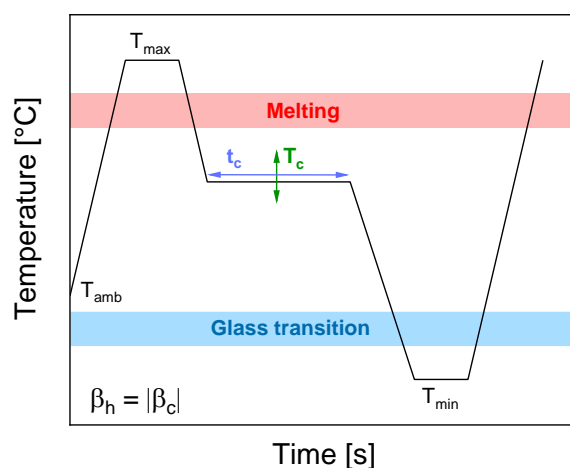
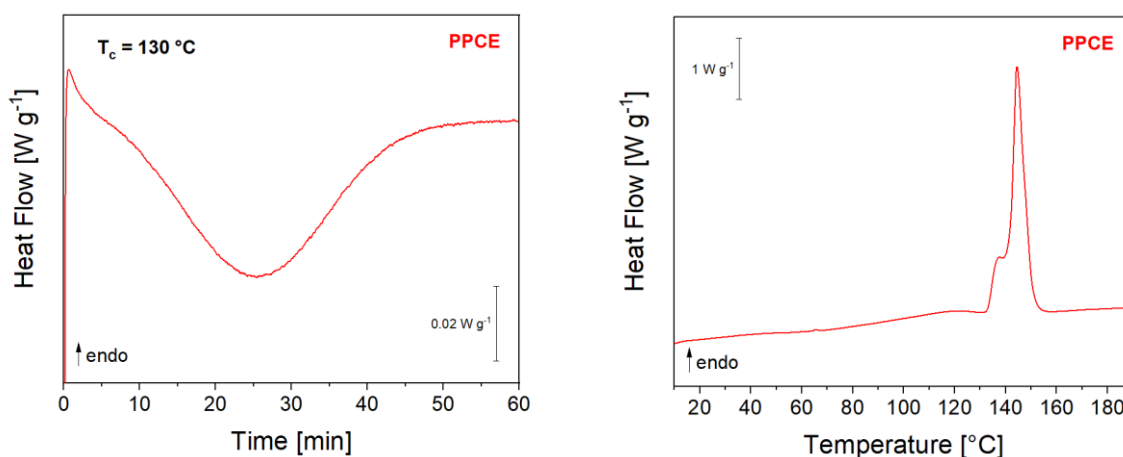


Figure IV.23. Thermal protocol used to investigate the isothermal crystallization kinetics of the PCHs. The samples were first heated to a temperature T_{max} above their respective melting temperatures, held for 5 min, and then quenched to the crystallization temperature T_c . After isothermal holding at T_c for 60 min, the samples were cooled to T_{min} below their respective T_g and reheated to T_{max} . The crystallization temperatures are adapted to each polyester and were determined from the DSC cooling curves in **Figure IV.10**.



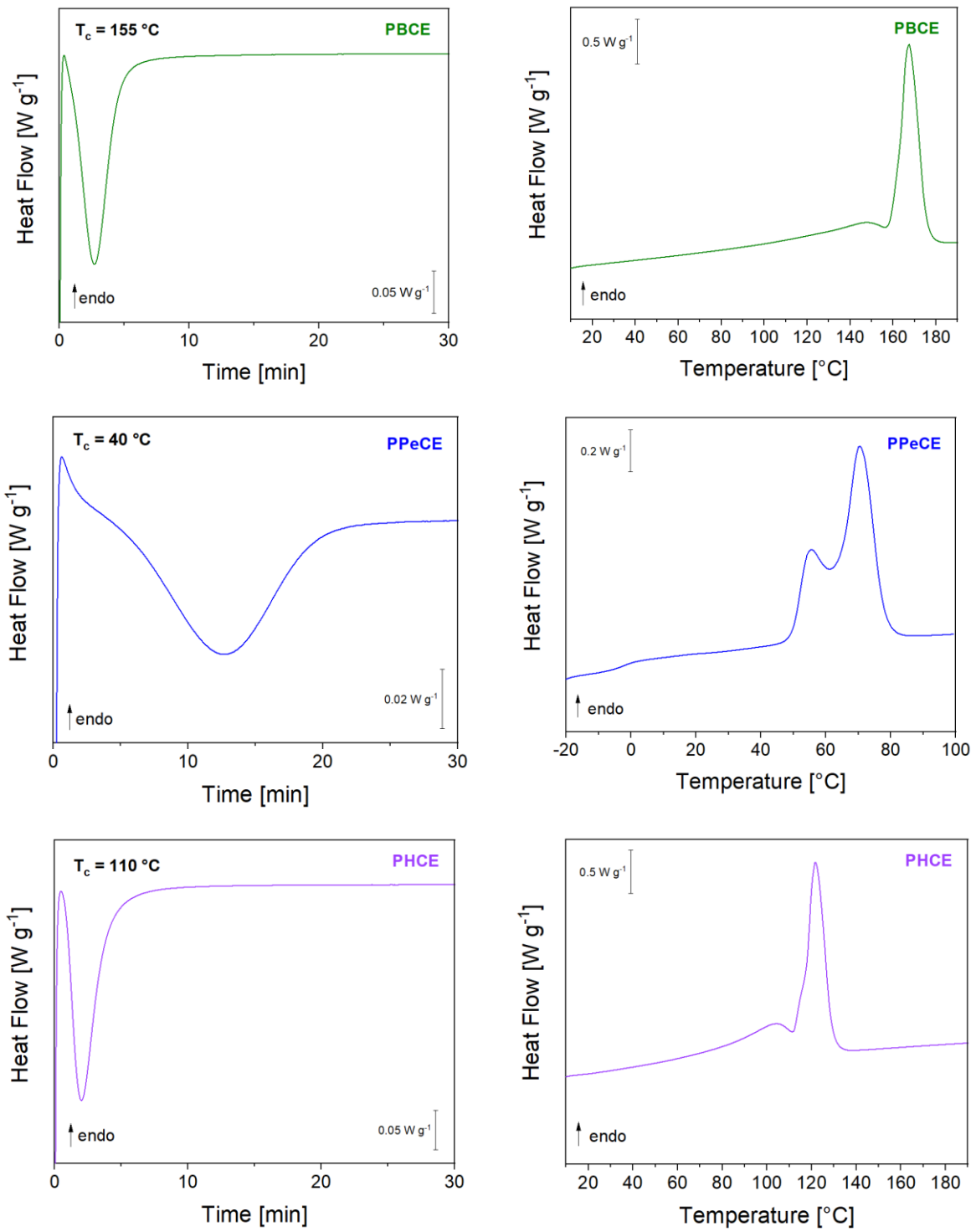


Figure IV.24. Heat flows measured during isothermal crystallization (left column) and during the subsequent heating (right column) for all the PCHs.

Table IV.3. Values of the Avrami index estimated from the isothermal crystallization curves (**Figure IV.24**, left column). T_c is the isothermal crystallization temperature, $t_{1/2}$ is the half-crystallization time when the relative crystalline fraction α reaches 0.5 and n is the Avrami index.

Sample	T_c [°C]	$t_{1/2}$ [min]	Avrami index n	K [min^{-1}]
PPCE	130	26	2.5	$6.9 \cdot 10^{-4}$
PBCE	155	3	2.8	$5.2 \cdot 10^{-2}$
PPeCE	40	13	2.6	$2.9 \cdot 10^{-3}$
PHCE	110	2	2.9	$1.3 \cdot 10^{-1}$

The odd-even effect is clearly visible on the isothermal crystallization behavior when considering the heating flow recorded during the crystallization process (**Figure IV.24**, left column), with even-numbered PCHs having lower half-crystallization time in comparison with their odd-even counterparts. The Avrami indices are usually expected to be integers between 1 and 4 [32], however obtaining rational numbers is not uncommon [43, 44]. The overlapping of primary and secondary crystallizations, for instance, can complicate the evaluation of the crystallization kinetics [44]. The melting endotherms recorded after completion of crystallization show multiple peaks, as also observed during the first thermal analysis, suggesting the occurrence of recrystallization processes, even though the relatively high crystallization temperature should increase mobility and help the refolding of the molecular chains, leading to less structural defects and thus the formation of stable crystals [28]. This reorganization upon heating may be favored by the relatively low heating rate (30 K min^{-1}). Nonetheless, values of the Avrami index close to 3 are obtained for the even-numbered PCHs, suggesting a three-dimension growth. **Figure IV.25** shows the micrographs obtained with Polarized Optical Microscopy on samples submitted to the same thermal protocol. POM micrographs reveal a large nucleation density with consequently numerous and small spherulites for all the PCHs, even at low supercooling where the growth regime is prevalent. This behavior is similar to what has been previously observed for poly (ethylene 2,5-furanoate) PEF in contrast to poly (ethylene terephthalate) (PET) or poly (ethylene naphthalate) (PEN) [50].

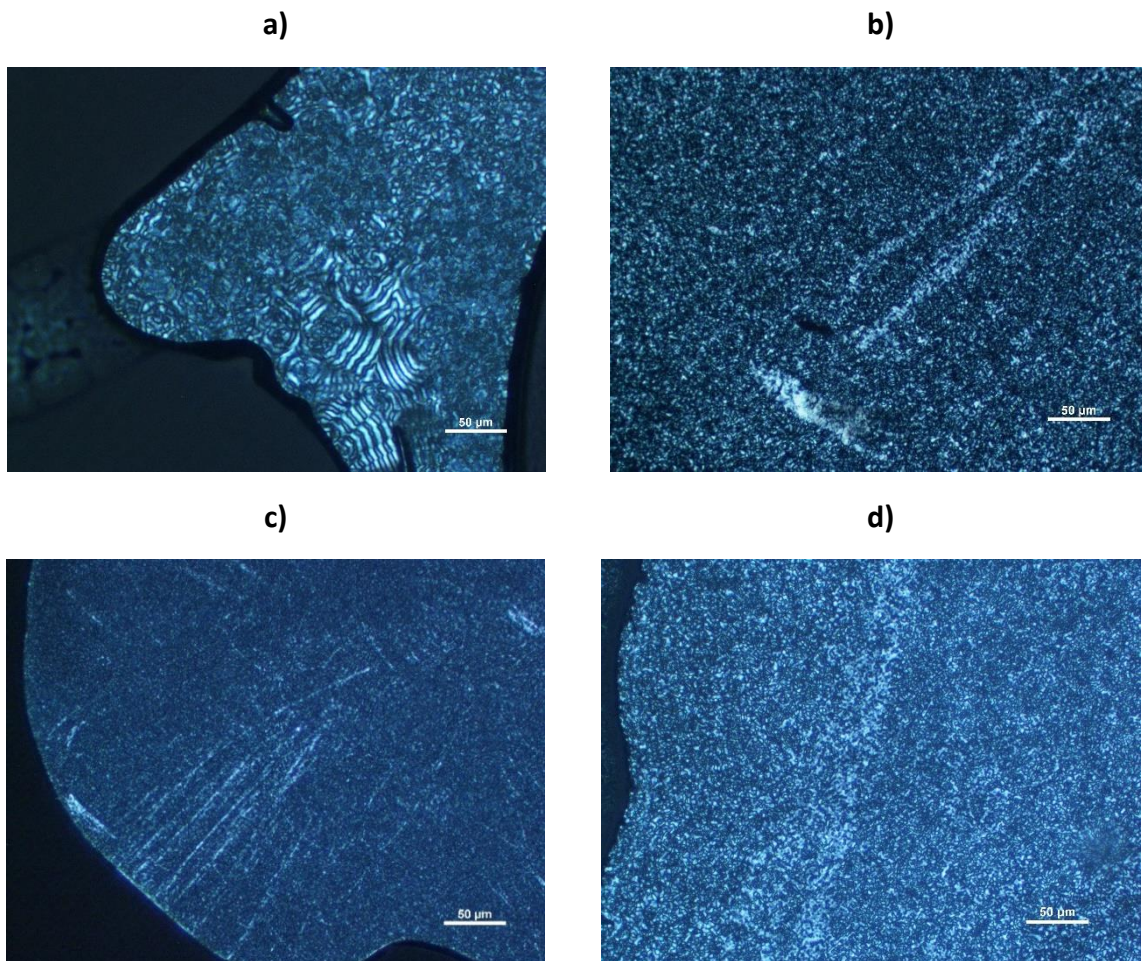


Figure IV.25. POM micrographs of **a)** PPCE after isothermal crystallization at 130 °C, **b)** PBCE after isothermal crystallization at 155 °C, **c)** PPeCE after isothermal crystallization at 40 °C, **d)** PHCE after isothermal crystallization at 110°C..

Eder's approximation states that the critical cooling rate is proportional to the ratio of the cubic root of the nuclei density at the maximum temperature rate over the width of the crystallization temperature's range over which crystallization occurs [51, 52]. As a result, for higher critical cooling rates and narrower crystallization temperature's ranges, higher nuclei density is expected. The formation of small spherulites with a high density can however be advantageous for mechanical properties, in particular impact strength, contrarily to large spherulitic materials as the ones developed by PHB and its close copolymers, which are in general more brittle and possess poor mechanical properties [53, 54]. PPCE forms larger structures akin to banded spherulites, that are not observed for the other PCHs. The presence of banded spherulites could be related to the regime behavior of nucleation [55] or to the distortion of the lamella during growth (twisting) [16]. **Figure IV.26** shows the POM micrographs of PPeCE centered on the same area after two iterations of the same protocol.

Similar profiles are obtained with higher reflectance occurring along preferential directions, and nucleation is therefore supposed to be mostly heterogeneous.

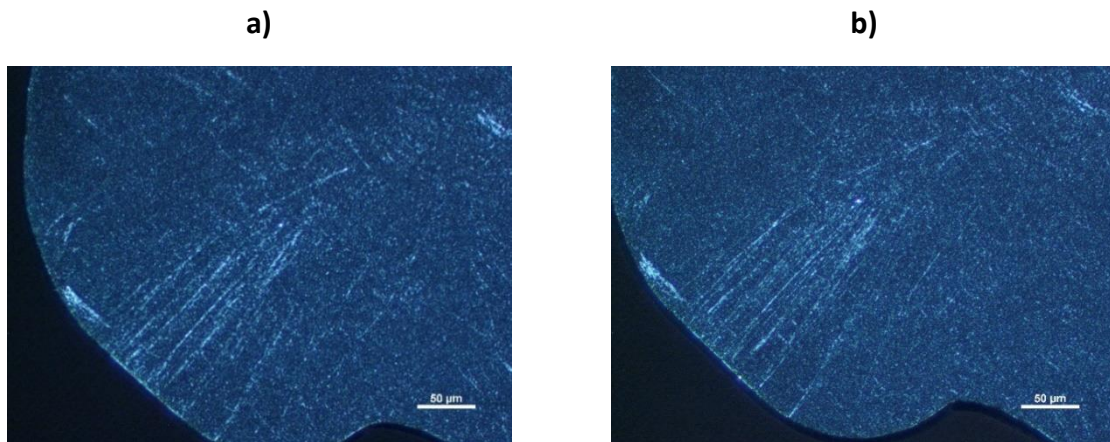


Figure IV.26. a) POM micrographs of PPeCE after isothermal crystallization at 40 °C. b) represents the micrograph of the same sample area after repetition of the same protocol.

III.4 Crystallization kinetics of PPeCE

Among the investigated PCHs, PPeCE is the only one that can be amorphized by melt-quenching with conventional DSC. The following section will therefore focus on the crystallization kinetics of PPeCE in isothermal conditions. The same thermal protocol presented in **Figure IV.23** was used with crystallization temperatures ranging from 20 °C to 40 °C and a crystallization time of one hour. The Avrami parameters extracted from **Figure IV.27** are reported in **Table IV.4**.

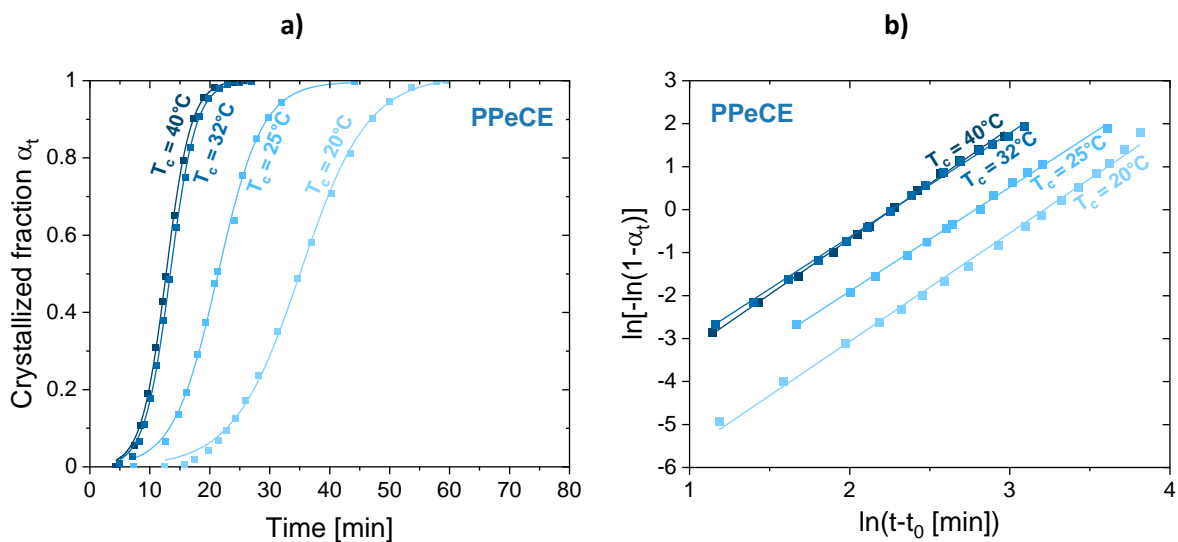
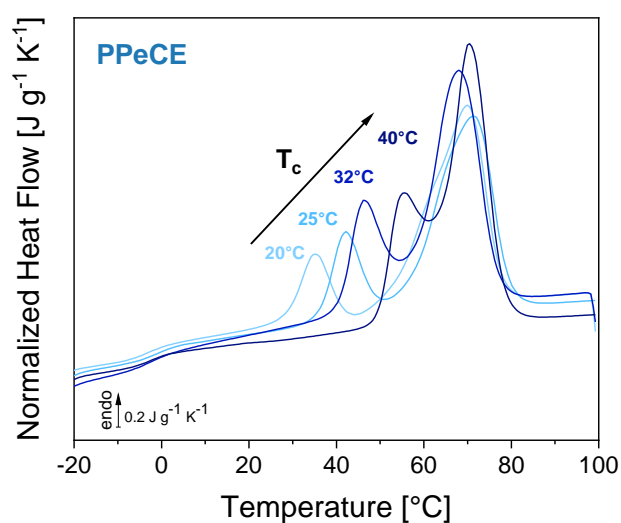


Figure IV.27. a) Evolution of the crystallization fraction α_t with time at different crystallization temperature T_c . b) Avrami plots at different T_c . The solid lines represent the linear regressions from Eq. 3.

Table IV.4. Avrami parameters corresponding to the isothermal crystallization of PPeCE at different T_c .

T_c [°C]	Avrami index n	K [min ⁻¹]
20	2.5	$3.0 \cdot 10^{-4}$
25	2.4	$1.2 \cdot 10^{-3}$
32	2.4	$4.2 \cdot 10^{-3}$
40	2.6	$2.9 \cdot 10^{-3}$

A characteristic sigmoidal time dependence of the crystallization fraction was obtained (**Figure IV.27.a**). With decreasing T_c , the crystallization time gets longer with lower rate constant K. No significant change in n is evidenced in **Table IV.4**, and fractioned values are obtained for all the investigated crystallization temperatures. The fastest growth rate is obtained for a crystallization temperature of 32 °C. The subsequent heating curves are shown in **Figure IV.28** and reports a double melting peak. The low-temperature endotherm is shifted to higher temperature with an increase in T_c , whereas the high-temperature endotherm is always found at 70 °C. This behavior is similar to the transition from the less ordered α' crystals to the more stable α crystals in PLLA [40]. During the α' -to- α transition the unit cell dimensions are reduced and chain conformations are adjusted to yield a more energy-favorable state [40]. Similar behavior is also observed in furan-based polyesters [56].

**Figure IV.28.** Normalized heat flows recorded upon heating at 30 K min⁻¹ on PPeCE after crystallization at temperatures ranging from 20 °C to 40 °C.

III.5 Time-Temperature-Transformation diagrams

TTT diagrams are commonly used in metallurgy, and to a less extent in polymer physics [57]. In order to get a better understanding of the different crystalline structures evidenced by the DRX spectra, and to test the critical cooling rates $\beta_{c,crit}$ estimated earlier in this work, Time-Temperature-Transformation (TTT) diagrams were established using a combination of FSC and DSC over a broad temperature range. The thermal protocol used is the same represented in **Figure IV.23** but adapted to FSC with a holding time of 0.01 s.

The kinetics of isothermal crystallization is generally evaluated directly from the heat flows recorded in isothermal conditions. POM micrographs showed that the high nucleation driving force leads to a high density of small spherulites, even at high temperature where the growth regime is prevalent. As a result, no exothermic peak is observable during isothermal crystallization measurements on FSC, essentially because of a low signal-to-noise ratio. However, as stated by Gradys et al. [32], crystallization is an exothermic process associated with heat release, and therefore the time-dependent monitoring of sample temperature (T_s) could also be used to pinpoint the time corresponding to the beginning of the crystallization process t_0 , which also depends on the crystallization temperature T_c . **Figure IV.29.a** and **Figure IV.29.b** show the time dependence of T_s during isothermal crystallization at 25 °C using FSC and DSC respectively, taking the example of PPeCE.

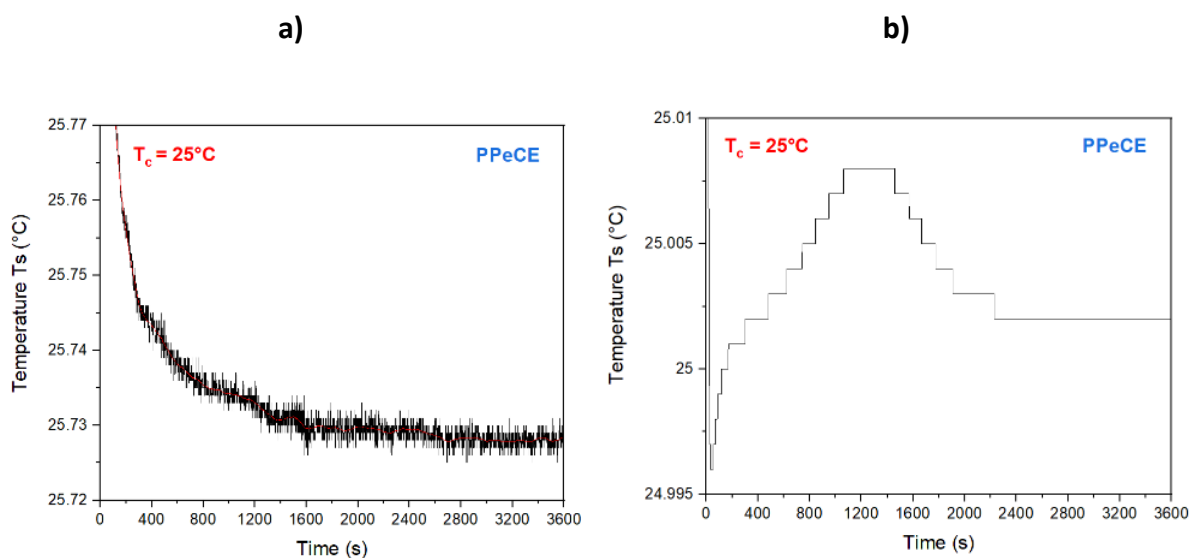


Figure IV.29. Time dependence of the sample temperature (T_s) during isothermal crystallization at 25 °C for **a)** FSC (sample mass of 46 ng) and **b)** DSC (sample mass of 10 mg).

The time dependence of the sample temperature correlates well with the exotherm recorded using DSC. However, the signal-to-noise ratio does not allow to pinpoint the beginning of the crystallization process with FSC. To evaluate the crystallization kinetics, different isothermal holds were therefore done at different temperatures depending on the material under study. The presence of a melting peak on the subsequent heating scan gives an estimation of the time needed for the material to crystallize for a given time t_c . The Time-Temperature-Transformation (TTT) diagrams obtained with this procedure are shown in **Figure IV.30**.

For PBCE, as seen in **Section II.1**, the maximum cooling rate used to build the diagram is below the critical cooling rate β_{CHG} necessary to obtain a chemically homogeneous glass, resulting in the formation of a self-doped glass, and therefore in self-nucleation, which can alter the characteristic times for crystal formation in comparison with a chemically homogeneous glass (as is the case for the other PCHs). Moreover, the short crystallization time (0.01 s) is close to the FSC time resolution. Nonetheless, a quite good agreement is achieved between DSC and FSC measurements, indicating that crystallization kinetics was not affected by the fact that very small sample masses have to be used for FSC experiments.

The TTT diagrams presented in **Figure IV.30** vary considerably depending on the number of methylene group in the repeating unit. All PCHs present a polymorphic character except for PPeCE. Hu et al. [8] reported at least two polymorphs for PBCE, one referred to as α -PBCE (triclinic unit cell) and the other referred to as β -PBCE (metastable), with the α form obtained either by slow cooling or stretching of the β form. In this work, the two polymorphs previously reported by Hu et al. [8] for PBCE are noted accordingly. For the other polyesters, for which no literature exists in terms of polymorphism, the phases are named HT and LT for high and low-temperature, respectively. As evidenced by TOPEM, the PCHs are prone to melt-recrystallization upon heating, enabling the perfection of the crystalline structures formed at low temperature (typically around ambient temperature in the case of the PCHs).

At low temperature, the PCHs have enough mobility to crystallize, even when the temperature is close to their respective T_g . Isothermal crystallizations performed on PBCE and PHCE at temperatures below their respective T_g show that nucleation is possible given enough time, and that once the aging of the amorphous phase is complete, nucleation could occur in a sequential way through six distinctive steps [58]: structural relaxation, nucleation or incubation period of nucleation, nuclei formation, crystallization toward a metastable crystalline phase, and finally perfection of the crystalline structure by crystal growth and polymorphic transformation to a more stable crystalline state. Finally, the star symbols correspond to the secondary crystallization observed during non-isothermal measurements,

and form a front that could indicate an additional ordered structure formed in high supercooling conditions.

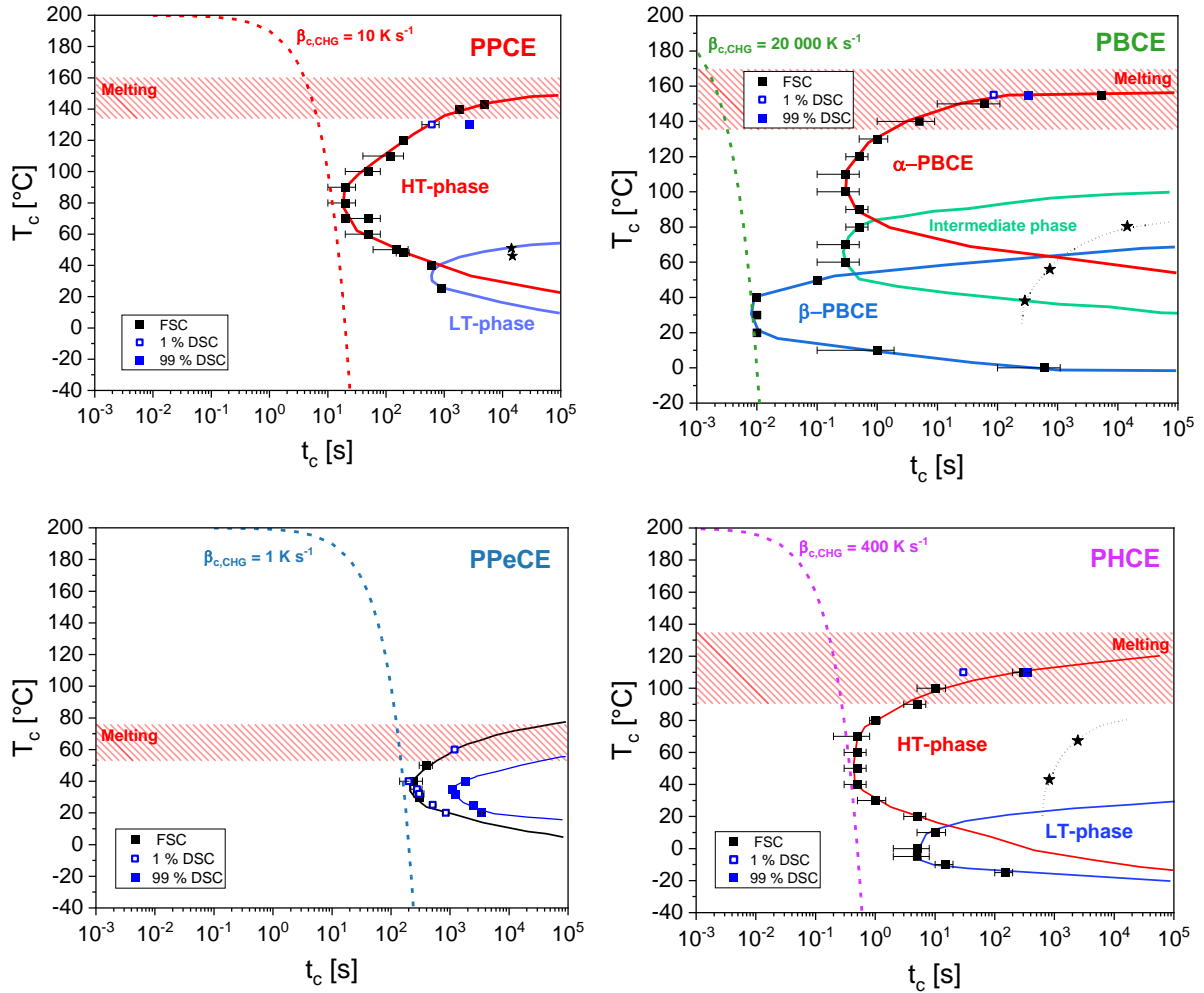


Figure IV.30. TTT diagrams obtained using a combination of FSC (black squares) with the DSC (blue squares) measurements reported in **Section III.3**. The empty and filled squares correspond to transformations of 1 % and 99 % respectively of the relative crystalline fraction α from the DSC isothermal crystallization. The stars symbols correspond to the secondary crystallization observed upon cooling from TOPEM and conventional DSC measurements. The lines were arbitrarily added to delimitate the various crystallization zones.

Conclusion

The combination of several calorimetric techniques with structural characterization techniques allows to get a good understanding of the microstructures formed by the PCHs under different conditions. The variation of the alkyl chain length from three to six methylene groups induces an odd-even effect impacting the melting and crystallization temperatures, but also the critical cooling rate and by extension the glass-forming ability. Stronger coupling between the amorphous and the crystalline phases is observed for even-numbered PCHs in comparison with their odd-numbered counterparts. X-ray diffractions evidenced the formation of different crystalline structures and confirmed the presence of different polymorphs for PBCE. TTT diagrams highlighted the existence of different polymorphs for PBCE (confirming the XRD results), but also for PPCE and PHCE. The analysis of the crystallization kinetics by calorimetry in association with POM showed the formation of tiny spherulites with a large density even at high temperature, and that PCHs crystallization is mainly driven by the nucleation regime. On a more applicative level, for purposes such as minimizing the cycle time for injection molding and yet developing a semi-crystalline microstructure, even-numbered PCHs would be preferable because of their high crystallization temperature and fast crystallization kinetics.

References

- [1] G. Fredi, A. Dorigato, M. Bortolotti, A. Pegoretti, and D. N. Bikiaris, "Mechanical and Functional Properties of Novel Biobased Poly(decylene-2,5-furanoate)/Carbon Nanotubes Nanocomposite Films," *Polymers*, vol. 12, no. 11, p. 2459, Oct. 2020, doi: 10.3390/polym12112459.
- [2] G. Z. Papageorgiou, V. Tsanaktsis, and D. N. Bikiaris, "Crystallization of poly(butylene-2,6-naphthalate-co-butylene adipate) copolymers: regulating crystal modification of the polymorphic parent homopolymers and biodegradation," *CrystEngComm*, vol. 16, no. 34, pp. 7963–7978, 2014, doi: 10.1039/C4CE00651H.
- [3] C. Berti, A. Celli, P. Marchese, E. Marianucci, G. Barbiroli, and F. D. Credico, "The effect of aliphatic chain length on thermal properties of poly(alkylene dicarboxylate)s," *e-Polymers*, vol. 7, no. 1, Dec. 2007, doi: 10.1515/epoly.2007.7.1.658.
- [4] L. Genovese, N. Lotti, M. Gazzano, L. Finelli, and A. Munari, "New eco-friendly random copolyesters based on poly(propylene cyclohexanedicarboxylate): Structure-properties relationships," *Express Polym. Lett.*, vol. 9, no. 11, Art. no. 11, 2015, doi: 10.3144/expresspolymlett.2015.88.
- [5] V. Siracusa, L. Genovese, C. Ingraio, A. Munari, and N. Lotti, "Barrier Properties of Poly(Propylene Cyclohexanedicarboxylate) Random Eco-Friendly Copolyesters," *Polymers*, vol. 10, no. 5, Art. no. 5, May 2018, doi: 10.3390/polym10050502.
- [6] G. Guidotti, M. Soccio, V. Siracusa, M. Gazzano, A. Munari, and N. Lotti, "Novel Random Copolymers of Poly(butylene 1,4-cyclohexane dicarboxylate) with Outstanding Barrier Properties for Green and Sustainable Packaging: Content and Length of Aliphatic Side Chains as Efficient Tools to Tailor the Material's Final Performance," *Polymers*, vol. 10, no. 8, Art. no. 8, Aug. 2018, doi: 10.3390/polym10080866.
- [7] G. Guidotti *et al.*, "Chemical Modification of Poly(butylene trans-1,4-cyclohexanedicarboxylate) by Camphor: A New Example of Bio-Based Polyesters for Sustainable Food Packaging," *Polymers*, vol. 13, no. 16, p. 2707, Aug. 2021, doi: 10.3390/polym13162707.
- [8] W. Hu *et al.*, "Crystal Structure and Polymorphism of Poly(butylene- trans -1,4-cyclohexane dicarboxylate)," *Macromolecules*, vol. 57, no. 9, pp. 4374–4384, May 2024, doi: 10.1021/acs.macromol.4c00234.
- [9] J. S. Gaffney, N. A. Marley, and D. E. Jones, "Fourier Transform Infrared (FTIR) Spectroscopy," in *Characterization of Materials*, 1st ed., E. N. Kaufmann, Ed., Wiley, 2012, pp. 1–33. doi: 10.1002/0471266965.com107.pub2.
- [10] R. A. Pérez-Camargo *et al.*, "Even–Odd Effect in Aliphatic Polycarbonates with Different Chain Lengths: from Poly (Hexamethylene Carbonate) to Poly (Dodecamethylene Carbonate)," *Macromolecules*, vol. 54, no. 1, pp. 259–271, Jan. 2021, doi: 10.1021/acs.macromol.0c02374.
- [11] A. A. Cuadri and J. E. Martín-Alfonso, "Thermal, thermo-oxidative and thermomechanical degradation of PLA: A comparative study based on rheological, chemical and thermal properties," *Polymer Degradation and Stability*, vol. 150, pp. 37–45, Apr. 2018, doi: 10.1016/j.polymdegradstab.2018.02.011.
- [12] B. G. Girija, R. R. N. Sailaja, and G. Madras, "Thermal degradation and mechanical properties of PET blends," *Polymer Degradation and Stability*, vol. 90, no. 1, pp. 147–153, Oct. 2005, doi: 10.1016/j.polymdegradstab.2005.03.003.
- [13] "Aurélie Bourdet. Relationship between the structure and the physical properties of polymers based on furandicarboxylic acid obtained from biomass. Materials Science [cond-mat.mtrl-sci]. Normandie Université, 2020. English. (NNT : 2020NORMR113). (tel-03376525)."
- [14] G. Z. Papageorgiou, D. G. Papageorgiou, V. Tsanaktsis, and D. N. Bikiaris, "Synthesis of the bio-based polyester poly(propylene 2,5-furan dicarboxylate). Comparison of thermal behavior and solid state structure with its terephthalate and naphthalate homologues," *Polymer*, vol. 62, pp. 28–38, Apr. 2015, doi: 10.1016/j.polymer.2015.01.080.
- [15] O. Wachsen, K. Platkowski, and K.-H. Reichert, "Thermal degradation of poly-l-lactide—studies on kinetics, modelling and melt stabilisation," *Polymer Degradation and Stability*, vol. 57, no. 1, pp. 87–94, Jul. 1997, doi: 10.1016/S0141-3910(96)00226-1.
- [16] C. Zhou *et al.*, "Biobased long-chain aliphatic polyesters of 1,12-dodecanedioic acid with a variety of diols: Odd-even effect and mechanical properties," *Materials Today Communications*, vol. 19, pp. 450–458, Jun. 2019, doi: 10.1016/j.mtcomm.2019.05.005.
- [17] T. Masubuchi, M. Sakai, K. Kojio, M. Furukawa, and T. Aoyagi, "Structure and Properties of Aliphatic Poly(carbonate) glycols with Different Methylene Unit Length," *e-J. Soft Mater.*, vol. 3, pp. 55–63, 2007, doi: 10.2324/ejsm.3.55.

- [18] M. J. Duer and C. Roper, "A solid-state NMR investigation of the odd–even effect in a series of liquid-crystal dimers," *Phys. Chem. Chem. Phys.*, vol. 5, no. 14, pp. 3034–3041, 2003, doi: 10.1039/B303475P.
- [19] I. Flores *et al.*, "Unexpected Structural Properties in the Saturation Region of the Odd–Even Effects in Aliphatic Polyethers: Influence of Crystallization Conditions," *Macromolecules*, p. acs.macromol.1c02235, Jan. 2022, doi: 10.1021/acs.macromol.1c02235.
- [20] Y. Furushima, S. Kumazawa, H. Umetsu, A. Toda, E. Zhuravlev, and C. Schick, "Melting and recrystallization kinetics of poly(butylene terephthalate)," *Polymer*, vol. 109, pp. 307–314, Jan. 2017, doi: 10.1016/j.polymer.2016.12.053.
- [21] Y. Furushima, C. Schick, and A. Toda, "Crystallization, recrystallization, and melting of polymer crystals on heating and cooling examined with fast scanning calorimetry," *Polymer Crystallization*, vol. 1, no. 2, Aug. 2018, doi: 10.1002/pcr2.10005.
- [22] J. A. S. Puente, A. Esposito, F. Chivrac, and E. Dargent, "Effect of boron nitride as a nucleating agent on the crystallization of bacterial poly(3-hydroxybutyrate)," *J of Applied Polymer Sci*, vol. 128, no. 5, pp. 2586–2594, Jun. 2013, doi: 10.1002/app.38182.
- [23] J. A. S. Puente, A. Esposito, F. Chivrac, and E. Dargent, "Effects of Size and Specific Surface Area of Boron Nitride Particles on the Crystallization of Bacterial Poly(3-hydroxybutyrate- *co* -3-hydroxyvalerate)," *Macromolecular Symposia*, vol. 328, no. 1, pp. 8–19, Jun. 2013, doi: 10.1002/masy.201350601.
- [24] Y. Kong and J. N. Hay, "Multiple melting behaviour of poly(ethylene terephthalate)," *Polymer*, vol. 44, no. 3, pp. 623–633, Jan. 2003, doi: 10.1016/S0032-3861(02)00814-5.
- [25] N. Herrera, A. M. Salaberria, A. P. Mathew, and K. Oksman, "Plasticized polylactic acid nanocomposite films with cellulose and chitin nanocrystals prepared using extrusion and compression molding with two cooling rates: Effects on mechanical, thermal and optical properties," *Composites Part A: Applied Science and Manufacturing*, vol. 83, pp. 89–97, Apr. 2016, doi: 10.1016/j.compositesa.2015.05.024.
- [26] J. E. K. Schawe and J. F. Löffler, "Existence of multiple critical cooling rates which generate different types of monolithic metallic glass," *Nat Commun*, vol. 10, no. 1, p. 1337, Mar. 2019, doi: 10.1038/s41467-018-07930-3.
- [27] J. C. A. Martins, K. M. Novack, and A. S. Gomes, "Non-isothermal crystallization kinetics of thermotropic polyesters with flexible spacers in the main chain," *Polymer*, vol. 39, no. 26, pp. 6941–6944, Dec. 1998, doi: 10.1016/S0032-3861(98)00158-X.
- [28] D. Heidrich and M. Gehde, "The 3-Phase Structure of Polyesters (PBT, PET) after Isothermal and Non-Isothermal Crystallization," *Polymers*, vol. 14, no. 4, p. 793, Feb. 2022, doi: 10.3390/polym14040793.
- [29] A. Wurm *et al.*, "Crystallization and Homogeneous Nucleation Kinetics of Poly(ϵ -caprolactone) (PCL) with Different Molar Masses," *Macromolecules*, vol. 45, no. 9, pp. 3816–3828, May 2012, doi: 10.1021/ma300363b.
- [30] J. M. Barandiarán and J. Colmenero, "Continuous cooling approximation for the formation of a glass," *Journal of Non-Crystalline Solids*, vol. 46, no. 3, pp. 277–287, Dec. 1981, doi: 10.1016/0022-3093(81)90006-5.
- [31] Y. Chen, K. Xie, Y. He, and W. Hu, "Fast-Scanning Chip-Calorimetry Measurement of Crystallization Kinetics of Poly(Glycolic Acid)," *Polymers*, vol. 13, no. 6, p. 891, Mar. 2021, doi: 10.3390/polym13060891.
- [32] A. Gradys, P. Sajkiewicz, E. Zhuravlev, and C. Schick, "Kinetics of isothermal and non-isothermal crystallization of poly(vinylidene fluoride) by fast scanning calorimetry," *Polymer*, vol. 82, pp. 40–48, Jan. 2016, doi: 10.1016/j.polymer.2015.11.020.
- [33] F. Kagawa and H. Oike, "Quenching of Charge and Spin Degrees of Freedom in Condensed Matter," *Advanced Materials*, vol. 29, no. 25, p. 1601979, Jul. 2017, doi: 10.1002/adma.201601979.
- [34] T. A. Mukhametzhanov, R. A. Andrianov, D. N. Bolmatenkov, M. I. Yagofarov, B. N. Solomonov, and C. Schick, "Nucleation and crystallization of deeply supercooled benzocaine, a rapidly crystallizing organic compound: A Fast scanning calorimetry investigation," *Thermochimica Acta*, vol. 730, p. 179613, Dec. 2023, doi: 10.1016/j.tca.2023.179613.
- [35] D. G. Papageorgiou *et al.*, "Fast Crystallization and Melting Behavior of a Long-Spaced Aliphatic Furandicarboxylate Biobased Polyester, Poly(dodecylene 2,5-furanoate)," *Ind. Eng. Chem. Res.*, vol. 55, no. 18, pp. 5315–5326, May 2016, doi: 10.1021/acs.iecr.6b00811.
- [36] M. Salmerón Sánchez, V. B. F. Mathot, G. Vanden Poel, and J. L. Gómez Ribelles, "Effect of the Cooling Rate on the Nucleation Kinetics of Poly(L-Lactic Acid) and Its Influence on Morphology," *Macromolecules*, vol. 40, no. 22, pp. 7989–7997, Oct. 2007, doi: 10.1021/ma0712706.
- [37] G. Stoclet, G. Gobius du Sart, B. Yeniad, S. de Vos, and J. M. Lefebvre, "Isothermal crystallization and structural characterization of poly(ethylene-2,5-furanoate)," *Polymer*, vol. 72, pp. 165–176, Aug. 2015, doi: 10.1016/j.polymer.2015.07.014.

- [38] J. D. Hoffman and J. J. Weeks, "Rate of Spherulitic Crystallization with Chain Folds in Polychlorotrifluoroethylene," *The Journal of Chemical Physics*, vol. 37, no. 8, pp. 1723–1741, Oct. 1962, doi: 10.1063/1.1733363.
- [39] Clément Fosse, Antonella Esposito, Massima Gazzano, Nadia Lotti, and Michelina Soccio, "thermal characterization of a series of poly(alkylene *trans*-1,4-cyclohexanedicarboxylate)s" under preparation.
- [40] M. C. Righetti and E. Tombari, "Crystalline, mobile amorphous and rigid amorphous fractions in poly(L-lactic acid) by TMDSC," *Thermochimica Acta*, vol. 522, no. 1–2, pp. 118–127, Aug. 2011, doi: 10.1016/j.tca.2010.12.024.
- [41] J. Chen *et al.*, "Structural evolutions of the amorphous fraction of polyethylene terephthalate during the secondary crystallization," *Polymer*, vol. 253, p. 124987, Jun. 2022, doi: 10.1016/j.polymer.2022.124987.
- [42] T. Ozawa, "Kinetics of non-isothermal crystallization," *Polymer*, vol. 12, no. 3, pp. 150–158, Mar. 1971, doi: 10.1016/0032-3861(71)90041-3.
- [43] A. Toda, Y. Furushima, and C. Schick, "Crystal Domains and Crystallization Kinetics of Poly(butylene terephthalate)," *Macromolecules*, vol. 56, no. 17, pp. 6891–6902, Sep. 2023, doi: 10.1021/acs.macromol.3c01081.
- [44] J. E. K. Schawe, "Comments on isothermal crystallization kinetics of polymers: Polypropylene at high supercooling," *Thermochimica Acta*, vol. 718, p. 179370, Dec. 2022, doi: 10.1016/j.tca.2022.179370.
- [45] G. Strobl, "From the melt via mesomorphic and granular crystalline layers to lamellar crystallites: A major route followed in polymer crystallization?," *The European Physical Journal E*, vol. 3, no. 2, pp. 165–183, Oct. 2000, doi: 10.1007/s101890070030.
- [46] T. Konishi, K. Nishida, and T. Kanaya, "Crystallization of Isotactic Polypropylene from Prequenched Mesomorphic Phase," *Macromolecules*, vol. 39, no. 23, pp. 8035–8040, Nov. 2006, doi: 10.1021/ma060191b.
- [47] Q. Ding *et al.*, "Smectic liquid crystal Schlieren texture in rapidly cooled poly(butylene naphthalate)," *European Polymer Journal*, vol. 101, pp. 90–95, Apr. 2018, doi: 10.1016/j.eurpolymj.2018.02.010.
- [48] A. Celli, P. Marchese, S. Sullalti, C. Berti, and G. Barbiroli, "Eco-friendly Poly(butylene 1,4-cyclohexanedicarboxylate): Relationships Between Stereochemistry and Crystallization Behavior," *Macro Chemistry & Physics*, vol. 212, no. 14, pp. 1524–1534, Jul. 2011, doi: 10.1002/macp.201100052.
- [49] M. Gigli, N. Lotti, M. Vercellino, L. Visai, and A. Munari, "Novel ether-linkages containing aliphatic copolyesters of poly(butylene 1,4-cyclohexanedicarboxylate) as promising candidates for biomedical applications," *Materials Science and Engineering: C*, vol. 34, pp. 86–97, Jan. 2014, doi: 10.1016/j.msec.2013.08.013.
- [50] G. Z. Papageorgiou, V. Tsanaktis, and D. N. Bikiaris, "Synthesis of poly(ethylene furandicarboxylate) polyester using monomers derived from renewable resources: thermal behavior comparison with PET and PEN," *Phys. Chem. Chem. Phys.*, vol. 16, no. 17, pp. 7946–7958, 2014, doi: 10.1039/C4CP00518J.
- [51] H. Janeschitz-Kriegl, G. Eder, M. Stadlbauer, and E. Ratajski, "A Thermodynamic Frame for the Kinetics of Polymer Crystallization under Processing Conditions," *Monatshefte für Chemie*, vol. 136, no. 7, pp. 1119–1137, Jul. 2005, doi: 10.1007/s00706-005-0328-5.
- [52] E. Zhuravlev, V. Madhavi, A. Lustiger, R. Androsch, and C. Schick, "Crystallization of Polyethylene at Large Undercooling," *ACS Macro Lett.*, vol. 5, no. 3, pp. 365–370, Mar. 2016, doi: 10.1021/acsmacrolett.5b00889.
- [53] A. El-Hadi, R. Schnabel, E. Straube, G. Müller, and S. Henning, "Correlation between degree of crystallinity, morphology, glass temperature, mechanical properties and biodegradation of poly(3-hydroxyalkanoate) PHAs and their blends," *Polymer Testing*, vol. 21, no. 6, pp. 665–674, 2002, doi: 10.1016/S0142-9418(01)00142-8.
- [54] A. Esposito, N. Delpouve, V. Causin, A. Dhotel, L. Delbreilh, and E. Dargent, "From a Three-Phase Model to a Continuous Description of Molecular Mobility in Semicrystalline Poly(hydroxybutyrate-co-hydroxyvalerate)," *Macromolecules*, vol. 49, no. 13, pp. 4850–4861, Jul. 2016, doi: 10.1021/acs.macromol.6b00384.
- [55] P.-D. Hong, W.-T. Chung, and C.-F. Hsu, "Crystallization kinetics and morphology of poly(trimethylene terephthalate)," *Polymer*, vol. 43, no. 11, pp. 3335–3343, May 2002, doi: 10.1016/S0032-3861(02)00163-5.
- [56] C. Fosse *et al.*, "Cooperativity and fragility in furan-based polyesters with different glycolic subunits as compared to their terephthalic counterparts," *Journal of Non-Crystalline Solids*, vol. 597, p. 121907, Dec. 2022, doi: 10.1016/j.jnoncrysol.2022.121907.
- [57] M. Frey *et al.*, "Determining and modelling a complete time-temperature-transformation diagram for a Pt-based metallic glass former through combination of conventional and fast scanning calorimetry," *Scripta Materialia*, vol. 215, p. 114710, Jul. 2022, doi: 10.1016/j.scriptamat.2022.114710.

- [58] J. E. K. Schawe and J. F. Löffler, "Kinetics of structure formation in the vicinity of the glass transition," *Acta Materialia*, vol. 226, p. 117630, Mar. 2022, doi: 10.1016/j.actamat.2022.117630.

Chapter V – Molecular mobility of the amorphous phase

Parts of this chapter are extracted from:

K. Hallavant, M. Mejres, J.E.K Schawe, A. Esposito, A. Saiter-Fourcin, Influence of chemical composition and structure on the cooperative fluctuation in supercooled glass-forming liquids, *J. Phys. Chem. Lett.* (2024) 15, 4508-4514

Content

I. Glass transition kinetics of poly (lactic acid)	158
I.1. Vitrification function.....	159
I.2. Fragility index	160
I.3. Temperature fluctuation δT	162
I.4. Characteristic length ξ_α	164
I.5. Frequency dependence of the glass transition temperature.....	165
I.6 Comparison between calorimetric and dielectric relaxation spectroscopy experiments.....	167
II. Glass transition kinetics of the PCHs	167
II.1 Vitrification function.....	168
II.2 Fragility index	169
II.3 Characteristic length ξ_α	171
III. Towards a generalization of the temperature dependence of ξ_α?	177
Conclusion.....	181

This last chapter aims at giving some insight in the molecular dynamics of the amorphous phase of the PCHs, first through the concept of fragility introduced by Angell, and then by the application of Donth's approach to investigate the cooperativity over a broad range of cooling rates (from 10^{-3} up to 10^4 K s⁻¹). The fragility index and the characteristic length of the Cooperative Rearranging Regions (CRR) will be estimated for a "model" polyester, poly (lactic acid) (PLA), which has already been extensively studied in the literature. The soundness of this new method will be tested and the fragility index will be confronted to the one found in the literature. Then this calorimetric method will be applied to the PCHs and the obtained results will be compared with similar systems, such as the terephthalic-based and furan-based polyesters, to get a better understanding of the impact of both the acidic unit and the alkyl chain length on the relaxation of the amorphous phase with and without the influence of a crystalline phase.

I. Glass transition kinetics of poly (lactic acid)

As mentioned in **Chapter I**, the properties of glass-forming liquids are commonly described by the concept of Cooperative Rearranging Regions (CRR) proposed by Adam and Gibbs, in which a CRR is defined as the smallest subsystem where relaxing units can reorganize without affecting their neighbors. The CRR can be characterized by their size (cooperative volume V_α or characteristic length ξ_α) or by the number of relaxing units they contain (N_α). The knowledge of these characteristics is deemed of outstanding importance to understand both thermodynamic and kinetic properties of the systems under consideration [1], and a special attention has been paid to the experimental methods allowing their determination. Though many techniques have been employed such as Dynamic Mechanical Analysis (DMA), Dielectric Relaxation Spectroscopy (DRS) or Atomic Force Microscopy (AFM), the most well-known is Donth's approach with calorimetry, which relies on the analysis of the shape of the thermal relaxation spectrum given the hypothesis of temperature fluctuations δT . However, most of the available calorimetric methods (Heat Capacity Spectroscopy (HCS), Modulated-Temperature Differential Scanning Calorimetry (MT-DSC)) rely on relatively slow scanning rates that can involve microstructures changes in the case of fast crystallizing systems. As evidenced by Hamonic et al., the presence of a crystalline phase can modify the temperature dependence of the relaxation time $\tau(t)$ and the number of relaxing units N_α in a CRR [2, 3]. This experimental limitation can be a major issue if one desires to probe the molecular dynamics of the amorphous phase without interference from a crystalline phase, which can be of interest especially for applications requiring high cooling rate processing, as mentioned in **Chapter III**. To overcome this challenge, a new method relying on Fast Scanning Calorimetry (FSC) has been tested to estimate the temperature dependence of the characteristic length ξ_α . The high scanning rates provided by FSC (up to 10^4 K s^{-1}) make it possible to quench to the fully amorphous state fast crystallizing materials with high $\beta_{c,crit}$ as is the case for the PCHs. This method will first be tested on a "model" polyester, poly (lactic acid) (PLA), which has been extensively studied in the literature. On a second hand it will be applied to the PCHs. For that two prerequisites are needed:

-Because the definition of the relaxing unit has been debated [4] and is by convenience often taken as the repeating unit, only the characteristic length will be investigated, and no assumption will be made on the relaxing unit.

- The measurements will be done upon cooling, to avoid the presence of a recovering peak that could deform the thermal spectrum. However, because of the high cooling rates involved, it will

be necessary to take into account smearing effects due to vitrification, that could also distort the glass transition.

I.1. Vitrification function

The PLA sample was cooled down from 150 °C to -95 °C with cooling rates $|\beta_c|$ between 1 and 15,000 K s⁻¹, and a heating scan was subsequently recorded with $\beta_h = |\beta_c|$. The limiting fictive temperature T_f , which is the temperature that best describes the glass transition, was determined from both the cooling and the heating curves [5]. Data reproducibility and sample stability were ensured by comparing the results obtained with the same thermal cycle before and after each series of measurements [6]. Correction of the smearing effect was realized following the procedure described in **Chapter II**. The corrected and normalized heat flow recorded upon cooling at different cooling rates is shown in **Figure V.1**:

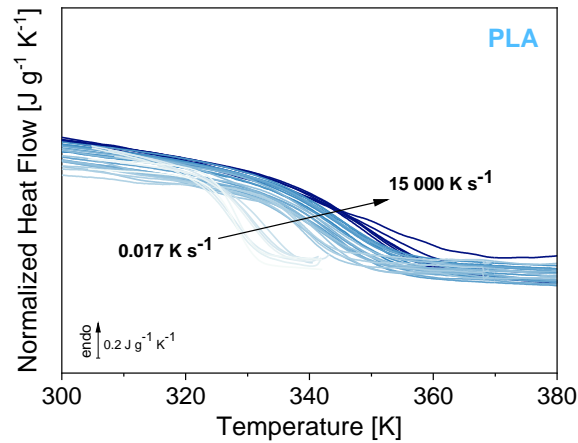


Figure V.1. Corrected and normalized heat flow measured upon cooling through the glass transition with cooling rates ranging from 0.017 up to 15 000 K s⁻¹.

The width of the dynamic glass transition ΔT_ω measured upon cooling at a frequency ω is related to the temperature fluctuation as $\Delta T_\omega \approx 2 \delta T$ [7]. The temperature fluctuation δT is usually estimated from heat capacity spectroscopy or MT-DSC, but δT can also be measured from the shape of the heat flow curve recorded upon cooling at a constant rate β_c . Due to the non-linearity of the vitrification process, which occurs through a progressive viscous slowing down of molecular motions, the width ΔT_{β_c} is broader than the width ΔT_ω . To describe this effect, Schawe et al. introduced the vitrification function κ [7]:

$$\kappa(T) = \frac{\Delta T_{\beta_c}(T)}{\Delta T_\omega(T)} \quad \text{Eq. 1}$$

The cooling-rate dependence of ΔT_{β_c} was evaluated for PLA (**Figure V.2.a**). Measurements performed on polystyrene had previously suggested that κ is invariant with respect to temperature ($\kappa \approx 2.5$) [7]. The vitrification function was therefore calculated over the entire range of cooling rates for PLA (**Figure V.2.b**). The obtained value ($\kappa \approx 1.4$) is indeed constant, but smaller than the one previously reported for polystyrene [7]. Knowing κ , the temperature fluctuation δT can be accurately estimated from the cooling curves by:

$$\delta T = \frac{\Delta T_{\beta_c}}{2 \kappa} \quad \text{Eq. 2}$$

This method was previously used, but assuming an estimated value of κ [8]. However, the experimental determination of κ is essential for this method, due to the significant influence of δT on ξ_α .

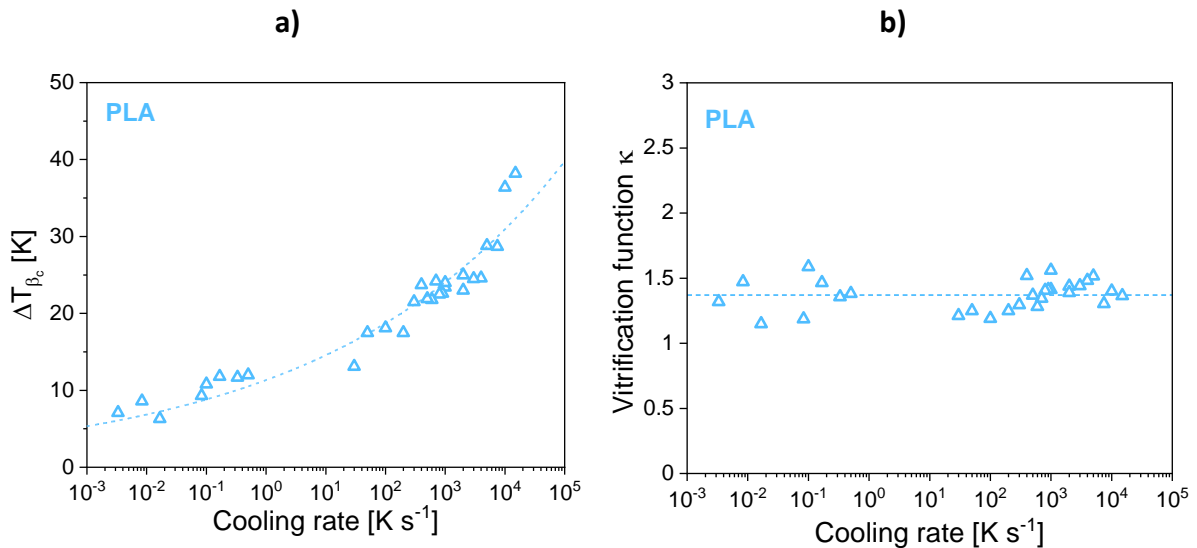


Figure V.2. a) Cooling-rate dependence of the glass transition width ΔT_{β_c} for PLA (blue triangles). The dotted line is a guide to the eye. **b)** Cooling-rate dependence of the vitrification function κ . The dotted line corresponds to the mean value.

1.2. Fragility index

The Frenkel-Kobeko-Reiner (FKR) hypothesis considers that the cooling-rate dependence of the vitrification is analogous to the frequency dependence of the thermal relaxation [7]. The determination of the fragility index m can thus be done through the glass transition temperature shifts induced by a variation of the cooling rate. The correlation between the cooling-rate dependence of T_g and the temperature dependence of the equilibrium liquid viscosity or relaxation time can be expressed with the FKR relationship:

$$|\beta_c| \tau = C \quad \text{Eq. 3}$$

where τ is the relaxation time and C is a constant. In the logarithmic form, **Eq. 3** becomes:

$$\log (|\beta_c|) = \log \left(\frac{1}{\tau} \right) + \log(C) \quad \text{Eq. 4}$$

Assuming the FKR hypothesis, the cooling-rate dependence of the glass transition follows the Vogel-Fulcher-Tammann (VFT) equation:

$$\log (|\beta_c|) = A_\beta - \frac{B}{T_g - T_v} \quad \text{Eq. 5}$$

where A_β and B are fitting parameters, and T_v is the Vogel temperature below T_g . This relation has been verified for various materials [9-11]. The concept of fragility introduced by Angell [12] is commonly used to describe the deceleration of the relaxation dynamics in a glass-forming liquid approaching its glass transition. The cooling-rate dependence of the glass transition can therefore be used to estimate the fragility index m based on the VFT equation:

$$m = \left[\frac{d(\log|\beta_c|)}{d\left(\frac{T_g}{T}\right)} \right]_{T=T_g} = \frac{B T_g}{(T_g - T_v)^2} \quad \text{Eq. 6}$$

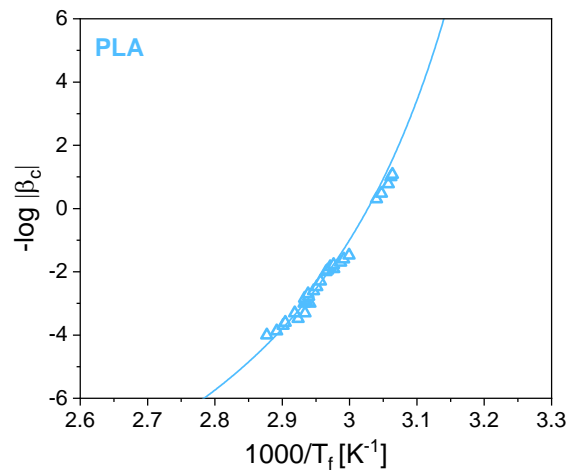


Figure V.3. Cooling-rate dependence of the limiting fictive temperature. The solid line corresponds to the VFT fit.

The cooling-rate dependence of the limiting fictive temperature T_f obtained with different cooling rates is plotted in **Figure V.3** accompanied by the VFT fitting curve (the corresponding fitting parameters are listed in **Table V.1**). The fragility index obtained is 139, which agrees well with the data reported in the literature (144 for amorphous PLA [4]).

Table V.1. Thermal glass transition temperature (T_g), VFT fitting parameters (A , B and T_v), and Angell's fragility index (m) measured for PLA.

Material	T_g (K)	A	B (K)	T_v (K)	m
PLA	327 ± 1	14.4	580	290 ± 10	139 ± 11

I.3. Temperature fluctuation δT

The presence of temperature fluctuation is a question that has been studied for a long time [1, 13]. The temperature fluctuation as described by the Von Laue approach to thermodynamics [14] is used to derive the characteristic length ξ_α and is thus an important parameter which has been studied for the last decades [15, 16].

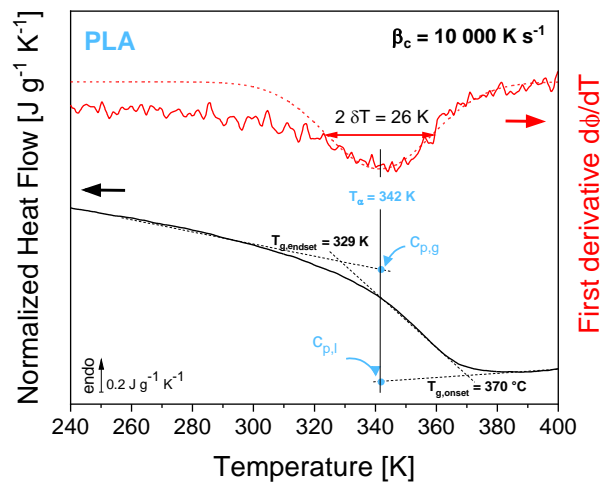


Figure V.4. Normalized heat flow measured at a cooling rate $|\beta_c| = 10\,000\text{ K s}^{-1}$ (black curve) and first derivative of the normalized heat flow with respect to temperature (red curve). The dotted red line is the Gaussian function used to estimate δT .

The peak on the first derivative of the normalized heat flow is approximated by a Gaussian curve:

$$\frac{dc_p}{dT} = \text{const.} \exp \left[\frac{-(-T - T_\alpha)^2}{2 \delta T^2} \right] \quad \text{Eq. 7}$$

where δT is determined as the dispersion of this approximation [17]. In correspondence with the linear response theory, the temperature of the maximum on the first derivative of the normalized heat flow with respect to temperature is taken as the characteristic temperature for the relaxation process T_α [18]. **Figure V.4** shows the estimation of δT from the first derivative of the normalized heat flow with respect to temperature for a cooling rate of $10\,000 \text{ K s}^{-1}$. The vitrification effect is notable on the symmetry of the first derivative, and more particularly on the low temperature wing. Similar observation was made in the out-of-phase component of the specific heat capacity by Saiter et al. [19]. This vitrification effect, which is due to a partial and progressive freezing-in of the glass-forming liquid, can be overcome by evaluating the glass transition with a modified Narayanaswamy-Moynihan (MNM) procedure [17, 20]. The decoupling between vitrification and molecular mobility was also recently evidenced by Monnier et al. [21, 22].

To circumvent this issue, the dispersion on the left side is taken as the symmetric of the right-hand side of the glass transition, thus approximating the whole shape of the dynamic α relaxation. The cooling-rate dependence of δT is represented in **Figure V.5.a**. The temperature dependence of δT shown in **Figure V.5.b** can be described using the VFT parameters B and T_v [7]:

$$\delta T(T) = \frac{\delta q (T - T_v)^2}{B \ln 10} \quad \text{Eq. 8}$$

The fitting parameter δq characterizes the logarithmic frequency width of the thermal α -relaxation spectrum in the supercooled liquid. The fitting curve in **Figure V.5.b** provides a value of δq equal to 3.2 for PLA. The relaxation spectrum is often described by the Fourier-transformed relaxation function ϕ containing a stretched exponential:

$$\phi(t) = \exp \left(\left(-\frac{t}{\tau_k} \right)^{\beta_k} \right) \quad \text{Eq. 9}$$

where τ_k is the characteristic relaxation time and β_k is the Kohlrausch exponent. These parameters are related to each other, and their relation can be approximated as $\delta q \approx 1.07/\beta_k$ [23].

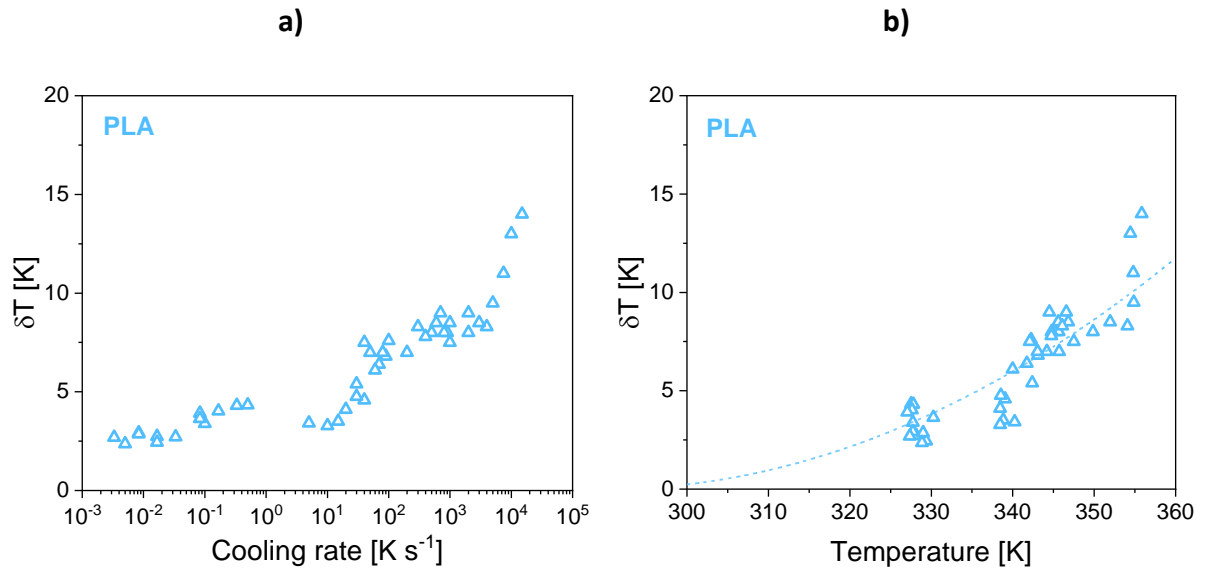


Figure V.5. a) Cooling-rate dependence and b) temperature dependence of the temperature fluctuation δT for PLA. The dotted line represents the fit using Eq. 8.

I.4. Characteristic length ξ_α

Assuming a spherical shape for the CRR, the characteristic length of the α -relaxation ξ_α can be calculated as:

$$\xi_\alpha = \left(\frac{6}{\pi} V_\alpha \right)^{\frac{1}{3}} \quad \text{Eq. 10}$$

The formula for the estimation of a CRR volume, V_α , is given in **Chapter I (Section II.2.2)**.

Figures V.6.a and **V.6.b** show the variations of ξ_α with cooling rate and temperature, respectively. As expected, ξ_α decreases when the cooling rate used for vitrification increases. The cooperativity length increases as T_g is approached from the supercooled liquid-like state, whereas at high temperatures it flattens down to a constant value.

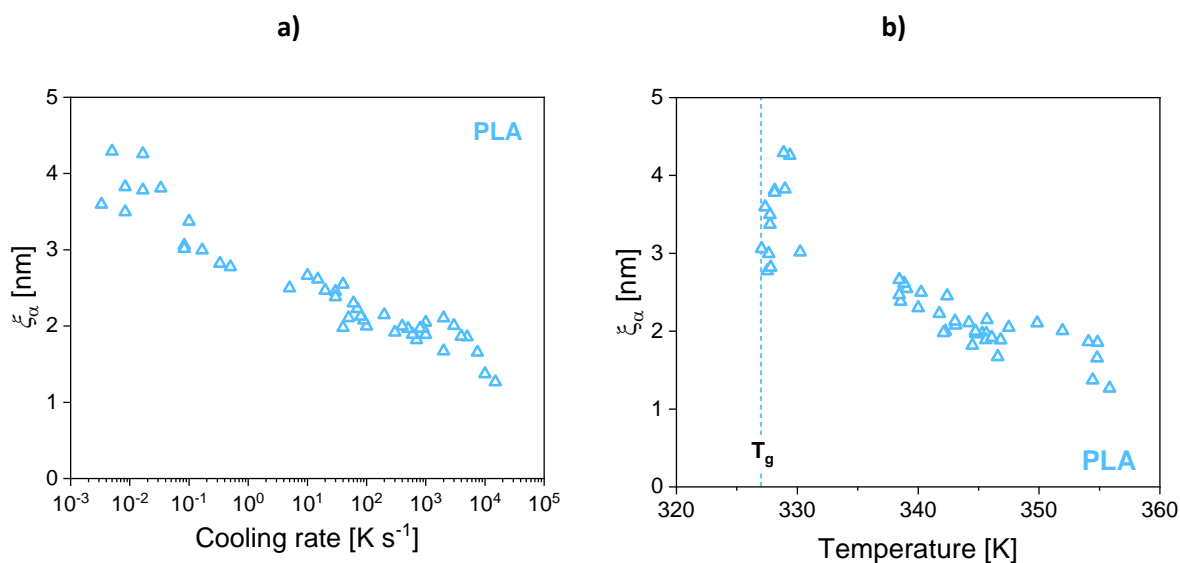


Figure V.6. a) Cooling-rate dependence of the characteristic length ξ_α and **b)** temperature dependence of the characteristic length ξ_α for PLA.

This expected increase of ξ_α with β_c can be explained by the fact that, at high cooling rates, the time Δt spent at a temperature ΔT is smaller than the relaxation time τ needed by the system to reach equilibrium. As a result, the system “freezes” and the excess free volume gets trapped, providing the molecules more space to relax without involving their neighbors. The increasing heterogeneity of the molecular dynamics is thus related to a wider glass transition and a broader distribution of the relaxing times (as well as to a larger temperature fluctuation within the CRR), which in turn corresponds to a less cooperative system. As the cooling rate decreases, the excess free volume diffuses and the movement of the relaxing units gets restrained, leading to an increase in cooperativity.

1.5. Frequency dependence of the glass transition temperature

The applicability of the FKR hypothesis has been verified using the vitrification function. To empirically assess the shift between cooling rate dependence and relaxation time dependence, stochastic modulated temperature (TOPEM) is used. As mentioned in **Chapter II**, TOPEM can inform about the frequency dependence of the specific heat capacity, and more particularly of the dynamic glass transition T_{α}^* . About 17 mg of PLA were heated up to 180 °C to erase thermal history. The sample was then quenched at 20 K min⁻¹ down to 30 °C and reheated up to 70 °C at 20 K min⁻¹. The sample was cooled from 70 down to 30 °C at 0.3 K min⁻¹, with a pulse of 0.5 K and a temperature modulation Δt

between 15 and 500 s to enable frequency evaluation. The frequency dependence of the specific heat capacity is represented in **Figure V.7**.

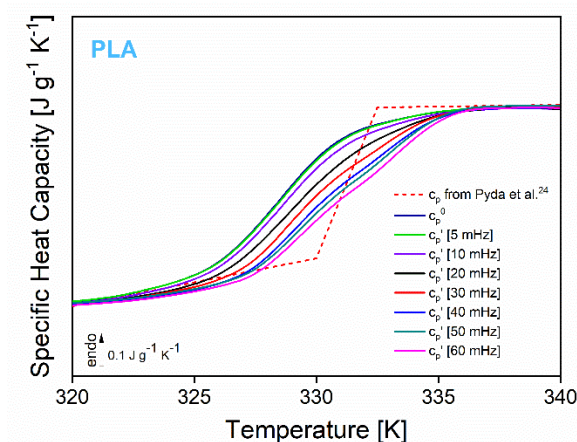


Figure V.7. Quasi-static specific heat capacity c_p^0 (f tending to zero) and in-phase specific heat capacity c_p^1 computed at different frequencies from 5 to 60 mHz. Specific heat capacity proposed by Pyda et al. is added for comparison (red dotted line) [24].

The dynamic glass transition temperatures T_α are estimated for each frequency from the specific heat capacity curves presented in **Figure V.7** to plot the activation diagram in **Figure V.8**. The y-shift between the frequency dependence (red) and the cooling-rate dependence (black) arises from the FKR relationship established in **Eq. 4**. In the literature, $\log C$ is generally comprised between 0.3 [25] and 1.5 [7, 10]. When comparing the activation diagrams obtained using DSC and TOPEM for PLA (**Figure V.8**), a value of 0.6 is obtained for $\log C$. In this case, a single TOPEM measurement was used. This value is close to one estimated from combined FSC and DRS data (0.87) by Moghadam et al. [26].

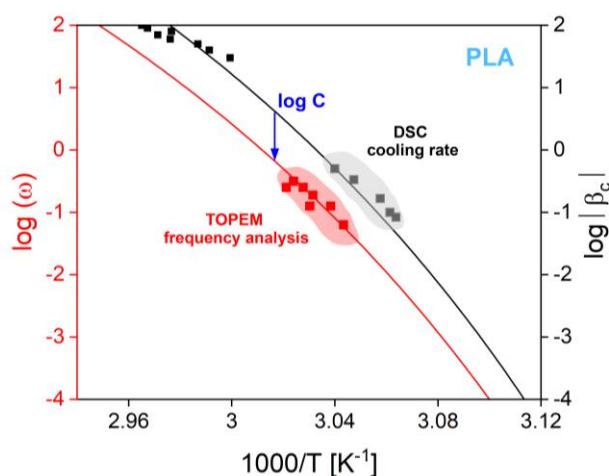


Figure V.8. Activation diagram of PLA using a combination of conventional DSC (black points) and TOPEM (red points). The curves correspond to the VFT fits using the same B and T_v parameters from **Table V.1**.

I.6 Comparison between calorimetric and dielectric relaxation spectroscopy experiments

Figure V.9 shows the temperature dependence of the characteristic length ξ_α obtained with DRS and calorimetric experiments. The same trend is observed with both experimental techniques, however the values of ξ_α derived from calorimetric curves are notably smaller (about 20 %). This discrepancy between DRS and FSC experimental data can be explained by the uncertainty surrounding the calorimetric estimation of the characteristic length ξ_α (generally comprised between 20 % and 30 %) [23]. This uncertainty arises mainly from the approximation of the extrapolation of the tangent curves for $c_{p,g}(T)$ and $c_{p,l}(T)$, from heat transfer problems as well as from the Gaussian fit to estimate δT [16]. The influence of non-equilibrium processes (vitrification or partial freezing-in) should also be accounted for. Last but not least, the sample preparation and its thermal history can also impact the characteristic length.

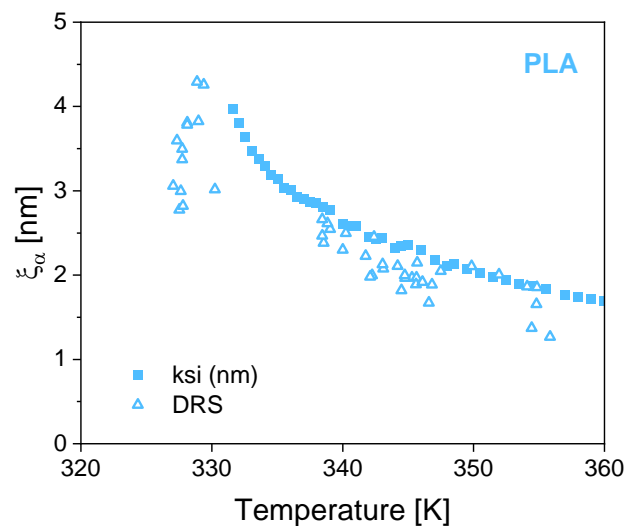


Figure V.9. Comparison between Dielectric Relaxation Spectroscopy (squares) and shifted calorimetric data (empty triangles). DRS data is from Bidur Rijal's PhD thesis [27].

II. Glass transition kinetics of the PCHs

The methodology relying on calorimetric measurements to assess the fragility index and the cooperativity length from the cooling curves has been successfully tested with PLA, and experimental data were found to be in good agreement with previous results, even though they are affected by

some uncertainty. In this second section, this methodology will be used on the PCHs to get some insight on the molecular mobility of the amorphous phase.

II.1 Vitrification function

The PCHs were cooled down from 200 °C to -95 °C with cooling rates $|\beta_c|$ adapted to each sample. The corrected and normalized heat flow recorded upon cooling at different cooling rates is shown in **Figure V.10**.

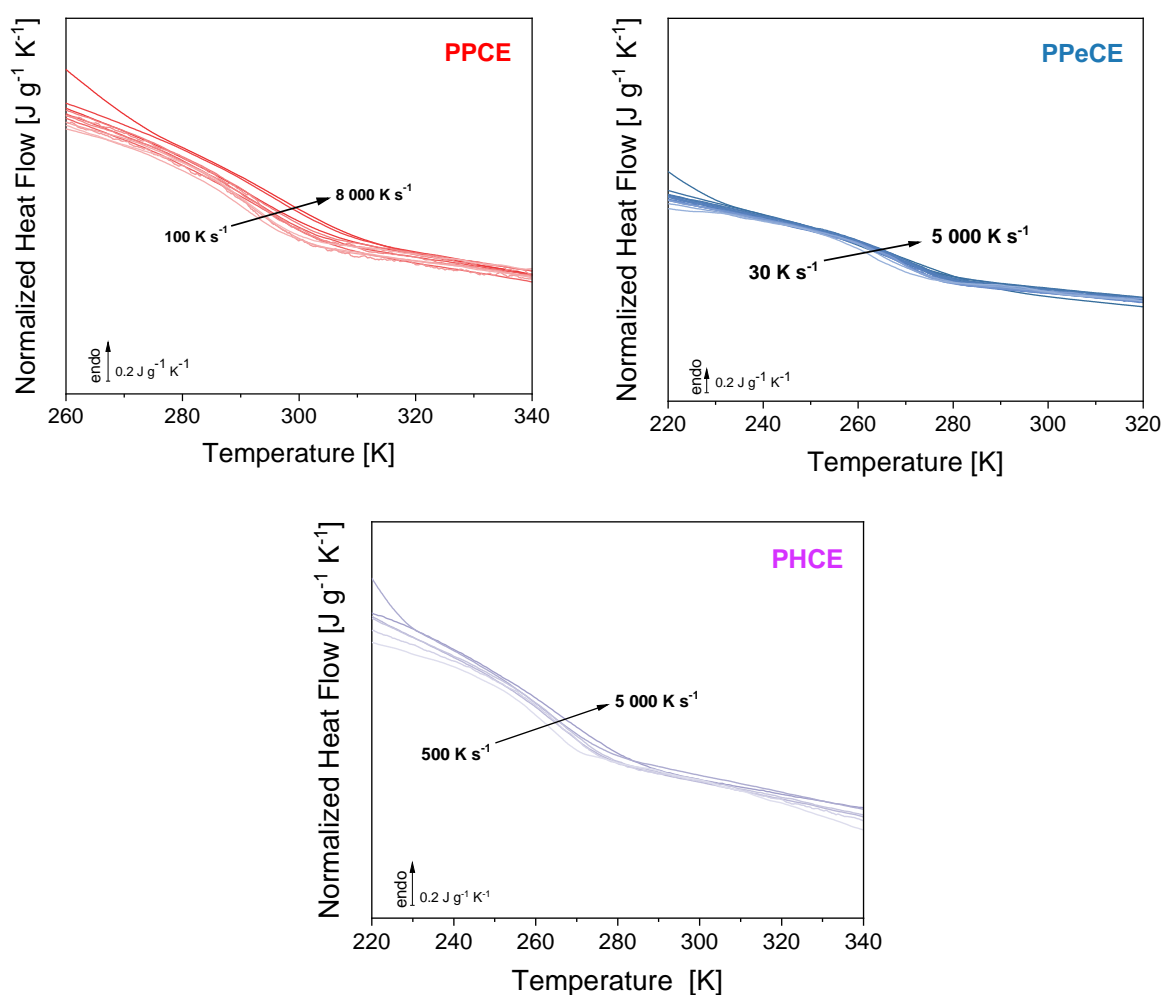


Figure V.10. Corrected and normalized heat flow measured upon cooling through the glass transition with different cooling rates for PPCE, PPeCE and PHCE.

The vitrification function κ was estimated for the PCHs on the whole range of investigated cooling rates (**Figure V.11**), in the same way as previously done for PLA. The mean value varies between 1.1 for PPCE and 1.4 for PHCE and PBCE, the latter being similar to the value found for PLA (1.4). The vitrification

function κ appears to be higher for the even-numbered samples in comparison with the odd-numbered. Nonetheless, this value is constant over the whole range of cooling rates. The dispersion found in the data is somewhat larger (± 0.3 around the mean value depicted by the colored dashed lines).

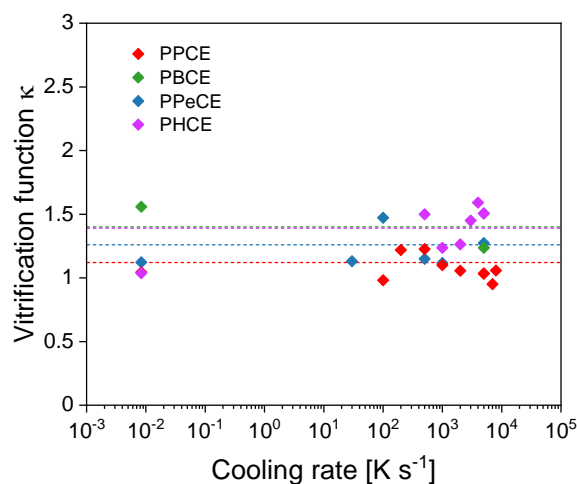


Figure V.11. Cooling-rate dependence of the vitrification function κ for the PCHs. The dotted lines correspond to the mean value.

II.2 Fragility index

The VFT parameters extracted from the fitting curves in **Figure V.12** are presented in **Table V.2**. An increase in the fragility index is observed when the alkyl chain length is reduced from 5 to 3 methylene groups (149 for PPCE, 118 for PPeCE, and 128 for PHCE). The limited number of experimental points used for the estimation may bring some uncertainty. Indeed, the small number of experimental points is a major limiting factor for PHCE, because the amorphous character is guaranteed only for cooling rates over 1000 K s^{-1} , which could lead to an overestimation of m . The presence of the alicyclic ring in the PCHs hinders the molecular mobility, whereas the alkyl chain adds flexibility. This leads to two opposite influences, and the chemical ratio of the alicyclic ring over the alkyl length appears to be the main factor influencing the mobility of PCHs macromolecular chains. As the alkyl chain length is reduced, the influence of the alicyclic ring becomes preponderant and leads to an increase of the fragility index.

A decrease in the fragility index with a rising number of methylene groups has already been observed for various materials [17]. The fragility index m is supposed to be strongly dependent on the packing

efficiency of the macromolecules and therefore related to free volume, as materials with lower fragility were shown to have less free volume [28].

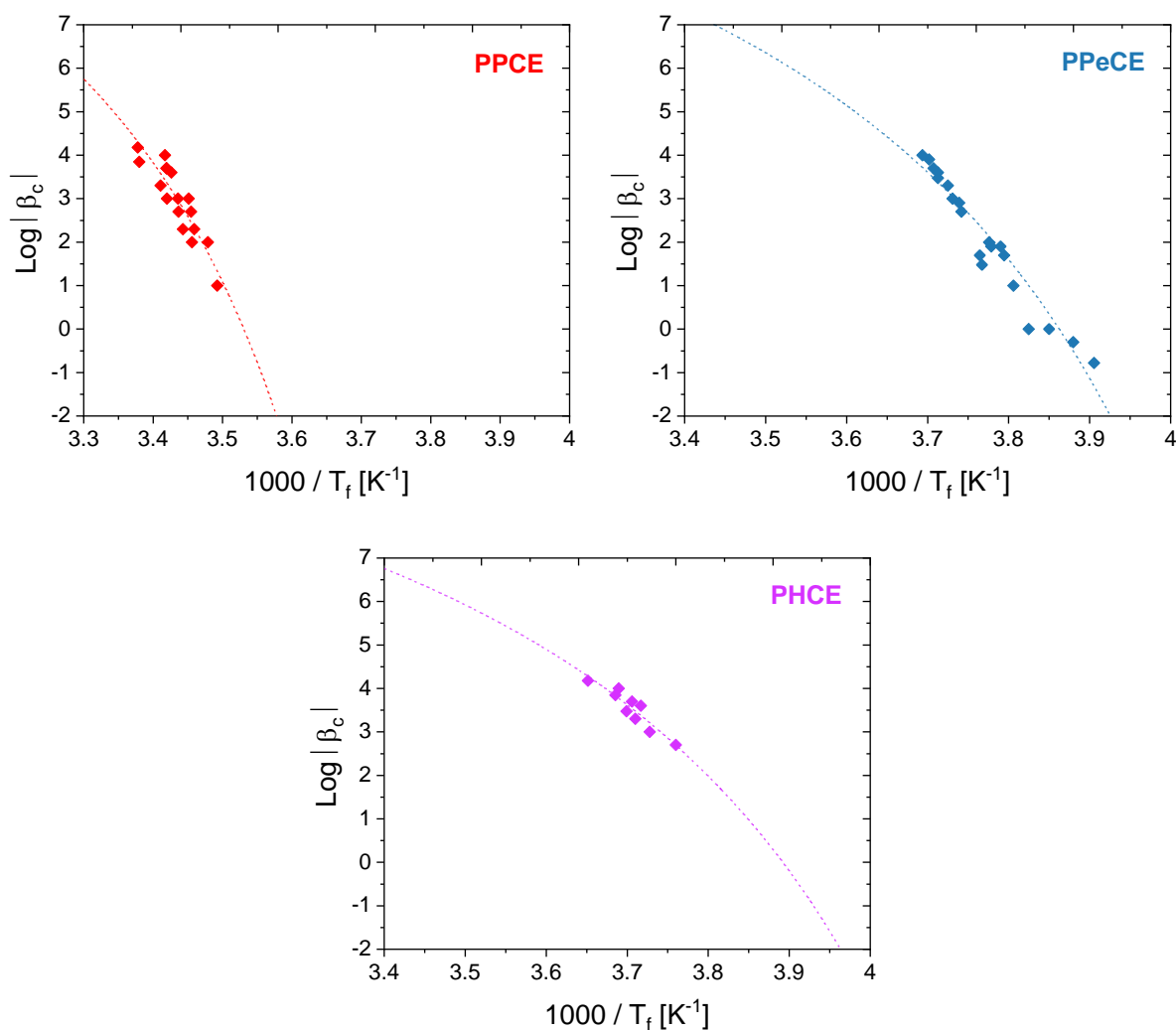


Figure V.12. VFT plots of PPCE, PPeCE and PHCE.

Table V.2. VFT parameters obtained for the investigated PCHs. It should be noted that T_g corresponds to the thermal glass transition estimated by DSC at 10 K min^{-1} (see **Chapter IV**); under these conditions, all the PCHs are in a semi-crystalline state.

Material	T_g (K)	A	B (K)	T_v (K)	m
PPCE	281	15.0	477	251	149 ± 15
PBCE	280	/	/	/	/
PPeCE	258	14.5	498	225	118 ± 11
PHCE	252	13.1	458	222	128 ± 20

Polymers tend to have higher values of fragility compared to metallic glasses and small molecules. Depending on the structural characteristics of the polymer chains, polymers can be sorted in different categories, that is to say low fragility (simple backbone and side structures), intermediate fragility (flexible chains with bulky and stiff side groups), and high fragility (bulky and stiff backbones) [29]. The PCHs fall in the latter category, due to the stiff cyclohexane groups present in their backbone. Even though the cyclohexane is less rigid than the aromatic cycle, PPCE has a fragility close to the one found for its terephthalic counterpart, poly(trimethylene terephthalate) (PTT) [30]. Iyer et al. found that the incorporation of a more flexible 1,4-cyclohexanedimethanol (CHDM, similar to CHDA) monomer results in a slight broadening of the α -relaxation distribution on the faster relaxation side, and only a slight increase in fragility compared to the terephthalic counterparts [31]. On the other hand, PPeCE and PHCE have similar values of fragility compared to other aliphatic polyesters [32]. Moreover, the fragility of poly(furanoate)s with alkyl length varying from 3 to 6 methylene groups decreases from 116 for $n_{CH_2} = 3$ (PTF) to 103 for $n_{CH_2} = 5$ (PPEF) and 105 for $n_{CH_2} = 6$ (PHF). The fragility dependence on alkyl length is found more important for a cyclohexane ring than for a furan ring.

II.3 Characteristic length ξ_α

II.3.1 Comparison of the characteristic length ξ_α for amorphous PCHs

In order to compare the CRR size of the amorphous PCHs, the samples were cooled down from the melt at $5\,000\text{ K s}^{-1}$. The resulting normalized heat flow curves are presented in **Figure V.13**. The temperature fluctuation δT and the characteristic length ξ_α associated to each cooling curve are reported in **Table V.3**.

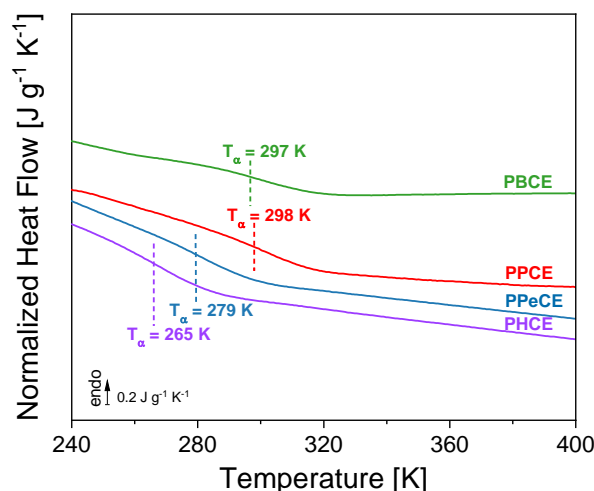


Figure V.13. Normalized heat flow measured upon cooling at $5\,000\text{ K s}^{-1}$ for all the investigated PCHs.

A decrease in the glass transition temperature T_α is evidenced as the alkyl chain length in the backbone increases, resulting in more flexible macromolecular chains. The alkyl chain acts as an internal plasticizer by facilitating the relaxation of the amorphous segments, similar to the effect produced by side chains [33]. However, the T_α measured for PPCE and PBCE are close, indicating similar backbone flexibility for a number of methylene groups n_{CH_2} of 3 and 4. No major change is evidenced about the CRR temperature fluctuation, with δT ranging from 14 to 17 K. Concerning the characteristic length, a decrease is observed from 1.73 nm for PPeCE down to 1.29 nm for PHCE. When investigating the cooperativity in a series of furanoate and terephthalate polyesters with a number of methylene groups n_{CH_2} ranging from 2 to 4, Fosse et al. evidenced a decrease in cooperativity associated with the increase of the alkyl length in the backbone of the repeating unit [30]. In the absence of crystalline phases, they explained this cooperativity decrease by a loss in intermolecular interactions. However, the effect was observed only for an increase in the number of methylene groups n_{CH_2} from 2 to 3, and they found that the presence of an additional methylene ($n_{CH_2} = 4$) did not have any influence on the value of ξ_α . The possible existence of a “cooperativity threshold” for $n_{CH_2} > 4$ was therefore mentioned. In the case of PCHs no such threshold is observed, and on the contrary an increase in ξ_α occurs with n_{CH_2} increasing from 3 to 5.

Table V.3. Cooperativity parameters estimated for the amorphous PCHs at 5 000 K s⁻¹.

Sample	T_α (°C ± 1)	δT (°C ± 1)	ξ_α (nm)
PPCE	25	16 ± 1	1.46 ± 0.03
PBCE	24	14 ± 1	1.57 ± 0.05
PPeCE	6	16 ± 1	1.73 ± 0.04
PHCE	-8	17 ± 1	1.29 ± 0.03

II.3.2 Comparison of the characteristic length ξ_α for semi-crystalline PCHs

To better understand the relationship between molecular mobility and macroscopic properties, it is important to investigate the mobility of the amorphous phase of the PCHs both in the amorphous state and in the presence of semi-crystalline structures. The reversing heat capacity c_p of the as-synthesized polymers was recorded using MT-DSC, with the heat-cool protocol proposed by Rijal et al. [34] (heating rate 0.5 K min⁻¹, period 60 s, amplitude ± 1 K). **Figure V.14.a** depicts the reversing heat capacity c_p for all the PCHs from -40 °C to 180 °C. A complex shape of the glass transition step is observed; one may even assume a double step in the case of PPCE. Since the PCHs have been stored at ambient temperature without any specific thermal treatment before measurement, they had enough time to

develop a semi-crystalline microstructure. The crystalline phase could also be somehow involved in the measurements performed over this temperature range. The curves in **Figure V.14.b** were y-shifted for clarity sake, and show a good alignment of the specific heat capacity in the liquid state for the four polyesters.

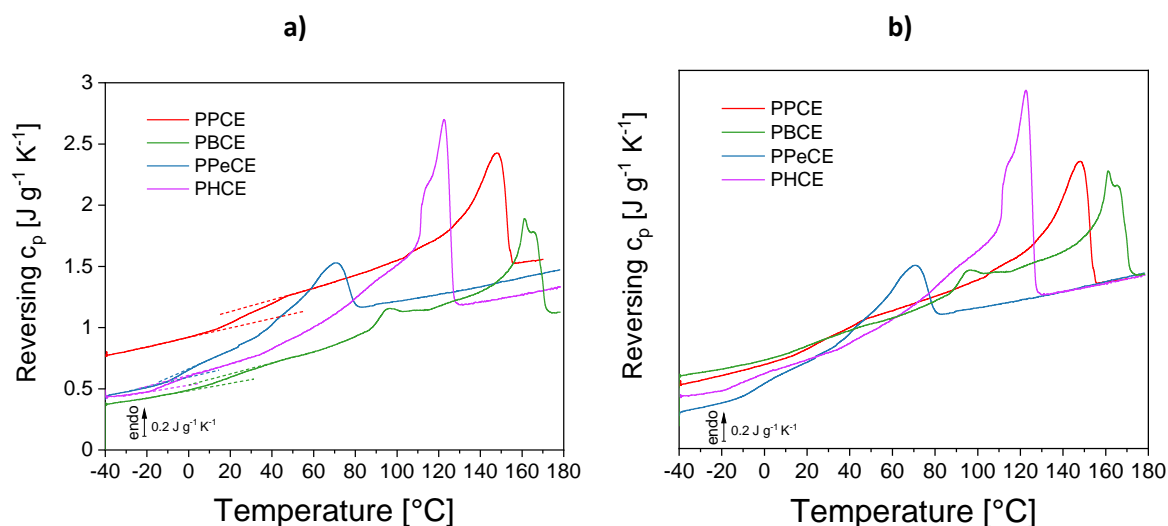


Figure V.14. Reversing c_p as a function of temperature measured for all the considered PCHs with a heating rate of 0.5 K min^{-1} , a period of 60 s, and an amplitude of 1 K. The dotted lines represent the extrapolated $c_{p,g}$ and $c_{p,l}$; **a)** non-shifted curves and **b)** same curves after y-shifting.

Table V.4. Cooperativity parameters estimated for the semi-crystalline PCHs at 0.5 K min^{-1}

Sample	$T_\alpha (\pm 1)$	$\delta T (\pm 1)$	$\xi_\alpha (\text{nm})$
PPCE	24 ± 1	9 ± 1	1.2 ± 0.1
PBCE	20 ± 2	12 ± 2	1.4 ± 0.3
PPeCE	1.0 ± 0.5	7 ± 1	1.3 ± 0.2
PHCE	-5 ± 1	8 ± 1	0.9 ± 0.1

The characteristic lengths measured for the as-synthesized polymers (**Table V.4**) are higher than those measured upon cooling at 5000 K s^{-1} (**Table V.3**). PBCE has the highest value for ξ_α , closely followed by PPCE and PPeCE, with PHCE being the less cooperative system. The glass transition temperatures are slightly lower than those measured at 5000 K s^{-1} on the amorphous samples, except for PHCE. The temperature fluctuations are lower as well.

Polymers do not fully occupy all the available specific volume due to packing inefficiencies and chain mobility. According to Ferry [35], the specific volume v of a polymer can be described as the sum of the occupied volume v_0 and the free volume v_f (or fractional free volume, FFV). The unoccupied free volume is continuously redistributed as a result of thermally-stimulated random segmental motions

[31]. Experiments with Positron Annihilation Lifetime Spectroscopy (PALS) revealed that the size of individual free space has a distribution, which depends on temperature [36]. The FFV is an important structural parameter that determines transport properties and permeability through the entangled polymer chains [31]. By investigating glass transition dynamics in neat and plasticized PLA, Araujo et al. recently correlated the scale of the cooperative motions, i.e., the CRR) size, with the FFV which plays a significant role in the diffusion processes [37].

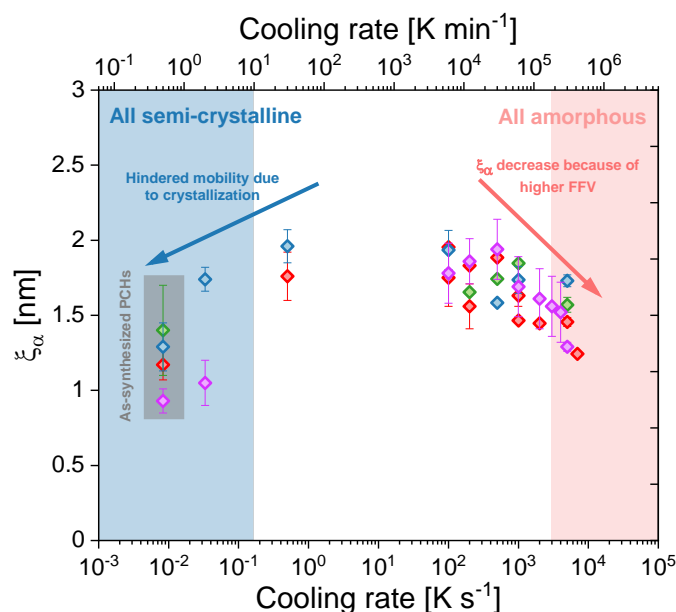


Figure V.15. Cooling-rate dependence of the characteristic length for all the investigated PCHs. The values measured at 0.008 K s^{-1} (0.5 K min^{-1}) upon heating were obtained from the curves in **Figure V.14**.

Figure V.15 shows the dependence of the characteristic length ξ_α on the cooling rate β_c . For the highest cooling rates, the CRR size increases as β_c decreases, similarly to what was observed with PLA. A maximum of ξ_α is reached for PBCE and PHCE at a cooling rate of 1000 and 500 K s^{-1} respectively, close to their critical cooling rate. The effect of the microstructure is evident from the sharp decrease in cooperativity with the further decrease in the cooling rate, as the mobility of the amorphous phase is hindered by the development of the crystalline fraction. On the other hand, a decrease in cooperativity is observed as the cooling rate increases, because of the trapped free volume (higher FFV) within the PCH microstructure. A higher value of FFV means less intermolecular interactions, and thus less cooperativity. A maximum in ξ_α is obtained for intermediate cooling rates, when the influence of the crystallization fraction and the FFV is less preponderant.

II.3.3 Temperature dependence of the characteristic length ξ_α

The complex relationship between the temperature dependence of the viscous slowing down of a glass-forming liquid (associated to the fragility index m) and the size of the CRR (ξ_α) at the glass transition is still a debated topic to this day, and finding a correlation between m and ξ_α has been attempted by many researchers in the last decades [38, 39]. It has been shown that a more fragile material tends to be more cooperative in nature [40, 41]. Hempel et al. investigated a large panel of substances and showed that N_α tends to increase with m , although some exceptions were found [42]. A correlation between the fragility of glass forming systems and their dynamic heterogeneity / cooperativity was investigated by Hong, Novikov and Sokolov [39]. They showed that a glass-forming liquid with a high fragility also has a higher value of the characteristic length, even though such correlation is more straightforward for polymeric systems. However, by investigating the segmental mobility of a series of poly (ethylene-vinyl acetate) copolymers, Puente et al. concluded that fragility and cooperativity are not governed by the same macromolecular properties [43]. Likewise, Fosse et al. found no direct correlation between the fragility index and the cooperativity in furan-based polyesters containing glycolic subunits of different lengths [30]. In summary, no universal trends have been evidenced so far, although a wide variety of polymers have already been investigated, probably because of their complex interactions between chain segments [44].

Usually, the fragility index is directly compared to the characteristic length measured at the glass transition; however, as observed before different experimental techniques can provide diverging values for ξ_α . Even with the same experimental technique (say, calorimetry), different data are obtained depending on the method used for the estimation of the temperature fluctuation, either from the width of the peak of the imaginary part of the complex heat capacity C'' or from the dispersion width of the relaxation spectrum [45]. This lack of standardization in the measurement procedure is a drawback for the comparison and interpretation of experimental data from different sources. Taking the example of fragility index, it is a great tool to compare the increase in the relaxation time associated to the slowing down of the molecular dynamics upon cooling. It requires to know the temperature dependence of the relaxation time $\tau(T)$ of a material as it goes through the glass transition to give an idea of the deceleration of the relaxation motions. Since the cooperative rearrangement occur from the crossover temperature down to the Kauzmann temperature, where the glass formed is supposedly frozen, the knowledge of the characteristic length only at T_g gives only a partial picture of the cooperative process. By varying the cooling rate, the temperature dependence of ξ_α could be

evidenced for PLA (**Figure V.6.b**), but for comparison purposes a way to fit the temperature dependence $\xi_\alpha(T)$ is needed. By inserting **Eq. 8** in **Eq. 10**, ξ_α can be rewritten under the form:

$$\xi_\alpha = b \left(\frac{T}{(T - T_v)^2} \right)^{\frac{2}{3}} \quad \text{Eq. 11}$$

where $b = a (\delta q / \ln 10 B)^{-2/3}$ and T_v is the Vogel temperature. **Figure V.16** represents the mathematical function given in **Eq. 11**. The parameter b appears to give an indication on the steepness of $\xi_\alpha(T)$ as the temperature approaches T_v , in a way similar to the fragility index, which indicates the steepness of $\tau(T)$ approaching T_g . However, a decrease in fragility indicates a decreased steepness of $\tau(T)$, whereas a decrease in the parameter b indicates an increased steepness for $\xi_\alpha(T)$.

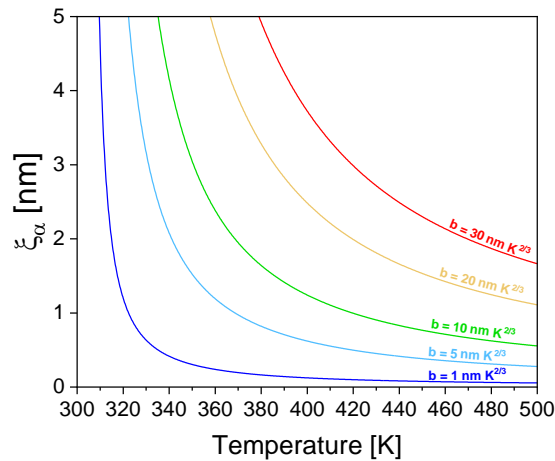


Figure V.16. Representation of the function in **Eq. 11** for the same T_v and different values of the parameter b .

Figure V.17 shows the temperature dependence of ξ_α for the amorphous PPCE, PPeCE and PHCE. As pointed before, the size of the CRR are roughly similar at their respective T_g , however the extrapolation shows that at the same given temperature, PPCE is more cooperative compared to PPeCE and PHCE. The b parameter obtained is 5.1 for PPCE, 6.0 for PPeCE and 5.8 for PHCE.

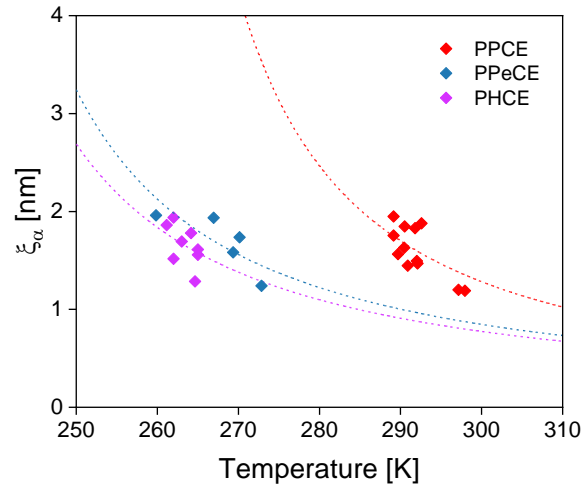


Figure V.17. Temperature dependence of the characteristic length for PPCE (red diamonds), PPeCE (blue diamonds), and PHCE (purple diamonds). The dotted lines correspond to the fit in Eq. 11 using the Vogel temperature T_v from Table V.2.

III. Towards a generalization of the temperature dependence of ξ_α ?

In order to test the soundness of Eq. 11, the temperature dependence of the characteristic length ξ_α has been studied using different experimental techniques for a wide panel of glass formers. The dependence of the characteristic length with temperature $\xi_\alpha(T)$ is showed in Figure V.18.a and fitted using Eq. 11. The T_v values were fixed at the ones extracted from VFT fits found in the literature (the corresponding references are provided later on in Table V.5).

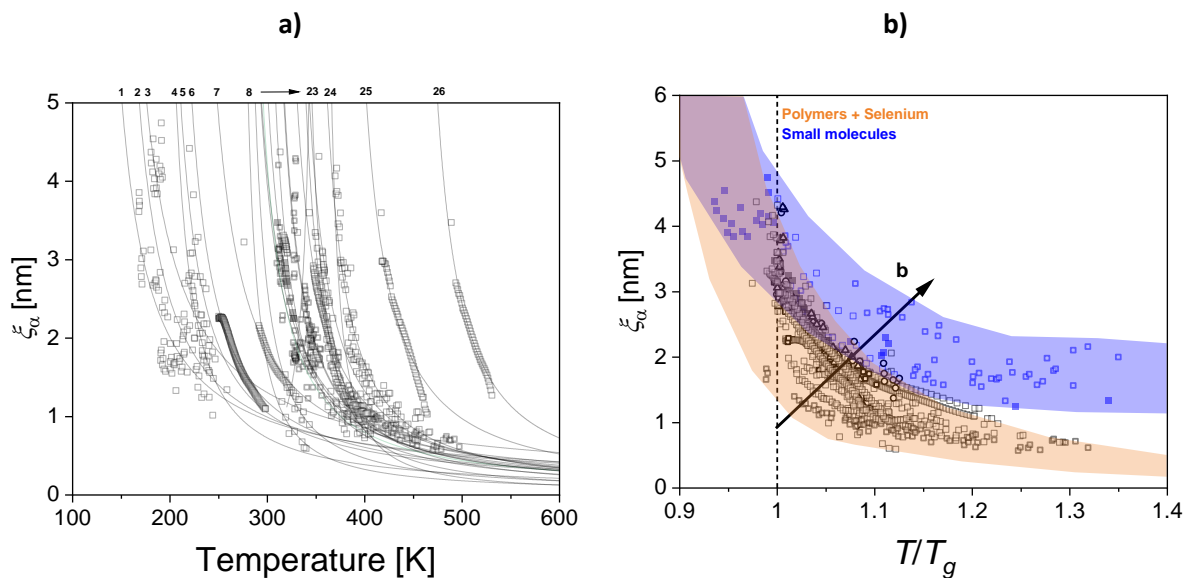


Figure V.18. a) Temperature dependence of the characteristic length for several glass-formers. The solid lines correspond to the fit using Eq. 11; **b)** Characteristic length against the reduced temperature T/T_g .

Introducing a reduced temperature, i.e., replacing T with T/T_g , could help verify if such a temperature dependence of ξ_α is a universal behavior among glass-forming liquids. From **Figure V.18.b**, two main trends can be distinguished between the polymeric glass formers (orange area) and the small molecules (blue area). The size of the CRR seems to be more sensitive to temperature variations in the case of the polymeric glass-formers. **Figure V.18.b** shows that, within this category and within the order of experimental uncertainty, all the considered materials behave identically over the entire temperature range. This seems to suggest that the chemical composition and structure, and in particular the intermolecular interactions, have no significant influence on nanoscale cooperative fluctuation in supercooled glass-forming liquids approaching the glass transition upon cooling.

Table V.5. Different sources from which the data in **Figure V.18** is extracted.

Number	Materials	Experimental Technique	T_v [K]	Reference	b
1	Propylene glycol	AC calorimetry, laser modulated AC calorimetry, MT-DSC	112.5	Chua et al. [46]	22.8
2	PIB	HCS DSC	131	Korus et al. [47]	20.7
3	Glycerol	HCS DSC	128	Korus et al. [47]	27.8
4	SBR1500	3 ω -method	184	Huth et al. [16]	9.2
5	benzoin isobutylether (BIBE)	HCS	180	Kahle et al. [15]	13.8
6	EVA_60	MT-DSC, DRS	190.6	Rijal et al. [48]	13.9
7	EVA_80	MT-DSC, DRS	209.9	Rijal et al. [48]	16.7
8	PnBMA2%	HCS DSC	266	Kahle et al. [49]	4.1
9	PnBMA19%	HCS DSC	269	Kahle et al. [49]	5.7
10	Selenium	TOPEM, DSC, FSC	260	Hallavant et al. [50]	12.6
11	PVAc	TOPEM, DSC, FSC	267	Hallavant et al. [50]	10
12	PBF	MT-DSC, DRS	271	Fosse et al. [30]	10.4
13	PEMA	AC calorimetry	261.7	Chua et al. [1]	11.4
14	PPT	MT-DSC, DRS	283.9	Fosse et al. [30]	7.9
15	PPF	MT-DSC, DRS	289.4	Fosse et al. [30]	9.0
16	PLA	TOPEM, DSC, FSC	290	This work	9.0
17	2,4-PEF	MT-DSC, DRS	300	Bourdet et al. [51]	10.1
18	PE-2,4[50]-2,5[50]F	MT-DSC, DRS	304	Bourdet et al. [51]	11.6
19	2,5-PEF	MT-DSC, DRS	304.4	Fosse et al. [30]	12.0
20	PETg	MT-DSC, DRS	317	Rijal et al. [4]	6.7
21	PET	MT-DSC, DRS	314	Fosse et al. [30]	9.3
22	PMMA	Broadband HCS	354.3	Chua et al. [52]	2.7
23	PVC	MT-DSC, DRS	329	Rijal et al. [4]	4.5
24	PS (168N)	Broadband HCS	334.4	Chua et al. [52]	8.2
25	PBAC	MT-DSC, DRS	367	Rijal et al. [4]	10.5

26	PEI	MT-DSC, DRS	442	Rijal et al. [4]	8.7
27	PPCE	FSC	251	This work	5
28	PPeCE	DSC, FSC	225	This work	6
29	PHCE	FSC	222	This work	5.8

Figure V.19 shows the dependence of the parameter b from Eq. 11 with the fragility index corresponding to the same panel of materials. The dependence of b with the fragility index m can be fitted using a linear function:

$$b = \frac{a}{(m - m_0)} + b_{min} \quad \text{Eq. 12}$$

where a and b_{min} are constant parameters, and m_0 is a limiting fragility index.

The variation of b with m is fitted using Eq. 12. The so-called reference curve is obtained with a m_0 fixed at 16 (theoretical limiting value of the fragility). The coefficient of determination is $R^2 = 0.68$, and b_{min} reaches 2.4. An asymptotic behavior is noted when the fragility index gets close to 16, which is the lowest fragility index that can be expected for a glass-forming liquid according to Angell's definition of fragility [53], whereas values of the fragility index over 200 correspond to the most fragile glass-forming liquids. Strong glass-forming liquids (propylene glycol, PIB, glycerol) have the highest parameter b , and the CRR size are found to be less sensitive on temperature variations. Most polymers are associated to a value of b varying between 13.9 (EVA_60) and 2.7 (PMMA).

By looking at the series of poly (alkylene furanoate)s (orange) and poly (alkylene terephthalate)s (green), it appears that the diol length has some impact on the variation of the characteristic length $\xi\alpha$ with temperature. Even-numbered samples ($n_{CH_2} = 2$ or 4) generally have higher b values compared to their odd-numbered counterparts ($n_{CH_2} = 3$ or 5), for which the cooperative reorganization appears to be more temperature dependent. However, within the PCHs series, PHCE seems to be an exception to this odd-even effect, with similar b as PPeCE. Perhaps this is due to the saturation effect mentioned earlier, even though such saturation effect was not evidenced by the investigation of the crystallization kinetics.

For a given number of methylene groups in the glycolic subunit ($n_{CH_2}=3$), the rigidity of the acidic moiety should also be examined. The cyclohexane moiety is less stiff than the benzene ring, and a furanic ring is less flexible than a benzene ring. This variation in flexibility of the acidic moiety is visible on the glass transition temperature, with T_g (PPCE) $<$ T_g (PPT) \approx T_g (PPF). Concerning the fragility index, it appears that m (PPF) $<$ m (PPCE) \approx m (PPT), with PPCE having a packing efficiency similar to that of

PPT and lower to that of PPF. However, from $b(\text{PPCE}) > b(\text{PPT}) > b(\text{PPF})$, it appears that the higher flexibility of the acidic moiety is correlated with a higher temperature dependence of the CRR size.

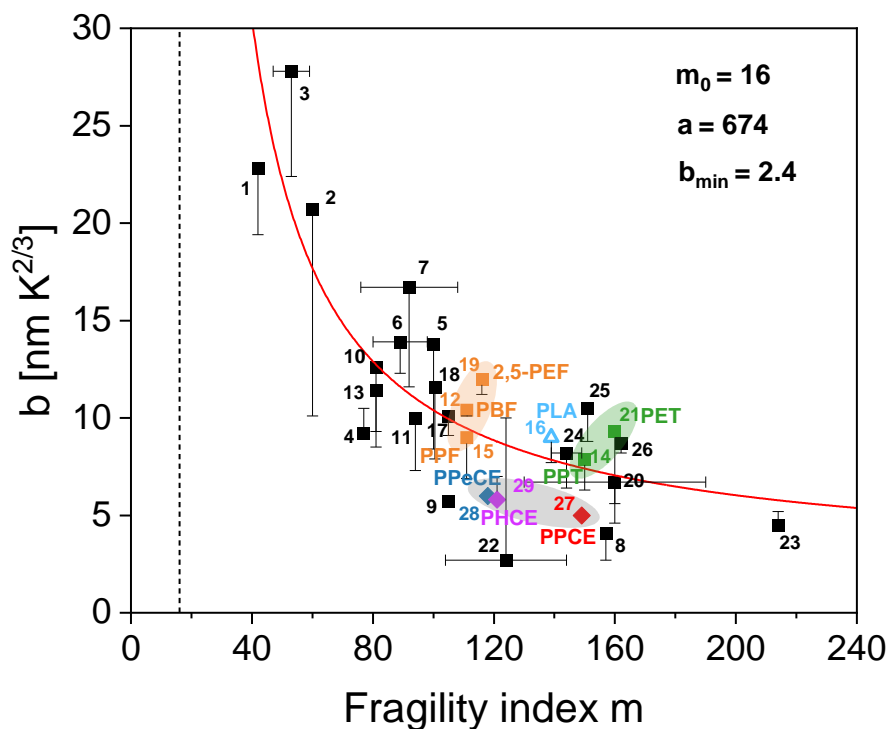


Figure V.19. Variation of b with the fragility index m . The uncertainties on the x-axis (horizontal bars) correspond to the different values for the fragility index m found in literature. The dotted line corresponds to a fragility index of 16. Vertical error bars correspond to the best fit for the derivation of b .

Conclusion

The cooperativity parameters can be extracted from FSC curves using different cooling rates, given that the vitrification function remains constant. The fragility index can be deduced as well from FSC curves with different cooling rates, given a sufficient number of experimental points. Increased cooling rate results in smaller CRR, seemingly due to an excess free volume available for molecular reorganization. An increase in the alkyl chain length within the backbone of the repeating unit does not have a major effect on the characteristic length, but induces a lower fragility for a number of methylene groups increasing from 3 to 5.

References

- [1] Y. Z. Chua, R. Zorn, J. W. P. Schmelzer, C. Schick, O. Holderer, and M. Zamponi, "Determination of Cooperativity Length in a Glass-Forming Polymer," *ACS Phys. Chem Au*, vol. 3, no. 2, pp. 172–180, Mar. 2023, doi: 10.1021/acspchemau.2c00057.
- [2] F. Hamonic, A. Saiter, and E. Dargent, "Evidence of cooperativity length anisotropy in drawn polymers," *Materials Letters*, vol. 128, pp. 12–14, Aug. 2014, doi: 10.1016/j.matlet.2014.04.090.
- [3] F. Hamonic, D. Prevosto, E. Dargent, and A. Saiter, "Contribution of chain alignment and crystallization in the evolution of cooperativity in drawn polymers," *Polymer*, vol. 55, no. 12, pp. 2882–2889, Jun. 2014, doi: 10.1016/j.polymer.2014.04.030.
- [4] B. Rijal, L. Delbreilh, and A. Saiter, "Dynamic Heterogeneity and Cooperative Length Scale at Dynamic Glass Transition in Glass Forming Liquids," *Macromolecules*, vol. 48, no. 22, pp. 8219–8231, Nov. 2015, doi: 10.1021/acs.macromol.5b01152.
- [5] C. T. Moynihan, A. J. Easteal, M. A. Bolt, and J. Tucker, "Dependence of the Fictive Temperature of Glass on Cooling Rate," *J American Ceramic Society*, vol. 59, no. 1–2, Art. no. 1–2, Jan. 1976, doi: 10.1111/j.1151-2916.1976.tb09376.x.
- [6] J. E. K. Schawe, S. Pogatscher, and J. F. Löffler, "Thermodynamics of polymorphism in a bulk metallic glass: Heat capacity measurements by fast differential scanning calorimetry," *Thermochimica Acta*, vol. 685, p. 178518, Mar. 2020, doi: 10.1016/j.tca.2020.178518.
- [7] J. E. K. Schawe, "Vitrification in a wide cooling rate range: The relations between cooling rate, relaxation time, transition width, and fragility," *The Journal of Chemical Physics*, vol. 141, no. 18, p. 184905, Nov. 2014, doi: 10.1063/1.4900961.
- [8] T. Sasaki, M. Ichimura, and S. Irie, "Correlation between fragility and cooperativity in segmental dynamics of glass-forming para-substituted polystyrenes," *Polym J*, vol. 47, no. 10, pp. 687–694, Oct. 2015, doi: 10.1038/pj.2015.50.
- [9] J. E. K. Schawe, "Measurement of the thermal glass transition of polystyrene in a cooling rate range of more than six decades," *Thermochimica Acta*, vol. 603, pp. 128–134, Mar. 2015, doi: 10.1016/j.tca.2014.05.025.
- [10] A. Dhotel, B. Rijal, L. Delbreilh, E. Dargent, and A. Saiter, "Combining Flash DSC, DSC and broadband dielectric spectroscopy to determine fragility," *J Therm Anal Calorim*, vol. 121, no. 1, Art. no. 1, Jul. 2015, doi: 10.1007/s10973-015-4650-9.
- [11] S. Gao and S. L. Simon, "Measurement of the limiting fictive temperature over five decades of cooling and heating rates," *Thermochimica Acta*, vol. 603, pp. 123–127, Mar. 2015, doi: 10.1016/j.tca.2014.08.019.
- [12] C. A. Angell, "Spectroscopy simulation and scattering, and the medium range order problem in glass," *Journal of Non-Crystalline Solids*, vol. 73, no. 1–3, pp. 1–17, Aug. 1985, doi: 10.1016/0022-3093(85)90334-5.
- [13] E. Donth, "Does temperature fluctuate? The fluctuation-dissipation theorem considered as an equation describing quantum mechanical experiments, and application to the dynamic glass transition," *J. Phys.: Condens. Matter*, vol. 12, no. 50, pp. 10371–10388, Dec. 2000, doi: 10.1088/0953-8984/12/50/302.
- [14] M. Von Laue, vol. *Phys. Z.*, no. 18 542, 1917.
- [15] S. Kahle, K. Schröter, E. Hempel, and E. Donth, "Calorimetric indications of a cooperativity onset in the crossover region of dynamic glass transition for benzoin isobutylether," *The Journal of Chemical Physics*, vol. 111, no. 14, pp. 6462–6470, Oct. 1999, doi: 10.1063/1.479942.
- [16] H. Huth, M. Beiner, S. Weyer, M. Merzlyakov, C. Schick, and E. Donth, "Glass transition cooperativity from heat capacity spectroscopy—temperature dependence and experimental uncertainties," *Thermochimica Acta*, vol. 377, no. 1–2, pp. 113–124, Oct. 2001, doi: 10.1016/S0040-6031(01)00546-9.
- [17] E. Hempel, G. Hempel, A. Hensel, C. Schick, and E. Donth, "Characteristic Length of Dynamic Glass Transition near T_g for a Wide Assortment of Glass-Forming Substances," *J. Phys. Chem. B*, vol. 104, no. 11, pp. 2460–2466, Mar. 2000, doi: 10.1021/jp991153f.
- [18] A. Hensel, J. Dobbartin, J. E. K. Schawe, A. Boller, and C. Schick, "Temperature modulated calorimetry and dielectric spectroscopy in the glass transition region of polymers," *Journal of Thermal Analysis*, vol. 46, no. 3–4, pp. 935–954, Mar. 1996, doi: 10.1007/BF01983612.
- [19] A. Saiter, L. Delbreilh, H. Couderc, K. Arabeche, A. Schönhals, and J.-M. Saiter, "Temperature dependence of the characteristic length scale for glassy dynamics: Combination of dielectric and specific heat spectroscopy," *Phys. Rev. E*, vol. 81, no. 4, p. 041805, Apr. 2010, doi: 10.1103/PhysRevE.81.041805.

- [20] S. Weyer, H. Huth, and C. Schick, "Application of an extended Tool–Narayanaswamy–Moynihan model. Part 2. Frequency and cooling rate dependence of glass transition from temperature modulated DSC," *Polymer*, vol. 46, no. 26, pp. 12240–12246, Dec. 2005, doi: 10.1016/j.polymer.2005.10.097.
- [21] X. Monnier and D. Cangialosi, "Thermodynamic Ultrastability of a Polymer Glass Confined at the Micrometer Length Scale," *Phys. Rev. Lett.*, vol. 121, no. 13, p. 137801, Sep. 2018, doi: 10.1103/PhysRevLett.121.137801.
- [22] X. Monnier, D. Cangialosi, B. Ruta, R. Busch, and I. Gallino, "Vitrification decoupling from α -relaxation in a metallic glass," *Sci. Adv.*, vol. 6, no. 17, p. eaay1454, Apr. 2020, doi: 10.1126/sciadv.aay1454.
- [23] E. Donth, "The size of cooperatively rearranging regions at the glass transition," *Journal of Non-Crystalline Solids*, vol. 53, no. 3, pp. 325–330, Dec. 1982, doi: 10.1016/0022-3093(82)90089-8.
- [24] M. Pyda, R. C. Bopp, and B. Wunderlich, "Heat capacity of poly(lactic acid)," *The Journal of Chemical Thermodynamics*, vol. 36, no. 9, pp. 731–742, Sep. 2004, doi: 10.1016/j.jct.2004.05.003.
- [25] J. Morikawa and T. Hashimoto, "Estimation of frequency from a temperature scanning rate in differential scanning calorimetry at the glass transition of polystyrene," *Polymer*, vol. 52, no. 18, pp. 4129–4135, Aug. 2011, doi: 10.1016/j.polymer.2011.06.052.
- [26] S. M. Moghaddam *et al.*, "Fragility of short-chain poly(lactic acid)s derivatives by combining dielectric spectroscopy and fast scanning calorimetry," *Journal of Polymer Science*, vol. 59, no. 14, Art. no. 14, Jul. 2021, doi: 10.1002/pol.20210129.
- [27] B. Rijal, "Etude des phénomènes de relaxation et des mouvements coopératifs à la transition vitreuse dans les liquides formateurs de verres," PhD Thesis, 2015. [Online]. Available: <http://www.theses.fr/2015ROUES020>
- [28] S. Matsuoka, "Entropy, free volume, and cooperative relaxation," *J. Res. Natl. Inst. Stand. Technol.*, vol. 102, no. 2, p. 213, Mar. 1997, doi: 10.6028/jres.102.017.
- [29] J. Dudowicz, K. F. Freed, and J. F. Douglas, "Fragility of Glass-Forming Polymer Liquids," *J. Phys. Chem. B*, vol. 109, no. 45, pp. 21350–21356, Nov. 2005, doi: 10.1021/jp053693k.
- [30] C. Fosse *et al.*, "Cooperativity and fragility in furan-based polyesters with different glycolic subunits as compared to their terephthalic counterparts," *Journal of Non-Crystalline Solids*, vol. 597, p. 121907, Dec. 2022, doi: 10.1016/j.jnoncrysol.2022.121907.
- [31] K. A. Iyer, "Chain mobility, secondary relaxation, and oxygen transport in terephthalate copolyesters with rigid and flexible cyclic diols," *Polymer*, vol. 129, pp. 117–126, Oct. 2017, doi: 10.1016/j.polymer.2017.09.049.
- [32] A. Bourdet *et al.*, "Molecular Mobility in Amorphous Biobased Poly(ethylene 2,5-furandicarboxylate) and Poly(ethylene 2,4-furandicarboxylate)," *Macromolecules*, vol. 51, no. 5, pp. 1937–1945, Mar. 2018, doi: 10.1021/acs.macromol.8b00108.
- [33] C. Fosse *et al.*, "Effect of Chemical Composition on Molecular Mobility and Phase Coupling in Poly(3-hydroxybutyrate-co-3-hydroxyvalerate) and Poly(3-hydroxybutyrate-co-3-hydroxyhexanoate) with Different Comonomer Contents," *J Polym Environ*, vol. 31, no. 10, pp. 4430–4447, Oct. 2023, doi: 10.1007/s10924-023-02882-2.
- [34] B. Rijal, L. Delbreilh, J.-M. Saiter, A. Schönhals, and A. Saiter, "Quasi-isothermal and heat-cool protocols from MT-DSC: Influence on the values extracted for the cooperativity length calculation," *J Therm Anal Calorim*, vol. 121, no. 1, pp. 381–388, Jul. 2015, doi: 10.1007/s10973-015-4671-4.
- [35] J. D. Ferry, *Viscoelastic Properties of Polymers*, 3rd ed. Wiley, New York, 1980.
- [36] J. Liu, Q. Deng, and Y. C. Jean, "Free-volume distributions of polystyrene probed by positron annihilation: comparison with free-volume theories," *Macromolecules*, vol. 26, no. 26, pp. 7149–7155, 1993.
- [37] S. Araujo *et al.*, "Cooperativity Scaling and Free Volume in Plasticized Polylactide," *Macromolecules*, vol. 52, no. 16, pp. 6107–6115, Aug. 2019, doi: 10.1021/acs.macromol.9b00464.
- [38] L. Hong, P. D. Gujrati, V. N. Novikov, and A. P. Sokolov, "Molecular cooperativity in the dynamics of glass-forming systems: A new insight," *J. Chem. Phys.*, vol. 131, no. 19, p. 194511, 2009, doi: 10.1063/1.3266508.
- [39] L. Hong, V. N. Novikov, and A. P. Sokolov, "Is there a connection between fragility of glass forming systems and dynamic heterogeneity/cooperativity?," *Journal of Non-Crystalline Solids*, vol. 357, no. 2, pp. 351–356, Jan. 2011, doi: 10.1016/j.jnoncrysol.2010.06.071.
- [40] A. Saiter, J. M. Saiter, and J. Grenet, "Cooperative rearranging regions in polymeric materials: Relationship with the fragility of glass-forming liquids," *European Polymer Journal*, vol. 42, no. 1, pp. 213–219, Jan. 2006, doi: 10.1016/j.eurpolymj.2005.06.026.

- [41] N. Delpouve, A. Vuillequez, A. Saiter, B. Youssef, and J. M. Saiter, "Fragility and cooperativity concepts in hydrogen-bonded organic glasses," *Physica B: Condensed Matter*, vol. 407, no. 17, pp. 3561–3565, Sep. 2012, doi: 10.1016/j.physb.2012.05.024.
- [42] E. Hempel, G. Hempel, A. Hensel, C. Schick, and E. Donth, "Characteristic Length of Dynamic Glass Transition near T_g for a Wide Assortment of Glass-Forming Substances," *J. Phys. Chem. B*, vol. 104, no. 11, pp. 2460–2466, Mar. 2000, doi: 10.1021/jp991153f.
- [43] J. A. S. Puente, B. Rijal, L. Delbreilh, K. Fatyeyeva, A. Saiter, and E. Dargent, "Segmental mobility and glass transition of poly(ethylene-vinyl acetate) copolymers: Is there a continuum in the dynamic glass transitions from PVAc to PE?," *Polymer*, vol. 76, pp. 213–219, Oct. 2015, doi: 10.1016/j.polymer.2015.09.007.
- [44] A. Sato and T. Sasaki, "Cooperativity of dynamics in supercooled polymeric materials and its temperature dependence predicted from a surface controlled model," *European Polymer Journal*, vol. 99, pp. 485–494, Feb. 2018, doi: 10.1016/j.eurpolymj.2018.01.003.
- [45] K. Schröter, "Characteristic length of glass transition heterogeneity from calorimetry," *Journal of Non-Crystalline Solids*, vol. 352, no. 30–31, pp. 3249–3254, Sep. 2006, doi: 10.1016/j.jnoncrysol.2006.05.024.
- [46] Y. Z. Chua, R. Zorn, O. Holderer, J. W. P. Schmelzer, C. Schick, and E. Donth, "Temperature fluctuations and the thermodynamic determination of the cooperativity length in glass forming liquids," *The Journal of Chemical Physics*, vol. 146, no. 10, p. 104501, Mar. 2017, doi: 10.1063/1.4977737.
- [47] J. Korus, E. Hempel, M. Beiner, S. Kahle, and E. Donth, "Temperature dependence of α glass transition cooperativity," *Acta Polymerica*, vol. 48, no. 9, pp. 369–378, Sep. 1997, doi: 10.1002/actp.1997.010480904.
- [48] B. Rijal *et al.*, "Correlated and cooperative motions in segmental relaxation: Influence of constitutive unit weight and intermolecular interactions," *Phys. Rev. E*, vol. 94, no. 6, p. 062502, Dec. 2016, doi: 10.1103/PhysRevE.94.062502.
- [49] S. Kahle *et al.*, "Glass-Transition Cooperativity Onset in a Series of Random Copolymers Poly(*n*-butyl methacrylate-*stat*-styrene)," *Macromolecules*, vol. 30, no. 23, pp. 7214–7223, Nov. 1997, doi: 10.1021/ma961933b.
- [50] K. Hallavant, M. Mejres, J. E. K. Schawe, A. Esposito, and A. Saiter-Fourcin, "Influence of Chemical Composition and Structure on the Cooperative Fluctuation in Supercooled Glass-Forming Liquids," *J. Phys. Chem. Lett.*, vol. 15, no. 16, pp. 4508–4514, Apr. 2024, doi: 10.1021/acs.jpcclett.4c00632.
- [51] A. Bourdet, S. Araujo, S. Thiyagarajan, L. Delbreilh, A. Esposito, and E. Dargent, "Molecular mobility in amorphous biobased copolyesters obtained with 2,5- and 2,4-furandicarboxylate acid," *Polymer*, vol. 213, p. 123225, Jan. 2021, doi: 10.1016/j.polymer.2020.123225.
- [52] Y. Z. Chua *et al.*, "Glass transition cooperativity from broad band heat capacity spectroscopy," *Colloid Polym Sci*, vol. 292, no. 8, pp. 1893–1904, Aug. 2014, doi: 10.1007/s00396-014-3280-2.
- [53] R. Brüning and M. Sutton, "Fragility of glass-forming systems and the width of the glass transition," *Journal of Non-Crystalline Solids*, vol. 205–207, pp. 480–484, Oct. 1996, doi: 10.1016/S0022-3093(96)00264-5.

Conclusions and prospects

The aim of this work was to get a better understanding of the complex relationship between the chemical composition/structure and the molecular mobility through the variation of two parameters: the crosslinking density for the co-polyesters extracted from tomato peels, and the alkyl chain length within the backbone of the repeating unit for poly (alkylene *trans*-1,4-cyclohexanedicarboxylate)s. The results highlighted how a small change in the chemical structure (one methylene group when comparing PBCE and PPeCE, for instance, or a short increase in the polymerization time for the purified CM) can have dramatic consequences on the macroscopic properties of a material (such as its glass forming ability and melting temperature) and therefore on the potential processing conditions for future applications.

The co-polyesters of hydroxy fatty acids investigated in this work develop complex microstructures depending on the processing conditions (crystallization temperature and cooling rate) and on the chemical structure (polymerization and crosslinking density). Long storage at ambient temperature results in the formation of β and β' -crystals for the purified CM, and only β' -crystals for the polyester network. High cooling rates lead to the formation of metastable α -crystals characterized by a hexagonal packing with an interplanar distance $d = 4.1 \text{ \AA}$. Storage at ambient temperature following rapid cooling leads to a solid-solid transformation of the metastable α -crystals to the more stable β' -crystals for the polyester network, and β -crystals for the purified CM. From a combination of calorimetry and X-ray diffraction, the extrapolated melting enthalpy Δh_m° was measured for the different polymorphs and found to be 77 J g^{-1} for the α -form, 118 J g^{-1} for the β' -form, and 213 J g^{-1} for the β -form. The long methylene sequences allow the purified CM to crystallize completely, and the polyester network to reach a crystalline fraction of 78 %.

Concerning the PCHs, the variation of the alkyl chain length from three to six methylene groups induces an odd-even effect affecting the melting and crystallization temperatures, but also the critical cooling rate and by extension the glass-forming ability. Higher coupling between the amorphous and the crystalline phases is observed for even-numbered PCHs in comparison with their odd-numbered counterparts. X-ray diffractions and isothermal crystallizations evidenced the presence of different polymorphs for all the investigated PCHs. The analysis of the crystallization kinetics with calorimetry in association with POM showed the formation of tiny spherulites with a high density even at high temperature, and showed that the PCHs crystallization process is mainly driven by nucleation.

The cooperativity parameters can be extracted from FSC curves using different cooling rates, given that the vitrification function remains constant from one cooling rate to another. The fragility index

can be deduced as well from FSC curves with different cooling rates, given a sufficient number of experimental points. Increased cooling rate results in smaller CRR, seemingly due to an excess in free volume available for molecular reorganization. An increase in the alkyl chain length in the backbone of the repeating unit does not have a major effect on the characteristic length and the cooperative motions.

The materials investigated in this work are relatively recent, therefore many different aspects can still be considered for future research. For the prospects concerning the series of co-polyesters synthesized from hydroxy-fatty acids, isolating the different polymorphs would be essential to better understand their complex melting behavior. XRD spectra of the samples could be recorded after isothermal crystallization at various T_c for a better knowledge of the temperature conditions required for the formation of the different polymorphs. Since the formation of the β -polymorph seems to be dependent on the polymerization and crosslinking density, a higher number of different polymerization times should be considered to pinpoint the critical molar mass required for the inhibition of the β -form. However, because of the mass loss evidenced through this work, bulk polymerization should be favored if the quantity of raw material allows it.

Concerning the PCHs series, long storage at low temperature could induce microscopic changes through the relaxation of the amorphous phase, impacting the macroscopic properties. Even though it was not mentioned in this thesis, the investigation of the physical aging of the amorphous phase at temperature below T_g performed with PPeCE during the internship of Marouane Mejres (GPM, 2023) could be extended to the other PCHs, namely PPCE, PBCE and PHCE. Moreover, monitoring the enthalpy of relaxation over time evidenced the presence of difference plateaus potentially related to sub- T_g relaxations modes. Dielectric Relaxation Spectroscopy (DRS) could then be considered for the investigation of the time and temperature dependence of the different relaxation processes related to the PCHs.

Concerning the crystallization kinetics, a refinement of the TTT diagram is needed as well as the estimation of the driving force for crystallization of the different polymorphs and on the growth rate G at different temperatures.

On another hand, the *cis* / *trans* ratio is known to influence the crystallization ability and the GFA. For comparison purposes, the ratio was kept the same in the present work for all PCHs, however the synthesis of the materials with different *cis* / *trans* ratios could highlight the importance of the isomerism of the cyclohexane group in the PCHs, and could also be advantageous for future applications. Finally, the synthesis of the PCH containing two methylene groups in the alkyl chain of the repeating unit ($n_{CH_2} = 2$), namely the poly (ethylene *trans*-1,4-cyclohexanedicarboxylate) (PECE),

could give more light on the odd-even effect and on the role of the acidic unit by direct comparison with its 2,5-PEF and PET counterparts.

Appendix 1: Table of acronyms and notations

Poly (alkylene <i>trans</i>-1,4-cyclohexanedicarboxylate)	
PPCE	Poly (propylene <i>trans</i> -1,4-cyclohexanedicarboxylate)
PBCE	Poly (butylene <i>trans</i> -1,4-cyclohexanedicarboxylate)
PPeCE	Poly (pentamethylene <i>trans</i> -1,4-cyclohexanedicarboxylate)
PHCE	Poly (hexamethylene <i>trans</i> -1,4-cyclohexanedicarboxylate)
Poly (alkylene furandicarboxylate)	
2,4-PEF	poly (ethylene furan-2,4-dicarboxylate)
2,5-PEF	poly (ethylene furan-2,5-dicarboxylate)
2,5-PPF	poly (proylene furan-2,5-dicarboxylate)
2,5-PBF	poly (buthylene furan-2,5-dicarboxylate)
2,5-PpeF	poly (pentamethylene furan-2,5-dicarboxylate)
2,5-PHF	poly (hexamethylene furan-2,5-dicarboxylate)
2,5-PdeF	poly (decylene furan-2,5-dicarboxylate)
2,5-PdoF	poly (dodecylene furan-2,5-dicarboxylate)
Poly (alkylene terephthalate)	
PET	Poly (ethylene terephthalate)
PPT	Poly (propylene terephthalate)
PBT	Poly (butylene terephthalate)
Others	
EVA_60	Poly (ethylene-co-vinyl acetate) with 60 wt% VAc
EVA_80	Poly (ethylene-co-vinyl acetate) with 80 wt% VAc
P₁₀MS	Poly (decamethylene sebacate)
PBAC	Poly (bisphenol A carbonate)
PBS	Poly (butylene succinate)
PCL	Poly (ϵ -caprolactone)
PE	Polyethylene
PE-2,4[50]-2,5[50]F	Copolymer of 50:50 mol % 2,4-FDCA and 2,5-FDCA
PEI	Poly (ether imide)
PEMA	Poly (ethyl methacrylate)
PEN	Poly (ethylene naphthalate)
PETg	Poly (ethylene 1,4-cyclohexylenedimethylene terephthalate glycol)
PGA	Poly (glycolic acid)
PIB	Polyisobutylen
PHA	Polyhydroxyalkanoate
PLA	Poly (lactic acid)
PLLA	Poly (L-lactic acid)
PMMA	Poly (methyl methacrylate)
PnBMA2%	Copolymers of n-butyl methacrylate with 2 wt% styrene
PnBMA19%	Copolymers of n-butyl methacrylate with 19 wt% styrene
PP	Polypropylene
PPN	Poly (propylene naphthalate)
PS	Polystyrene
PVAc	Poly (vinyl acetate)
PVC	Polyvinyl chloride
PVDF	Poly (vinylidene fluoride)
SBR1500	Styrene butadiene rubber with 23 wt% styrene

Temperatures

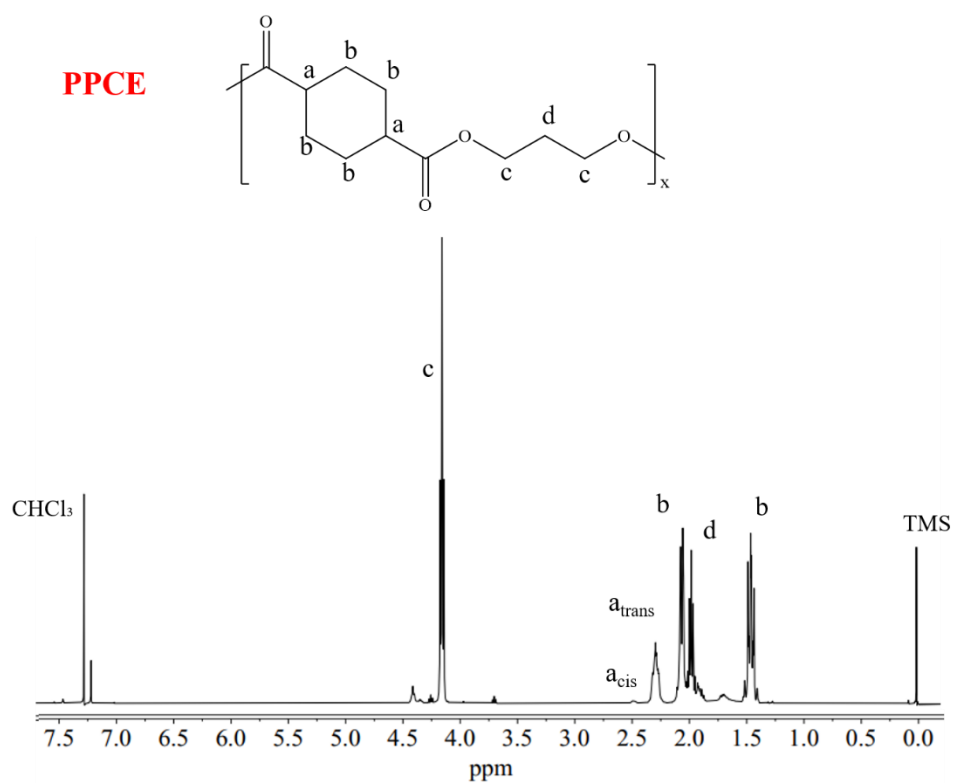
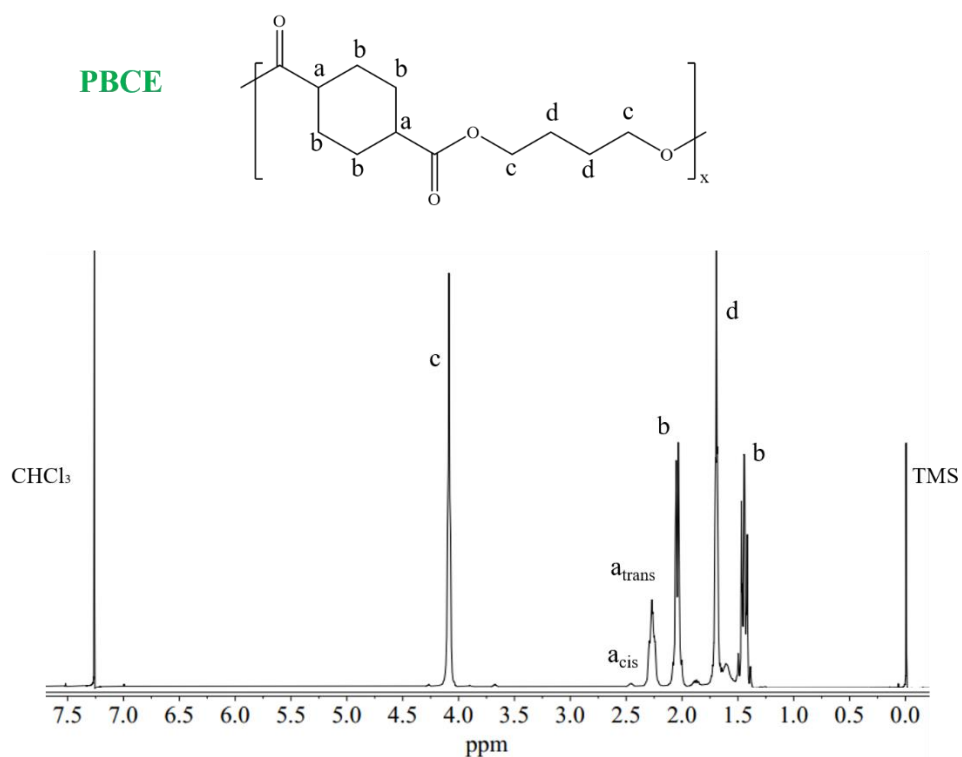
T_{ag}	Aging temperature
T_c	Crystallization temperature
T_{cc}	Cold crystallization temperature
T_f	Fictive temperature
T_g	Glass transition temperature
T_K	Kauzmann temperature
T_m°	Equilibrium melting temperature
T_m	Melting temperature
T_s	Sample temperature
T_{ss}	Sensor support temperature
T_v	Vogel temperature

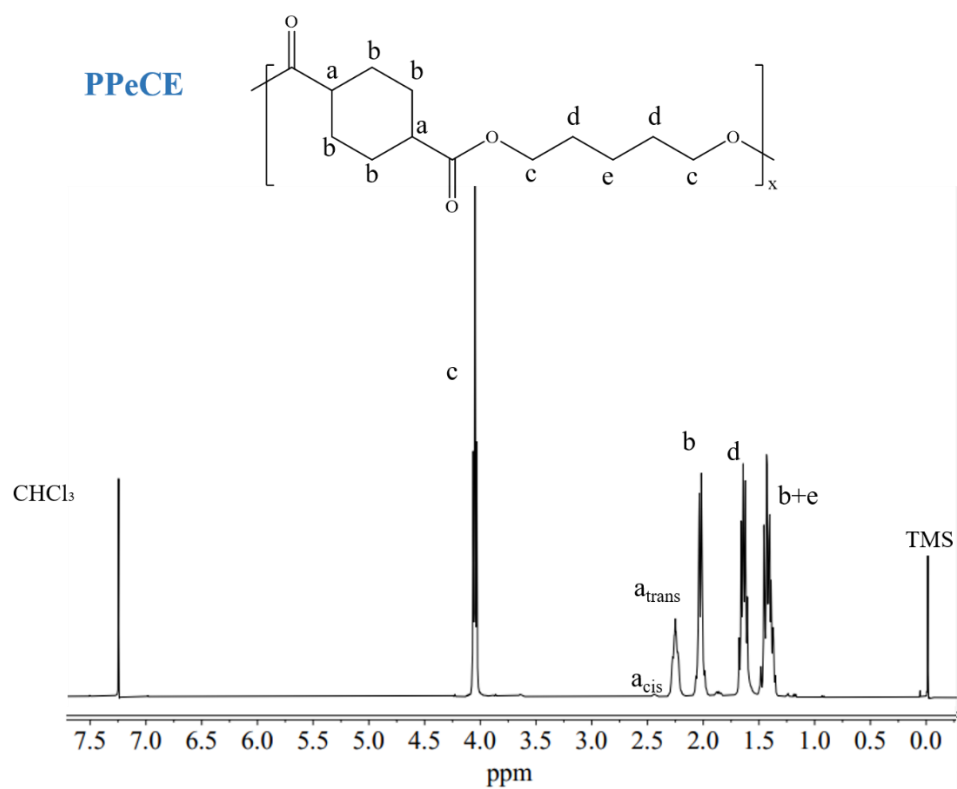
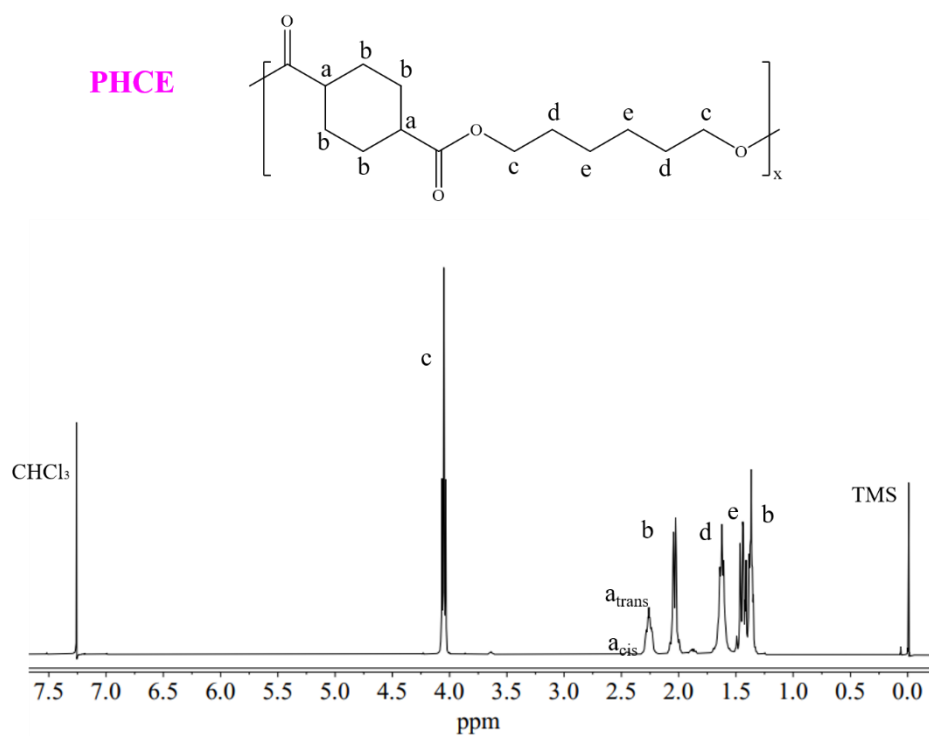
Scanning rates

β_0	Minimum cooling rate under which no cold crystallization happens during heating
β_c	Cooling rate
$\beta_{c,CHG}$	Critical cooling rate needed to form a chemically homogeneous glass
$\beta_{c,SDG}$	Critical cooling rate needed to form a self-doped glass
β_h	Heating rate

Time constants

t_0	Induction time
t_c	Crystallization time
t_{pol}	Polymerization time

Appendix 2: $^1\text{H-NMR}$ spectraFigure 1. $^1\text{H-NMR}$ spectrum of PPCE with the corresponding peak assignment.Figure 22. $^1\text{H-NMR}$ spectrum of PBCE with the corresponding peak assignment.

Figure 3. $^1\text{H-NMR}$ spectrum of PPeCE with the corresponding peak assignment.Figure 4. $^1\text{H-NMR}$ spectrum of PHCE with the corresponding peak assignment.

Scientific communications

Posters

“Vieillesse physique d’un polymère alicyclique biodégradable : le poly (pentaméthylène *trans*-1,4-cyclohexanedicarboxylate)” [Marouane Mejres](#), Kylian Hallavant, Giulia Guidotti, Michelina Soccio, Nadia Lotti, Antonella Esposito, Allisson Saiter-Fourcin. **VIP, 2024, Paris (France)**

“Étude de la coopérativité sur une large gamme de température dans un verre modèle : le sélénium” [Marouane Mejres](#), Kylian Hallavant, Antonella Esposito, Allisson Saiter-Fourcin. **JCAT53, 2023, Palaiseau (France)**

“Study of physical aging phenomena in biodegradable polymer materials” [Marouane Mejres](#), Kylian Hallavant, Antonella Esposito, Allisson Saiter-Fourcin. **LabEx EMC³ and GS MES Scientific Days, 2023, Rouen (France)**

“Investigation of the thermal stability of new bio-based polyesters under N₂ and O₂” Kylian Hallavant, [Antonella Esposito](#), Michelina Soccio, Nadia Lotti, Allisson Saiter-Fourcin. **Biopol, 2022, Alicante (Spain)**

“Estimation of the fragility index in new bio-based polymers by fast scanning calorimetry” [Kylian Hallavant](#), Antonella Esposito, Allisson Saiter-Fourcin, Nadia Lotti, Michelina Soccio. **JCAT52, 2022, Colmar (France)**

Oral communications

“Influence of chemical composition and structure on the cooperative fluctuation in supercooled glass-forming liquids” [Kylian Hallavant](#), Marouane Mejres, Jürgen E.K. Schawe, Antonella Esposito, Allisson Saiter-Fourcin. **18th International Congress on Thermal Analysis and Calorimetry, 2024, Madras (India)**

“Comparison of the Ozawa-Flynn-Wall method with temperature-modulated thermogravimetry for lifetime production” Frédéric Hoppenot, [Christophe Soares](#), Kylian Hallavant, Marie-Rose Garda, Allisson Saiter-Fourcin, Antonella Esposito, Carlton G. Slough. **19^{ème} Journée Scientifique, GFP-Section Est, 2024, Strasbourg (France)**

“Influence of cooling rate on the molecular mobility of a series of biodegradable thermoplastic polyesters” [Kylian Hallavant](#), Antonella Esposito, Allisson Saiter-Fourcin. **Poly-K, international conference, 2023, Terni (Italy)**

“Investigation of cooperativity in bio-based polyesters with a new calorimetric method” [Kylian Hallavant](#), Antonella Esposito, Eric Dargent, Allisson Saiter-Fourcin. **JCAT52, national conference, 2022, Colmar (France)**

Articles (displayed in the following pages)

“Physical aging of a biodegradable alicyclic polymer: Poly (pentaméthylène *trans*-1,4-cyclohexanedicarboxylate)” Marouane Mejres, Kylian Hallavant, Giulia Guidotti, Michelina Soccio, Nadia Lotti, Antonella Esposito, Allisson Saiter-Fourcin. *J. Non Cryst. Solids*, **2024**, 629, 122874 DOI: 10.1016/j.jnoncrysol.2024.122874

“Influence of chemical composition and structure on the nanoscale cooperative fluctuation in supercooled glass-forming liquids” Kylian Hallavant, Marouane Mejres, Jürgen E.K. Schawe, Antonella Esposito, Allisson Saiter-Fourcin. *J. Phys. Chem. Lett.*, **2024**, 15, 4508-4514 DOI: 10.1021/acs.jpcllett.4c00632

“Critical cooling rate of fast-crystallizing polyesters: the example of Poly (alkylène *trans*-1,4-cyclohexanedicarboxylate)” Kylian Hallavant, Michelina Soccio, Giulia Guidotti, Nadia Lotti, Antonella Esposito, Allisson Saiter-Fourcin. *Polymers*, **2024**, 16, 2792 DOI: 10.3390/polym16192792



Contents lists available at ScienceDirect

Journal of Non-Crystalline Solids

journal homepage: www.elsevier.com/locate/jnoncrysol

Physical aging of a biodegradable alicyclic polymer: poly (pentamethylene *trans*-1,4-cyclohexanedicarboxylate)

Marouane Mejres^a, Kylian Hallavant^a, Giulia Guidotti^b, Michelina Soccio^{b,c,d}, Nadia Lotti^{b,c,e}, Antonella Esposito^a, Allisson Saiter-Fourcin^{a,*}

^a Univ Rouen Normandie, INSA Rouen Normandie, CNRS, Groupe de Physique des Matériaux UMR 6634, F-76000 Rouen, France

^b Department of Civil, Chemical, Environmental and Materials Engineering, University of Bologna, Via Terracini 28, 40131 Bologna, Italy

^c Interdepartmental Center for Industrial Research on Advanced Applications in Mechanical Engineering and Materials Technology, CIRI-MAM, Viale del Risorgimento 2, 40136, Bologna, Italy

^d Interdepartmental Center for Industrial Research on Buildings and Construction CIRI-EC, Via del Lazzaretto 15/5, 40131, Bologna, Italy

^e Interdepartmental Center for Agro-Food Research, CIRI-AGRO, Via Quinto Bucci 336, 47521, Cesena, Italy

ARTICLE INFO

Keywords:

Enthalpy of recovery
Relaxation processes
FSC
DSC
Polyesters

ABSTRACT

Physical aging of poly (pentamethylene *trans*-1,4-cyclohexanedicarboxylate) (PPECE), a biodegradable alicyclic polyester, was investigated using Fast Scanning Calorimetry (FSC), a recent calorimetric technique allowing to accelerate physical aging and study the associated relaxation processes at different aging temperatures in an experimentally-reasonable time scale. Different mechanisms were highlighted by varying the aging temperature on a temperature range of more than 60 °C. At aging temperatures well below the glass transition temperature, several relaxation mechanisms were evidenced, probably related to secondary relaxation processes (β relaxations). When the aging temperature approaches the glass transition temperature, the primary relaxation process (α relaxation) becomes predominant.

1. Introduction

Many studies have recently focused on developing biobased and/or biodegradable plastics that could be competitive with traditional plastics. Ideally, these materials would be made from renewable resources and, at their end-of-life, provided specific conditions, they would degrade into carbon dioxide and/or methane, water, and other substances harmless to their degradation environment. Traditionally, the development of biodegradable polymers has been limited to linear aliphatic polyesters, such as polyglycolide (PGA), polylactides (PLAs), polycaprolactone (PCL) or polyhydroxyalkanoates (PHAs). Indeed, aliphatic polyesters have a very strong aptitude to biodegrade, mostly due to the potential of ester groups to undergo hydrolytic chain scissions; their performance, though, is generally poor compared to petroleum-based aromatic polymers [1]. Poly (alkylene 1,4-cyclohexanedicarboxylate)s (PCHs) are alicyclic polyesters with an in-chain aliphatic ring and a variable number of methylene groups, depending on the diol selected to react with 1,4-cyclohexanedicarboxylic acid (CHDA). *trans*-1,4-CHDA may be either petroleum-based or derived from renewable sources, specifically from succinic acid [2–8] and

biobased terephthalic acid, which is in turn sourced from limonene [9]. PLAs can be counted amongst the first biobased and biodegradable polyesters that were developed and scaled up from laboratory to industrial scale, eventually finding some applications in the packaging domain; however, PLAs have relatively poor mechanical and barrier properties, which forces the industrials to either modify or incorporate them into complex formulations [10–14]. Polyesters containing alicyclic units, such as PCHs, offer several benefits in terms of tensile strength, stiffness, impact resistance and thermal stability, along with the advantage of being potentially degradable [15]. These features make them particularly suitable for packaging [16–18] and biomedical [19, 20] applications. Irrespective of the application expected for these polyesters, understanding and predicting their behavior over time is crucial and requires the investigation of physical aging, because any rearrangement of the macromolecular chains in the amorphous phase over time has the potential of significantly affect not only the relaxation dynamics [21], but also the macroscopic behavior, including barrier, adhesion and mechanical properties [22–28].

Physical aging is a natural phenomenon implying the molecular mobility in the amorphous phase, and modifying its density. As

* Corresponding author.

E-mail address: allisson.saiter@univ-rouen.fr (A. Saiter-Fourcin).

<https://doi.org/10.1016/j.jnoncrysol.2024.122874>

Received 20 December 2023; Received in revised form 9 February 2024; Accepted 12 February 2024

Available online 21 February 2024

0022-3093/© 2024 The Author(s). Published by Elsevier B.V. This is an open access article under the CC BY-NC-ND license (<http://creativecommons.org/licenses/by-nc-nd/4.0/>).

highlighted by Kovacs [29], this phenomenon is nonlinear and non-exponential, depending on the time and temperature at which it occurs. Whatever the nature of the material (thermoplastic polymers [30–32], thermosets [33], chalcogenide glasses [34,35], pharmaceutical compounds [36], etc.), and whether it is fully amorphous or semi-crystalline with a residual amorphous phase, the latter will undergo physical aging anytime the material is maintained at an aging temperature (T_{ag}) below its glass transition temperature (T_g) [37]. Physical aging is associated with a so-called enthalpy of recovery, an endothermic peak superimposed to the specific heat capacity step at the glass transition during a heating ramp recorded on an aged sample. As such, physical aging can be investigated through calorimetric measurements, and its quantification is directly related to the area of this endothermic peak superimposed to the specific heat capacity step at T_g [38,39]. However, physical aging is also a self-slowning phenomenon; for this reason, it is sometimes impossible to fully investigate it at the laboratory time-scale, enforcing researchers to make predictions based on models [40–43] that are not always reliable, especially to predict the consequences of long-term aging [44]. In recent years, the development of Fast Scanning Calorimetry (FSC) has provided a possibility to experimentally investigate physical aging in acceptable times on its entire time-scale, which represents a major step forward with respect to classical DSC analysis [45–47]. Indeed, FSC allows cooling down a glass-forming liquid at extremely high rates (from 0.1 K/s up to 40 000 K/s), vitrifying it at high glass transition temperatures, i.e. with more free volume and higher molecular mobility, which in turn accelerates physical aging.

When the cooling rate is too high for a glass-forming liquid to maintain an equilibrium state, the obtained glass is intrinsically out-of-equilibrium, i.e. its specific volume, enthalpy, and entropy are higher than they would have been in the corresponding equilibrium state (liquid-like state extrapolated to low temperatures). This thermodynamic excess initiates a progressive relaxation process towards equilibrium. Calorimetric analysis can be used to monitor the enthalpy of recovery associated with physical aging for a given time (t_{ag}) in isothermal conditions (T_{ag}) by integrating the enthalpy difference between the scans recorded on an aged and successively rejuvenated sample, according to Eq. (1):

$$\Delta H(T_{ag}, t_{ag}) = \int_{T_1}^{T_2} [c_{p,a}(T) - c_{p,r}(T)] dT \quad (1)$$

Where $c_{p,a}(T)$ and $c_{p,r}(T)$ are the specific heat capacities of the aged and rejuvenated sample respectively, and T_1 and T_2 are arbitrary temperatures below and above the glass transition temperature T_g . Under the assumption that the thermodynamic equilibrium is reached for an infinite aging time, the expected enthalpy of recovery (ΔH_{∞}) can be estimated according to Eq. (2):

$$\Delta H_{\infty} = \Delta c_{p,(T_g \text{ mid})} \cdot (T_g \text{ mid} - T_{ag}) \quad (2)$$

Where T_{ag} corresponds to the aging temperature, $T_g \text{ mid}$ is the glass transition temperature taken at half-height of the glass transition step, and $\Delta c_{p,(T_g \text{ mid})}$ is the step in specific heat capacity extrapolated at $T_g \text{ mid}$.

One way for checking if a glass has reached its equilibrium state, is to compare the experimental enthalpy of recovery calculated from Eq. (1) after a given t_{ag} at a given T_{ag} , to the theoretical value estimated from Eq. (2) at the same aging temperature.

However, it is still unclear how a glass reaches its equilibrium state after an extended time of physical aging. In 1995, J.L. Gomez Ribelles et al. [43] believed that polymeric glasses could never reach the thermodynamic equilibrium due to their large steric constraints. In 2013, D. Cangialosi et al. [48] suggested that the thermodynamic equilibrium could still be achieved, but with the emergence of a variable number of intermediate states, whose number depends on the gap between T_g and T_{ag} . This hypothesis has been confirmed in recent studies on different

materials [49,50]. In 2018, R. Androsch et al. [51] added that not only the thermodynamic equilibrium is achievable, but it is also possible to eventually reach the crystalline state; this hypothesis has been successively confirmed in the case of chalcogenide glasses [52]. In 2000, J.M. Hutchinson et al. [42] suggested that only a fraction of a glass-forming liquid is actually vitrified during the glass transition. As a consequence, the theoretical thermodynamic equilibrium would never be reached as expected due to the coexistence of two types of relaxation processes, i.e. a slow one for the vitrified polymer fraction, and a fast one for the non-vitrified polymer fraction. In 2022, Z. Song et al. [53] evidenced fast equilibration mechanisms in the amorphous phase of polymers related to slow liquid dynamics, called Slow Arrhenius Process (SAP).

The aim of this work is to investigate the physical aging of an alicyclic polyester out of the PCHs family, i.e. poly (pentamethylene *trans*-1,4-cyclohexanedicarboxylate) (PpCE), which has been anticipated as a good candidate to replace petroleum-based polymers, having interesting biodegradability properties yet acceptable performances. To this purpose, classical DSC and FSC measurements have been performed at different aging temperatures and durations. The kinetics of the observed aging processes were discussed according to the different models proposed in the literature.

2. Experimental section

2.1. Synthesis

The synthesis of poly (pentamethylene *trans*-1,4-cyclohexanedicarboxylate) (PpCE) was carried out in bulk by a two-step melt polycondensation procedure, starting from *trans*-1,4-cyclohexanedicarboxylic acid, 1,5-pentanediol (in a 100% molar excess) and titanium tetrabutoxide (TBT, 200 ppm) as catalyst, within a stirred 250-mL glass reactor in a thermostated bath. The large molar excess of diol with respect to the diacid promoted the dissolution of the latter. In brief, during the first stage, which was carried out at 1 atm under pure nitrogen flow, the temperature was set to 190 °C and kept constant for about 1.5 h after the complete dissolution of the diacid. During this time, about 90% of the theoretical amount of water was distilled off. At the beginning of the second stage, the temperature was raised to 210 °C and pressure was gradually reduced until 0.06 mbar to promote the transesterification reactions and the removal of the glycolic excess. The synthesis was carried out for 2 additional hours, until a high and constant torque value was measured, indicating that a high molecular weight was reached. After the synthesis, the polymer was purified by dissolving it in chloroform and precipitating it in a beaker filled with methanol in large excess (chloroform:methanol / 1:10). After purification by dissolution in chloroform and precipitation in methanol, the sample was dried under vacuum (1 h at 0.1 mbar).

2.2. Molecular characterization

^1H NMR analysis was carried out to confirm the chemical structure of PpCE given in Fig. 1. The spectrum was acquired using a Varian XL-400 NMR spectrometer (Palo Alto, CA, USA) at room temperature (relaxation time = 0 s, acquisition time = 1 s, 100 repetitions). The polymer was dissolved by introducing about 15 mg of sample in 1 mL of deuterated chloroform (containing 0.03% tetramethylsilane, TMS, as internal reference).

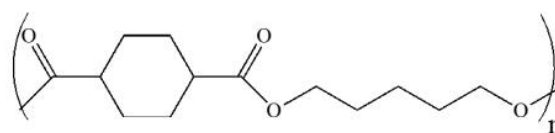


Fig. 1. Chemical structure of poly (pentamethylene *trans*-1,4-cyclohexanedicarboxylate).

The number average molecular weight (\overline{M}_n) and the dispersity (\mathcal{D}) were estimated by Gel Permeation Chromatography (GPC) analysis performed at 30 °C using an HPLC 1100 chromatograph (Agilent Technologies, Santa Clara, CA, USA) equipped with a PLgel 5 mm MiniMIX-C column. A chloroform solution was used as eluent with a flow of 0.3 mL/min, and sample concentrations of about 2 mg/mL were adopted. The calibration curve was obtained using polystyrene standards with a molecular range of 800–100 000 g/mol.

2.3. Thermal characterization

Before any thermal characterization, the material was stored under vacuum in a desiccator in the presence of P_2O_5 to reduce the exposure to humidity. Preliminary characterizations of the glass transition temperature domain were conducted by Differential Scanning Calorimetry (DSC), using a DSC 3+ (Mettler Toledo) equipped with an FRS6 sensor, and with the support of the STARE software for data analysis. Calibrations for temperature, enthalpy, and tau lag were achieved using zinc, indium, and water standards. A sample of PPeCE with a mass of 1.86 mg was placed in a 40 μ l sealed aluminum pan and a continuous nitrogen gas flow of 50 mL/min was maintained in the cell. The measurements consisted in rejuvenating the sample by heating it up above the melt (110 °C), then cooling it down to -80 °C at a rate of 30 K/min, identified as the slowest cooling rate to achieve amorphization. Subsequently, a heating scan at a rate of 10 K/min was performed to obtain the curve corresponding to the rejuvenated sample (Fig. S1). This curve provided the specific heat capacity step at the glass transition temperature (Δc_p), which is necessary for estimating the sample mass in FSC measurements.

Fast Scanning Calorimetry (FSC) experiments were performed with a Flash DSC2+ (Mettler Toledo) equipped with a Huber TC100 intra cooler, which allows to cool the sample down to -95 °C at extremely high cooling rates. Few nanograms (51 ± 5 ng) of PPeCE were placed on a MultiSTAR UFH chip sensor with the help of a microscope. The FSC measurements were all performed on the same sample. The FSC chamber was continuously flushed by 50 mL/min nitrogen gas flow to avoid water condensation [54]. FSC calibration consisted in conditioning the chip sensor and making the necessary corrections for temperature lags (as detailed in the Results and discussion section). The heating and cooling scanning rates were fixed at $\beta_h = |\beta_c| = 1500$ K/s. These conditions prevented both the crystallization from the melt (during cooling) and the subsequent cold crystallization (during heating), ensuring that the sample always remains amorphous. As proposed in the literature [55], the sample mass was estimated by comparing the heat flow step measured by FSC (at $\beta_h = |\beta_c| = 1500$ K/s) with the specific heat capacity step measured by DSC (at $\beta_h = |\beta_c| = 10$ K/min), under the assumption that the specific heat capacity step is the same for both techniques. Physical aging was then investigated by performing the thermal protocol illustrated in Fig. 2:

The first heating-cooling-heating cycle between -95 °C and 110 °C was performed to erase any possible thermal history of the sample and ensure a good contact between the sample and the membrane of the chip sensor. Then, the system was cooled down from the melt to the selected aging temperature (T_{ag}) and kept in isothermal conditions during the selected aging time (t_{ag}). After aging, the system was cooled down again to -95 °C for the final heating ramp. Finally, another cooling-heating cycle was applied to record the response of the rejuvenated sample to be compared with the response of the aged sample.

3. Results and discussion

The spectrum obtained by 1H NMR (Fig. S2) confirms the chemical structure of a PPeCE homopolymer, as illustrated in Fig. 1. Besides the signals due to the solvent and to TMS, one can clearly detect the peaks related to the cyclohexane moiety, i.e. a *trans* (2.25 ppm), a *cis* (2.41 ppm), and b (2.00 and 1.42 ppm), as well as the signals referring to the

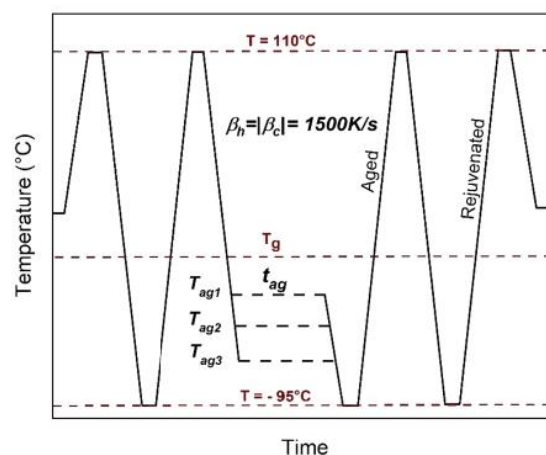


Fig. 2. Experimental protocol for physical aging experiments on PPeCE. The aging temperatures are $T_{ag1} = -15$ °C, $T_{ag2} = -20$ °C, $T_{ag3} = -30$ °C, the aging time is $t_{ag} = 10$ min, and T_g corresponds to the glass transition temperature estimated from FSC curves, i.e. $T_g = 3$ °C. The scanning rates are $\beta_h = |\beta_c| = 1500$ K/s.

pentamethylene subunit, i.e. c (4.11 ppm), d (1.63 ppm), and e (1.42 ppm). The percentage of *cis*-isomer in the 1,4-cyclohexanedicarboxylate subunit was calculated from the ratio of the areas under the a *cis* and a *trans* signals, and found to be of 5.4%. A careful control over the aforementioned synthesis procedure ensured a good distribution of the molecular weights, with a high value of \overline{M}_n (57 855 g/mol) and a narrow value of dispersity ($\mathcal{D} = 1.4$).

Fig. 3a shows the normalized heat flow recorded during the heating and cooling ramps with a scanning rate of 1500 K/s. As expected, the glass transition is shifted to higher temperatures in comparison to the value obtained by classical DSC (Fig. S1). Indeed, the higher the cooling rate used to form a glass, the higher its glass transition temperature. By comparing the heating and cooling scans, one may note that T_g on cooling is slightly shifted to lower temperatures compared to T_g on heating. This shift can be attributed to the dynamic thermal lag due to the large scanning rates, which makes it necessary to apply a correction for the estimation of the glass transition temperature prior to perform the aging protocols [55]. Fig. 3b shows the fictive temperatures estimated both on cooling ($T_{f,c}$) and on heating ($T_{f,h}$) using the method proposed by Moynihan et al. [56]. The difference between $T_{f,h} = 2.5$ °C and $T_{f,c} = 0.6$ °C is used to calculate the dynamic correction factor $\Delta T_D = \frac{T_{f,h} - T_{f,c}}{2}$ [55]. In this case, ΔT_D is about 1 °C; such a small value of dynamic thermal lag confirms that the sample thickness and shape are optimal, ensuring an efficient thermal transfer. The corrected value of T_g is then estimated by adding ΔT_D to the value of $T_{g, mid (Cooling)}$ calculated from the cooling ramp, i.e. $T_g = 2$ °C + $\Delta T_D = 3$ °C. This value was chosen as the reference glass transition temperature for all the subsequent physical aging thermal protocols. Thus, concerning the calculation of the infinite enthalpy of recovery (Eq. (2)), the value taken for $T_{g, mid}$ is 3 °C.

To evaluate the influence of temperature on the relaxation behavior occurring during the physical aging processes, isochronal measurements were first carried out with a fixed time of 10 min at different aging temperatures going from -60 °C up to 10 °C. The results are reported in Fig. 4a.

Irrespective of the aging temperature, the value of the specific heat capacity step at the glass transition Δc_p is constant, proving that the amount of amorphous phase implied in the aging process is constant, and that there is no mass loss and no degradation during the cycling. This proves that only physical aging occurs and the process is totally reversible as expected. When T_{ag} is far from the glass transition, more

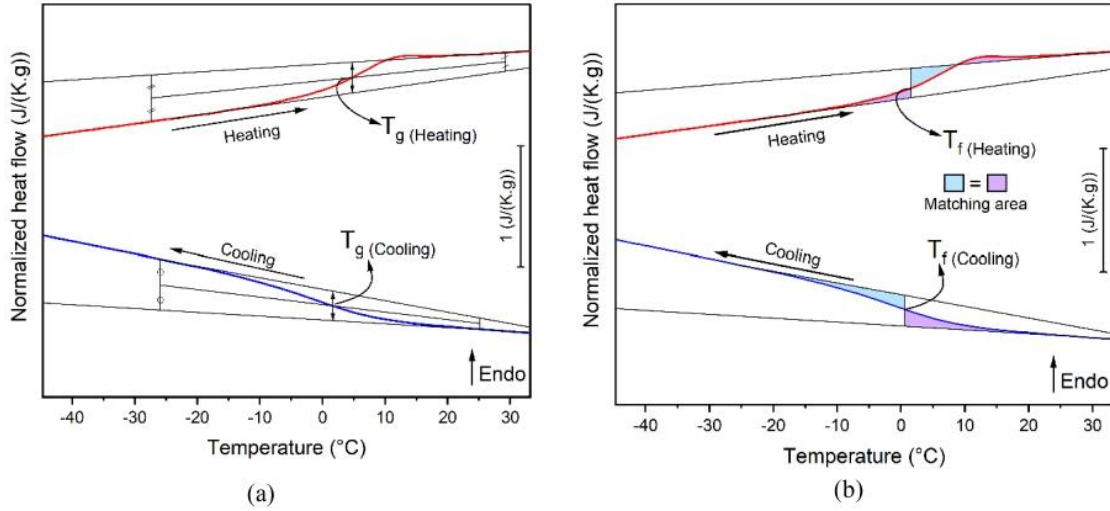


Fig. 3. Normalized heat flow recorded for PPeCE on heating and cooling with scanning rates $\beta_h = |\beta_c| = 1500$ K/s. (a) Method used to determine the mid-point glass transition temperature $T_{g, \text{mid}}$ from the cooling and heating ramps. (b) Estimation of the fictive temperature T_f from the cooling and heating ramps according to the method of the matching areas [56].

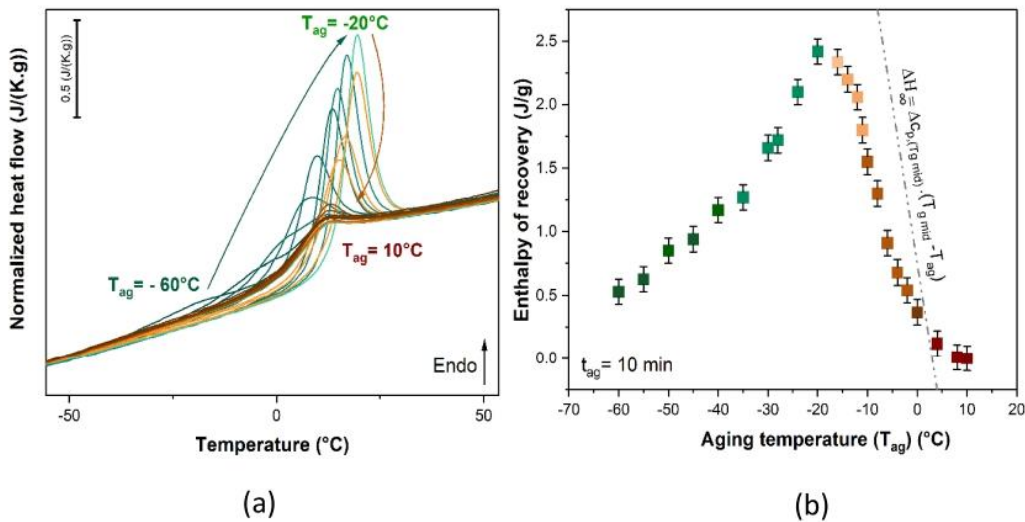


Fig. 4. (a) FSC curves for PPeCE aged during 10 min at different aging temperatures (from -60°C up to 10°C). (b) Enthalpy of recovery estimated from Fig. 4(a) and Eq. (1) for each aging temperature. Error bars of 0.2 J/g were added based on the measurement uncertainty for area calculations in the OriginPro software. The dotted line corresponds to the evolution of ΔH_∞ as a function of T_{ag} .

precisely at -50°C and -60°C , an endothermic overshoot appears before the specific heat capacity step at the glass transition. This unexpected signature has been recently discussed by X. Monnier et al. [49]. They confirmed that this endothermic peak is a real feature of the physical aging process. Thus, this behavior supports the hypothesis that other mechanisms are involved during the aging processes, whose signature is well visible at temperatures far below the glass transition temperature, and could correspond to secondary relaxation processes related to motions at a smaller scale than the repeating unit [57]. When T_{ag} is increased from -60°C up to -20°C , an expected increase of the endothermic peak area superimposed to the specific heat capacity step at the glass transition is observed, along with an expected shift of this peak towards higher temperatures. When T_{ag} is further increased from -20°C up to 10°C (i.e. until entering the glass transition range), the opposite behavior is observed, with a decrease of the endothermic peak area and its shift back to lower temperatures. Fig. 4b shows the evolution of the enthalpy of recovery estimated from Eq. (1) for each

aging temperature when the sample is aged during 10 min. These results evidence two different behaviours highlighted by cold and hot color palettes, respectively. Furthermore, the enthalpy of recovery drops to zero when the glass transition temperature is reached, i.e. for $T_{ag} \geq 3^\circ\text{C}$. This bell-shaped behavior has been already shown in the literature [58–60] and explained by considering two different contributions to the physical aging process, i.e. one kinetic and one thermodynamic. For a given aging time t_{ag} at temperatures far from the glass transition temperature, the molecular mobility and consequently the rate of densification are very low, resulting in small values of the enthalpy of recovery, which means that physical aging is mainly kinetically controlled. If aging time is kept constant and the aging temperature is slightly increased, the molecular mobility is facilitated and therefore the enthalpy of recovery increases. As the aging temperature further approaches the glass transition temperature, the difference between ΔH_∞ and $\Delta H(T_{ag}, t_{ag})$ further decreases; the aging process is then thermodynamically controlled, and any increase in T_{ag} implies a decrease in ΔH_∞ .

and $\Delta H(T_{ag}, t_{ag})$. The maximum of the bell-shaped behavior is observed when the aging process turns from mainly kinetically to thermodynamically controlled.

After evaluating the influence of the aging temperature for a given aging time, the same sample was aged at selected aging temperatures (-15°C , -20°C and -30°C) during different aging times (from 0.1 s up to 20,000 s). The results are reported in Fig. 5.

$T_{ag} = -20^\circ\text{C}$ has been chosen because it corresponds to the temperature at which the aging process starts to be thermodynamically controlled (Fig. 4(b)); two additional temperatures have been selected to investigate physical aging process mostly dominated by either kinetics ($T_{ag} = -30^\circ\text{C}$) or thermodynamics ($T_{ag} = -15^\circ\text{C}$).

Fig. 5 shows that PPeCE's physical aging follows the expected trend irrespective of the selected aging temperature, i.e. with an increasing aging time, the endothermic peak superimposed to the specific heat capacity step at the glass transition becomes more pronounced and gets shifted towards higher temperatures. Furthermore, irrespective of the aging temperature and of the aging time, the value of the specific heat capacity step at the glass transition Δc_p is constant, proving that the amount of amorphous phase implied in the aging process is constant, confirming that there is no mass loss and no degradation during the cycling.

For each aging temperature and each aging time, the enthalpy of recovery ΔH_{tag} was calculated according to Eq. (1). The difference between the infinite enthalpy of recovery ΔH_∞ (maximum enthalpy of

recovery expected at an infinite aging time) and ΔH_{tag} is then calculated and plotted as a function of the aging time (Fig. 6). As expected, and whatever the aging temperature, the longer the aging time, the smaller the difference between ΔH_∞ and ΔH_{tag} , proving that the sample tries to reach its equilibrium state, but unsuccessfully for aging times as long as 20,000 s since zero is not reached. This means that the physical aging process needs longer times to be fully achieved. Interestingly, a stepwise decrease is observed, as highlighted by the gray dotted lines traced between 10 and 500 s in Fig. 6. Even more interestingly, the slope of these lines is the same, irrespective of the aging temperature T_{ag} , suggesting that the rate of physical aging at the considered aging temperatures in this range of aging times is identical. One may wonder how the chemical composition and structure affect physical aging; for this reason, the results obtained for PPeCE were compared to the ones previously obtained for poly (lactic acid) (PLA) in equivalent conditions, i.e. when aging is performed 18°C below the glass transition temperature during 20,000 s [47]. It appears that physical aging has similar kinetics in both systems, irrespective of their chemical composition and structure, because $(\Delta H_\infty - \Delta H_{tag}) = 2 \text{ J/g}$ for PLA [47] and 1.5 J/g for PPeCE.

By selecting different aging temperatures T_{ag} , the presence of intermediate plateaus is clearly evidenced (Fig. 6), revealing the existence of multi-time scales for glass equilibration. As recently proposed by Cangialosi et al. [48,49], this could be attributed to additional relaxation modes supporting the main structural relaxation, which are faster and less cooperative because associated with local molecular motions. This

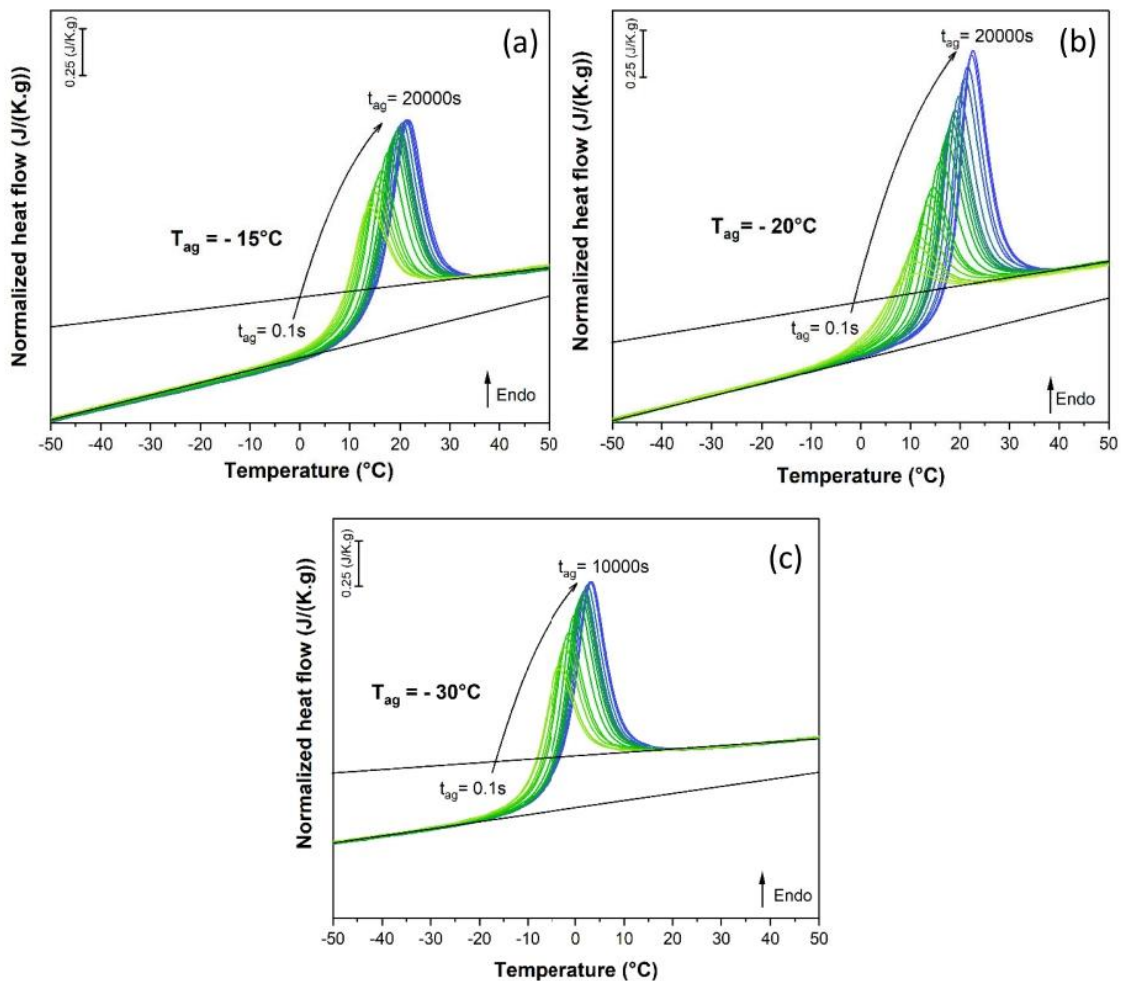


Fig. 5. FSC curves for PPeCE after different aging times (from 0,1 s up to 20000s) at three aging temperatures, i.e. (a) $T_{ag} = -15^\circ\text{C}$, (b) $T_{ag} = -20^\circ\text{C}$, and (c) $T_{ag} = -30^\circ\text{C}$.

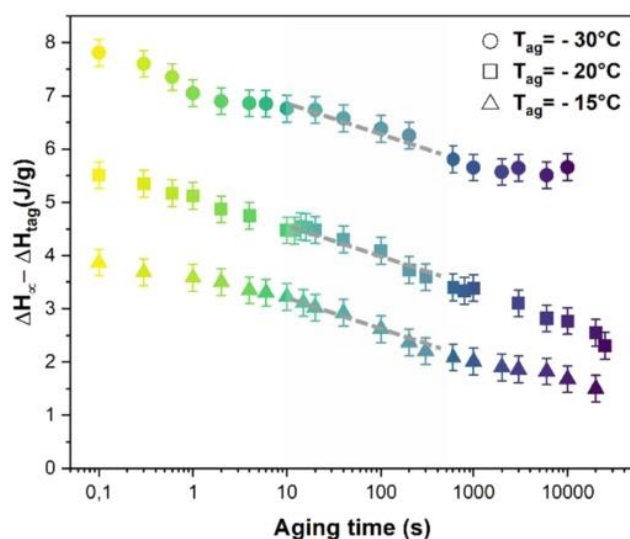


Fig. 6. Evolution of the difference between the infinite enthalpy of recovery ΔH_{∞} (maximum enthalpy of recovery expected at an infinite aging time) and the actual enthalpy of recovery ΔH_{tag} for PPeCE aged at three temperatures: $T_{ag} = -30^{\circ}\text{C}$ (circles), $T_{ag} = -20^{\circ}\text{C}$ (squares), and $T_{ag} = -15^{\circ}\text{C}$ (triangles). The aging times range between 0.1 s and 20,000 s. Error bars of 0.2 J/g were added based on the measurement uncertainty for area calculations in the OriginPro software. The gray dotted lines are guides for the eye.

observation agrees with the fact that dielectric relaxation spectroscopy previously evidenced the presence of two secondary relaxation processes (β_1 and β_2) in poly (trimethylene *trans*-1,4-cyclohexanedicarboxylate) (PPCE) [61], which also belongs to the PCHs family and differs from PPeCE only in terms of number of methylene groups (3 in PPCE, 5 in PPeCE). In PPCE, these two distinct contributions have been attributed to changes in the conformation of the flexible bonds within the repeating unit, eventually leading to intramolecular movements. In particular, the high-frequency mode (β_1) has been related to the rotation of the ester oxygen bound to the aliphatic carbon in the diol subunit, whereas the low-frequency mode (β_2) would be related to the chemical bond between the aliphatic ring carbon and the ester carbon. It is reasonable to assume that the secondary relaxation modes observed in PPCE also occur in PPeCE, given the similarity of their repeating units. Considering all the evidences, and the discussions previously reported in the literature about similar cases, it seems likely to attribute the plateaus in Fig. 6 to the support brought by local secondary relaxation modes to the main relaxation process, that is still dominating the process of physical aging [49].

4. Conclusion

Physical aging of a potentially biobased and biodegradable alicyclic polyester, poly (pentamethylene *trans*-1,4-cyclohexanedicarboxylate) (PPeCE), was investigated by calorimetric analyses (DSC and FSC). Thanks to the extremely fast heating and cooling scanning rates provided by FSC, the relaxation processes involved in physical aging have been evidenced for a specific aging time at different aging temperatures. At aging temperatures far below the glass transition temperature, several mechanisms have been observed, likely linked to secondary relaxation processes (β relaxations). When the aging process is performed at a temperature close to the glass transition temperature, the main relaxation process (α relaxation) becomes predominant. Despite the differences in chemical composition and configuration of the repeating unit, the kinetics of physical aging observed for PPeCE appear to be equivalent to the one observed for PLA in equivalent aging conditions, i.e. equivalent aging time and equivalent gap between T_g and

T_{ag} . PLA is one of the most investigated and currently developed biobased and biodegradable polyester, and this suggests that PPeCE could be a potential concurrent of PLA for packaging, especially in the case of frozen food.

CRediT authorship contribution statement

Marouane Mejres: Writing – original draft, Methodology, Investigation, Formal analysis, Data curation. **Kylian Hallavant:** Writing – review & editing, Methodology, Investigation, Formal analysis, Data curation. **Giulia Guidotti:** Writing – review & editing, Investigation, Funding acquisition, Formal analysis, Data curation. **Michelina Soccio:** Writing – review & editing, Investigation, Funding acquisition, Formal analysis, Data curation. **Nadia Lotti:** Funding acquisition. **Antonella Esposito:** Writing – review & editing, Supervision, Project administration, Funding acquisition. **Allisson Saiter-Fourcin:** Writing – review & editing, Writing – original draft, Validation, Supervision, Resources, Project administration, Methodology, Funding acquisition, Conceptualization.

Declaration of competing interest

The authors declare that they have no known competing financial interests or personal relationships that could have appeared to influence the work reported in this paper.

Data availability

Data will be made available on request.

Acknowledgements

The authors acknowledge the financial support provided by the Normandy Region through the Graduate School Materials & Energy Sciences (GS-MES) and the Laboratory of Excellence Energy, Materials & Clean Combustion Center (LabEx EMC3). Furthermore, the authors acknowledge Mettler Toledo for lending the DSC 3+.

Supplementary materials

Supplementary material associated with this article can be found, in the online version, at doi:10.1016/j.jnoncrysol.2024.122874.

References

- [1] A. Larrañaga, E. Lizundia, A review on the thermomechanical properties and biodegradation behaviour of polyesters, *Eur. Polym. J.* 121 (2019) 109296, <https://doi.org/10.1016/j.eurpolymj.2019.109296>.
- [2] B. Vanhaecht, M.N. Teerenstra, D.R. Suwier, R. Willem, M. Biesemans, C.E. Koning, Controlled stereochemistry of polyamides derived from *cis/trans*-1,4-cyclohexanedicarboxylic acid, *J. Polym. Sci. Part Polym. Chem.* 39 (2001) 833–840, [https://doi.org/10.1002/1099-0518\(20010315\)39:6<833::AID-POLA1056>3.0.CO;2-5](https://doi.org/10.1002/1099-0518(20010315)39:6<833::AID-POLA1056>3.0.CO;2-5).
- [3] D.J. Brunelle, T. Jang, Optimization of poly(1,4-cyclohexylidene cyclohexane-1,4-dicarboxylate) (PCDD) preparation for increased crystallinity, *Polymer* 47 (2006) 4094–4104, <https://doi.org/10.1016/j.polymer.2006.02.070>.
- [4] T.E. Sandhya, C. Ramesh, S. Sivaram, Copolyesters based on poly(butylene terephthalate)s containing cyclohexyl and cyclopentyl ring: effect of molecular structure on thermal and crystallization behavior, *Macromolecules* 40 (2007) 6906–6915, <https://doi.org/10.1021/ma071272q>.
- [5] I. Bechthold, K. Bretz, S. Kabasci, R. Kopitzky, A. Springer, Succinic acid: a new platform chemical for biobased polymers from renewable resources, *Chem. Eng. Technol.* 31 (2008) 647–654, <https://doi.org/10.1002/cent.200800063>.
- [6] F. Liu, J. Zhang, J. Wang, H. Na, J. Zhu, Incorporation of 1,4-cyclohexanedicarboxylic acid into poly(butylene terephthalate)-*b*-poly(tetramethylene glycol) to alter thermal properties without compromising tensile and elastic properties, *RSC Adv.* 5 (2015) 94091–94098, <https://doi.org/10.1039/C5RA18389H>.
- [7] F. Liu, J. Qiu, J. Wang, J. Zhang, H. Na, J. Zhu, Role of *cis*-1,4-cyclohexanedicarboxylic acid in the regulation of the structure and properties of a poly(butylene adipate-co-butylene 1,4-cyclohexanedicarboxylate) copolymer, *RSC Adv.* 6 (2016) 65889–65897, <https://doi.org/10.1039/C6RA13495E>.

- [8] F. Liu, D.-Q. Chi, H.-N. Na, J. Zhu, Isothermal crystallization kinetics and crystalline morphologies of poly(butylene adipate-co-butylene 1,4-cyclohexanedicarboxylate) copolymers, *Chin. J. Polym. Sci.* 36 (2018) 756–764, <https://doi.org/10.1007/s10118-018-2051-9>.
- [9] G. Guidotti, M. Soccio, V. Siracusa, M. Gazzano, A. Munari, N. Lotti, Novel random copolymers of poly(butylene 1,4-cyclohexane dicarboxylate) with outstanding barrier properties for green and sustainable packaging: content and length of aliphatic side chains as efficient tools to tailor the material's final performance, *Polymers* 10 (2018) 866, <https://doi.org/10.3390/polym10080866>.
- [10] S. Singha, M.S. Hedenqvist, A review on barrier properties of poly(lactic acid)/clay nanocomposites, *Polymers* 12 (2020) 1095, <https://doi.org/10.3390/polym12051095>.
- [11] S. Mohan, K. Panneerselvam, A short review on mechanical and barrier properties of polylactic acid-based films, *Mater. Today Proc.* 56 (2022) 3241–3246, <https://doi.org/10.1016/j.rinp.2021.09.375>.
- [12] S. Marano, E. Laudadio, C. Minelli, P. Stipa, Tailoring the barrier properties of PLA: a state-of-the-art review for food packaging applications, *Polymers* 14 (2022) 1626, <https://doi.org/10.3390/polym14081626>.
- [13] U. Meekum, A. Khiansanoi, PLA and two components silicon rubber blends aiming for frozen foods packaging applications, *Results Phys.* 8 (2018) 79–88, <https://doi.org/10.1016/j.rinp.2017.11.030>.
- [14] N. Delpouve, A. Saiter-Fourcin, S. Coiai, F. Cicogna, R. Spiniello, W. Oberhauser, S. Legnaioli, R. Ishak, E. Passaglia, Effects of organo-LDH dispersion on thermal stability, crystallinity and mechanical features of PLA, *Polymer (Guildf)* 208 (2020) 122952, <https://doi.org/10.1016/j.polymer.2020.122952>.
- [15] V. Siracusa, L. Genovese, C. Ingrao, A. Munari, N. Lotti, Barrier properties of poly(propylene cyclohexanedicarboxylate) random eco-friendly copolymers, *Polymers* 10 (2018) 502, <https://doi.org/10.3390/polym10050502>.
- [16] M. Gigli, N. Lotti, M. Gazzano, V. Siracusa, L. Finelli, A. Munari, M. Dalla Rosa, Fully aliphatic copolymers based on poly(butylene 1,4-cyclohexanedicarboxylate) with promising mechanical and barrier properties for food packaging applications, *Ind. Eng. Chem. Res.* 52 (2013) 12876–12886, <https://doi.org/10.1021/ie401781d>.
- [17] G. Guidotti, G. Burzotta, M. Soccio, M. Gazzano, V. Siracusa, A. Munari, N. Lotti, Chemical modification of poly(butylene *trans*-1,4-cyclohexanedicarboxylate) by camphor: a new example of bio-based polyesters for sustainable food packaging, *Polymers* 13 (2021) 2707, <https://doi.org/10.3390/polym13162707>.
- [18] G. Guidotti, L. Genovese, M. Soccio, M. Gigli, A. Munari, V. Siracusa, N. Lotti, Block copolymers containing 2,5-furan and *trans*-1,4-cyclohexane subunits with outstanding gas barrier properties, *Int. J. Mol. Sci.* 20 (2019) 2187, <https://doi.org/10.3390/ijms20092187>.
- [19] N. Bloise, E. Berardi, C. Gualandi, E. Zaghi, M. Gigli, R. Duellen, G. Ceccarelli, E. Cortesi, D. Costamagna, G. Bruni, N. Lotti, M. Focarete, L. Visai, M. Sampaioles, Ether-oxygen containing electropun microfibrillar and sub-microfibrillar scaffolds based on poly(butylene 1,4-cyclohexanedicarboxylate) for skeletal muscle tissue engineering, *Int. J. Mol. Sci.* 19 (2018) 3212, <https://doi.org/10.3390/ijms19103212>.
- [20] M. Gigli, N. Lotti, M. Vercellino, L. Visai, A. Munari, Novel ether-linkages containing aliphatic copolymers of poly(butylene 1,4-cyclohexanedicarboxylate) as promising candidates for biomedical applications, *Mater. Sci. Eng. C* 34 (2014) 86–97, <https://doi.org/10.1016/j.msec.2013.08.013>.
- [21] A. Esposito, N. Delpouve, V. Causin, A. Dhotel, L. Delbreilh, E. Dargent, From a three-phase model to a continuous description of molecular mobility in semicrystalline poly(hydroxybutyrate-co-hydroxyvalerate), *Macromolecules* 49 (2016) 4850–4861, <https://doi.org/10.1021/acs.macromol.6b00384>.
- [22] P. Pan, B. Zhu, Y. Inoue, Enthalpy relaxation and embrittlement of poly(L-lactide) during physical aging, *Macromolecules* 40 (2007) 9664–9671, <https://doi.org/10.1021/ma071737c>.
- [23] M. Kwon, S.C. Lee, Y.G. Jeong, Influences of physical aging on enthalpy relaxation behavior, gas permeability, and dynamic mechanical property of polylactide films with various D-isomer contents, *Macromol. Res.* 18 (2010) 346–351, <https://doi.org/10.1007/s13233-010-0410-7>.
- [24] I.N. Haugan, B. Lee, M.J. Maher, A. Zografos, H.J. Schibur, S.D. Jones, M. A. Hillmyer, F.S. Bates, Physical aging of polylactide-based graft block polymers, *Macromolecules* 52 (2019) 8878–8894, <https://doi.org/10.1021/acs.macromol.9b01434>.
- [25] S. Oumnas, B. Quelelennec, E. Richaud, A. Duthoit, N. Delpouve, L. Delbreilh, Post-curing and structural relaxation of epoxy networks during early stages of aging for civil engineering applications, *Appl. Res.* 2 (2023) e202200090, <https://doi.org/10.1002/appl.202200090>.
- [26] A. Vashchuk, T. Missaoui, N. Delpouve, E. Dargent, Accelerated aging of 18 years rejuvenated polylactide bottles by fast scanning calorimetry, *Appl. Res.* 2 (2023) e202200084, <https://doi.org/10.1002/appl.202200084>.
- [27] B. Quelelennec, Z. Duan, R. Delannoy, N. Gay, M. Briffaut, V. Tognetti, N. Delpouve, L. Delbreilh, L. Bredif, A. Duthoit, E. Richaud, Effect of physical and chemical ageing on barrier properties of epoxy coating, *Constr. Build. Mater.* 409 (2023) 133908, <https://doi.org/10.1016/j.conbuildmat.2023.133908>.
- [28] I. Kada, D. Trinh, S. Mallarino, S. Touzain, Physical ageing effect on water uptake and adhesion of epoxy coatings by EIS and the blister test, *Electrochim. Acta* 454 (2023) 142381, <https://doi.org/10.1016/j.electacta.2023.142381>.
- [29] A.J. Kovacs, Transition vitreuse dans les polymères amorphes. Etude phénoménologique. *Fortschritte Hochpolym.-Forsch.*, Springer-Verlag, Berlin/Heidelberg, 1964, pp. 394–507, <https://doi.org/10.1007/BFb0050366>.
- [30] M.C. Righetti, M. Gazzano, N. Delpouve, A. Saiter, Contribution of the rigid amorphous fraction to physical ageing of semi-crystalline PLLA, *Polymer* 125 (2017) 241–253, <https://doi.org/10.1016/j.polymer.2017.07.089>.
- [31] S. Xu, C. Sun, W. Yuan, J. Zhou, W. Xu, Y. Zheng, C. Yu, P. Pan, Evolution of thermal behavior, mechanical properties, and microstructure in stereocomplexable poly(lactic acid) during physical ageing, *Polymer (Guildf)* 249 (2022) 124840, <https://doi.org/10.1016/j.polymer.2022.124840>.
- [32] A.T. Weyhe, E. Andersen, R. Mikkelsen, D. Yu, Accelerated physical aging of four PET copolymers: enthalpy relaxation and yield behaviour, *Polymer* 278 (2023) 125987, <https://doi.org/10.1016/j.polymer.2023.125987>.
- [33] S.G. Nunes, R. Joffe, N. Emami, P. Fernberg, S. Saseendran, A. Esposito, S. C. Amico, J. Varma, Physical aging effect on viscoelastic behavior of polymers, *Compos. Part C* 7 (2022) 100223, <https://doi.org/10.1016/j.jcomc.2021.100223>.
- [34] A. Kozdras, R. Golovchak, O. Shpotyuk, S. Szymura, A. Saiter, J.-M. Saiter, Light-assisted physical aging in chalcogenide glasses: dependence on the wavelength of incident photons, *J. Mater. Res.* 26 (2011) 2420–2427, <https://doi.org/10.1557/jmr.2011.264>.
- [35] R. Golovchak, J. Oelgoetz, M. Vlcek, A. Esposito, A. Saiter, J.-M. Saiter, H. Jain, Complex structural rearrangements in As-Se glasses, *J. Chem. Phys.* 140 (2014) 054505, <https://doi.org/10.1063/1.4863561>.
- [36] B. Atawa, N. Couvrat, G. Coquerel, E. Dargent, A. Saiter, Chirality impact on physical ageing: an original case of a small organic molecule, *Mater. Lett.* 228 (2018) 141–144, <https://doi.org/10.1016/j.matlet.2018.05.133>.
- [37] L.C.E. Struik, Physical aging in plastics and other glassy materials, *Polym. Eng. Sci.* 17 (1977) 165–173, <https://doi.org/10.1002/pen.760170305>.
- [38] Y. Tanaka, H. Asano, Y. Okuya, Enthalpy relaxation near the glass transition for comb-like polymer: power law relaxation revealed by DSC experiment, *J. Non-Cryst. Solids* 363 (2013) 147–151, <https://doi.org/10.1016/j.jnoncrysol.2012.11.050>.
- [39] Y. Zhang, H. Hahn, Study of the kinetics of free volume in Zr₄₅O₅₅Al₇O₄₈Ag_{8.7} bulk metallic glasses during isothermal relaxation by enthalpy relaxation experiments, *J. Non-Cryst. Solids* 355 (2009) 2616–2621, <https://doi.org/10.1016/j.jnoncrysol.2009.09.003>.
- [40] A.J. Kovacs, J.J. Aklonis, J.M. Hutchinson, A.R. Ramos, Isothermal volume and enthalpy recovery of glasses. II. A transparent multiparameter theory, *J. Polym. Sci.* 17 (1979) 1097–1162, <https://doi.org/10.1002/pol.1979.180170701>.
- [41] C.T. Moynihan, A.J. Eastel, M.A. Bolt, J. Tucker, Dependence of the fictive temperature of glass on cooling rate, *J. Am. Ceram. Soc.* 59 (1976) 12–16, <https://doi.org/10.1111/j.1151-2916.1976.tb09376.x>.
- [42] J.M. Hutchinson, S. Montserrat, Y. Calventus, P. Cortés, Application of the Adam–Gibbs equation to the non-equilibrium glassy state, *Macromolecules* 33 (2000) 5252–5262, <https://doi.org/10.1021/ma992015r>.
- [43] J.L. Gomez Ribelles, M. Monleon Pradas, A. Vidaurre Garayo, F. Romero Colomer, J. Mas Estelles, J.M. Meseguer Duenas, Structural relaxation of glass-forming polymers based on an equation for configurational entropy. 2. structural relaxation in polymethacrylates, *Macromolecules* 28 (1995) 5878–5885, <https://doi.org/10.1021/ma00121a026>.
- [44] J. Grenet, E. Bouthegourd, A. Esposito, A. Saiter, J.M. Saiter, Is the configurational entropic model able to predict the final equilibrium state reached by Se glasses after very long ageing durations? *Philos. Mag.* 93 (2013) 2932–2946, <https://doi.org/10.1080/14786435.2013.793482>.
- [45] R. Pilar, P. Honcová, G. Schulz, C. Schick, J. Málek, Enthalpy relaxation of selenium observed by fast scanning calorimetry, *Thermochim. Acta* 603 (2015) 142–148, <https://doi.org/10.1016/j.tca.2014.09.026>.
- [46] Y.P. Koh, L. Grassia, S.L. Simon, Structural recovery of a single polystyrene thin film using nanocalorimetry to extend the aging time and temperature range, *Thermochim. Acta* 603 (2015) 135–141, <https://doi.org/10.1016/j.tca.2014.08.025>.
- [47] X. Monnier, A. Saiter, E. Dargent, Physical aging in PLA through standard DSC and fast scanning calorimetry investigations, *Thermochim. Acta* 648 (2017) 13–22, <https://doi.org/10.1016/j.tca.2016.12.006>.
- [48] D. Cangialosi, V.M. Boucher, A. Alegría, J. Colmenero, Direct evidence of two equilibration mechanisms in glassy polymers, *Phys. Rev. Lett.* 111 (2013) 095701, <https://doi.org/10.1103/PhysRevLett.111.095701>.
- [49] X. Monnier, S. Marina, X. Lopez de Pariza, H. Sardon, J. Martin, D. Cangialosi, Physical aging behavior of a glassy polyether, *Polymers* 13 (2021) 954, <https://doi.org/10.3390/polym13060954>.
- [50] A. Morvan, N. Delpouve, A. Vella, A. Saiter-Fourcin, Physical aging of selenium glass: assessing the double mechanism of equilibration and the crystallization process, *J. Non-Cryst. Solids* 570 (2021) 121013, <https://doi.org/10.1016/j.jnoncrysol.2021.121013>.
- [51] R. Androsch, E. Zhuravlev, J.W.P. Schmelzer, C. Schick, Relaxation and crystal nucleation in polymer glasses, *Eur. Polym. J.* 102 (2018) 195–208, <https://doi.org/10.1016/j.eurpolymj.2018.03.026>.
- [52] A. Morvan, L. Calvez, A. Vella, A. Saiter-Fourcin, Physical aging of the 62.5GeS₂-12.5Sb₂S₃-25CsCl chalcogenide glass: assessing the mechanisms of equilibration and crystallization, *J. Non-Cryst. Solids* 598 (2022) 121955, <https://doi.org/10.1016/j.jnoncrysol.2022.121955>.
- [53] Z. Song, C. Rodríguez-Tinoco, A. Mathew, S. Napolitano, Fast equilibration mechanisms in disordered materials mediated by slow liquid dynamics, *Sci. Adv.* 8 (2022) eabm7154, <https://doi.org/10.1126/sciadv.abm7154>.
- [54] V. Mathot, M. Pyda, T. Pijpers, G. Vanden Poel, E. van de Kerkhof, S. van Herwaarden, F. van Herwaarden, A. Leenaers, The Flash DSC 1, a power compensation twin-type, chip-based fast scanning calorimeter (FSC): first findings on polymers, *Thermochim. Acta* 522 (2011) 36–45, <https://doi.org/10.1016/j.tca.2011.02.031>.
- [55] J.E.K. Schawe, Measurement of the thermal glass transition of polystyrene in a cooling rate range of more than six decades, *Thermochim. Acta* 603 (2015) 128–134, <https://doi.org/10.1016/j.tca.2014.05.025>.

- [56] C.T. Moynihan, A.J. Easteal, J. Wilder, J. Tucker, Dependence of the glass transition temperature on heating and cooling rate, *J. Phys. Chem.* 78 (1974) 2673–2677, <https://doi.org/10.1021/j100619a008>.
- [57] M.C. Righetti, E. Mele, Structural relaxation in PLLA: contribution of different scale motions, *Thermochim. Acta* 672 (2019) 157–161, <https://doi.org/10.1016/j.tca.2018.12.027>.
- [58] W.D. Cook, M. Mehrabi, G.H. Edward, Ageing and yielding in model epoxy thermosets, *Polymer* 40 (1999) 1209–1218, [https://doi.org/10.1016/S0032-3861\(98\)00343-7](https://doi.org/10.1016/S0032-3861(98)00343-7).
- [59] M.C. Righetti, G.P. Johari, Enthalpy and entropy changes during physical ageing of 20% polystyrene–80% poly(*o*-methylstyrene) blend and the cooling rate effects, *Thermochim. Acta* 607 (2015) 19–29, <https://doi.org/10.1016/j.tca.2015.03.012>.
- [60] X. Monnier, N. Delpouve, A. Saiter-Fourcin, Distinct dynamics of structural relaxation in the amorphous phase of poly(L-lactic acid) revealed by quiescent crystallization, *Soft Matter* 16 (2020) 3224–3233, <https://doi.org/10.1039/C9SM02541C>.
- [61] L. Genovese, M. Soccio, N. Lotti, A. Munari, A. Szymczyk, S. Paszkiewicz, A. Linares, A. Nogales, T.A. Ezquerra, Effect of chemical structure on the subglass relaxation dynamics of biobased polyesters as revealed by dielectric spectroscopy: 2,5-furandicarboxylic acid vs. *trans*-1,4-cyclohexanedicarboxylic acid, *Phys. Chem. Chem. Phys.* 20 (2018) 15696–15706, <https://doi.org/10.1039/C8CP01810C>.

Influence of Chemical Composition and Structure on the Cooperative Fluctuation in Supercooled Glass-Forming Liquids

Kylian Hallavant, Marouane Mejres, Jürgen E. K. Schawe,* Antonella Esposito, and Allisson Saiter-Fourcin*

Cite This: *J. Phys. Chem. Lett.* 2024, 15, 4508–4514

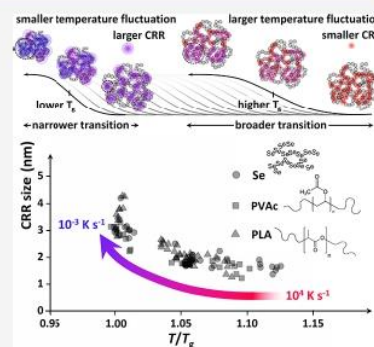
Read Online

ACCESS |

Metrics & More

Article Recommendations

ABSTRACT: The kinetics of the glass transition and the characteristic size of the fluctuating spatio-temporal domains in supercooled glass-forming liquids, i.e., the Cooperatively Rearranging Regions (CRR), were measured upon cooling over a broad range of cooling rates using Differential Scanning Calorimetry (DSC) and chip-based Fast Scanning Calorimetry (FSC). The investigations were conducted on a selection of fragile glass formers (fragility indices between 80 and 140), with a large variance in the atomic or molecular structure but comparable thermal glass transition temperatures T_g , with the aim of evaluating the influence of chemical composition and structure on the CRR size and the associated temperature fluctuation. The selected materials are two polymers (poly(vinyl acetate) (PVAc), poly(lactic acid) (PLA)) as well as the simplest chalcogenide glass-former (selenium). It turned out that the CRR size plotted against the reduced temperature T/T_g follows the same trend, irrespective of the considered glass-former.



A basic explanation of vitrification, i.e., the formation of glasses by rapid cooling, was given by Tammann about 120 years ago in his famous book on phase transformation.¹ This period could be described as the starting point of modern physical science of glass formation. Of course, much progress has been made since then, but a general understanding of the glass transition has not yet been achieved.² The most recent steps forward have been made possible by the improvement of experimental techniques such as X-ray Positron Correlation Spectroscopy (XPCS),^{3,4} Electron Correlation Microscopy (ECM),⁵ and Neutron Spin Echo (NSE) spectroscopy.⁶ The development of Fast Scanning Calorimetry (FSC) with high time resolution^{7,8} and spectroscopy of the heat capacity over a wide frequency range^{9,10} also provides a deeper insight into the kinetics of the glass transition.^{11–13}

The vitrification process depends on the molecular or atomic rearrangements in the deeply supercooled melt, which are usually described by spatially and temporally fluctuating associations of particles. Depending on the selected material and characterization method, these associations are referred to as Medium Range Order (MRO) correlation regions,^{14,15} dynamic heterogeneities,¹⁶ or spatial heterogeneities,¹⁷ but all of them describe spatio-temporal domains in which the molecular or atomic mobility is not homogeneous^{16,18} and drastically changes during the vitrification process.^{14,19} These dynamic domains, the so-called Cooperatively Rearranging Regions (CRR),²⁰ affect not only the kinetics of the glass transition (e.g., the fragility index)²¹ but also other properties, such as thermal expansion,²² microhardness,²³ and any

eventual subsequent crystalline structure.²⁴ In other words, the stability and macroscopic properties of any amorphous system depend on their spatio-temporal nanostructure, i.e., on their nanoscale cooperative fluctuation.

Given the hypothesis of temperature fluctuation,^{25,26} Donth developed a method to estimate the average size of the thermodynamic subsystems whose particles rearrange cooperatively (CRR) based on the analysis of the shape of the thermal relaxation spectrum.²⁷ A good approximation of the characteristic volume of a CRR can be obtained by eq 1:^{6,28}

$$V_{\alpha} = \frac{k_B}{\rho} \left(\frac{T_{\alpha}}{\delta T} \right)^2 \left(\frac{1}{c_{p,g}} - \frac{1}{c_{p,l}} \right) \quad (1)$$

where k_B is the Boltzmann constant, ρ is the density, T_{α} is the transformation temperature, $c_{p,g}$ and $c_{p,l}$ are the specific heat capacities of the glass and of the supercooled liquid respectively measured at T_{α} and δT represents the temperature fluctuation. The temperature fluctuation is obtained from the width of the thermal relaxation spectrum.

Comparisons between the free volume estimated using Positron Annihilation Lifetime Spectroscopy (PALS) and the

Received: February 27, 2024

Revised: March 18, 2024

Accepted: March 20, 2024

cooperative volume V_α estimated by Donth's approach revealed that the appearance of open-volume defects leads to a significant decrease of V_α in As–Se chalcogenide glasses.²⁹ The same behavior was observed for a polymeric glass former, poly(lactic acid) (PLA).³⁰ A very recent work compared the CRR sizes measured by NSE spectroscopy and heat capacity spectroscopy, confirming the soundness of Donth's approach (eq 1).⁶ The typical spatial extent of a CRR decreases with increasing temperature, and eventually drops to the order of 1 nm.⁶

In this work, the cooling-rate dependence of the vitrification process was evaluated over a broad range of cooling rates (10^{-3} to 10^4 K s⁻¹) and a relatively wide temperature range (about 40 K) and then used to estimate the temperature dependence of the spatial extent of CRR in two polymeric glass formers and a chalcogenide glass former having comparable glass transition temperatures.

One high-purity atomic chalcogenide glass former (selenium) and two macromolecular organic glass formers (poly(vinyl acetate) (PVAc) and poly(lactic acid) (PLA)) with possible compositional fluctuations were selected to investigate the influence of structural and compositional complexity on molecular dynamics. The molar mass of the repeating unit M_0 and the density ρ of the selected materials are 79 g mol⁻¹ and 4.28 g cm⁻³ (amorphous selenium), 86 g mol⁻¹ and 1.19 g cm⁻³ (PVAc), and 72 g mol⁻¹ and 1.25 g cm⁻³ (PLA). Selenium (99.99% purity) was provided by CERAC Inc. and was used as received. PVAc pellets were purchased from Sigma-Aldrich, oven-dried (24 h at 50 °C), hot-pressed (2 min at 120 °C under 1.5 tons), and left to cool to room temperature, providing films with a controlled thickness of about 500 μ m. PLA pellets with 95.7% L and 4.3% D isomer contents (PLA4042D) were purchased from NatureWorks, oven-dried (12 h at 60 °C), hot-pressed (3 min at 200 °C under 2 tons), and quenched in water to obtain amorphous films with a controlled thickness of about 200 μ m. The polymer pellets were hot-pressed into films to ease sample preparation (improved contact surface and reduced thermal lag through the thickness of the sample). All of the samples remained fully amorphous throughout the experiments.

Differential Scanning Calorimetry (DSC) and stochastic modulated-temperature DSC (TOPEM) measurements were carried out using a Mettler-Toledo DSC 3+ equipped with a FRS6 sensor. Temperature, enthalpy, and thermal lag calibrations were performed using zinc, indium, and water standards. The samples for both DSC and TOPEM measurements were placed in 40 μ L sealed aluminum pans. The experiments were performed under nitrogen (flow rate 50 mL min⁻¹). DSC measurements consisted in rejuvenating the sample at $T_g + 20$ °C for 10 min before cooling down to $T_g - 20$ °C at rates $|\beta_c|$ between 1 and 30 K min⁻¹. The thermal glass transition temperature T_g was obtained from DSC curves subsequently recorded with a heating rate of $\beta_h = 10$ K min⁻¹. TOPEM measurements consisted of cooling segments from $T_g + 20$ °C down to $T_g - 20$ °C at rates $|\beta_c|$ between 0.2 and 2 K min⁻¹ with a pulse height of 0.5 K and pulse widths between 20 and 40 s. An extrapolation to zero frequency was performed to obtain the quasistatic heat capacity $c_{p,0}$ as a function of the temperature. More details about TOPEM can be found elsewhere.³¹

FSC measurements were performed using a Mettler-Toledo Flash DSC 2+ instrument equipped with a Huber intracooler TC100. The samples for FSC were cut into small pieces under

a microscope and then transferred by using a paint brush hair onto the center of the active zone of a conditioned and temperature-corrected MultiSTAR sensor. For selenium, silicon oil was used as a contact medium. Depending on the targeted range of cooling rates, different sensors (UFS1 or UFH1) were used, with samples masses between 20 and 500 ng, to increase sensibility and reduce the effects of thermal lag and instrument drift.³² A constant nitrogen flow of 30 mL min⁻¹ was used to prevent oxidative degradation. The sensor support temperature was -95 °C. The sample mass was estimated by comparing the step height of heat capacity at the thermal glass transition temperature obtained with FSC and TOPEM respectively, according to eq 2:

$$m = \frac{\Delta C_{p,\text{FSC}}}{\Delta c_{p,\text{TOPEM}}} \quad (2)$$

where $\Delta C_{p,\text{FSC}}$ is the step of heat capacity measured by FSC (in J K⁻¹) and $\Delta c_{p,\text{TOPEM}}$ is the corresponding change in specific heat capacity measured by TOPEM (in J g⁻¹ K⁻¹) both at the thermal glass transition temperature.

The samples were cooled down to -95 °C from 150 °C (PVAc and PLA) or 230 °C (selenium) with cooling rates $|\beta_c|$ between 1 and 15,000 K s⁻¹. A heating scan was subsequently recorded with $\beta_h = |\beta_c|$. The limiting fictive temperature T_f , which is the temperature that best describes the glass transition, was determined from both the cooling and the heating curves.³³ Data reproducibility and sample stability were ensured by comparing the results obtained with the same thermal cycle before and after each series of measurements.³⁴

An increase in the cooling rate makes the glass transition broaden and shift toward the high temperature range.³⁵ A thorough investigation of the temperature dependence of the relaxation process requires correcting the smearing due to thermal inertia. The corrected heat flow Φ_m^0 can be obtained with the Tian equation:³⁶

$$\Phi_m^0 = \Phi_m + \tau_0 \frac{d(\Phi_m)}{dt} \quad (3)$$

where Φ_m is the measured heat flow and τ_0 is a time constant, that for glass transition can be calculated as

$$\tau_0 = \frac{T_{f,h} - T_{f,c}}{2\beta} \quad (4)$$

where $T_{f,h}$ and $T_{f,c}$ are the limiting fictive temperatures measured upon heating and cooling respectively, and $\beta = \beta_h = |\beta_c|$ is the rate.

The corrected and normalized heat flow recorded upon cooling at different cooling rates is shown in Figure 1 for all of the selected glass formers.

The temperature fluctuation is usually estimated from heat capacity spectroscopy data. The width of the glass transition measured upon cooling at a frequency ω is related to the temperature fluctuation as $\Delta T_\omega \approx 2 \delta T$.¹³ In principle, δT can also be estimated from the shape of the heat flow curve recorded upon cooling at a constant rate β_c . Due to the nonlinearity of the vitrification process, which occurs through a progressive viscous slowing down of molecular motions, the width ΔT_{β_c} is broader than the width ΔT_ω . This effect is described by the vitrification function κ :¹³

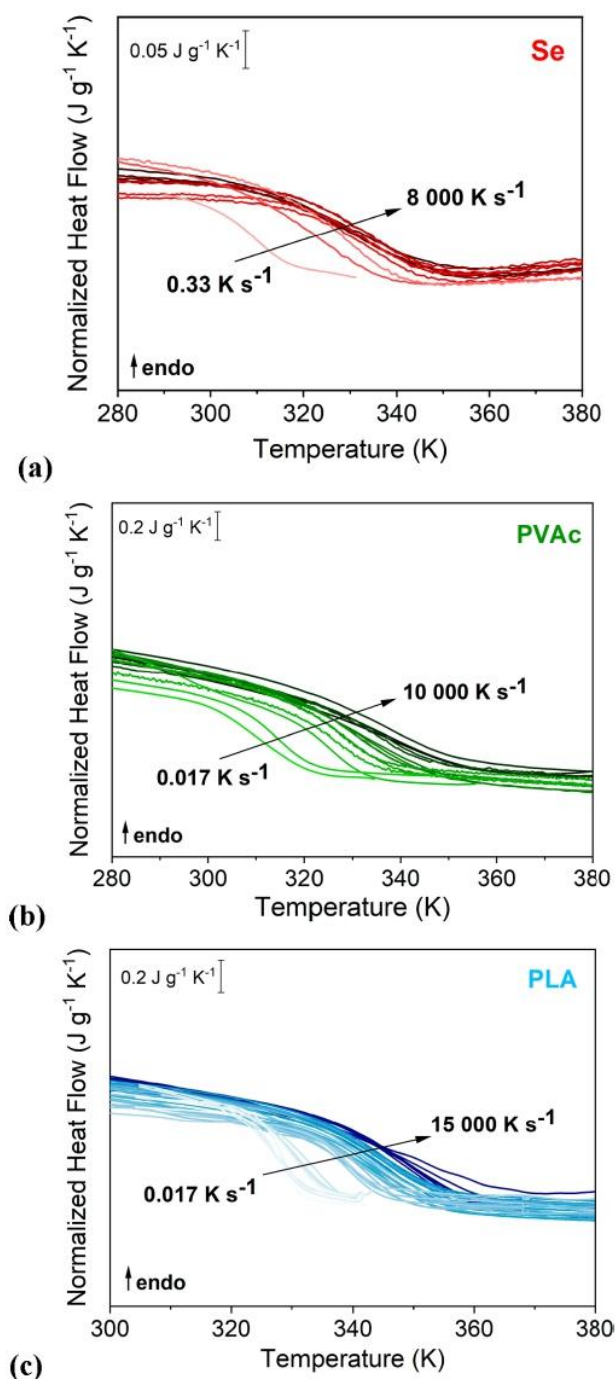


Figure 1. Corrected and normalized heat flow measured upon cooling through the glass transition with cooling rates ranging from 0.017 to 15,000 K s⁻¹ for (a) selenium, (b) PVAc, and (c) PLA.

$$\kappa(T) = \frac{\Delta T_{\beta_c}(T)}{\Delta T_{\alpha}(T)} \quad (5)$$

The cooling-rate dependence of ΔT_{β_c} was evaluated for all of the selected glass formers (Figure 2a), and selenium showed the biggest change over the investigated range. Measurements performed on polystyrene had previously suggested that κ is invariant with respect to temperature ($\kappa \approx 2.5$).¹³ The vitrification function was therefore calculated over the entire

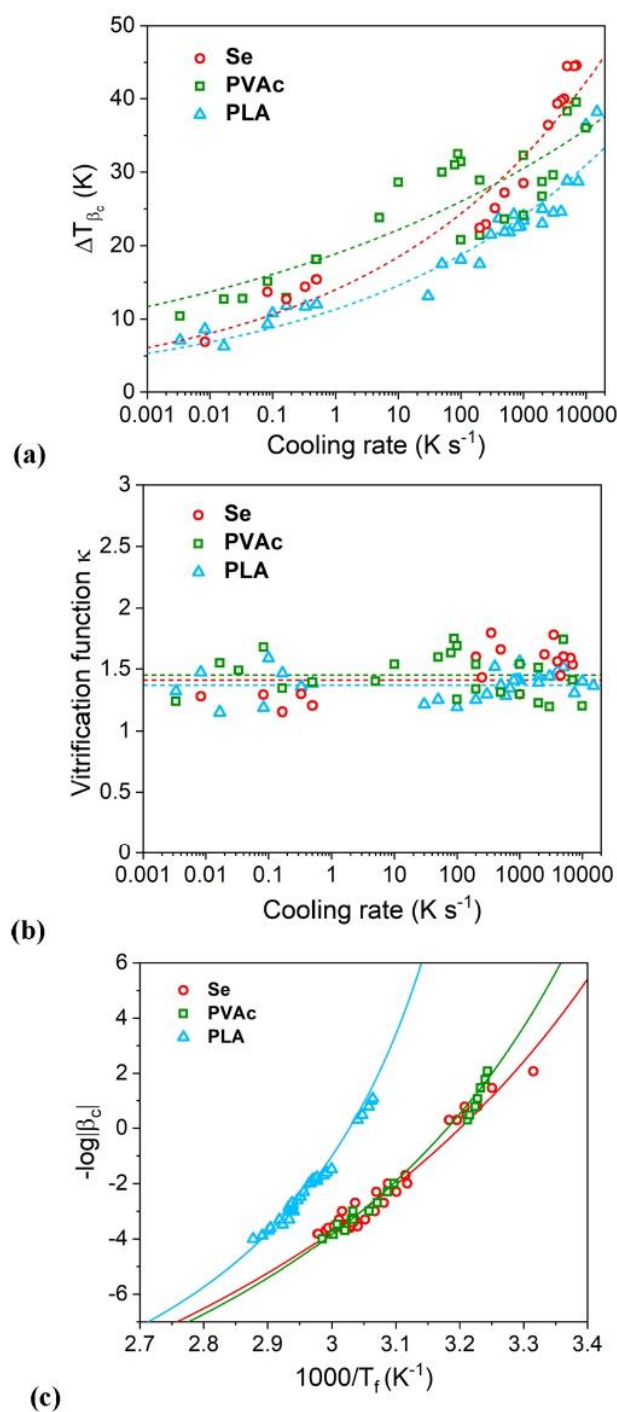


Figure 2. (a) Cooling-rate dependence of the glass transition width ΔT_{β_c} for selenium (red circles), PVAc (green squares), and PLA (blue triangles). The dotted lines are guides to the eye. (b) Cooling-rate dependence of the vitrification function κ . The dotted lines correspond to the mean value. (c) Cooling-rate dependence of the limiting fictive temperature. The solid lines are the VFT fits.

range of cooling rates for all of the considered glass formers (Figure 2b). The obtained value ($\kappa \approx 1.4$) is indeed constant, but smaller than the one previously reported for polystyrene.¹³ It is reasonable to assume that the vitrification function κ

contains fundamental information about the vitrification process, but this has not yet been investigated.

Knowing κ , the temperature fluctuation δT can be accurately estimated from the cooling curves by

$$\delta T = \frac{\Delta T_{\beta c}}{2\kappa} \quad (6)$$

This method was previously used, but assuming an estimated value of κ .³⁷ However, the experimental determination of κ is essential for this method, due to the significant influence of δT on ξ_{α} .

The Frenkel–Kobeko–Reiner (FKR) hypothesis considers that the cooling-rate dependence of the vitrification is analogous to the frequency dependence of the thermal relaxation.¹³ The FKR hypothesis is also known as the Bartenev–Ritland hypothesis, whose representation was given by Schmelzer.³⁸ Assuming the FKR hypothesis, the cooling-rate dependence of the glass transition follows the Vogel–Fulcher–Tammann (VFT) equation:

$$\log|\beta_c| = A - \frac{B}{T - T_v} \quad (7)$$

where A and B are fitting parameters, and T_v is the Vogel temperature below T_g . This relation has been verified for various materials.^{39–42}

The concept of fragility introduced by Angell⁴³ is commonly used to describe the deceleration of the relaxation dynamics in a glass-forming liquid approaching its glass transition. The cooling-rate dependence of the glass transition can be used to estimate the fragility index m_f based on the VFT equation:

$$m_f = \left[\frac{d(\log|\beta_c|)}{d\left(\frac{T_g}{T}\right)} \right]_{T=T_g} = \frac{BT_g}{(T_g - T_v)^2} \quad (8)$$

The cooling-rate dependence of the limiting fictive temperature T_f ³³ obtained with different cooling rates is plotted in Figure 2c accompanied by the VFT fitting curves (the corresponding fitting parameters are listed in Table 1). The

Table 1. Thermal Glass Transition Temperature (T_g), VFT Fitting Parameters (A , B , and T_v), and Angell's Fragility Index (m_f) for Selenium, PVAc, and PLA

Material	T_g (K)	A	B (K)	T_v (K)	m_f
Selenium	310 ± 1	12.6	652	260 ± 28	81 ± 7
PVAc	312 ± 1	13.0	608	267 ± 15	94 ± 4
PLA	327 ± 1	14.4	580	290 ± 10	139 ± 11

fragility indexes obtained for selenium, PLA, and PVAc are 81, 139, and 94, respectively. These values agree well with the data reported in the literature (87 for selenium,⁴⁴ 144 for amorphous PLA,⁴⁵ 89 and 95 for PVAc^{45,46}).

The temperature dependence of δT shown in Figure 3 can be described using the VFT parameters B and T_v :

$$\delta T(T) = \frac{\delta q(T - T_v)^2}{B \ln 10} \quad (9)$$

The fitting parameter δq characterizes the logarithmic frequency width of the thermal α -relaxation spectrum in the supercooled liquid. The fitting curves in Figures 3a, 3b, and 3c provide values of δq equal to 3.0 for selenium and 3.2 for both

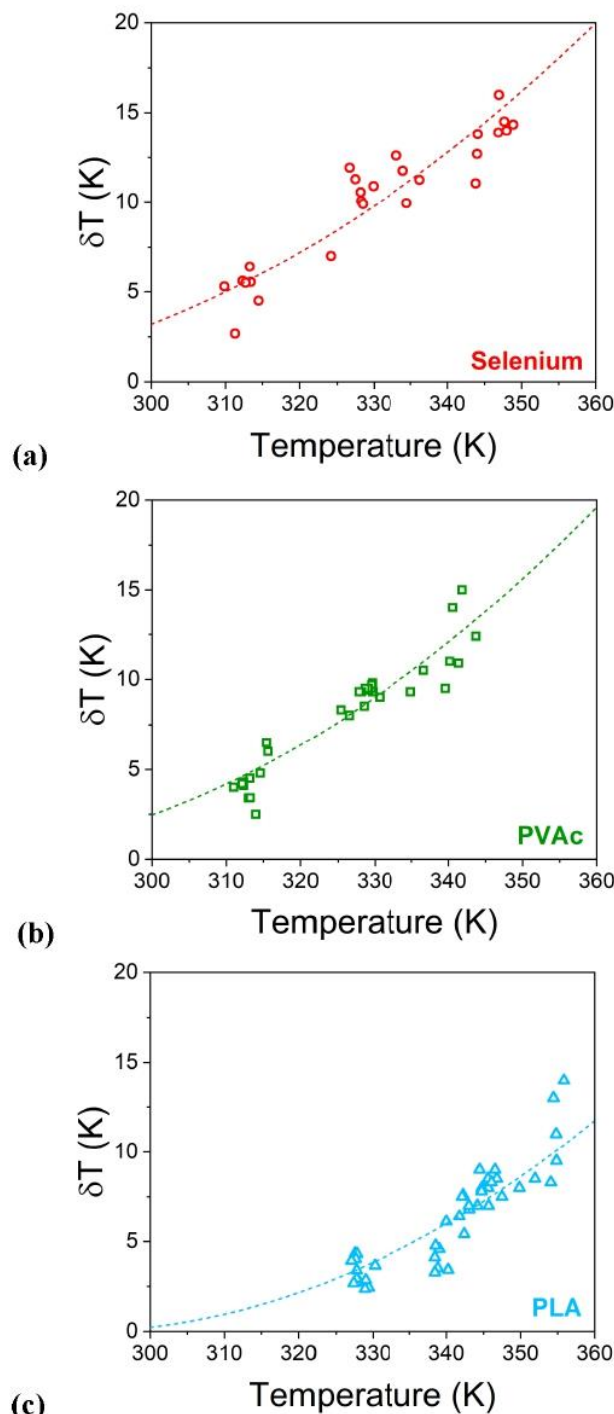


Figure 3. Temperature dependence of the temperature fluctuation δT for (a) selenium, (b) PVAc, and (c) PLA. The dashed lines represent the fitting curves according to eq 9.

PVAc and PLA. A kinetic model for the temperature dependence of the width of the glass transition was presented by Schmelzer et al.⁴⁷ This model appears to agree, at least qualitatively, with the data shown in Figure 3. The relaxation spectrum is often described by the Fourier-transformed relaxation function ϕ containing a stretched exponential:

$$\phi(t) = \exp\left(-\frac{t}{\tau_k}\right)^{\beta_K} \quad (10)$$

where τ_k is the characteristic relaxation time and β_K is the Kohlrausch exponent. These parameters are related to each other, and their relation can be approximated as $\delta q \approx 1.07/\beta_K$.²⁸

Assuming a spherical shape for CRR, the characteristic length of the α -relaxation ξ_α can be calculated as

$$\xi_\alpha = \left(\frac{6}{\pi} V_\alpha\right)^{1/3} \quad (11)$$

where the volume of CRR, V_α is given by eq 1.

Figure 4a and 4b show the variations of ξ_α with the cooling rate and temperature, respectively. As expected, ξ_α decreases when the cooling rate used for vitrification increases. The temperature dependence of ξ_α is similar for all the considered materials; the cooperativity length increases as T_g is approached from the supercooled liquid-like state, whereas at high temperatures it flattens down to a constant value. Introducing a reduced temperature, i.e., replacing T with T/T_g could help verify if such a temperature dependence of ξ_α is a universal behavior. Indeed, Figure 4c shows that within the order of experimental uncertainty all the considered materials behave identically over the entire temperature range. This seems to suggest that the chemical composition and structure, and in particular the intermolecular interactions, have no significant influence on nanoscale cooperative fluctuation in supercooled glass-forming liquids approaching the glass transition upon cooling.

In summary, this work investigates the kinetics of the glass transition of three glass formers with different chemical compositions and structures, but comparable thermal glass transition temperature and kinetics of vitrification. The investigations were performed on fragile glass formers with fragility indexes between 81 and 139. The temperature fluctuation δT represents a key parameter for an accurate estimation of the characteristic length ξ_α of the cooperative rearrangements in the supercooled melt. A modified technique is proposed that utilizes the vitrification function κ to provide a simple method for estimating δT from DSC curves recorded upon cooling.

For all of the considered materials, ξ_α behaves identically when plotted against the reduced temperature T/T_g over a wide temperature range. The CRR size of the atomic chalcogenide glass former (selenium) follows the exact same trend as the two polymeric systems. This means that the chemical structure of the glass-forming liquid (atomic or macromolecular) has no significant influence on ξ_α in the vicinity of T_g . A possible explanation is that the moieties involved in the cooperative rearrangements are so small that neither the covalent bonds within the macromolecules nor the intermolecular interactions can actually affect the temperature dependence of the CRR size. The most relevant parameter, which is indeed material dependent, is the glass transition temperature itself, which is controlled by the mobility of the relaxing moieties, as well as by the strength of their interactions. The fragile glass formers selected for this study have comparable thermal glass transition temperatures T_g , and indeed no difference was detected in the temperature evolution of ξ_α as a function of the reduced temperature T/T_g . The difference that one might expect between polymers and

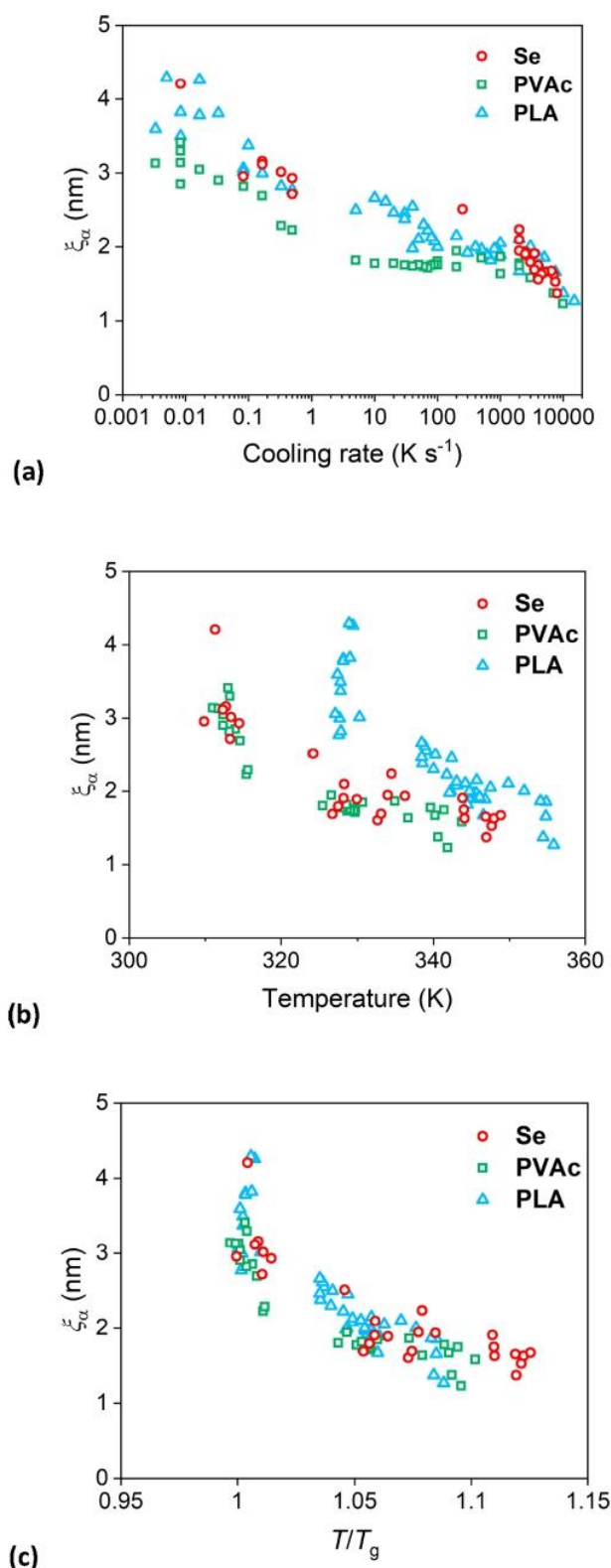


Figure 4. (a) Cooling-rate dependence of the characteristic length ξ_α and (b) temperature dependence of the characteristic length ξ_α for selenium (red circles), PVAc (green squares), and PLA (blue triangles). (c) Characteristic length ξ_α versus reduced temperature T/T_g .

simpler (i.e., non-macromolecular) glass formers due to the presence of intra-macromolecular barriers⁴⁸ is actually not related to the size of the fluctuating heterogeneities accompanying the cooperative rearrangements. In conclusion, the amplitude of the nanoscale dynamic heterogeneities in highly supercooled liquids is only related to the macroscopic kinetics of the glass transition but is not significantly influenced by the chemical composition and structure, unless these latter significantly affect the glass transition temperature itself or the fragility.

AUTHOR INFORMATION

Corresponding Authors

Jürgen E. K. Schawe – *Mettler-Toledo GmbH, 8606 Nänikon, Switzerland; Laboratory of Metal Physics and Technology, Department of Materials, ETH Zurich, 8093 Zurich, Switzerland; orcid.org/0000-0002-2246-2236; Email: juergen.schawe@mt.com*

Allison Saiter-Fourcin – *Univ Rouen Normandie, INSA Rouen Normandie, CNRS, F-76000 Rouen, France; orcid.org/0000-0001-9275-6865; Email: allison.saiter@univ-rouen.fr*

Authors

Kylian Hallavant – *Univ Rouen Normandie, INSA Rouen Normandie, CNRS, F-76000 Rouen, France*

Marouane Mejres – *Univ Rouen Normandie, INSA Rouen Normandie, CNRS, F-76000 Rouen, France*

Antonella Esposito – *Univ Rouen Normandie, INSA Rouen Normandie, CNRS, F-76000 Rouen, France; orcid.org/0000-0003-0507-1417*

Complete contact information is available at: <https://pubs.acs.org/10.1021/acs.jpcl.4c00632>

Author Contributions

K.H.: Investigation, Formal analysis, Writing-original draft. M.M.: Investigation. J.E.K.S.: Conceptualization, Methodology, Validation, Writing-original draft. A.E.: Supervision, Validation, Writing-review and editing. A.S.F.: Resources, Conceptualization, Methodology, Writing-review and editing, Supervision, Project administration.

Notes

The authors declare no competing financial interest.

ACKNOWLEDGMENTS

The authors acknowledge the financial support provided by the Normandy Region through the Graduate School Materials & Energy Sciences (GS-MES) and the Laboratory of Excellence Energy, Materials & Clean Combustion Center (LabEx EMC3), as well as Mettler Toledo for lending the DSC 3+.

REFERENCES

- (1) Tammann, G. *Kristallisieren Und Schmelzen*; Verlag J.A. Barth.: Leipzig, 1903.
- (2) Sato, A.; Sasaki, T. Cooperativity of Dynamics in Supercooled Polymeric Materials and Its Temperature Dependence Predicted from a Surface Controlled Model. *Eur. Polym. J.* **2018**, *99*, 485–494.
- (3) Ruta, B.; Baldi, G.; Chushkin, Y.; Rufflé, B.; Cristofolini, L.; Fontana, A.; Zanatta, M.; Nazzari, F. Revealing the Fast Atomic Motion of Network Glasses. *Nat. Commun.* **2014**, *5* (1), 3939.
- (4) Hechler, S.; Ruta, B.; Stolpe, M.; Pineda, E.; Evenson, Z.; Gross, O.; Bernasconi, A.; Busch, R.; Gallino, I. Microscopic Evidence of the Connection between Liquid-Liquid Transition and Dynamical

Crossover in an Ultraviscous Metallic Glass Former. *Phys. Rev. Mater.* **2018**, *2* (8), 085603.

- (5) Zhang, P.; Maldonis, J. J.; Liu, Z.; Schroers, J.; Voyles, P. M. Spatially Heterogeneous Dynamics in a Metallic Glass Forming Liquid Imaged by Electron Correlation Microscopy. *Nat. Commun.* **2018**, *9* (1), 1129.

- (6) Chua, Y. Z.; Zorn, R.; Schmelzer, J. W. P.; Schick, C.; Holderer, O.; Zamponi, M. Determination of Cooperativity Length in a Glass-Forming Polymer. *ACS Phys. Chem. Au* **2023**, *3* (2), 172–180.

- (7) Zhuravlev, E.; Schick, C. Fast Scanning Power Compensated Differential Scanning Nano-Calorimeter: 1. The Device. *Thermochim. Acta* **2010**, *505* (1–2), 1–13.

- (8) Mathot, V.; Pyda, M.; Pijpers, T.; Vanden Poel, G.; van de Kerkhof, E.; van Herwaarden, S.; van Herwaarden, F.; Leenaers, A. The Flash DSC 1, a Power Compensation Twin-Type, Chip-Based Fast Scanning Calorimeter (FSC): First Findings on Polymers. *Thermochim. Acta* **2011**, *522* (1–2), 36–45.

- (9) Huth, H.; Minakov, A. A.; Schick, C. Differential AC-chip Calorimeter for Glass Transition Measurements in Ultrathin Films. *J. Polym. Sci., Part B: Polym. Phys.* **2006**, *44* (20), 2996–3005.

- (10) Shoifet, E.; Chua, Y. Z.; Huth, H.; Schick, C. High Frequency Alternating Current Chip Nano Calorimeter with Laser Heating. *Rev. Sci. Instrum.* **2013**, *84* (7), 073903.

- (11) Monnier, X.; Colmenero, J.; Wolf, M.; Cangialosi, D. Reaching the Ideal Glass in Polymer Spheres: Thermodynamics and Vibrational Density of States. *Phys. Rev. Lett.* **2021**, *126* (11), 118004.

- (12) Monnier, X.; Cangialosi, D.; Ruta, B.; Busch, R.; Gallino, I. Vitrification Decoupling from α -Relaxation in a Metallic Glass. *Sci. Adv.* **2020**, *6* (17), No. eaay1454.

- (13) Schawe, J. E. K. Vitrification in a Wide Cooling Rate Range: The Relations between Cooling Rate, Relaxation Time, Transition Width, and Fragility. *J. Chem. Phys.* **2014**, *141* (18), 184905.

- (14) Ryu, C. W.; Egami, T. Medium-Range Atomic Correlation in Simple Liquids. I. Distinction from Short-Range Order. *Phys. Rev. E* **2021**, *104* (6), 064109.

- (15) Sørensen, S. S.; Biscio, C. A. N.; Bauchy, M.; Fajstrup, L.; Smedskjaer, M. M. Revealing Hidden Medium-Range Order in Amorphous Materials Using Topological Data Analysis. *Sci. Adv.* **2020**, *6* (37), No. eabc2320.

- (16) Wang, X.; Xu, W.-S.; Zhang, H.; Douglas, J. F. Universal Nature of Dynamic Heterogeneity in Glass-Forming Liquids: A Comparative Study of Metallic and Polymeric Glass-Forming Liquids. *J. Chem. Phys.* **2019**, *151* (18), 184503.

- (17) Debenedetti, P. G.; Stillinger, F. H. Supercooled Liquids and the Glass Transition. *Nature* **2001**, *410* (6825), 259–267.

- (18) Alzate-Vargas, L.; Onofrio, N.; Strachan, A. Universality in Spatio-Temporal High-Mobility Domains Across the Glass Transition from Bulk Polymers to Single Chains. *Macromolecules* **2020**, *53* (21), 9375–9385.

- (19) Nie, Y.; Ye, X.; Zhou, Z.; Yang, W.; Tao, L. Intrinsic Correlations between Dynamic Heterogeneity and Conformational Transition in Polymers during Glass Transition. *J. Chem. Phys.* **2014**, *141* (7), 074901.

- (20) Adam, G.; Gibbs, J. H. On the Temperature Dependence of Cooperative Relaxation Properties in Glass-Forming Liquids. *J. Chem. Phys.* **1965**, *43* (1), 139–146.

- (21) Shi, Y.; Deng, B.; Gulbitten, O.; Bauchy, M.; Zhou, Q.; Neufeind, J.; Elliott, S. R.; Smith, N. J.; Allan, D. C. Revealing the Relationship between Liquid Fragility and Medium-Range Order in Silicate Glasses. *Nat. Commun.* **2023**, *14* (1), 13.

- (22) Firlus, A.; Stoica, M.; Michalik, S.; Schäublin, R. E.; Löffler, J. F. Atomic Structure Evolution Related to the Invar Effect in Fe-Based Bulk Metallic Glasses. *Nat. Commun.* **2022**, *13* (1), 1082.

- (23) Nomoto, K.; Ceguerra, A. V.; Gammner, C.; Li, B.; Bilal, H.; Hohenwarter, A.; Gludovatz, B.; Eckert, J.; Ringer, S. P.; Kruzic, J. J. Medium-Range Order Dictates Local Hardness in Bulk Metallic Glasses. *Mater. Today* **2021**, *44*, 48–57.

- (24) Lan, S.; Zhu, L.; Wu, Z.; Gu, L.; Zhang, Q.; Kong, H.; Liu, J.; Song, R.; Liu, S.; Sha, G.; Wang, Y.; Liu, Q.; Liu, W.; Wang, P.; Liu,

C.-T.; Ren, Y.; Wang, X.-L. A Medium-Range Structure Motif Linking Amorphous and Crystalline States. *Nat. Mater.* **2021**, *20* (10), 1347–1352.

(25) Landau, L. D.; Lifschitz, E. M. *Statistical Physics*; Akademie Verlag: 1987.

(26) Mandelbrot, B. B. Temperature Fluctuation: A Well-Defined and Unavoidable Notion. *Phys. Today* **1989**, *42* (1), 71–73.

(27) Hempel, E.; Hempel, G.; Hensel, A.; Schick, C.; Donth, E. Characteristic Length of Dynamic Glass Transition near T_g for a Wide Assortment of Glass-Forming Substances. *J. Phys. Chem. B* **2000**, *104* (11), 2460–2466.

(28) Donth, E. The Size of Cooperatively Rearranging Regions at the Glass Transition. *J. Non-Cryst. Solids* **1982**, *53* (3), 325–330.

(29) Saiter, A.; Saiter, J.-M.; Golovchak, R.; Shpotyuk, M.; Shpotyuk, O. Cooperative Rearranging Region Size and Free Volume in As-Se Glasses. *J. Phys.: Condens. Matter* **2009**, *21* (7), 075105.

(30) Varol, N.; Delpouve, N.; Araujo, S.; Domenek, S.; Guinault, A.; Golovchak, R.; Ingram, A.; Delbreilh, L.; Dargent, E. Amorphous Rigidification and Cooperativity Drop in Semi-crystalline Plasticized Polylactide. *Polymer* **2020**, *194*, 122373.

(31) Schawe, J. E. K.; Hütter, T.; Heitz, C.; Alig, I.; Lellinger, D. Stochastic Temperature Modulation: A New Technique in Temperature-Modulated DSC. *Thermochim. Acta* **2006**, *446* (1–2), 147–155.

(32) Schawe, J. E. K.; Pogatscher, S. Material Characterization by Fast Scanning Calorimetry: Practice and Applications. In *Fast Scanning Calorimetry*; Schick, C., Mathot, V., Eds.; Springer International Publishing: Cham, 2016; pp 3–80. DOI: 10.1007/978-3-319-31329-0_1.

(33) Moynihan, C. T.; Macedo, P. B.; Montrose, C. J.; Montrose, C. J.; Gupta, P. K.; DeBolt, M. A.; Dill, J. F.; Dom, B. E.; Drake, P. W.; Eastal, A. J.; Elterman, P. B.; Moeller, R. P.; Sasabe, H.; Wilder, J. A. STRUCTURAL RELAXATION IN VITREOUS MATERIALS*. *Ann. N.Y. Acad. Sci.* **1976**, *279* (1), 15–35.

(34) Schawe, J. E. K.; Pogatscher, S.; Löffler, J. F. Thermodynamics of Polymorphism in a Bulk Metallic Glass: Heat Capacity Measurements by Fast Differential Scanning Calorimetry. *Thermochim. Acta* **2020**, *685*, 178518.

(35) Chua, Y. Z.; Schulz, G.; Shoifet, E.; Huth, H.; Zorn, R.; Schmelzer, J. W. P.; Schick, C. Glass Transition Cooperativity from Broad Band Heat Capacity Spectroscopy. *Colloid Polym. Sci.* **2014**, *292* (8), 1893–1904.

(36) Vyazovkin, S.; Sbirrazzuoli, N. Nonisothermal Crystallization Kinetics by DSC: Practical Overview. *Processes* **2023**, *11* (5), 1438.

(37) Sasaki, T.; Ichimura, M.; Irie, S. Correlation between Fragility and Cooperativity in Segmental Dynamics of Glass-Forming Para-Substituted Polystyrenes. *Polym. J.* **2015**, *47* (10), 687–694.

(38) Schmelzer, J. W. P. Kinetic Criteria of Glass Formation and the Pressure Dependence of the Glass Transition Temperature. *J. Chem. Phys.* **2012**, *136* (7), 074512.

(39) Schawe, J. E. K. Measurement of the Thermal Glass Transition of Polystyrene in a Cooling Rate Range of More than Six Decades. *Thermochim. Acta* **2015**, *603*, 128–134.

(40) Dhotel, A.; Rijal, B.; Delbreilh, L.; Dargent, E.; Saiter, A. Combining Flash DSC, DSC and Broadband Dielectric Spectroscopy to Determine Fragility. *J. Therm. Anal. Calorim.* **2015**, *121* (1), 453–461.

(41) Gao, S.; Simon, S. L. Measurement of the Limiting Fictive Temperature over Five Decades of Cooling and Heating Rates. *Thermochim. Acta* **2015**, *603*, 123–127.

(42) Schawe, J. E. K.; Hess, K.-U. The Kinetics of the Glass Transition of Silicate Glass Measured by Fast Scanning Calorimetry. *Thermochim. Acta* **2019**, *677*, 85–90.

(43) Angell, C. A. Spectroscopy Simulation and Scattering, and the Medium Range Order Problem in Glass. *J. Non-Cryst. Solids* **1985**, *73* (1–3), 1–17.

(44) Prots', I. V.; Malinovsky, V. K.; Surovtsev, N. V. Investigation of the Fast Relaxation in Glass-Forming Selenium by Low-Frequency Raman Spectroscopy. *Glass Phys. Chem.* **2008**, *34* (1), 30–36.

(45) Rijal, B.; Delbreilh, L.; Saiter, A. Dynamic Heterogeneity and Cooperative Length Scale at Dynamic Glass Transition in Glass Forming Liquids. *Macromolecules* **2015**, *48* (22), 8219–8231.

(46) Huang, D.; McKenna, G. B. New Insights into the Fragility Dilemma in Liquids. *J. Chem. Phys.* **2001**, *114* (13), 5621–5630.

(47) Schmelzer, J. W. P.; Tropin, T. V.; Fokin, V. M.; Zhang, R.; Abdelaziz, A.; Chua, Y. Z.; Madhavi, V.; Shaffer, T. D.; Schick, C. Correlation between Glass Transition Temperature and the Width of the Glass Transition Interval. *Int. J. Appl. Glass Sci.* **2019**, *10* (4), 502–513.

(48) Colmenero, J. Are Polymers Standard Glass-Forming Systems? The Role of Intramolecular Barriers on the Glass-Transition Phenomena of Glass-Forming Polymers. *J. Phys.: Condens. Matter* **2015**, *27* (10), 103101.

Article

Critical Cooling Rate of Fast-Crystallizing Polyesters: The Example of Poly(alkylene *trans*-1,4-cyclohexanedicarboxylate)

Kylian Hallavant ¹, Michelina Soccio ^{2,3,4}, Giulia Guidotti ², Nadia Lotti ^{2,3,5}, Antonella Esposito ^{1,*}
and Allisson Saiter-Fourcin ¹

- ¹ INSA Rouen Normandie, CNRS, Groupe de Physique des Matériaux UMR 6634, University Rouen Normandie, F-76000 Rouen, France; kylian.hallavant@univ-rouen.fr (K.H.); allisson.saiter@univ-rouen.fr (A.S.-F.)
 - ² Department of Civil, Chemical, Environmental and Materials Engineering, University of Bologna, Via Terracini 28, 40131 Bologna, Italy; m.socio@unibo.it (M.S.); giulia.guidotti9@unibo.it (G.G.); nadia.lotti@unibo.it (N.L.)
 - ³ Interdepartmental Center for Industrial Research on Advanced Applications in Mechanical Engineering and Materials Technology, CIRI-MAM, Viale del Risorgimento 2, 40136 Bologna, Italy
 - ⁴ Interdepartmental Center for Industrial Research on Buildings and Construction, CIRI-EC, Via del Lazzaretto 15/5, 40131 Bologna, Italy
 - ⁵ Interdepartmental Center for Agro-Food Research, CIRI-AGRO, Via Quinto Bucci 336, 47521 Cesena, Italy
- * Correspondence: antonella.esposito@univ-rouen.fr

Abstract: Controlling the cooling rate experienced by a material during a manufacturing process is a challenge and a major issue. Industrial processing techniques are very diverse and may involve a whole range of cooling rates, which are sometimes extremely high for small and/or thin manufactured parts. For polymers, the cooling rate has consequences on both the microstructure and the time-dependent properties. The common cooling rates associated with conventional calorimetric measurements are generally limited to a few tens of degrees per minute. This work combines several calorimetric techniques (DSC, modulated-temperature DSC, stochastically-modulated DSC and Fast Scanning Calorimetry) to estimate the critical cooling rate required to melt-quench fast-crystallizing polyesters to their fully amorphous state, based on the example of a series of poly(alkylene *trans*-1,4-cyclohexanedicarboxylate) (PCHs) with a number of methylene groups in the main structure of the repeating unit n_{CH_2} varying from 3 to 6. The even-numbered ones require faster cooling rates (about 3000 K s^{-1} for $n_{CH_2} = 4$, between 500 and 1000 K s^{-1} for $n_{CH_2} = 6$) compared to the odd-numbered ones (between 50 K min^{-1} and 100 K s^{-1} for $n_{CH_2} = 3$, between 10 and 30 K min^{-1} for $n_{CH_2} = 5$).

Keywords: crystallization kinetics; odd-even effect; microstructure control; quenching



Citation: Hallavant, K.; Soccio, M.; Guidotti, G.; Lotti, N.; Esposito, A.; Saiter-Fourcin, A. Critical Cooling Rate of Fast-Crystallizing Polyesters: The Example of Poly(alkylene *trans*-1,4-cyclohexanedicarboxylate). *Polymers* **2024**, *16*, 2792. <https://doi.org/10.3390/polym16192792>

Academic Editor: Nicolas Sbirrazzuoli

Received: 8 September 2024

Revised: 28 September 2024

Accepted: 29 September 2024

Published: 1 October 2024



Copyright: © 2024 by the authors. Licensee MDPI, Basel, Switzerland. This article is an open access article distributed under the terms and conditions of the Creative Commons Attribution (CC BY) license (<https://creativecommons.org/licenses/by/4.0/>).

1. Introduction

Polymers play an increasing role in manufacturing processes and their production keeps on growing, especially in the packaging industry [1], which is the biggest consumer and producer of plastic waste. However, the decline of fossil resources, and the raise of collective awareness about the impact that waste has on the environment, impose to look for possible alternatives to petroleum-based polymers with reduced carbon footprint and environmental risks. Plastic waste started accumulating in increasingly large amounts in the fifties, and nowadays the environmental pollution due to plastic waste is becoming severe. For this reason, bio-sourced and/or biodegradable polymers, in particular polyesters, have attracted much attention from both academic researchers and industrials—because they appear as one of the most promising solutions for next-generation sustainable packaging, with improved barrier properties against gas and water vapor, and balanced mechanical properties [2,3].

Industrial processing techniques, such as injection molding or additive manufacturing (laser bed fusion, 3D-printing...), involve a whole range of cooling rates (Figure 1), which

depends on the surface-to-volume ratio of the manufactured item, the cooling technology and the temperature of the cooling medium, the covered temperature range, and the thermal conductivity of the material. Sometimes the cooling rates experienced by the material are extremely high, especially when the manufactured parts are small and/or thin. Of course, increasing the cooling rates used for processing helps increasing cost-effectiveness, however it is appropriate to recall that cooling may also have major consequences on polymer microstructure and molecular mobility [4]. In any case, controlling the local cooling rate and understanding its consequences on polymer properties remain a major challenge.

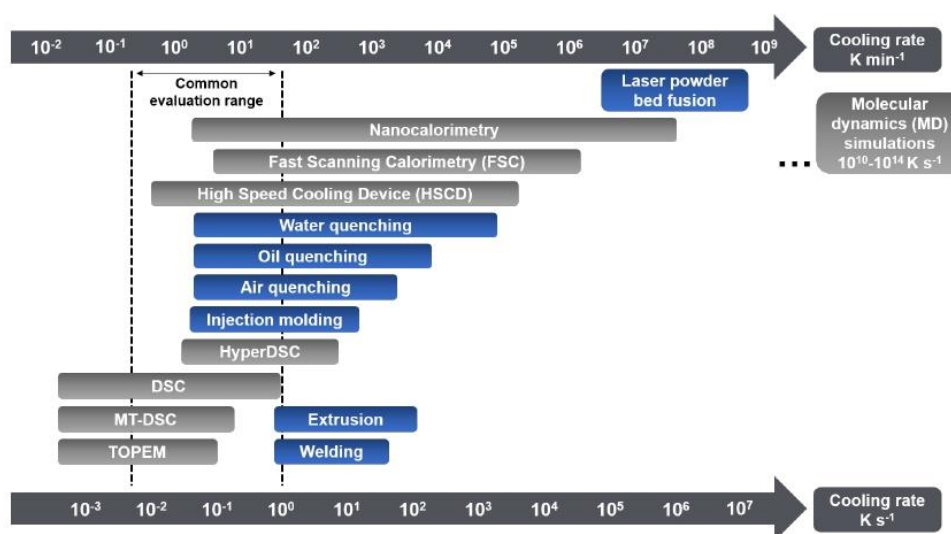


Figure 1. Typical range of cooling rates achievable with different processing and characterization techniques for different materials including polymers [5–24].

A series of biodegradable and potentially bio-based thermoplastic polyesters has been recently synthesized from *trans*-1,4-cyclohexanedicarboxylic acid and linear diols of different lengths. These materials showed interesting barrier and mechanical properties for food packaging applications [25–29], but also a very different aptitude to crystallize depending on the number of methylene groups $-CH_2-$ in their repeating unit (odd-even effect) [30–35]. The cooling rate required for full quenching is expected to be very different for each one of these materials, with different consequences for the ones that are able to crystallize compared to the ones that cannot [36]. It has already been shown that, besides making a difference in terms of nucleus density [37], crystal fraction [38], crystallite size, lamellar thickness and spherulite morphology [39], playing on the cooling rate may significantly affect physical ageing [40] and consequently any other time-dependent property [41,42], even when the polymers are melt-quenched to their fully amorphous state and kept at temperatures below their glass transition.

Schawe and Löffler [43] took the example of Au-based glasses to discuss the existence of multiple critical cooling rates for the generation of different types of glasses. They identified three thresholds, which they called $\beta_{c,SCG}$ (critical cooling rate to obtain a semi-crystalline glass), $\beta_{c,SDG}$ (critical cooling rate to obtain a self-doped glass), and $\beta_{c,CHG}$ (critical cooling rate to obtain a chemically-homogeneous glass). Transposing and adapting this terminology to macromolecular glasses, one may expect that (1) increasing the cooling rate is an efficient way to melt-quench polymers that are intrinsically able to crystallize, (2) crystallization is observed only if the cooling rate is kept below a critical value $\beta_{c,SDG}$, (3) crystallinity reaches different extents depending on the applied cooling rate $\beta_{c,SCG}$ (faster cooling reduces it since it shortens the time allowed for chain folding and vice-versa), (4) because of chain entanglements, crystallinity increases as the cooling rate decreases, until hitting a plateau (100% crystallinity is never reached, not even at the lowest values of

$\beta_{c,SCG}$ or in isothermal conditions), (5) when the cooling rate reaches the threshold $\beta_{c,SDG}$, a self-doped glass (SDG) is obtained, and (6) it is necessary to reach values of cooling rate at least equal to a further threshold $\beta_{c,CHG}$ to obtain a so-called chemically-homogeneous glass (CHG). Cooling down crystallizable polymers at different cooling rates $\beta_c < \beta_{c,SDG}$ may affect their crystalline phase not only quantitatively, but also qualitatively, worsening the intrinsic complexity due to chemistry (polymorphism [44–47], imperfect chain folding with extended coupling between the crystalline and amorphous domains [48–50], development of mesophases [51,52]...). In general, reducing the cooling rate favors the development of larger amounts of more perfect crystals, with positive consequences on properties such as the Young's modulus [53], whereas increasing the cooling rate improves transparency, toughness and elongation at break [54].

Conventional calorimetric measurements are performed at scanning rates generally limited to a few tens of degrees per minute. Fast Scanning Calorimetry (FSC) allows the extension of the experimental window of several orders of magnitude in terms of scanning rate, giving access to cooling rates up to 40,000 K s⁻¹ [41,55], which is ideal to reproduce industrial processing conditions (Figure 1). This work illustrates how to estimate the critical cooling rate $\beta_{c,SDG}$ (threshold between semi-crystalline and fully amorphous samples obtained during melt-quenching) for fast-crystallizing polyesters, taking the example of a series of poly(alkylene *trans*-1,4-cyclohexanedicarboxylate) (PCHs) with a number of methylene groups in the main structure of the repeating unit n_{CH_2} varying from 3 to 6, and combining several calorimetric techniques, i.e., Differential Scanning Calorimetry (DSC), stochastically-modulated DSC (TOPEM) and Fast Scanning Calorimetry (FSC).

2. Materials and Methods

2.1. Reagents

Trans-1,4-cyclohexanedicarboxylic acid (95%, 5 mol% *cis*-isomers) (CHDA) was purchased from Fluorochem (Hadfield, UK). 1,3-propanediol (PD) (98%) was purchased from Carbosynth. 1,4-butanediol (BD) (99%) was purchased from Sigma-Aldrich. 1,5-pentanediol (PeD) (97%) was purchased from Fluka Chemika. 1,6-hexanediol (HD) (>97%) was purchased from TCI. Titanium tetrabutoxide Ti(OBu)₄ (TBT) was purchased from Sigma-Aldrich. All reagents were used as received.

2.2. Polymer Synthesis

Four poly(alkylene *trans*-1,4-cyclohexanedicarboxylate)s (PCHs) were synthesized by a two-step solvent-free melt polycondensation procedure consisting in the esterification reaction between a bifunctional alicyclic acid (CHDA) and a bifunctional linear aliphatic glycol. Depending on the selected glycol, four homopolymers were obtained with a variable number of methylene groups n_{CH_2} in the glycolic fraction of their repeating unit. Poly(propylene *trans*-1,4-cyclohexanedicarboxylate) (PPCE) with $n_{CH_2} = 3$ was obtained with PD. Poly(butylene *trans*-1,4-cyclohexane dicarboxylate) (PBCE) with $n_{CH_2} = 4$ was obtained with BD. Poly(pentamethylene *trans*-1,4-cyclohexanedicarboxylate) (PPECE) with $n_{CH_2} = 5$ was obtained with PeD. Poly(hexamethylene *trans*-1,4-cyclohexanedicarboxylate) (PHCE) with $n_{CH_2} = 6$ was obtained with HD. Each synthesis was carried out starting from CHDA, the selected diol (100% molar excess with respect to the diacid), and TBT (200 ppm) as catalyst, within a 250-mL glass reactor stirred at about 50 rpm in a thermostated oil bath connected to a six-bulb condenser to prevent the evaporation of the reagents. The molar excess of diol promoted the dissolution of the diacid. In the first step, the temperature was set to 190 °C and kept constant for about 1.5 h under a continuous flow of pure nitrogen (50 mL min⁻¹) and a pressure of 1 atm, allowing to distill off up to 90% of the theoretical amount of water. At the beginning of the second step, stirring was increased to 100 rpm and the temperature was raised to 200 °C to remove the excess of diol, then the temperature was further raised to 210 °C and the pressure was gradually reduced to 0.06 mbar to promote the transesterification reactions. The synthesis was carried out for 2 h, until a high and constant torque value was measured indicating that a high molecular weight was reached,

and no more distillation was observed. After the synthesis, all the PCHs were purified by dissolution in chloroform and precipitation in a beaker filled with methanol in large excess (chloroform:methanol 1:10). After purification by dissolution/precipitation, the samples were dried under vacuum (1 h at 0.1 mbar). The samples were continuously stored under vacuum at room temperature, in a desiccator with phosphorus pentoxide P_2O_5 to reduce exposure to humidity until characterization.

2.3. Chemical Characterizations

1H -NMR analyses were carried out to confirm the chemical structure and the *cis/trans* isomer ratio of the synthesized PCHs. The spectra were acquired using a Varian XL-400 NMR spectrometer (Palo Alto, CA, USA) at room temperature (relaxation time = 0 s, acquisition time = 1 s, 100 repetitions). The polymers were dissolved by introducing about 15 mg of sample in 1 mL of deuterated chloroform (containing 0.03 % tetramethylsilane, TMS, as internal reference). The number-average molecular weight (\overline{M}_n), the weight-average molecular weight (\overline{M}_w), the dispersity (\mathcal{D}) and the degree of polymerization (DP_n) of the samples were estimated thanks to the data obtained by Gel Permeation Chromatography (GPC) analysis performed at 30 °C using an HPLC 1100 chromatograph (Agilent Technologies, Santa Clara, CA, USA) equipped with a PLgel 5 mm MiniMIX-C column. A chloroform solution was used as eluent with a flow of 0.3 mL min⁻¹, and sample concentrations of about 2 mg mL⁻¹ were adopted. The calibration curve was obtained using polystyrene standards with a molecular range of 800–100,000 g mol⁻¹. 1H -NMR spectra of the four polyesters can be found in the Supporting Information (Figures S1–S4). A summary of the chemical features of the investigated PCHs is given in Table 1.

Table 1. List of poly(alkylene *trans*-1,4-cyclohexanedicarboxylate)s (PCHs) investigated in this study, along with their repeating unit, the molar mass of their repeating unit (M_0), the number-average molecular weight (\overline{M}_n), the weight-average molecular weight (\overline{M}_w), the dispersity (\mathcal{D}), the degree of polymerization (DP_n) and the percentage of *cis*-isomers in 1,4-cyclohexanedicarboxylic acid.

Sample	Repeating Unit	M_0 (g mol ⁻¹)	\overline{M}_n (g mol ⁻¹)	\overline{M}_w (g mol ⁻¹)	\mathcal{D}	DP_n	<i>cis</i> -Isomers (%)
PPCE		212	62,462	96,657	1.5	295	6.6
PBCE		226	68,703	93,382	1.4	304	5.5
PPeCE		240	57,855	83,592	1.4	241	5.4
PHCE		254	38,666	58,734	1.5	152	9.4

PPCE = poly(propylene *trans*-1,4-cyclohexanedicarboxylate); PBCE = poly(butylene *trans*-1,4-cyclohexanedicarboxylate); PPeCE = poly(pentamethylene *trans*-1,4-cyclohexanedicarboxylate); PHCE = poly(hexamethylene *trans*-1,4-cyclohexanedicarboxylate).

2.4. Thermal Characterizations

Given the aim of the study, the thermal characterizations mostly consisted in calorimetric investigations. Different equipments were used to cover the largest possible range of cooling rates. The lowest cooling rates were covered by Differential Scanning Calorimetry (DSC) and stochastically-modulated DSC (TOPEM), whereas the highest cooling rates were covered by Fast Scanning Calorimetry (FSC) with either UFS1 (lower range) or UFH1 (upper range) MultiSTAR sensors.

DSC and TOPEM experiments were performed using a DSC 3+ (Mettler Toledo) equipped with a FRS 6+ sensor and piloted by the STARe software. Calibrations for temperature, enthalpy, and thermal lag (τ lag) were achieved using zinc, indium, and water standards. The samples for both DSC and TOPEM (masses comprised between 2 and 10 mg) were placed in 40 μ L sealed aluminum pans. The measurements were conducted under a constant nitrogen flow (50 mL min^{-1}). TOPEM measurements were performed with a pulse height of 0.1 K and pulse widths stochastically varying between 15 and 30 s, then an extrapolation to zero frequency was performed to obtain the quasi-static heat capacity $c_{p,0}$ as a function of temperature. More details about TOPEM can be found elsewhere [56].

FSC measurements were performed using a Flash DSC 2+ (Mettler Toledo) equipped with a Huber intracooler TC100 and also piloted by the STARe software. The samples for FSC (masses comprised between 10 and 200 ng) were obtained by successively cutting bulk samples into smaller pieces under a microscope, and then transferred by a hair of a paint brush onto the center of the active zone of a conditioned and temperature-corrected MultiSTAR sensor. The measurements were conducted under a constant argon flow (60 mL min^{-1}). The sensor support temperature was set at -95 $^{\circ}\text{C}$.

For samples that could be successfully melt-quenched by conventional DSC, the mass deposited onto the FSC sensor was estimated according to Equation (1), i.e., by comparing the change in heat capacity at the glass transition temperature ΔC_p obtained with FSC and DSC, as previously reported in the literature [40].

$$m = \frac{\Delta C_p^{FSC}}{\Delta C_p^{DSC}} \quad (1)$$

where ΔC_p^{FSC} [J K^{-1}] is the heat capacity step estimated by FSC and ΔC_p^{DSC} [$\text{J g}^{-1} \text{K}^{-1}$] is the heat capacity step measured by DSC, both at the glass transition temperature.

For samples that could not be obtained in their fully amorphous state within the cooling range provided by conventional DSC, the mass deposited onto the FSC sensor was estimated by comparing the values of heat capacity measured by FSC and specific heat capacity measured by TOPEM at the same temperature, according to Equation (2).

$$m = \frac{C_p^{FSC}(T)}{c_p^{TOPEM}(T)} \quad (2)$$

where C_p^{FSC} [J K^{-1}] is the heat capacity measured by FSC and c_p^{TOPEM} [$\text{J g}^{-1} \text{K}^{-1}$] is the specific heat capacity measured by TOPEM at the same temperature T . At least two temperatures were selected, one in the glassy and one in the liquid state, and the results were averaged.

Preliminary characterizations of the thermal behavior of each PCH were done by DSC through typical heating-cooling-heating ramps, with heating and cooling rates $\beta_h = |\beta_c| = 10$ K min^{-1} . The first heating ramp brought the samples up to the melt, thus ensuring the best thermal contact with the bottom of the aluminum pan and erasing any previous thermal history. The subsequent cooling ramp allowed to compare the relative aptitude to crystallize when the four samples were cooled from the melt at a constant arbitrary cooling rate, providing the temperature range over which crystallization is expected to occur. The second heating ramp provided a glimpse on the microstructural differences induced on each sample due to their different chemical composition, despite the common cooling conditions.

Based on these preliminary results, a thermal protocol consisting in a series of successive cooling and heating ramps was designed for each PCH, with the purpose of evaluating its critical cooling rate $\beta_{c,SDG}$, i.e., the minimum cooling rate at which no crystallization is observed when the polymer is cooled down from the melt. The protocol consisted in heating up each sample with a constant heating rate β_h to a temperature slightly above its melting, holding it for 0.1 s to ensure that melting is complete, cooling it down through the glass transition to -90°C at a constant cooling rate β_c , then heating it up again at 1000 K s^{-1} to check for any possible sign of crystals through melting. The protocol, whose temperature ranges and cooling rates were adjusted to each sample's thermal behavior (crystallization temperature T_c , glass transition temperature T_g , melting temperature range ΔT_m), is schematically represented in Figure 2. Five decades of cooling rates (from 2 K min^{-1} to 5000 K s^{-1}) were investigated to assess the critical cooling rates of PPCE, PBCE, PPeCE and PHCE.

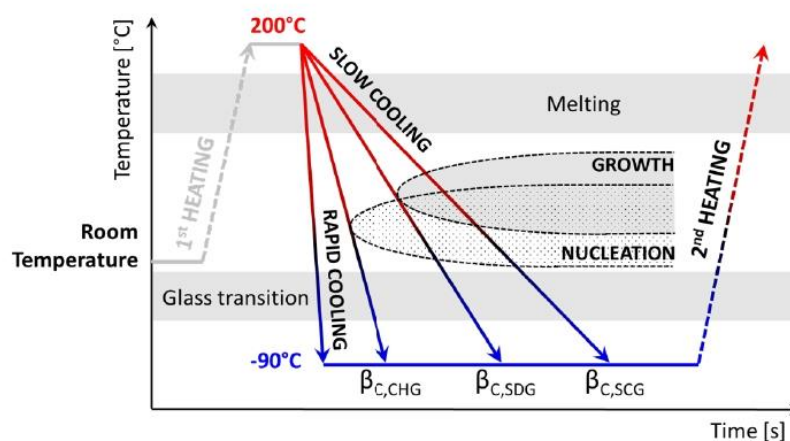


Figure 2. Schematic representation of the thermal protocol used to evaluate the critical cooling rate $\beta_{c,SDG}$, i.e., the minimum cooling rate allowing to obtain a fully amorphous polymer upon quenching from the molten state. The scans in terms of cooling rate covered five decades (from 2 K min^{-1} to 5000 K s^{-1}) thanks to a combination of different calorimetric techniques, i.e., Differential Scanning Calorimetry (DSC), stochastically-modulated DSC (TOPEM) and Fast Scanning Calorimetry (FSC).

3. Results and Discussion

Whenever an alicyclic moiety is introduced in a polymer backbone, the *cis/trans* isomer ratio is expected to potentially influence its crystallization behavior. In particular, the crystallization temperature T_c , glass transition temperature T_g and melting temperature T_m are known to depend on the *trans*-isomer content [57]. Even though the diacid selected for this work mostly contained *trans*-isomers (with only 5% *cis*-isomers), the *cis/trans* isomer ratio was evaluated for all the synthesized PCHs prior to any other thermal characterization (results reported in Table 1). Indeed, it cannot be excluded that the configuration of some molecules changes from *trans* to *cis* during polymerization, the process being generally favored by long exposures to relatively high temperatures in the presence of a catalyst. To minimize the occurrence of undesired *trans/cis* isomerization, i.e., to maintain the highest possible content of *trans*-isomers and consequently ensure high values of T_c , the temperature, time and catalyst content used for the synthesis should be minimized. On the other hand, these very same variables also control the increase in molecular weight during polymerization. Therefore, a compromise had to be found between the best conditions to get high values of T_c , and the best conditions to get a high molecular weight [58]. The synthesis performed in this work was optimized with respect to previous batches [36], for which slightly higher *cis*-isomer contents were obtained. The highest efficiency in maintaining a fixed *trans*-isomer content was observed when CHDA was combined with BD and PeD, i.e., for the synthesis of PBCE

($n_{CH_2} = 4$) and PPeCE ($n_{CH_2} = 5$). The largest extent of undesired *trans/cis* isomerization was observed during the synthesis of PHCE ($n_{CH_2} = 6$), with a *cis*-isomer content however limited to less than 10 %. Both the molecular weight and the degree of polymerization decreased as n_{CH_2} increased, to the point that PHCE ended with a two-fold smaller molecular weight and DP_n compared to PPCE. However, all PCHs were synthesized with satisfactory molecular weights and the same dispersity $D \approx 1.5$ (Table 1).

Figure 3 shows the preliminary results obtained by DSC on all the considered PCHs. The initial melting (first heating ramps) are not shown; the cooling ramps from the melt down to negative temperatures at $|\beta_c| = 10 \text{ K min}^{-1}$ are represented by solid lines; the subsequent heating ramps at $\beta_h = 10 \text{ K min}^{-1}$ are represented by dashed lines. A zoom into the glass transition temperature range is reported in the inset to each graph. The thermal characteristics evidenced by the preliminary results in Figure 3 are summarized in Table 2. The most striking result is that PBCE and PHCE, i.e., the PCHs with an even number of methylene groups ($n_{CH_2} = 4$ and 6), are prone to a very rapid crystallization process ($\Delta T_c < 10 \text{ }^\circ\text{C}$), whereas PPCE ($n_{CH_2} = 3$) crystallizes much slower and PPeCE ($n_{CH_2} = 5$) barely has the time to start the process and shows a wide crystallization peak (large ΔT_c) with a low intensity (Δh_c of 0.5 J g^{-1}). According to these results, the PCHs with an even value of n_{CH_2} are expected to have the highest critical cooling rates $|\beta_{c,SDG}|$, whereas the ones with an odd value of n_{CH_2} should be the easiest to melt-quench. In both cases, an increase in the number of methylene groups appears to profoundly change the crystallization behavior. When the number of methylene groups is even, the change is mostly seen in terms of T_c (with a decrease of about $45 \text{ }^\circ\text{C}$ as n_{CH_2} increases from 4 to 6) with no significant changes in ΔT_c . When the number of methylene groups is odd, the change is more dramatic. As n_{CH_2} increases from 3 to 5, the temperature range for crystallization spreads from about $20 \text{ }^\circ\text{C}$ to more than $40 \text{ }^\circ\text{C}$, and the crystal growth is almost entirely suppressed. For purposes such as minimizing the cycle time for injection molding and yet developing a semi-crystalline microstructure, PCHs with an even number of methylene groups would be the best choice, because crystallization starts at high temperatures and proceeds very fast; the subsequent heating ramp, though, suggests that the crystalline phase grown upon cooling is complex, with a marked trend to reorganization for improved crystal perfection (the melting temperature range ΔT_m spreads over $\approx 80 \text{ }^\circ\text{C}$, and the melting peak has a shape that recalls the double melting peak of polyhydroxyalkanoates [59,60], which are known to be prone to extensive crystalline reorganization upon heating). Crystalline reorganization occurs also in PCHs with an odd number of methylene groups, but apparently to a less extent, with a much narrower melting temperature range ($\Delta T_m < 25 \text{ }^\circ\text{C}$) and just a small exotherm preceding the melting endotherm.

Irrespective of the odd or even character of n_{CH_2} , the melting temperature generally decreases as the number of methylene groups increases. However, the lowest melting (and crystallization) temperature is observed for PPeCE ($n_{CH_2} = 5$). This particular behavior has been reported for other polymers containing five methylene groups in their backbone [31,35]. This phenomenon could be due to some local polarization that builds up in odd-numbered polyesters, hindering the crystallization process, whereas in even-numbered polyesters the dipoles are aligned in opposite directions, allowing a more efficient chain folding and packing [34,61]. NMR experiments conducted on flexible alkyl chains with mesogenic groups at either end showed that, for $n_{CH_2} = 5$, the alkyl chain is in an all-*trans* conformation, except that the conformation around the C-O single bonds was found to be approximately *gauche* [61]. This *gauche* conformation forces the molecule to bend more with respect to an all-*trans* conformation, causing less efficient packing and therefore improving its glass-forming ability. A recent investigation on the crystal structure of PBCE confirms the all-*trans* conformation of its alkyl segments [62]. The values of glass transition temperature T_g consistently decrease with the number of methylene groups introduced in the polymer backbone, from about $8 \text{ }^\circ\text{C}$ for PPCE ($n_{CH_2} = 3$) to about $-21 \text{ }^\circ\text{C}$ for PHCE ($n_{CH_2} = 6$).

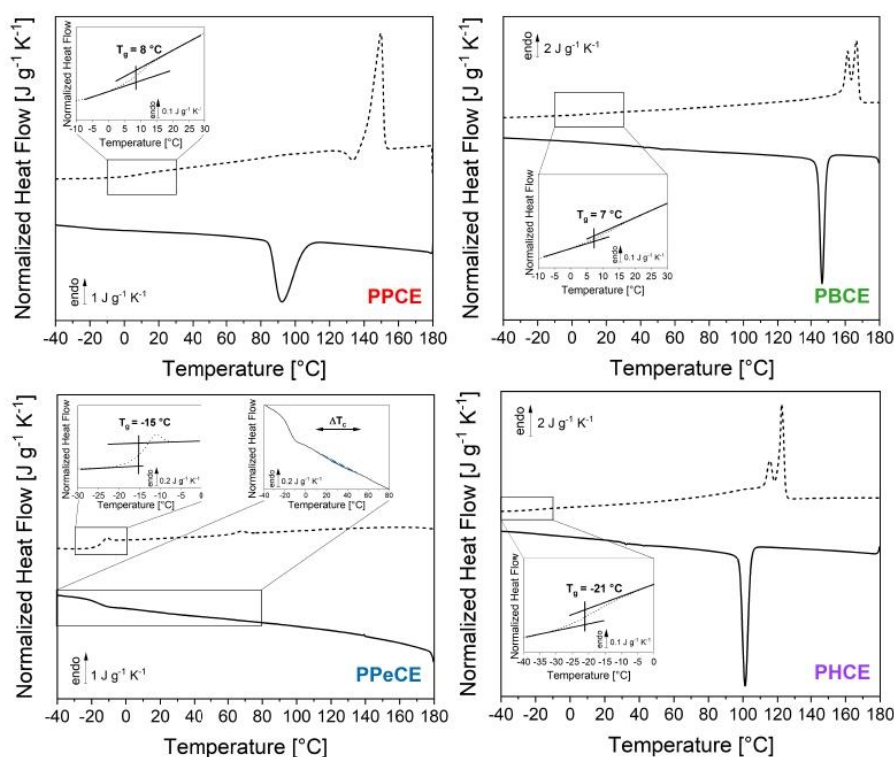


Figure 3. Thermal behavior recorded by DSC with cooling and heating rates $|\beta_c| = \beta_h = 10 \text{ K min}^{-1}$ after melting (the first heating ramp is not shown). A zoom into the glass transition temperature range is reported for each sample in the corresponding inset. For PPeCE, an additional inset zooms into the crystallization temperature range (dashed blue area). PPCE = poly(propylene *trans*-1,4-cyclohexanedicarboxylate). PBCE = poly(butylene *trans*-1,4-cyclohexanedicarboxylate) (PBCE). PPeCE = poly(pentamethylene *trans*-1,4-cyclohexanedicarboxylate). PHCE = poly(hexamethylene *trans*-1,4-cyclohexanedicarboxylate).

Table 2. Thermal characteristics of the investigated PCHs extracted from the thermograms in Figure 3. T_c is the crystallization temperature measured at the maximum of the exothermic peak observed upon cooling, ΔT_c is the temperature range over which crystallization occurs, Δh_c is the enthalpy of crystallization, T_g is the mid-point glass transition recorded upon heating (insets in Figure 3), ΔT_m is the melting temperature range, Δh_m is the enthalpy of melting calculated as the algebraic area under the curve in the melting temperature range.

SAMPLE	T_c (°C)	ΔT_c (°C)	Δh_c (J g ⁻¹)	T_g (°C)	ΔT_m (°C)	Δh_m (J g ⁻¹)
PPCE	92.2 ± 0.5	85–106	33 ± 1	8 ± 2	136–160	32 ± 2
PBCE	146.5 ± 0.5	144–150	39 ± 2	7 ± 2	92–171	55 ± 5
PPeCE	25 ± 5	6–51	0.5 ± 0.1	-15 ± 1	60–76	0.6 ± 0.1
PHCE	101.3 ± 0.5	98–105	43 ± 3	-21 ± 2	50–129	57 ± 5

PPCE = poly(propylene *trans*-1,4-cyclohexanedicarboxylate). PBCE = poly(butylene *trans*-1,4-cyclohexanedicarboxylate). PPeCE = poly(pentamethylene *trans*-1,4-cyclohexanedicarboxylate). PHCE = poly(hexamethylene *trans*-1,4-cyclohexanedicarboxylate).

Figure 4 (left column) reports the cooling ramps obtained for each PCH according to the thermal protocol sketched in Figure 2. The cooling ramps recorded at the lowest cooling rate $|\beta_c| = 0.033 \text{ K s}^{-1}$ were obtained by TOPEM (dashed-dotted lines). The cooling ramps plotted with dashed lines were obtained by conventional DSC. The cooling ramps recorded at the highest cooling rates were obtained by FSC (solid lines). A quick glance

at the cooling curves confirms that PPeCE is the easiest to melt-quench, whereas PBCE is the most challenging. It is indeed necessary, at first, to check that no exothermal signals associated with crystallization are recorded during the cooling ramp. Based on this criterion, a threshold cooling rate could be identified for each PCH (left column, curves in colors). The corresponding critical cooling rates would be somewhere between 0.833 K s^{-1} (50 K min^{-1}) and 100 K s^{-1} for PPCE, between 400 and 500 K s^{-1} for PBCE, between 0.167 K s^{-1} (10 K min^{-1}) and 0.5 K s^{-1} (30 K min^{-1}) for PPeCE, and between 100 and 200 K s^{-1} for PHCE. It is however necessary to double-check these values by considering the heating ramps recorded right after cooling.

In Figure 4 (right column), the heating ramps recorded by TOPEM and DSC were obtained with $\beta_h = |\beta_c|$, and all the heating ramps obtained by FSC were recorded at $\beta_h = 1000 \text{ K s}^{-1}$. The double-check consists in verifying that no endothermal signals associated with melting are recorded upon heating, or that the recorded enthalpy of melting is perfectly balanced by the enthalpy of cold crystallization (if cold crystallization occurs). Based on this additional criterion, the threshold cooling rate for melt-quenching can in some cases be readjusted (right column, curves in colors). About PPCE, for instance, Figure 4 shows that (1) the slowest cooling rate leads to a fully crystallized sample (TOPEM), (2) a progressive increase in the cooling rate hinders the crystallization process and let appears cold crystallization (DSC curves), and (3) FSC allows to melt-quench the sample (no cold crystallization is observed during the subsequent heating ramp because of the higher heating rate with respect to DSC measurements). In the case of PBCE, it is worth noting that (1) only FSC is able to provide sufficiently high cooling rates for an efficient melt-quenching, (2) the range of cooling rates previously identified as critical ($400\text{--}500 \text{ K s}^{-1}$) is sufficient to suppress the crystallization from the melt and cold crystallization occurs during the subsequent heating ramps, (3) a heating rate faster than 1000 K s^{-1} is required to suppress cold crystallization and any other possible melting-recrystallization process. Focusing on the heating ramps recorded after cooling at 300, 400, 500 and 600 K s^{-1} , one may notice that the peak of cold crystallization keeps on evolving, which confirms that vitrification is more and more efficient; the shape of the peak stabilizes between 500 and 600 K s^{-1} , which is therefore considered as a better estimation of the range within which the critical cooling rate is supposed to fall. PPeCE is easily quenched with conventional cooling rates. As for PHCE, based solely on the cooling ramps one may guess that the critical cooling rate is between 100 and 200 K s^{-1} (left column, curves in colors), however the heating ramps clearly show that a crystalline phase is formed for cooling rates up to $500\text{--}1000 \text{ K s}^{-1}$ (right column, curves in colors).

Of all the considered samples, PBCE is the only one being able to cold-crystallize despite the relatively high heating rates used in FSC experiments (1000 K s^{-1}) (Figure 4, right column). Figure 5 illustrates the additional criterion to meet to make sure that a polymer able to cold-crystallize is completely vitrified during melt-quenching. Figure 5 (left) shows a selection of heating ramps recorded after cooling from the melt at different $|\beta_c|$. The additional criterion consists in calculating the enthalpy of cold crystallization Δh_{cc} and the enthalpy of melting Δh_m , and then verifying if they are perfectly balanced. For cooling rates below 100 K s^{-1} , no cold crystallization is observed during the subsequent heating. When faster cooling rates are used, cold crystallization occurs, and the associated enthalpy Δh_{cc} gradually increases until reaching a plateau (18 J g^{-1} for $|\beta_c| = 1000 \text{ K s}^{-1}$). On the other hand, the enthalpy of melting Δh_m decreases from 40 to 18 J g^{-1} as the cooling rate increases up to 100 K s^{-1} , and then stabilizes at 18 J g^{-1} as well. Figure 5 (right) reports the values of Δh_{cc} , Δh_m , and their algebraic difference $\Delta h_m - \Delta h_{cc}$, plotted against the cooling rate $|\beta_c|$ previously used for melt-quenching. With this additional criterion, the critical cooling rate $|\beta_{c,SDG}|$ for PBCE is rather estimated at about 3000 K s^{-1} (when $\Delta h_m - \Delta h_{cc} = 0$).

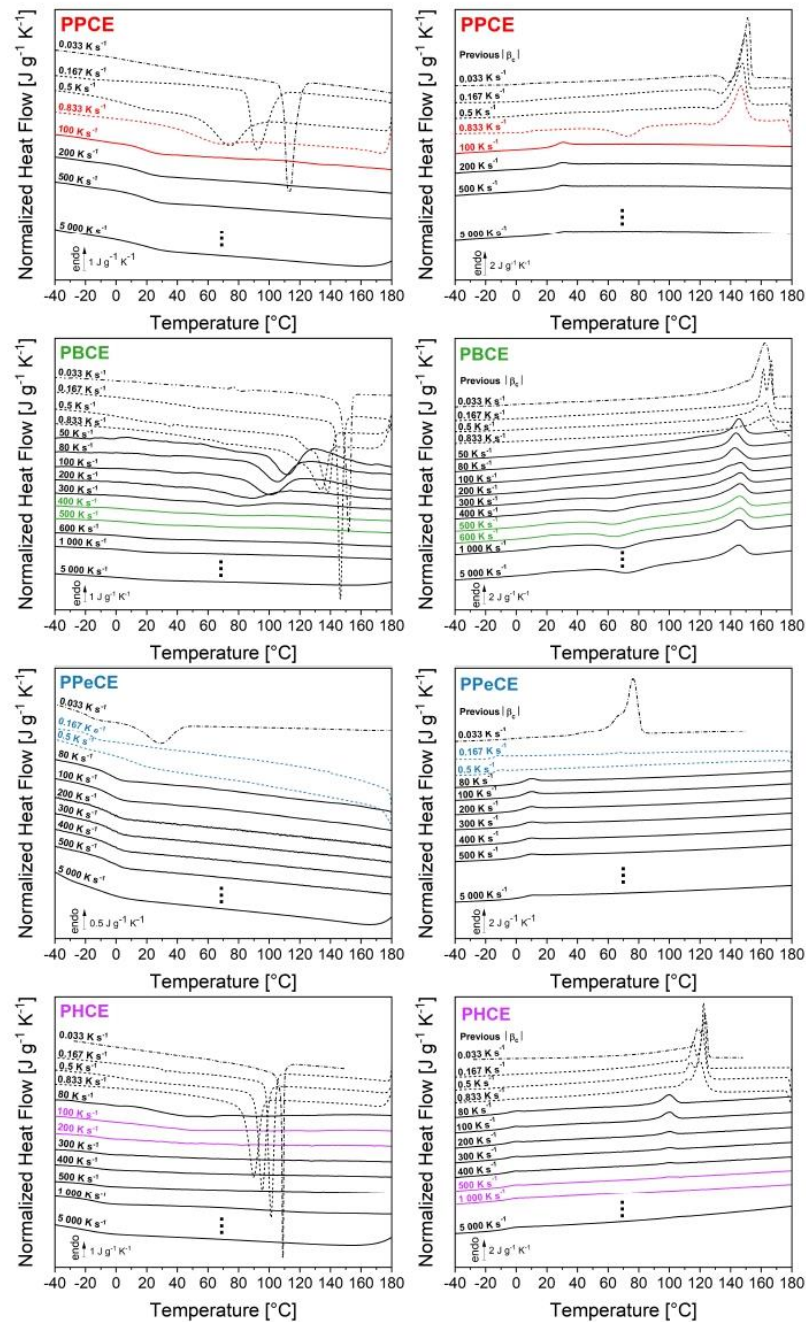


Figure 4. Normalized heat flow recorded upon cooling from the melt (left column) and during the subsequent heating ramp (right column). The curves at the lowest cooling rate $|\beta_c| = 0.033 \text{ K s}^{-1}$ (dashed-dotted lines) were obtained by TOPEM. The curves plotted with dashed lines were obtained by conventional DSC. The curves at the highest cooling rates were obtained by FSC (solid lines). The heating ramps were obtained with $\beta_h = |\beta_c|$ (TOPEM and DSC) or $\beta_h = 1000 \text{ K s}^{-1}$ (FSC). The curves in colors highlight the range within which the critical cooling rate $|\beta_{c,SDG}|$ is supposed to fall based on either crystallization (left column) or subsequent melting (right column). PPCE = poly(propylene *trans*-1,4-cyclohexanedicarboxylate). PBCE = poly(butylene *trans*-1,4-cyclohexanedicarboxylate). PPeCE = poly(pentamethylene *trans*-1,4-cyclohexanedicarboxylate). PHCE = poly(hexamethylene *trans*-1,4-cyclohexanedicarboxylate).

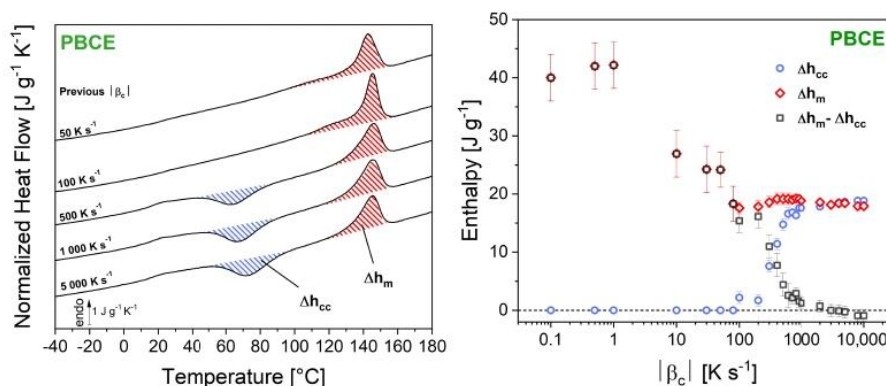


Figure 5. (Left) Calculation of the enthalpies of cold crystallization Δh_{cc} (blue-hatched areas) and melting Δh_m (red-hatched areas) for poly (butylene *trans*-1,4-cyclohexanedicarboxylate) (PBCE) previously cooled down from the melt at different cooling rates $|\beta_c|$. (Right) The enthalpies of cold crystallization Δh_{cc} (blue circles) and melting Δh_m (red diamonds), along with their algebraic difference $\Delta h_m - \Delta h_{cc}$ (black squares) are then plotted against the cooling rate β_c previously used to attempt melt-quenching.

Figure 6 shows the influence of the cooling rate on the crystallization temperature T_c (symbols), and more generally on the temperature range at which crystallization occurs (ΔT_{cc} , bars). Two phenomena are evidenced. The first observation is that, irrespective of n_{CH_2} , an increase in the cooling rate $|\beta_c|$ leads to a decrease in the crystallization temperature T_c and a broadening of the crystallization peak (increase in ΔT_{cc}), from less than 10°C at the slowest cooling rates to more than 30°C at the fastest cooling rates. The shift of T_c and the increase in ΔT_{cc} both prove that the observed transformation is controlled by nucleation; indeed, slow cooling enables the activation of the nuclei at higher temperature, whereas fast cooling retards and slows down the nucleation process [63].

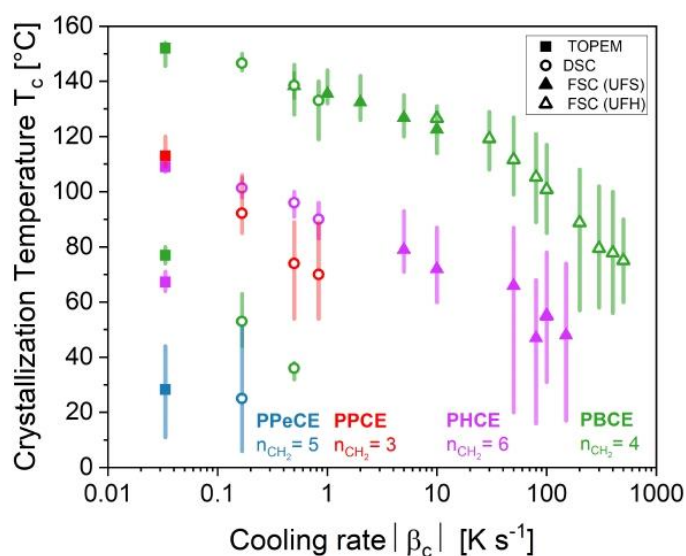


Figure 6. Crystallization temperatures T_c (symbols) and the temperature ranges at which crystallization occurs ΔT_{cc} (bars) measured upon cooling from the melt at different cooling rates $|\beta_c|$. The bars represent the temperature range between the onset ($T_{c,on}$) and endset ($T_{c,end}$) of the crystallization peak. PPeCE = poly(propylene *trans*-1,4-cyclohexanedicarboxylate). PBCE = poly(butylene *trans*-1,4-cyclohexanedicarboxylate). PPeCE = poly(pentamethylene *trans*-1,4-cyclohexanedicarboxylate). PHCE = poly(hexamethylene *trans*-1,4-cyclohexanedicarboxylate).

The second observation is that the odd-numbered polyesters are associated with larger crystallization peaks and lower crystallization temperatures in comparison with their even-numbered counterparts at the same cooling rate. It should also be mentioned that PBCE has recently been shown to crystallize in at least two polymorphic forms, α and β , with the α -form observed upon slow cooling, and the β -form generated with sufficiently fast cooling from the melt (however the explored range of cooling rates did not exceed 50 K min^{-1}) [62]. With this in mind, the shift of T_c from 80 to 150°C could be interpreted as the progressive transformation of the metastable β -form into the more stable α -form as the undercooling is reduced. One may also notice that both PBCE and PHCE have a double value of T_c at the lowest cooling rates. This could be due to either polymorphism (as previously mentioned for PBCE) or just to crystalline perfection through melting-recrystallization upon heating. So far, the literature has reported no evidence of polymorphism for PHCE.

Figure 7 shows a summary of the critical cooling rates $|\beta_{c,crit}|$ reported in the literature for common polymers and for a few other materials (silica, benzocaine, water). The critical cooling rates estimated in this work for PPCE, PBCE, PPeCE and PHCE are also reported for comparison purposes. As expected, the even-numbered PCHs (PBCE with $n_{CH_2} = 4$ and PHCE with $n_{CH_2} = 6$) require faster cooling rates to be effectively melt-quenched as compared to the odd-numbered PCHs (PPCE with $n_{CH_2} = 3$ and PPeCE with $n_{CH_2} = 5$). It also appears that, irrespective of the odd or even character of n_{CH_2} , the value of critical cooling rate decreases as the length of the alkyl chain within the repeating unit increases, suggesting that the methylene groups act as defects for crystal formation. This observation cannot be extended to other systems, such as poly (ethylene terephthalate) (PET) and poly (butylene terephthalate) (PBT), for which an increase of n_{CH_2} from 2 to 4 leads to a four-decade decrease in $|\beta_{c,crit}|$.

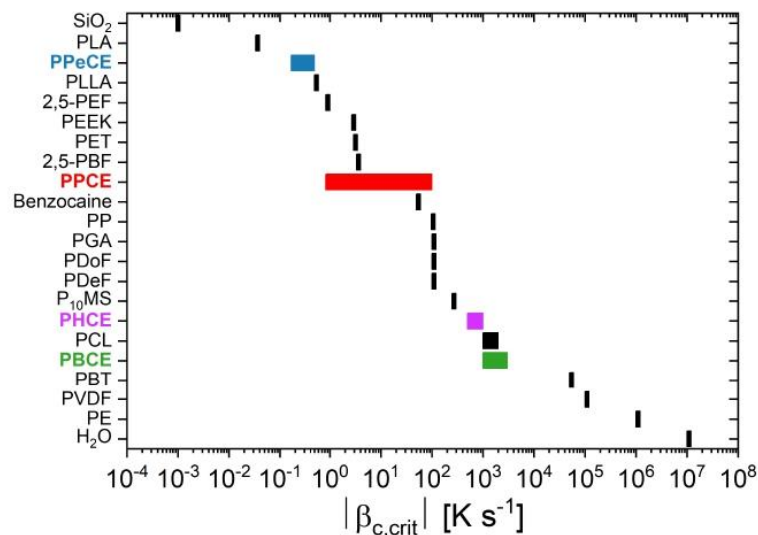


Figure 7. Values of critical cooling rates $|\beta_{c,crit}|$ issued from the literature [9,37,64–71] for common polymers as well as for a few other materials (silica, benzocaine, water). PPCE = poly(propylene *trans*-1,4-cyclohexanedicarboxylate). PBCE = poly(butylene *trans*-1,4-cyclohexanedicarboxylate). PPeCE = poly(pentamethylene *trans*-1,4-cyclohexanedicarboxylate). PHCE = poly(hexamethylene *trans*-1,4-cyclohexanedicarboxylate).

4. Conclusions

This work combines several calorimetric techniques, i.e., Differential Scanning Calorimetry (DSC), modulate-temperature DSC (MT-DSC), stochastically-modulated DSC (TOPEM) and Fast Scanning Calorimetry (FSC), to estimate the critical cooling rate necessary to melt-quench fast-crystallizing polyesters to their fully amorphous state. The method

is applied to a series of poly(alkylene *trans*-1,4-cyclohexanedicarboxylate) (PCHs) with a number of methylene groups n_{CH_2} varying from 3 to 6, i.e., poly(propylene *trans*-1,4-cyclohexanedicarboxylate) (PPCE), poly(butylene *trans*-1,4-cyclohexanedicarboxylate) (PBCE), poly(pentamethylene *trans*-1,4-cyclohexanedicarboxylate) (PPeCE), and poly(hexamethylene *trans*-1,4-cyclohexanedicarboxylate) (PHCE).

MT-DSC and TOPEM ($0.02\text{--}5\text{ K min}^{-1}$) cannot give an insight of what happens during quenching, and DSC ($5\text{--}50\text{ K min}^{-1}$) is limited to slow-crystallizing polymers. FSC is sometimes necessary to emulate the cooling rates experienced by a material during manufacturing, even in the most extreme industrial processing conditions. Since polyesters can crystallize both during the cooling ramp from the melt and during the subsequent heating ramp (cold crystallization), three criteria should be considered: (1) the absence of exothermic events recorded during the cooling ramp (crystallization), (2) the absence of endothermic events recorded during the heating ramp (melting), and (3) the balance of exothermic and endothermic events recorded during the heating ramp (cold crystallization followed by melting).

The results show that, among the four PCHs investigated in this work, the even-numbered ones (PBCE and PHCE) require faster cooling rates compared to the odd-numbered ones (PPCE and PPeCE). Irrespective of the odd or even number of methylene groups introduced in the main structure of the repeating unit, the critical cooling rate decreases as n_{CH_2} increases, suggesting that the methylene groups act as defects during crystal formation. This behaviour seems to be specific to alicyclic polyesters, since the opposite is observed in their aromatic counterparts (poly(butylene terephthalate) (PBT) has a critical cooling rate four-decade smaller compared to poly(ethylene terephthalate) (PET)). PCHs with an even number of methylene groups would be the best choice to minimize the cycle time for injection molding without renouncing to developing a semi-crystalline microstructure, because crystallization starts at high temperatures; however, controlling crystal perfection could be challenging, because their crystallization proceeds very fast and the risk of crystalline reorganization upon further heating is high. For vitrification purposes, PCHs with an odd number of methylene groups are recommended, in particular PPeCE, which is the easiest to melt-quench to its fully amorphous state.

Supplementary Materials: The following supporting information can be downloaded at: <https://www.mdpi.com/article/10.3390/polym16192792/s1>, Figure S1: $^1\text{H-NMR}$ spectrum of poly(propylene *trans*-1,4-cyclohexanedicarboxylate) (PPCE). Figure S2: $^1\text{H-NMR}$ spectrum of poly(butylene *trans*-1,4-cyclohexanedicarboxylate) (PBCE). Figure S3: $^1\text{H-NMR}$ spectrum of poly(pentamethylene *trans*-1,4-cyclohexanedicarboxylate) (PPeCE). Figure S4: $^1\text{H-NMR}$ spectrum of poly(hexamethylene *trans*-1,4-cyclohexanedicarboxylate) (PHCE).

Author Contributions: Conceptualization, A.E. and A.S.-F.; data curation, K.H. and G.G.; formal analysis, K.H.; funding acquisition, A.S.-F. and N.L.; investigation, K.H. and G.G.; methodology, A.E. and A.S.-F.; project administration, A.E. and A.S.-F.; resources, A.E., A.S.-F., M.S. and N.L.; supervision, A.E., A.S.-F., M.S. and N.L.; validation, A.E., A.S.-F., M.S. and N.L.; visualization, K.H.; writing—original draft preparation, A.E. and K.H.; writing—review and editing, A.E., K.H., A.S.-F., G.G., M.S. and N.L. All authors have read and agreed to the published version of the manuscript.

Funding: This research received no external funding besides the Erasmus+ mobility grant and the PhD financial support for Kylian Hallavant.

Institutional Review Board Statement: Not applicable.

Informed Consent Statement: Not applicable.

Data Availability Statement: Dataset available on request from the authors.

Acknowledgments: The authors acknowledge the Erasmus+ Agency for providing Kylian Hallavant a mobility grant that allowed him to go to Bologna and participate in polymer synthesis. The authors acknowledge the Normandy Region for providing the PhD financial support for Kylian Hallavant. Mettler-Toledo is acknowledged for lending the DSC 3+ apparatus. The LabEx EMC³ (Energy Materials and Clean Combustion Center) is acknowledged for financing the acquisition of the Flash DSC 2+

apparatus. Antonella Esposito is grateful to José Maria Kenny for having transmitted her the passion for scientific research about materials. It all started at Università degli Studi di Perugia, Terni, Italy.

Conflicts of Interest: The authors declare no conflicts of interest.

References

1. Geyer, R.; Jambeck, J.R.; Law, K.L. Production, use, and fate of all plastics ever made. *Sci. Adv.* **2017**, *3*, e1700782. [[CrossRef](#)] [[PubMed](#)]
2. Zia, K.M.; Noreen, A.; Zuber, M.; Tabasum, S.; Mujahid, M. Recent developments and future prospects on bio-based polyesters derived from renewable resources: A review. *Int. J. Biol. Macromol.* **2016**, *82*, 1028–1040. [[CrossRef](#)] [[PubMed](#)]
3. Wu, F.; Misra, M.; Mohanty, A.K. Challenges and new opportunities on barrier performance of biodegradable polymers for sustainable packaging. *Prog. Polym. Sci.* **2021**, *117*, 101395. [[CrossRef](#)]
4. Herrera, N.; Salaberria, A.M.; Mathew, A.P.; Oksman, K. Plasticized polylactic acid nanocomposite films with cellulose and chitin nanocrystals prepared using extrusion and compression molding with two cooling rates: Effects on mechanical, thermal and optical properties. *Compos. Part A Appl. Sci. Manuf.* **2016**, *83*, 89–97. [[CrossRef](#)]
5. Adamovsky, S.; Minakov, A.; Schick, C. Scanning microcalorimetry at high cooling rate. *Thermochim. Acta* **2003**, *403*, 55–63. [[CrossRef](#)]
6. Bardelcik, A.; Salisbury, C.P.; Winkler, S.; Wells, M.A.; Worswick, M.J. Effect of cooling rate on the high strain rate properties of boron steel. *Int. J. Impact Eng.* **2010**, *37*, 694–702. [[CrossRef](#)]
7. Buczek, A.; Telejko, T. Investigation of heat transfer coefficient during quenching in various cooling agents. *Int. J. Heat Fluid Flow* **2013**, *44*, 358–364. [[CrossRef](#)]
8. Carmeli, E.; Cavallo, D.; Tranchida, D. Instrument for mimicking fast cooling conditions of polymers: Design and case studies on polypropylene. *Polym. Test.* **2021**, *97*, 107164. [[CrossRef](#)]
9. Gradys, A.; Sajkiewicz, P.; Zhuravlev, E.; Schick, C. Kinetics of isothermal and non-isothermal crystallization of poly(vinylidene fluoride) by fast scanning calorimetry. *Polymer* **2016**, *82*, 40–48. [[CrossRef](#)]
10. Han, T.; Chen, J.; Wei, Z.; Qu, N.; Liu, Y.; Yang, D.; Zhao, S.; Lai, Z.; Jiang, M.; Zhu, J. Effect of cooling rate on microstructure and mechanical properties of AlCrFe2Ni2 medium entropy alloy fabricated by laser powder bed fusion. *J. Mater. Res. Technol.* **2023**, *25*, 4063–4073. [[CrossRef](#)]
11. Hyer, H.; Zhou, L.; Park, S.; Gottsfritz, G.; Benson, G.; Tolentino, B.; McWilliams, B.; Cho, K.; Sohn, Y. Understanding the Laser Powder Bed Fusion of AlSi10Mg Alloy. *Metallogr. Microstruct. Anal.* **2020**, *9*, 484–502. [[CrossRef](#)]
12. Kamal, M.R.; Kalyon, D. Heat transfer and microstructure in extrusion blowmolding. *Polym. Eng. Sci.* **1983**, *23*, 503–509. [[CrossRef](#)]
13. Li, X.; Song, W.; Yang, K.; Krishnan, N.A.; Wang, B.; Smedskjaer, M.M.; Mauro, J.C.; Sant, G.; Balonis, M.; Bauchy, M. Cooling rate effects in sodium silicate glasses: Bridging the gap between molecular dynamics simulations and experiments. *J. Chem. Phys.* **2017**, *147*, 074501. [[CrossRef](#)] [[PubMed](#)]
14. Minakov, A.A.; Schick, C. Dynamics of the temperature distribution in ultra-fast thin-film calorimeter sensors. *Thermochim. Acta* **2015**, *603*, 205–217. [[CrossRef](#)]
15. Pijpers, T.F.; Mathot, V.B.; Goderis, B.; Scherrenberg, R.L.; van der Vegte, E.W. High-Speed Calorimetry for the Study of the Kinetics of (De)vitrification, Crystallization, and Melting of Macromolecules. *Macromolecules* **2002**, *35*, 3601–3613. [[CrossRef](#)]
16. Poorhaydari, K.; Patchett, B.M.; Ivey, D.G. Estimation of cooling rate in the welding of plates with intermediate thickness. *Weld. J.* **2005**, *84*, 149s–155s.
17. Seppala, J.E.; Migler, K.D. Infrared thermography of welding zones produced by polymer extrusion additive manufacturing. *Addit. Manuf.* **2016**, *12*, 71–76. [[CrossRef](#)]
18. Shen, Y.; Li, Y.; Chen, C.; Tsai, H.L. 3D printing of large, complex metallic glass structures. *Mater. Des.* **2017**, *117*, 213–222. [[CrossRef](#)]
19. Suplicz, A.; Szabo, F.; Kovacs, J. Injection molding of ceramic filled polypropylene: The effect of thermal conductivity and cooling rate on crystallinity. *Thermochim. Acta* **2013**, *574*, 145–150. [[CrossRef](#)]
20. Vanden Poel, G.; Mathot, V.B. High performance differential scanning calorimetry (HPer DSC): A powerful analytical tool for the study of the metastability of polymers. *Thermochim. Acta* **2007**, *461*, 107–121. [[CrossRef](#)]
21. Takata, N.; Liu, M.; Li, H.; Suzuki, A.; Kobashi, M. Fast scanning calorimetry study of Al alloy powder for understanding microstructural development in laser powder bed fusion. *Mater. Des.* **2022**, *219*, 110830. [[CrossRef](#)]
22. Zhuravlev, E.; Schick, C. Fast scanning power compensated differential scanning nano-calorimeter: 1. The device. *Thermochim. Acta* **2010**, *505*, 1–13. [[CrossRef](#)]
23. Zuidema, H.; Peters, G.W.M.; Meijer, H.E.H. Influence of cooling rate on pVT-data of semicrystalline polymers. *J. Appl. Polym. Sci.* **2001**, *82*, 1170–1186. [[CrossRef](#)]
24. Monnier, X.; Maigret, J.E.; Lourdin, D.; Saiter, A. Glass transition of anhydrous starch by fast scanning calorimetry. *Carbohydr. Polym.* **2017**, *173*, 77–83. [[CrossRef](#)]
25. Genovese, L.; Lotti, N.; Gazzano, M.; Finelli, L.; Munari, A. New eco-friendly random copolyesters based on poly(propylene cyclohexanedicarboxylate): Structure-properties relationships. *EXPRESS Polym. Lett.* **2015**, *9*, 972–983. [[CrossRef](#)]
26. Gigli, M.; Lotti, N.; Gazzano, M.; Siracusa, V.; Finelli, L.; Munari, A.; Dalla Rosa, M. Fully Aliphatic Copolyesters Based on Poly(butylene 1,4-cyclohexanedicarboxylate) with Promising Mechanical and Barrier Properties for Food Packaging Applications. *Ind. Eng. Chem. Res.* **2013**, *52*, 12876–12886. [[CrossRef](#)]

27. Guidotti, G.; Soccio, M.; Siracusa, V.; Gazzano, M.; Munari, A.; Lotti, N. Novel Random Copolymers of Poly(butylene 1,4-cyclohexane dicarboxylate) with Outstanding Barrier Properties for Green and Sustainable Packaging: Content and Length of Aliphatic Side Chains as Efficient Tools to Tailor the Material's Final Performance. *Polymers* **2018**, *10*, 866. [[CrossRef](#)]
28. Soccio, M.; Lotti, N.; Finelli, L.; Gazzano, M.; Munari, A. Aliphatic poly(propylene dicarboxylate)s: Effect of chain length on thermal properties and crystallization kinetics. *Polymer* **2007**, *48*, 3125–3136. [[CrossRef](#)]
29. Siracusa, V.; Genovese, L.; Ingrao, C.; Munari, A.; Lotti, N. Barrier Properties of Poly(Propylene Cyclohexanedicarboxylate) Random Eco-Friendly Copolyesters. *Polymers* **2018**, *10*, 502. [[CrossRef](#)]
30. Kumar, N.; Chaudhary, S.; Singh, P.; Thapa, K.B.; Kumar, D. Electro-optical odd-even effect of APAPA liquid crystal molecules studied under the influence of an extraneous electric field (THz): A theoretical approach. *J. Mol. Liq.* **2020**, *318*, 114254. [[CrossRef](#)]
31. Zhou, C.; Wei, Z.; Yu, Y.; Shao, S.; Leng, X.; Wang, Y.; Li, Y. Biobased long-chain aliphatic polyesters of 1,12-dodecanedioic acid with a variety of diols: Odd-even effect and mechanical properties. *Mater. Today Commun.* **2019**, *19*, 450–458. [[CrossRef](#)]
32. Zhang, X.; Zuo, X.; Ortmann, P.; Mecking, S.; Alamo, R.G. Crystallization of Long-Spaced Precision Polyacetals I: Melting and Recrystallization of Rapidly Formed Crystallites. *Macromolecules* **2019**, *52*, 4934–4948. [[CrossRef](#)]
33. Pérez-Camargo, R.A.; Meabe, L.; Liu, G.; Sardon, H.; Zhao, Y.; Wang, D.; Müller, A.J. Even–Odd Effect in Aliphatic Polycarbonates with Different Chain Lengths: From Poly (Hexamethylene Carbonate) to Poly (Dodecamethylene Carbonate). *Macromolecules* **2021**, *54*, 259–271. [[CrossRef](#)]
34. Flores, I.; Pérez-Camargo, R.A.; Gabirondo, E.; Caputo, M.R.; Liu, G.; Wang, D.; Sardon, H.; Müller, A.J. Unexpected Structural Properties in the Saturation Region of the Odd–Even Effects in Aliphatic Polyethers: Influence of Crystallization Conditions. *Macromolecules* **2022**, *55*, 584–594. [[CrossRef](#)]
35. Masubuchi, T.; Sakai, M.; Kojio, K.; Furukawa, M.; Aoyagi, T. Structure and Properties of Aliphatic Poly(carbonate) glycols with Different Methylene Unit Length. *e-J. Soft Mater.* **2007**, *3*, 55–63. [[CrossRef](#)]
36. Guidotti, G.; Fosse, C.; Soccio, M.; Gazzano, M.; Siracusa, V.; Delbreilh, L.; Esposito, A.; Lotti, N. Synthesis and properties of poly(alkylene trans-1,4-cyclohexanedicarboxylate)s with different glycolic subunits. *Polym. Degrad. Stab.* **2024**, under review.
37. Salmerón Sánchez, M.; Mathot, V.B.F.; Vanden Poel, G.; Gómez Ribelles, J.L. Effect of the Cooling Rate on the Nucleation Kinetics of Poly(L-Lactic Acid) and Its Influence on Morphology. *Macromolecules* **2007**, *40*, 7989–7997. [[CrossRef](#)]
38. Hu, Y.; Liao, Y.; Zheng, Y.; Ikeda, K.; Okabe, R.; Wu, R.; Ozaki, R.; Xu, J.; Xu, Q. Influence of Cooling Rate on Crystallization Behavior of Semi-Crystalline Polypropylene: Experiments and Mathematical Modeling. *Polymers* **2022**, *14*, 3646. [[CrossRef](#)]
39. Boyer, S.; Haudin, J.M. Crystallization of polymers at constant and high cooling rates: A new hot-stage microscopy set-up. *Polym. Test.* **2010**, *29*, 445–452. [[CrossRef](#)]
40. Mejres, M.; Hallavant, K.; Guidotti, G.; Soccio, M.; Lotti, N.; Esposito, A.; Saiter-Fourcin, A. Physical aging of a biodegradable alicyclic polymer: Poly (pentamethylene trans-1,4-cyclohexanedicarboxylate). *J. Non-Cryst. Solids* **2024**, *629*, 122874. [[CrossRef](#)]
41. Hallavant, K.; Mejres, M.; Schawe, J.E.K.; Esposito, A.; Saiter-Fourcin, A. Influence of Chemical Composition and Structure on the Cooperative Fluctuation in Supercooled Glass-Forming Liquids. *J. Phys. Chem. Lett.* **2024**, *15*, 4508–4514. [[CrossRef](#)] [[PubMed](#)]
42. Monnier, X.; Saiter, A.; Dargent, E. Vitrification of PLA by fast scanning calorimetry: Towards unique glass above critical cooling rate? *Thermochim. Acta* **2017**, *658*, 47–54. [[CrossRef](#)]
43. Schawe, J.E.; Löffler, J. Existence of multiple critical cooling rates which generate different types of monolithic metallic glass. *Nat. Commun.* **2019**, *10*, 1337. [[CrossRef](#)] [[PubMed](#)]
44. Zheng, Y.; Pan, P. Crystallization of biodegradable and biobased polyesters: Polymorphism, cocrystallization, and structure-property relationship. *Prog. Polym. Sci.* **2020**, *109*, 101291. [[CrossRef](#)]
45. Corradini, P.; Guerra, G. Polymorphism in polymers. In *Macromolecules: Synthesis, Order And Advanced Properties*; Springer: Berlin/Heidelberg, Germany, 1992; pp. 183–217.
46. Di Lorenzo, M.L.; Cocca, M.; Malinconico, M. Crystal polymorphism of poly(l-lactic acid) and its influence on thermal properties. *Thermochim. Acta* **2011**, *522*, 110–117. [[CrossRef](#)]
47. Cocca, M.; Lorenzo, M.L.D.; Malinconico, M.; Frezza, V. Influence of crystal polymorphism on mechanical and barrier properties of poly(l-lactic acid). *Eur. Polym. J.* **2011**, *47*, 1073–1080. [[CrossRef](#)]
48. Esposito, A.; Delpouve, N.; Causin, V.; Dhotel, A.; Delbreilh, L.; Dargent, E. From a Three-Phase Model to a Continuous Description of Molecular Mobility in Semicrystalline Poly(hydroxybutyrate-co-hydroxyvalerate). *Macromolecules* **2016**, *49*, 4850–4861. [[CrossRef](#)]
49. Fosse, C.; Esposito, A.; Lemechko, P.; Salim, Y.S.; Causin, V.; Gaucher, V.; Bruzard, S.; Sudesh, K.; Delbreilh, L.; Dargent, E. Effect of Chemical Composition on Molecular Mobility and Phase Coupling in Poly(3-hydroxybutyrate-co-3-hydroxyvalerate) and Poly(3-hydroxybutyrate-co-3-hydroxyhexanoate) with Different Comonomer Contents. *J. Polym. Environ.* **2023**, *31*, 4430–4447. [[CrossRef](#)]
50. Bourdet, A.; Fosse, C.; Garda, M.R.; Thiagarajan, S.; Delbreilh, L.; Esposito, A.; Dargent, E. Microstructural consequences of isothermal crystallization in homo- and co-polyesters based on 2,5- and 2,4-furandicarboxylic acid. *Polymer* **2023**, *272*, 125835. [[CrossRef](#)]
51. Grady, A.; Sajkiewicz, P.; Minakov, A.; Adamovsky, S.; Schick, C.; Hashimoto, T.; Saijo, K. Crystallization of polypropylene at various cooling rates. *Mater. Sci. Eng. A* **2005**, *413–414*, 442–446. [[CrossRef](#)]
52. Androsch, R.; Di Lorenzo, M.L.; Schick, C.; Wunderlich, B. Mesophases in polyethylene, polypropylene, and poly(1-butene). *Polymer* **2010**, *51*, 4639–4662. [[CrossRef](#)]
53. Li, J.; Zhu, Z.; Li, T.; Peng, X.; Jiang, S.; Turng, L.S. Quantification of the Young's modulus for polypropylene: Influence of initial crystallinity and service temperature. *J. Appl. Polym. Sci.* **2020**, *137*, 48581. [[CrossRef](#)]

54. Wright, D.; Dunk, R.; Bouvart, D.; Autran, M. The effect of crystallinity on the properties of injection moulded polypropylene and polyacetal. *Polymer* **1988**, *29*, 793–796. [[CrossRef](#)]
55. Schick, C.; Mathot, V. (Eds.) *Fast Scanning Calorimetry*; Springer: Cham, Switzerland, 2016.
56. Schawe, J.; Hütter, T.; Heitz, C.; Alig, I.; Lellinger, D. Stochastic temperature modulation: A new technique in temperature-modulated DSC. *Thermochim. Acta* **2006**, *446*, 147–155. [[CrossRef](#)]
57. Klein, J.P.; Gdowski, Z.M.; Register, R.A. Controlling thermomechanical behavior of semicrystalline hydrogenated polynorbornene through the *cis*- to *trans*-cyclopentylene ratio. *J. Polym. Sci.* **2022**, *60*, 266–275. [[CrossRef](#)]
58. Brunelle, D.J.; Jang, T. Optimization of poly(1,4-cyclohexylidene cyclohexane-1,4-dicarboxylate) (PCCD) preparation for increased crystallinity. *Polymer* **2006**, *47*, 4094–4104. [[CrossRef](#)]
59. Puente, J.A.S.; Esposito, A.; Chivrac, F.; Dargent, E. Effects of Size and Specific Surface Area of Boron Nitride Particles on the Crystallization of Bacterial Poly(3-hydroxybutyrate-co-3-hydroxyvalerate). *Macromol. Symp.* **2013**, *328*, 8–19. [[CrossRef](#)]
60. Puente, J.A.S.; Esposito, A.; Chivrac, F.; Dargent, E. Effect of boron nitride as a nucleating agent on the crystallization of bacterial poly(3-hydroxybutyrate). *J. Appl. Polym. Sci.* **2013**, *128*, 2586–2594. [[CrossRef](#)]
61. Duer, M.J.; Roper, C. A solid-state NMR investigation of the odd–even effect in a series of liquid-crystal dimers. *Phys. Chem. Chem. Phys.* **2003**, *5*, 3034–3041. [[CrossRef](#)]
62. Hu, W.; Ma, T.; Zhou, Y.; Soccio, M.; Lotti, N.; Cavallo, D.; Wang, D.; Liu, G. Crystal Structure and Polymorphism of Poly(butylene-*trans*-1,4-cyclohexane dicarboxylate). *Macromolecules* **2024**, *57*, 4374–4384. [[CrossRef](#)]
63. Martins, J.C.; Novack, K.M.; Gomes, A.S. Non-isothermal crystallization kinetics of thermotropic polyesters with flexible spacers in the main chain. *Polymer* **1998**, *39*, 6941–6944. [[CrossRef](#)]
64. Barandiarán, J.; Colmenero, J. Continuous cooling approximation for the formation of a glass. *J. Non-Cryst. Solids* **1981**, *46*, 277–287. [[CrossRef](#)]
65. Chen, Y.; Xie, K.; He, Y.; Hu, W. Fast-Scanning Chip-Calorimetry Measurement of Crystallization Kinetics of Poly(Glycolic Acid). *Polymers* **2021**, *13*, 891. [[CrossRef](#)]
66. Furushima, Y.; Kumazawa, S.; Umetsu, H.; Toda, A.; Zhuravlev, E.; Schick, C. Melting and recrystallization kinetics of poly(butylene terephthalate). *Polymer* **2017**, *109*, 307–314. [[CrossRef](#)]
67. Kagawa, F.; Oike, H. Quenching of Charge and Spin Degrees of Freedom in Condensed Matter. *Adv. Mater.* **2017**, *29*, 1601979. [[CrossRef](#)]
68. Mukhametzyanov, T.A.; Andrianov, R.A.; Bolmatenkov, D.N.; Yagofarov, M.I.; Solomonov, B.N.; Schick, C. Nucleation and crystallization of deeply supercooled benzocaine, a rapidly crystallizing organic compound: A Fast scanning calorimetry investigation. *Thermochim. Acta* **2023**, *730*, 179613. [[CrossRef](#)]
69. Papageorgiou, G.Z.; Papageorgiou, D.G.; Tsanaktsis, V.; Bikiaris, D.N. Synthesis of the bio-based polyester poly(propylene 2,5-furan dicarboxylate). Comparison of thermal behavior and solid state structure with its terephthalate and naphthalate homologues. *Polymer* **2015**, *62*, 28–38. [[CrossRef](#)]
70. Papageorgiou, D.G.; Guigo, N.; Tsanaktsis, V.; Exarhopoulos, S.; Bikiaris, D.N.; Sbirrazzuoli, N.; Papageorgiou, G.Z. Fast Crystallization and Melting Behavior of a Long-Spaced Aliphatic Furandicarboxylate Biobased Polyester, Poly(dodecylene 2,5-furanoate). *Ind. Eng. Chem. Res.* **2016**, *55*, 5315–5326. [[CrossRef](#)]
71. Stoclet, G.; Gobius du Sart, G.; Yeniad, B.; de Vos, S.; Lefebvre, J. Isothermal crystallization and structural characterization of poly(ethylene-2,5-furanoate). *Polymer* **2015**, *72*, 165–176. [[CrossRef](#)]

Disclaimer/Publisher's Note: The statements, opinions and data contained in all publications are solely those of the individual author(s) and contributor(s) and not of MDPI and/or the editor(s). MDPI and/or the editor(s) disclaim responsibility for any injury to people or property resulting from any ideas, methods, instructions or products referred to in the content.

Étude de la mobilité moléculaire de polyesters biosourcés à structures chimiques contrôlées

Keywords

Semi-crystalline polymers, bio-sourced and biodegradable polyesters, microstructure, molecular mobility, thermal analysis, calorimetry.

Abstract

The decline of fossil resources and the raise of collective awareness about the impact of plastic waste on the environment impose to look for possible alternatives to petroleum-based polymers with reduced carbon footprint and environmental risks. For this reason, bio-sourced and/or biodegradable polyesters have attracted much attention from both academic researchers and industrials. This thesis focuses on the thermal characterization of co-polyesters based on hydroxy-fatty acids, which are extracted from tomato-peel agro-wastes, and poly (alkylene *trans*-1,4-cyclohexanedicarboxylate) (PCHs), which are biodegradable and potentially biobased materials with interesting barrier properties. This thesis shows that both systems have high crystallization rates and form complex microstructures involving several polymorphs with a high density of small spherulites. The microstructure depends on the processing conditions (cooling rate from the melt, crystallization temperature) and on the chemical nature of the material (crosslinking density for the hydroxy-fatty acids, and alkyl chain length within the main structure of the repeating unit for the PCHs). Crosslinking reduces the mobility of the macromolecular chains and inhibits crystallization, whereas the alkyl chain length induces an odd-even effect with consequences on the melting and crystallization temperatures, on the coupling between the amorphous and crystalline phases, on the fragility index and on the glass-forming ability.

Résumé

La diminution des ressources fossiles et la prise de conscience collective de l'impact des déchets plastiques sur l'environnement nécessitent la recherche d'alternatives possibles aux polymères issus du pétrole, avec une empreinte carbone et des risques environnementaux réduits. C'est pourquoi les polyesters biosourcés et/ou biodégradables ont attiré l'attention des chercheurs universitaires et des industriels. Cette thèse se concentre sur la caractérisation thermique des copolyesters à base d'acides gras hydroxylés, qui sont extraits des déchets agricoles de tomate, et de poly (alkylene *trans*-1,4-cyclohexanedicarboxylate) (PCHs), qui sont des matériaux biodégradables et potentiellement biosourcés avec d'intéressantes propriétés barrières. Cette thèse montre que les deux systèmes ont des vitesses de cristallisation élevées et forment des microstructures complexes impliquant plusieurs polymorphes avec une forte densité de petites sphérulites. La microstructure dépend des conditions de traitement (vitesse de refroidissement depuis le fondu, température de cristallisation) et de la nature chimique du matériau (densité de réticulation pour les acides gras hydroxylés et longueur de la chaîne alkyle dans la chaîne principale de l'unité répétitive pour les PCHs). La réticulation réduit la mobilité des chaînes macromoléculaires et inhibe la cristallisation, tandis que la longueur de la chaîne alkyle induit un effet pair-impair avec des conséquences sur les températures de fusion et de cristallisation, sur le couplage entre les phases amorphe et cristalline, sur l'indice de fragilité et sur l'aptitude à former un verre.